Plasma-assisted modifications and synthesis of nanomaterials

Tatiana Habib

Université Fédérale
Toulouse Midi-Pyrénées

THÈSE

En vue de l'obtention du
DOCTORAT DE L'UNIVERSITÉ DE TOULOUSE

Délivré par l'Université Toulouse 3 - Paul Sabatier

Cotutelle internationale: Université de São Paulo

Présentée et soutenue par

Tatiana HABIB

Le 20 octobre 2023

Modifications et synthèses de nanomatériaux assistées par plasma

Ecole doctorale : **GEETS - Génie Electrique Electronique,Télécommunications et Santé : du système au nanosystème**

Spécialité : **Ingénierie des Plasmas**

Unité de recherche :
DPHE - Diagnostic des plasmas hors équilibre

Thèse dirigée par
Bruno CAILLIER et José Maurício Almeida CAIUT

Jury

Mme Sandra CRUZ, Rapporteure
M. Jerome FRESNAIS, Rapporteur
M. Sidney J.L. RIBEIRAO, Examinateur
M. Marc VERELST, Examinateur
M. Bruno CAILLIER, Directeur de thèse
M. José Mauricio A. CAIUT, Co-directeur de thèse

This thesis represents a collaborative research under the framework of a cotutelle program. Over the course of three years, this work was conducted, with one year at the University of São Paulo in Ribeirão Preto, Brazil, and two years at the Institut National Universitaire de Champollion in Albi, France.

We would like to acknowledge the support provided by the Coordenação de Aperfeiçoamento de Pessoal de Nível Superior (CAPES) under Finance Code 001, and the Fundação de Amparo à Pesquisa do Estado de São Paulo (FAPESP), through Grants No. 2019/18828-1 and 2018/10172-7.

Acknowledgements

I wish to extend my sincere appreciation to all those who have contributed to the realization of this thesis. Foremost, I express my deepest gratitude to my supervisors, Bruno and Mauricio, for their trust, unwavering support, valuable advice and guidance without which this thesis would not have been possible.

Furthermore, I want to thank the members of the jury for accepting the responsibility of evaluating this thesis. Your insights and feedback were invaluable to the culmination of this academic endeavor.

I express my sincere gratitude to Alessandro Patelli for our collaborative efforts and his welcome to conduct some experimental work in his lab in Italy. His help and expertise was an important role in shaping and enriching this thesis.

My heartfelt thanks also go out to all the members of the labs in France and Brazil, whose warm welcome made me feel like a valued member of their scientific community.
In DPHE, starting with a special acknowledgment to Philippe for his valuable guidance, advice, and the laughter that lightened the journey in the lab. Cristina, your help and availability with the microbiology tests and your support were indispensable. To the members of the labs, Florent, Laurent, Juslan, and others – thank you for your contributions and support.
I am immensely grateful to the PhD students who walked alongside me in DPHE. Ibtissam, le sourire du labo, your warm welcome meant the world to me, especially when I was new to the country. We spent a lot of beautiful times together (in and out of the lab of course). Pierre (Peterrr), although we met in my last year in the lab, it felt like we knew each other for ages. Thank you for the fun times in the lab and, of course, in the gym. Abdoul, starting and finishing our thesis together, your wisdom and calm demeanor were a constant source of support for all of us. A special thanks to Guillaume who made our coffee breaks fun and dynamic.
Moving to the Nanolum lab, I can't thank the beautiful Brazilian people enough – Roberta, Eloisa, Francisco, Pedro, and Cintya. Your warmth and efforts made me feel at home and so welcomed. You always made me feel part of your group.

Finally, my heartfelt gratitude to my family – parents and brother – for their unwavering support. Without them, none of this would have been possible. You are the ones who pushed me to achieve this and not give up when living abroad is tough. To my best friend, Nour, words can't express my appreciation for you. Thank you for your presence during my toughest times and your advice.

I am truly grateful to have you all in my life.

List of Publications

Published articles

T. Habib, J. M. A. Caiut, and B. Caillier, "Synthesis of silver nanoparticles by atmospheric pressure plasma jet", Nanotechnology, vol. 33, no. 32, p. 325603, May 2022.

E. G. Hilario, **T. Habib**, C. V. T. Maciel, R. F. Da Silva, D. F. Luz, G. S. Soares, B. Caillier, C. Jacinto, L. Maia, J. M. A. Caiut, and A. L. Moura, "Metallic nanoparticles-decorated NdxY1-xAl3(BO3)4 sub-micrometric particles to enhance anti-Stokes excitation performance", Optical Materials: X, vol. 19, p. 100254, Jul. 2023.

T. Habib, L. Ceroni, A. Patelli, J. M. A. Caiut, and B. Caillier, "Impact of micropulse and radio frequency coupling in an atmospheric pressure plasma jet on the synthesis of gold nanoparticles," Plasma, vol. 6, no. 4, Dec. 2023.

Conferences

T. Habib, J. M. A. Caiut, and B. Caillier, "Plasma-assisted synthesis of silver nanoparticles", 2021 IEEE International Conference on Plasma Science (ICOPS), Sept. 2021.

T. Habib, J. M. A. Caiut, and B. Caillier, "Synthesis of silver nanoparticles by atmospheric pressure plasma jet", III Workshop do INCT de Fotonica, Brazil, Feb. 2022.

T. Habib, J. M. A. Caiut, and B. Caillier, "Plasma-assisted synthesis of silver and gold nanoparticles", 45a reuniao anual da SBQ, Maceio, Brazil, May 2022.

T. Habib, J. M. A. Caiut, and B. Caillier, "Gold nanoparticles synthesized by atmospheric pressure plasma jet", 2022 IEEE International Conference on Plasma Science (ICOPS), Seattle, USA, May 2022.

T. Habib, J. M. A. Caiut, and B. Caillier, "Synthesis of nanoparticles by plasma for biological applications", HappyBio GDR 2022, Albi, France, Nov. 2022.

T. Habib, J. M. A. Caiut, and B. Caillier, "Synthesis and characterization of metal nanoparticles by cold plasma jet in contact with a liquid", GEETS congress, Toulouse, France, Jun. 2023.

T. Habib, J. M. A. Caiut, and B. Caillier, "Atmospheric pressure plasma jet in contact with a liquid for the formation of silver and gold nanoparticles and their applications", Plasma Thin Film International Union Meeting PLATHINIUM, Antibes, France, Sept. 2023.

Table of Contents

List of Figures 3
List of Tables 7
Introduction 10
1 Literature Review 16
1.1 Introduction to nanotechnology 16
1.2 Nanomaterials: classifications and properties 19
1.2.1 Classifications of nanomaterials 20
1.2.2 Metallic nanoparticles and their properties 23
1.2.2.1 Surface energy 23
1.2.2.2 Optical properties 24
1.2.2.3 Chemical properties 26
1.2.2.4 Electrical properties 27
1.3 Applications of silver and gold nanoparticles 27
1.4 Synthesis methods 30
1.4.1 Top-down approach 31
1.4.2 Bottom-up approach 32
1.5 Introduction to nanotechnology 34
1.6 Plasmas: classifications and properties 35
1.6.1 Classifications of plasmas 36
1.6.2 Cold plasmas and their properties 40
1.7 Applications of plasma discharges 42
1.8 Plasma-liquid interactions 43
1.9 Metal nanoparticles synthesis by atmospheric pressure plasma discharge 46
1.9.1 Chemical parameters 47
1.9.2 Physical parameters 48
1.10 Aims and objectives of this thesis 48
1.11 Conclusions 49
2 Materials and Methods 52
2.1 Plasma experimental configurations 52
2.1.1 Plasma experimental devices 52
2.1.1.1 Atmospheric pressure plasma jet 52
2.1.1.2 Dual-frequency atmospheric pressure plasma jet 54
2.1.2 Plasma characterization techniques 55
2.1.2.1 Electrical diagnostics 55
2.1.2.2 Optical diagnostics - Optical emission spectroscopy (OES) 56
2.2 Plasma treated target 58
2.3 Liquid chemical characterization 58
2.4 Metallic nanoparticles 59
2.4.1 Synthesis of silver nanoparticles 59

2.4.2 Synthesis of gold nanoparticles 60
2.4.3 Nanoparticles characterization techniques 61
2.4.3.1 Ultraviolet-visible spectroscopy (UV-vis) 61
2.4.3.2 Dynamic light scattering (DLS) 63
2.4.3.3 Scanning electron microscopy (SEM) 64
2.4.3.4 Electron dispersive X-ray spectroscopy (EDX) 66
2.4.3.5 Transmission electron microscopy (TEM) 67
2.4.3.6 Atomic force microscopy (AFM) 69
2.4.3.7 X-ray diffraction (XRD) 70
2.5 Conclusions 72
3 Synthesis of Metallic Nanoparticles by Atmospheric Pressure Plasma Jet 75
3.1 Plasma characterization 76
3.1.1 Optical emission spectroscopy (OES) 76
3.1.1.1 Optical emission spectrum of the plasma jet 76
3.1.1.2 Intensity of reactive species along the plasma jet 79
3.2 Liquid chemical characterization 81
3.3 Synthesis of silver nanoparticles 83
3.3.1 Effect of the plasma interaction duration 87
3.3.2 Effect of the metal precursor's concentration 88
3.3.3 Effect of the capping agent's concentration 92
3.4 Synthesis of gold nanoparticles 100
3.4.1 Effect of the plasma interaction duration 103
3.4.2 Effect of the metal precursor's concentration 105
3.4.3 Effect of the capping agent's concentration 108
3.5 Conclusions 111
4 Synthesis of Metallic Nanoparticles by Dual-Frequency Atmospheric Pressure Plasma Jet 115
4.1 Plasma characterization 116
4.1.1 Optical emission spectroscopy (OES) 117
4.1.2 Charge collected 120
4.2 Influence of helium as process gas on gold nanoparticles morphology 122
4.3 Influence of argon as process gas on nanoparticles morphology 127
4.4 Implications of dual-frequency plasma configuration on gold nanoparticles production 130
4.5 Conclusions 131
Conclusions 135
Perspectives 141
Appendix 147
Bibliography 149

List of Figures

Figure 1. Schematic representations of Buckminsterfullerene C60 molecule [6]. 18
Figure 2. Classifications of nanoparticles based on their composition, dimension, and origin. Reproduced from [11]. 23
Figure 3. The Lycurgus cup appearing a) red in transmitted light and b) green in reflected light [33] 25
Figure 4. Schematic illustration of the localized surface plasmon resonance (LSPR) of metallic nanoparticles [35]. 25
Figure 5. UV-vis absorbance spectra of silver nanoparticles with diameters ranging from 10 to 100 nm with mass concentrations of 0.02 mg/ml [41]. 26
Figure 6. Schematic representation of the top-down and bottom-up approaches for the synthesis of nanoparticles. Reproduced from [69] 30
Figure 7. Schematic representation of the four states of matter. Reproduced from [84] 35
Figure 8. Classification of different plasmas based on their electron density and temperature [89]. 38
Figure 9. Classification of plasmas based on their degree of ionization, pressure, and origin. 39
Figure 10. Schematic representation of various cold plasmas at atmospheric pressure [87] ... 41
Figure 11. Schematic representation of different discharges: (A) plasma discharge in liquid phase, (B)-(D) plasma discharges above liquid phase, and (E)-(F) multiphase plasma discharges [99] 44
Figure 12. Schematic representation of the main interactions between the plasma and the liquid interface [102] 46
Figure 13. Schematic representation of a controlled nanoparticle nucleation and growth. 47
Figure 14. Experimental setup of the atmospheric pressure plasma jet. 53
Figure 15. Pictures of the power supply a) left side view, b) top view, c) right side view showing the different input/output outlets and d) control monitor interface. 53
Figure 16. Experimental setup of the plasma jet coupled with two power supplies. 54
Figure 17. The typical discharge current of the plasma as a function of time. 56
Figure 18. Experimental setup with three different targets: a) free plasma jet, b) flat surface, and c) solution. 57
Figure 19. Schematic representation of the optical setup for optical emission spectroscopy measurements. 57
Figure 20. Calibration curve of hydrogen peroxide in liquid phase. 59
Figure 21. Schematic representation of the instrumentation of a UV-vis spectrophotometer. 62
Figure 22. Schematic representation of a DLS measurement system. Reproduced from [109]. 64
Figure 23. Schematic representation of the core components of a scanning electron microscope [110]. 65
Figure 24. Schematic representation of X-ray generation principle [111]. 66
Figure 25. Schematic representation of the core components of a transmission electron microscope [110]. 68

Figure 26. Schematic representation of an atomic force microscope set-up [112]. 70
Figure 27 Schematic representation of X-ray diffraction principle. 71
Figure 28. Optical emission spectrum of the atmospheric pressure plasma jet at a power supply current of 8 A, frequency at 25 kHz and helium gas flux at 3 L.min^{-1}. 77
Figure 29. Distribution of the intensity of reactive species along the plasma jet when it's a) free plasma jet, b) in contact with a solution, and c) in contact with a non-conductive flat surface. The plasma is generated at an input power supply current of 8 A, a frequency of 25 kHz, and a helium flow rate of 3 L.min^{-1}..... 80
Figure 30. Concentration of hydrogen peroxide in water solution treated with a helium atmospheric pressure plasma jet at different exposure durations (0, 5 and 10 min). 81
Figure 31. Pictures showing the silver sample before and after the plasma jet treatment: (left) 1 min of plasma exposure (right) 5 min of plasma exposure. 83
Figure 32. EDX analysis graph, (inserted) SEM micrograph of silver nanoparticles. 84
Figure 33. UV-vis (a) absorbance (b) normalized absorbance spectra of the solutions with 1 mM of $AgNO_3$ and 1.5 mM of citrate at different plasma exposure durations ranging from 0 (considering 0 as no plasma treatment) to 10 min. 87
Figure 34. Normalized UV-vis absorbance spectra of different silver concentrations ranging from 1 to 5 mM and at 3 mM of citrate concentration. 89
Figure 35. The UV-vis deconvoluted absorption spectra with 3 mM citrate concentration at different silver nitrate concentrations: (a) 1 mM, (b) 2 mM, (c) 3 mM, (d) 4 mM, and (e) 5 mM (The black lines represent the original curves, the black dashed lines represent the deconvoluted curves and the red lines represent the cumulative fit)..... 91
Figure 36. The UV-vis absorption spectra at different citrate concentrations of 0.5 mM (green dot line), 1.5 mM (blue dash-dot line), 3 mM (red dash line), and 6.3 mM (black line) for various initial $AgNO_3$ concentrations: (a) 1 mM, (b) 2 mM, (c) 3 mM, (d) 4 mM, and (e) 5 mM. 94
Figure 37. Images graph showing the variations in color observed in the treated solutions with different concentrations of both the precursor and capping agent. 95
Figure 38. UV-vis absorbance spectra of silver/citrate solution before and after (left) one week at room temperature, and (right) 2 hours at high temperature and vigorous stirring..... 96
Figure 39. (a) The color change of the solutions with 1 mM $AgNO_3$ concentration for several citrate concentrations, from 0.05 mM (left) to 6 mM (right) at fixed plasma parameters. (b) The UV-vis absorption spectra of the solutions at 1 mM of silver nitrate concentration and citrate concentrations ranging from 0.05 mM to 1.5 mM at fixed plasma parameters. (c) Graph illustrating the relationship between citrate concentration and the maximum absorbance band intensity at 405 nm of the treated solutions. Inserted is a table presenting the corresponding values for each data point. 97
Figure 40. TEM micrographs of the silver nanoparticle solutions after 5 min of plasma exposure with 1 mM of $AgNO_3$ at (a) 0.1 mM, (b) 0.3 mM, (c) 0.5 mM, (d) 1 mM, and (e) 6 mM of HAuCl4 concentration. 98
Figure 41. Pictures showing the gold sample before and after the plasma jet treatment: (left) 1 min of plasma exposure (right) 5 min of plasma exposure. 100

Figure 42. X-ray diffraction pattern of the synthesized AuNPs after 5 min of plasma exposure with 1 mM of $HAuCl_4$ and 0.05 mM of PVP. 101
Figure 43. Picture of the samples with 1 mM of $HAuCl_4$ and 0.05 mM of PVP concentrations after treatment at different plasma exposure durations. 103
Figure 44. UV-vis (a) absorbance (b) normalized absorbance spectra of the solutions with 1 mM of $HAuCl_4$ and 0.05 mM of PVP at different plasma exposure durations (from 0 to 15 min). 104
Figure 45. Picture of the samples after 5 min of plasma treatment with 0.05 mM of PVP concentration at different $HAuCl_4$ concentrations ranging from 0.1 to 1.5 mM. 105
Figure 46. (a) UV-vis absorbance spectra (b) normalized UV-vis absorbance spectra of the solutions after 5 min of plasma exposure with 0.05 mM of PVP at $HAuCl_4$ concentrations ranging from 0.1 to 1.5 mM. 106
Figure 47. TEM micrographs of the gold nanoparticle solutions after 5 min of plasma exposure with 0.05 mM of PVP at (a) 0.1 mM, (b) 0.2 mM, (c) 0.5 mM, (d) 1 mM, and (e) 1.5 mM of $HAuCl_4$ concentration. 107
Figure 48. Picture of the samples after 5 min of plasma treatment with 0.1 mM of $HAuCl_4$ concentration at different PVP concentrations. 108
Figure 49. (a) UV-vis absorbance spectra (b) normalized UV-vis absorbance spectra of the solutions after 5 min of plasma exposure with 0.1 mM of $HAuCl_4$ at PVP concentrations ranging from 0 to 0.1 mM. 109
Figure 50. TEM micrographs of the solutions after 5 min of plasma exposure with 0.1 mM of $HAuCl_4$ at (a) 0 mM, (b) 0.0005 mM, (c) 0.005 mM, (d) 0.01 mM, (e) 0.05 mM, (f) 0.08 mM, and (g) 0.1 mM of PVP concentration 110
Figure 51. Size distribution measured by DLS of the synthesized AuNPs after 5 min of plasma exposure with 0.1 mM of $HAuCl_4$ and 0.05 mM of PVP concentrations. 111
Figure 52. Images of the dual frequency atmospheric pressure plasma jet at different RF power levels with (upper) helium, and (bottom) argon as process gases. 116
Figure 53. Optical emission spectra of the helium and argon plasma jet at 30 W RF power. In the upper part are shown the spectral zoom of the signals relative to the OH(A-X), NH(A-X), N_2(C-B) and H_α emissions. 117
Figure 54. OES analysis results as a function of the RF power for (blue) helium and (red) argon gases: (top) rotational temperature of OH from OH (A-H) band; (center) vibrational temperature of N_2 from N_2 SPS; and (bottom) optical emission intensity of He I 706 nm and Ar I 738 nm lines. 119
Figure 55 Charge collected by the sample in (top) argon and in (center) helium as a function of the (bottom) electrode pulse polarization. Charge is recorded in three RF power conditions 0 W, 15 W and 30 W, and on the right is a time zoom of the pulse. 122
Figure 56. UV-vis absorbance spectra of the obtained gold nanoparticles after (left) 10 min and (right) 20 min of helium plasma treatment at different RF power 0 W, 15 W and 30 W. The spectra have been normalized to the interband gold transitions. 123
Figure 57. UV-vis absorbance spectra of the obtained gold nanoparticles after 10 and 20 min of helium plasma treatment at a) 0 W, b) 15 W and c) 30 W of RF power. 124

Figure 58. SEM micrographs of the synthesized gold nanoparticles with a 10 min helium plasma jet exposure at a) 0 W, b) 15 W, and c) 30 W RF power.....125
Figure 59. AFM topographical images in 2D and 3D of the synthesized gold nanoparticles with a 10 min helium plasma jet exposure at a) 0 W, and b) 30 W RF power.....126
Figure 60. UV-vis absorbance spectra of the obtained gold nanoparticles after (left) 10 min and (right) 20 min of argon plasma treatment at different RF power 0 W, 15 W and 30 W. The spectra have been normalized to the interband gold transitions.....127
Figure 61. UV-vis absorbance spectra of the obtained gold nanoparticles after 10 and 20 min of argon plasma treatment at a) 0 W, b) 15 W and c) 30 W of RF power. 128
Figure 62. SEM micrographs of one gold nanoparticles synthesized at (left) 10 min and (right) 20 min of argon DF-APPJ exposure at a) and c) 0 W, and b) and d) 30 W RF power. 129
Figure 63. AFM topographical images in 2D and 3D of the synthesized gold nanoparticles with a 10 min argon plasma jet exposure at a) 0 W, and b) 30 W RF power. 130
Figure 64. Growth curves of (top) E. coli and (bottom) Staphylococcus aureus cells exposed to different concentrations of silver nanoparticles synthesized by plasma.....142
Figure 65. (a-c) TEM of the Ag:$Nd_xY_{1.00-x}Al_3(BO_3)_4$ (x = 0.1) and (d-f) TEM of the Au: $Nd_xY_{1.00-x}Al_3(BO_3)_4$ (x = 0.1). 144
Figure 66. Photoluminescence characterization by the input-output power dependences for the $Nd_xY_{1.00-x}Al_3(BO_3)_4$ powders (x = 0.10 (first row), 0.20 (second row), and 1.00 (third row)) without (first column) and with Ag (second column) and Au (third column) metallic nanoparticles on the surfaces of the crystalline particles.....144
Figure 67. HRTEM images of the nanoparticles obtained.....145

List of Tables

Table 1. Table summarizing the concentrations of silver nitrate and citrate concentrations used in this study..... 60
Table 2. Table summarizing the concentrations of chloroauric acid and PVP concentrations used in this study..... 60
Table 3. Species identified based on the lines observed in the optical emission spectrum obtained with their corresponding transitions..... 78
Table 4. Table summarizing the concentration of hydrogen peroxide in water solution treated with a helium atmospheric pressure plasma jet at different exposure durations (5 and 10 min)..... 82
Table 5. Table summarizing the concentration of hydrogen peroxide in distilled water after treatment by APPJ from different studies..... 82
Table 6. Elements identified in the measured sample via SEM-EDX analysis with their weight and atomic percentage..... 84
Table 7. Table summarizing different reduction methods for the synthesis of silver nanoparticles and the used chemical products, treatment time and the shape and size of the obtained nanoparticles..... 86
Table 8. Table summarizing the band max intensity and wavelengths of the treated solutions with 1 mM of $AgNO_3$ and 1.5 mM of citrate concentrations at different plasma exposure durations..... 88
Table 9. Table summarizing the experimental process parameters applied..... 88
Table 10. Effect of Silver Nitrate and Citrate Concentrations on Max Wavelength and Intensity of Silver Nanoparticles..... 95
Table 11. Table summarizing different reduction methods for the synthesis of gold nanoparticles and the used chemical products, treatment time and the shape and size of the obtained nanoparticles..... 102
Table 12. Table summarizing the FWHM and the max intensity band wavelength of the treated solutions at different plasma exposure durations..... 104
Table 13. Table summarizing the FWHM and the max intensity band wavelength of the treated solutions at different $HAuCl_4$ concentrations..... 106
Table 14. Species identified based on the lines observed in the optical emission spectrum obtained using the dual frequency atmospheric pressure plasma jet for helium and argon as process gases..... 118
Table 15. Table summarizing the absorbance band max wavelength as a function of RF power levels and plasma treatment duration using helium-DFAPPJ..... 124
Table 16. Table summarizing the absorbance band max wavelength as a function of RF power levels and plasma treatment duration using argon-DFAPPJ..... 128

Introduction

Introduction

Plasmas are ionized gases that emit light and produce a wide variety of chemical reactions. They have been described as the fourth state of matter, after the solid, liquid, and gaseous states. The principle of plasma generation is based on the creation of an electrical discharge in a gaseous medium, inducing the extraction of electrons from the atoms and molecules that constitute the gas. Plasma is composed of numerous reactive species, including both charged entities (ions and electrons) and neutral components (atoms, molecules, and radicals). Advances in plasma engineering have sparked an increased research into novel applications for non-thermal plasmas across various domains. While the treatment and surface modification of heat-sensitive materials were the initial applications of cold plasmas, recent breakthroughs have broadened its scope. For instance, non-thermal plasma is now harnessed in the food industry to engineer surfaces coated with antibacterial agents, to limit biofilm formation. Its use has extended to the biomedical field, notably in tissue regeneration, wound healing, and cancer treatment. Alongside these advances, plasmas have also found utility in microbiological decontamination of surfaces and liquids. Importantly, plasmas have emerged as a powerful tool for nanoparticle synthesis, where their controlled and dynamic properties contribute to shaping nanoparticle size, morphology, and other characteristics.

In an era characterized by rapid technological advancements, nanotechnology has emerged as a transformative field with applications spanning diverse industries. Nanoparticle synthesis, especially in the liquid phase, offers significant advantages, primarily the ability to tailor the surface properties of nanoparticles for specific applications. Among the most researched metallic nanoparticles are silver and gold nanoparticles due to their wide-ranging applications in photonics, electronics, biomedicine, sensors, and cosmetics.

In conventional solution chemistry, metal ions are typically exposed to an energy source such as heat or UV-light, along with a reducing agent, to convert metal ions into metal nanoparticles. These synthesis methods have limitations that hinder their alignment with environmentally friendly and efficient processes. Plasma synthesis of nanoparticles, on the other hand, generates highly energetic electrons from plasma discharges. These energetic species dissociate water molecules into radicals (O, H, OH) and ions (H_2O^+, O_2^-), which participate in the reduction of metal ions into nanoparticles. This brings us to the present study, which introduces a plasma reduction method for metallic nanoparticle synthesis that respects the following process criteria:

One-step process - A simple process, which requires the least synthesis steps possible

The approach is a straightforward process, characterized by its simplicity and efficiency, involving only a minimal number of synthesis steps. The process starts with sample solution preparation, an operation that demands little time and effort. This preparation entails the dissolution of the precursor and the capping agent in water. Once this solution is prepared, it will then be exposed to the plasma jet, initiating a sequence of reactions responsible for the formation of nanoparticles.

Time-efficient - A process with short reaction time for nanoparticle synthesis

A distinctive facet of this methodology is the almost immediate formation of nanoparticles, a characteristic that underscores the efficiency of this technique. The duration of treatment time occupies a central role within the scope of this investigation, where its influence on nanoparticle morphology and size is examined.

Environmentally friendly - A process that does not use harmful and hazardous reactants

This approach offers distinct advantages compared to conventional methodologies, which often involve the use of hazardous reactants, resulting in the generation of harmful by-products and wasteful residues. Notably, plasma-driven synthesis successfully reduces the metallic salts present in the solution, this is made possible by the plasma-created reactive species.

This thesis is structured into two main parts, each employing a distinct plasma jet configuration for the synthesis of metallic nanoparticles. The first part revolves around the utilization of a helium atmospheric pressure plasma jet, featuring an asymmetric borosilicate glass source connected to a pulse power supply. This section delves into the production of both silver and gold nanoparticles, separately. A comprehensive investigation is carried out, exploring the impact of plasma exposure duration, precursor concentration, and capping agent concentration on the characteristics of the nanoparticles synthesized.

In the second part of this thesis, a different plasma configuration is investigated. Here, a dual-frequency atmospheric pressure plasma jet, comprised of an alumina tube connected to both the pulsed power supply and an RF power generator, is employed. This configuration is leveraged to study the synthesis of gold nanoparticles. The investigation within this part centers on understanding the effects and implications of key physical process parameters, including

the choice of process gas and the addition of RF power levels on the characteristics of the synthesized gold nanoparticles.

The main goal of this study is to investigate the synthesis of silver and gold nanoparticles through a parametrical study with the use of an atmospheric pressure plasma jet in contact with an aqueous metal salt solution.

The present thesis consists of four chapters divided into sections:

Chapter 1 is intended to provide a literature review. It commences with an exploration into the fundamental concepts of nanotechnology. The classification and properties of nanomaterials are dissected, emphasizing their unique behaviors at the nanoscale. Next, this chapter focuses on metallic nanoparticles and their multifaceted properties where their optical, chemical, and electrical characteristics are detailed, explaining their remarkable potential for novel applications. Building upon this foundation, the next section outlines the applications of silver and gold nanoparticles and their pivotal roles in catalysis, electronics, medicine, and beyond. The synthesis methods of nanomaterials are explored, where the top-down and bottom-up approaches are detailed, showcasing their distinct pathways for synthesizing nanoparticles. The attention is then shifted to the concept of plasmas, where their classifications are discussed with a particular focus on cold plasmas. Finally, the applications of plasma discharges are presented, bridging the connection between plasmas and nanotechnology and paving the way for the exploration of metal nanoparticles synthesis using atmospheric pressure plasma discharge.

Chapter 2 provides details on the material and experimental methods applied throughout this work. First, the experimental configurations of both plasmas devices employed and power supplies with the different parameters for the generation of a plasma discharge are presented in detail. A description of the diagnostic tools used for the electric and optical characterizations of these plasma discharges is presented. Second, the experimental procedure to examine and quantify the concentration of the long-lived reactive specie hydrogen peroxide present in the liquid solution after plasma discharge exposition was explained. Third, the metallic silver and gold nanoparticles section followed, where their synthesis preparations are detailed along with the different characterization techniques and methodologies employed in this work in order to investigate their size, morphology, and dispersion status are also presented in detail.

Chapter 3 presents the results of the synthesis of silver and gold nanoparticles through atmospheric pressure plasma jet employing a micropulse power supply and helium as process gas for the generation of the plasma discharge. This chapter is divided into three separate sections.

In the first section, the plasma characterization is examined using optical emission spectroscopy (OES) to obtain the emission lines for identifying the reactive species present in the plasma jet. Also, the spatial distribution of reactive species along the plasma jet is also analyzed to better understand the plasma's behavior. After that, the solution chemical characterization is presented, where the concentration of hydrogen peroxide in the treated liquid is calculated as a function of treatment duration.

In the second section, the focus now shifts firstly to silver nanoparticle synthesis where the effects of plasma interaction duration, metal precursor concentration, and capping agent concentration on the synthesis process are dissected in the subsequent sections.
And in the third section, the same experimental order was followed for gold nanoparticles synthesis where we dissected the effect of the different parameters on their shape and size.

Chapter 4 presents the results of the synthesis of gold nanoparticles through dual-frequency atmospheric pressure plasma jet employing both a micropulse power supply and an RF power generator for the generation of the plasma discharge. Similar to the previous chapter, the study starts with the plasma characterization focusing on the optical emission spectroscopy analysis, where the distinct differences in plasma behavior are presented when employing helium and argon as process gases. The emission spectra, gas temperatures, and charge collection behavior illustrate how RF coupling transforms the plasma dynamics. This chapter then shifts its focus to gold nanoparticles synthesis, investigating the effects of helium and argon as process gases coupled with RF at different power levels on nanoparticle characteristics.

Finally, the present work rounds off with general conclusions where the outcomes of our research will be presented. Some preliminary assessments of the diverse applications of these metallic nanoparticles will also be discussed, offering an insight into the potential avenues of their utilization. Furthermore, future directions will be proposed for continued investigatio

Chapter 1.
Literature Review

1 Literature Review

The field of nanotechnology has revolutionized numerous scientific disciplines and opened up new avenues for technological advancements. In this chapter, we will delve into the world of nanotechnology, exploring its fundamental concepts, classifications, properties, and synthesis methods. The chapter begins with an introduction to nanotechnology, providing a comprehensive overview of its significance and impact in various fields. We will then shift our focus to nanomaterials, the building blocks of nanotechnology. Classifications and properties of nanomaterials will be explored in detail, offering insights into the diverse nature of these materials at the nanoscale. Specifically, metallic nanoparticles, particularly silver and gold nanoparticles, will be examined extensively. We will uncover their unique optical, chemical, and electrical properties, focusing on their potential applications in various domains. The synthesis methods employed for the fabrication of these nanoparticles will also be discussed, highlighting both top-down and bottom-up approaches. As our investigation continues, we will continue into the field of plasma science. An introduction to plasmas will provide a foundation for understanding their classifications and properties. We will discuss the diverse categories of plasmas and delve into the characteristics that define them. Cold plasmas, a type of plasma, will be thoroughly examined. Their distinctive properties, arising from non-equilibrium conditions and low gas temperatures, will be explored in depth. Furthermore, we will explore the applications of plasma discharges, uncovering the remarkable potential of these energetic phenomena in various scientific and technological endeavors. The chapter will also touch upon the intriguing interactions between plasmas and liquids, shedding light on the complex dynamics at the plasma-liquid interface. Within this context, we will investigate the synthesis of metal nanoparticles by plasma discharge, exploring both the chemical and physical parameters involved in the process. By delving into the literature, this chapter aims to provide a comprehensive understanding of nanotechnology, nanomaterials, and plasmas. It sets the stage for the subsequent chapters, laying the groundwork for the exploration of advanced synthesis techniques, unique applications, and the interplay between plasmas and nanoparticles.

1.1 Introduction to nanotechnology

Nanotechnology has emerged as a groundbreaking area of research and technological advancement, providing novel opportunities to engineer and manipulate materials at the nanoscale [1]. Nanotechnology is defined as the design, synthesis, manipulation and characterization of materials with dimensions ranging from 1 to 100 nanometers. Where at this scale, the behavior of matter can deviate significantly from that observed in bulk materials, giving rise to new applications [2]. The ability to engineer materials at the atomic and molecular levels offers tremendous potential for developing advanced materials with tailored

functionalities and improved performance, paving the way for a new era of scientific discovery and technological innovation. It is believed that the next industrial revolution will be driven by nanotechnology [3].
The history of nanotechnology can be traced to ancient times when humans unknowingly interacted with materials at the nanoscale. However, the formal study and development of nanotechnology as a distinct field began in the 20th century.
Richard Adolf Zsigmondy was the first to introduce the concept of nanoscale, he was awarded the Nobel Prize in chemistry in 1925. He was mainly recognized for his contributions in the field of colloid chemistry and for developing the ultramicroscope which is an effective tool for nanoscale particles and colloids studies and has extensive implications in various scientific disciplines, including physics, chemistry, and biology. Zsigmondy's work not only advanced the field of colloid chemistry but also laid the groundwork for further investigations into nanoparticles and nanomaterials, which have become crucial in the field of nanotechnology [4].

In 1959 at the American Physical Society annual meeting, Richard Feynman the 1965 Nobel Prize laureate in physics introduced the concept of manipulating matter at the atomic level in his influential lecture titled "There's Plenty of Room at the Bottom" discussing the potential for miniaturization and control of materials at dimensions far smaller than what was conventionally considered possible. He envisioned the development of nanoscale machines that could rearrange individual atoms and molecules to create new materials and devices with extraordinary precision. This novel idea inspired future researchers and set the stage for the development of nanotechnology as a distinct scientific field [2].
Almost 15 years after Feynman's lecture, Norio Taniguchi, a Japanese scientist, coined the term "nanotechnology" in 1974 to describe semiconductor processes and operations that occurred on a nanometer scale [5]. The use of this term helped define and popularize the concept of working on the order of a nanometer. He advocated for the idea that nanotechnology involved the separation, processing, consolidation, and deformation of materials at the level of individual atoms or molecules. While Taniguchi's contribution was primarily in terminology and early conceptualization, his work played a crucial role in shaping and understanding the development of nanotechnology as a scientific discipline [4].

The discovery of fullerenes, which is a class of carbon molecules arranged in a unique hollow cage-like structure, by Harry Kroto, a British chemist, Richard Smalley, an American chemist and physicist, and Robert Curl, an American chemist in 1985 opened up a new area of research in nanotechnology and carbon-based materials. This discovery introduced a new class of nanoscale materials with unique properties. Fullerenes have exceptional strength, electrical conductivity, and chemical reactivity, making them valuable for various applications in

nanotechnology [6]. Buckminsterfullerene (C60) named after Buckminster Fuller, is the smallest and most studied fullerenes; it consists of 60 carbon atoms made of 20 hexagons and 12 pentagons resembling a soccer ball demonstrated in Figure 1. These findings not only provided deeper understanding of carbon-based nanomaterials but also stimulated further research into the synthesis, characterization, and manipulation of nanoscale structures.

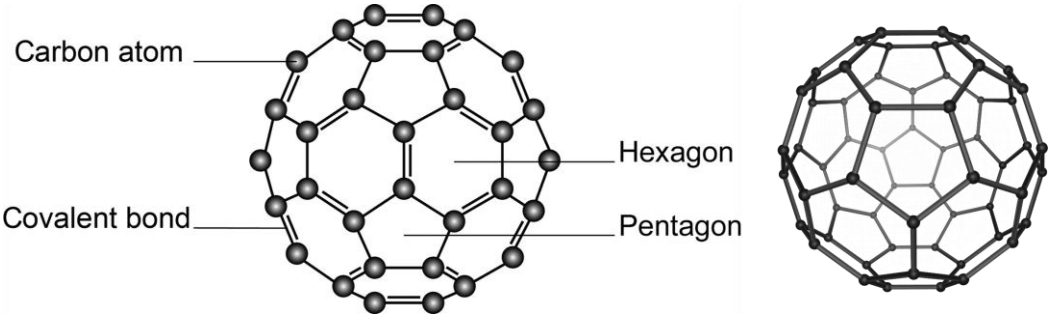

Figure 1. Schematic representations of Buckminsterfullerene C60 molecule [6].

At the same time, Eric Drexler an American engineer from Massachusetts Institute of Technology (MIT) University in Cambridge, was known for his groundbreaking ideas and contributions to the conceptual development of nanotechnology, particularly in the field of molecular nanotechnology (NMT). He used ideas from Feynman's "There's plenty of Room in the Bottom" and Taniguchi's term "nanotechnology" in his book titled "Engines of Creation: The Coming Era of Nanotechnology" published in 1986 [7]. He explored the potential of nanotechnology, envisioning a future where nanoscale machines called "assemblers" could manipulate matter at the atomic and molecular level with precision. He described the concept of nanoscale manufacturing, self-replicating machines, and the transformative impact of nanotechnology on various fields, including medicine, materials, and energy. This book played a significant role in popularizing the concept of molecular nanotechnology [8].

In 1991, a Japanese scientist, Sumio Iijima discovers carbon nanotubes which are cylindrical carbon structures with exceptional mechanical strength, electrical conductivity, and thermal properties. These properties made them promising nanomaterials with immense potential for technological advancements. Although the discovery of carbon nanotubes predates Iijima's work, it did not receive widespread recognition. In 1952, L. V. Radushkevich and V. M. Lukyanovich published clear images of carbon tubes with a diameter of approximately fifty nanometers in the Soviet Journal of Physical Chemistry. However, due to the article being in Russian, the information remained unnoticed. In 1979, John Abrahamson presented evidence of carbon nanotubes at a conference, describing them as carbon fibers formed on a carbon anode after an electric arc. Also, in 1981, Soviet scientists characterized carbon nanoparticles

produced through thermo-catalytic dismutation of carbon monoxide, suggesting the formation of multi-layered carbon tubular crystals by the rolling of graphene layers into cylinders.

The National Nanotechnology Initiative (NNI) was formally launched in the United States on February 21, 2000. It was initiated by President Bill Clinton during a speech at the California Institute of Technology (Caltech). In his speech, President Clinton emphasized the importance of nanotechnology and its potential to revolutionize various industries and improve the nation's economy and quality life [4].

Almost three years later, following President Clinton's announcement, the 21st Century Nanotechnology Research and development Act was signed into law by president George W. Bush on December 3, 2003. This legislation formalized the establishment of the NNI and provided a framework for coordinating and supporting nanotechnology research and development across federal agencies in the United States. This multi-agency initiative involves several federal agencies including the National Aeronautics and Space Administration (NASA), the National Science Foundation (NSF), and others. It aims to promote and coordinate nanoscale science, engineering, and technology research and development efforts, as well as the translation of nanotechnology discoveries into practical applications. It focuses also on various aspects of nanotechnology, including fundamental research, development of nanomaterials and nanodevices, environmental and safety implications, and education and workforce development. It facilitates collaboration among academia, industry, and government agencies to accelerate progress in nanotechnology and maximize its societal impact [9].

Today, nanotechnology has become a mature and interdisciplinary field with a broad range of applications. Many scientists continue to push boundaries of nanoscale manipulation, materials design, and nanodevice fabrication. This particular field holds immense potential for addressing global challenges and revolutionizing multiple industries with novel nanoscale technologies [4].

In conclusion, the rich history of nanotechnology demonstrates its profound impact on scientific and technological advancements. From its origins to the present day, nanotechnology has opened up new avenues for exploration and innovation. Next, we will delve into the realm of nanomaterials and their classifications to uncover their unique properties and immense potential in shaping the future of various fields.

1.2 Nanomaterials: classifications and properties

Having explored the historical development of nanotechnology, we will now explore the field of nanomaterials, the building blocks of this transformative field. Nanomaterials represent a class of materials engineered and manipulated at the nanoscale. The nanoscale dimensions lead to a higher surface-to-volume ratio, resulting in enhanced surface reactivity, increased quantum

confinement effects, and altered electronic, optical, magnetic, and catalytic properties. The study of nanomaterials is of immense importance due to their ability to revolutionize numerous fields of science and technology. By harnessing the distinctive properties of nanomaterials, researchers can explore novel phenomena and develop advanced materials with tailored functionalities. Nanomaterials have the potential to transform fields such as electronics, medicine, energy, and many others. In this fields of research, scientists can manipulate the composition, structure, and morphology of materials at the atomic and molecular levels. This level of control allows for precise tuning of properties. Additionally, the ability to integrate multiple components into nanoscale architectures offers new opportunities to design multifunctional materials with synergistic properties. In this section, we will examine the classification of nanomaterials and explore their properties that arise at the nanoscale.

1.2.1 Classifications of nanomaterials

To comprehend the world of nanomaterials and unlock their immense potential, it is essential to classify them. In general, nanomaterials can be classified based on their composition, structure, morphology, and dimension (Figure 2). By categorizing nanomaterials based on their composition provides insights into the types of materials that exist at the nanoscale and their distinct properties. Additionally, understanding the dimensionality of nanomaterials allows us to explore their structural features and the implications they hold in various applications [10] [11].

Firstly, based on composition, nanomaterials can be broadly categorized into organic and inorganic materials:

- **Organic nanomaterials**

Organic nanomaterials comprise carbon-based compounds and exhibit exceptional properties due to the unique structure and bonding of carbon atoms. Per example, fullerenes, discussed briefly in the previous paragraph, exhibit interesting electronic and photophysical properties [12] [13]. Graphene which is a single layer of carbon atoms arranged in a hexagonal lattice and carbon nanotubes (CNTs) which are tubular structures composed of rolled-up graphene sheets, are both known for their high mechanical strength [14], electrical conductivity [15], and thermal conductivity [16] making them suitable for electronics, sensors, and energy storage applications [17].

- **Inorganic nanomaterials**

Inorganic nanomaterials encompass a wide range of compounds, including metal-based nanomaterials, metal oxides, metal sulfides, and semiconductor materials. Metallic nanoparticles, such as silver, gold, platinum, and copper nanoparticles possess enhanced catalytic activity [18] and also display unique optical properties, including localized surface plasmon resonance (LSPR), making them valuable for sensing [19], imaging [20], and optical device applications [21]. Metal oxide nanomaterials, such as titanium dioxide (TiO_2) and zinc oxide (ZnO), exhibit excellent photocatalytic properties [22], making them useful for environmental remediation [23] and solar energy conversion [24]. Metal sulfide nanoparticles, such as cadmium sulfide (CdS) and lead sulfide (PbS), possess tunable bandgaps, allowing their application in optoelectronic devices [25] namely solar cells and photodetectors. Semiconductor nanomaterials, such as silicon (Si) and germanium (Ge) nanoparticles, have unique electronic properties and find use in nanoelectronics [26] and energy storage devices [27].

Secondly, nanomaterials can also be classified based on their dimensionality, which refers to the number of dimensions confined at the nanoscale:

- **0D nanomaterials**

0D nanomaterials are those with all three dimensions in the nanoscale, such as spherical nanoparticles, core-shell, hollow spheres, fullerenes, and quantum dots.

- **1D nanomaterials**

1D nanomaterials are elongated structures with two dimensions in the nanoscale range, such as nanowires, nanorods, nanotubes, and nanobelts.

- **2D nanomaterials**

2D nanomaterials are atomically thin layers, typically composed of a single layer or a few layers, like graphene, transition metal dichalcogenides (TMDs), nanoplates, nanosheets, and nanowalls.

Understanding the classifications of nanomaterials based on composition and dimensionality provides a framework to explore their distinct properties, behavior, and potential applications. By tailoring the composition and dimensions of nanomaterials, researchers can design materials with precise functionalities and address a wide range of scientific and technological challenges.

It is important to note that there may be an overlap between these categories, as nanomaterials can exhibit a combination of different nanostructures and properties. Building upon this classification, we will now shift our focus to metallic nanoparticles, specifically silver and gold nanoparticles, explore their properties and the wide range of applications they offer. Through this exploration, we will gain a deeper understanding of how metallic nanoparticles have revolutionized various fields and continue to shape the future of nanotechnology.

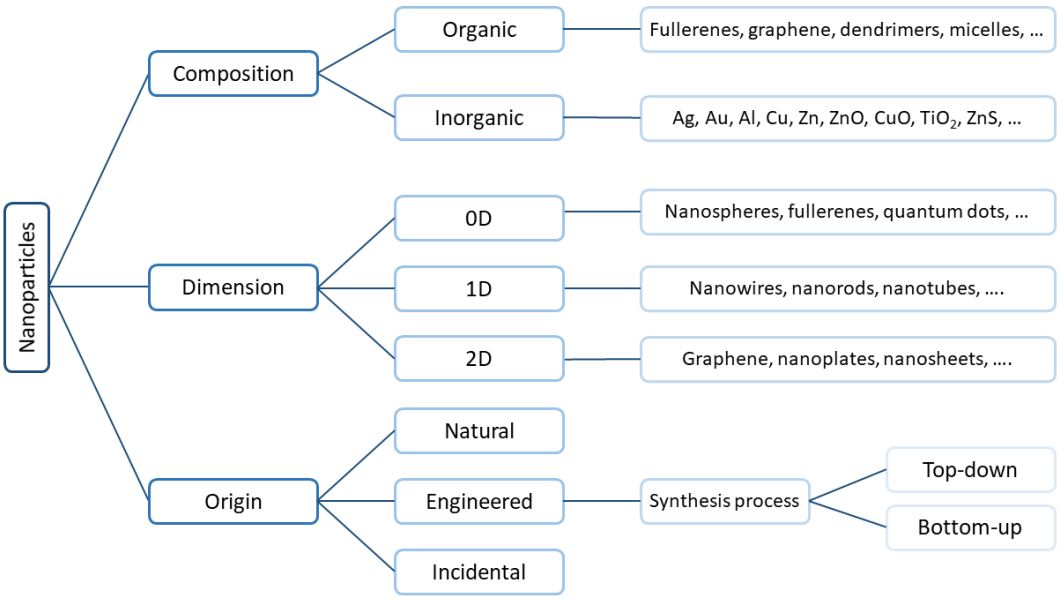

Figure 2. Classifications of nanoparticles based on their composition, dimension, and origin. Reproduced from [11].

1.2.2 Metallic nanoparticles and their properties

Metallic nanoparticles exhibit remarkable properties and hold immense potential in the realm of nanotechnology, driving extensive research and exploration [28]. By manipulating and harnessing the unique characteristics of these metallic nanoparticles, researchers have unlocked new avenues for technological advancements and groundbreaking applications [29]. In this section, we will discuss about the intriguing properties of metallic nanoparticles, specifically silver and gold nanoparticles. Through this exploration, we aim to gain a comprehensive understanding of the immense potential that metallic nanoparticles offer and how they have revolutionized numerous areas of scientific inquiry and technological innovation.

Nanomaterials possess a range of unique properties that distinguish them from their bulk counterparts. These properties arise due to their small size and high surface-to-volume ratio, leading to enhanced reactivity and novel behavior. Some key properties of metallic nanomaterials include optical, chemical, and electrical properties that will be detailed below.

1.2.2.1 Surface energy

The surface energy of nanoparticles is a material property that represents the excess energy associated with the atoms or molecules at the surface of the nanoparticle compared to those in the bulk of the material. It can vary depending on several factors, including the size and shape of the nanoparticles, the type of material, and the surrounding environment. The increase in surface energy of nanoparticles is a consequence of the reduced number of nearest

neighbors experienced by surface atoms as the particle size decreases [30]. As nanoparticles become smaller, the atoms or molecules at the surface have fewer adjacent atoms to bond with, leading to an excess of energy associated with these unfulfilled bonds. This phenomenon is a result of the increased surface curvature, which reduces the coordination of surface atoms. Moreover, the binding energy between surface atoms and their neighbors is also affected by the decreasing particle size, weakening the interactions between them. These factors combine to elevate the surface energy of nanoparticles, which has significant implications for their properties, including reactivity, stability, and interactions with other materials [31]. Understanding surface energy is crucial in the field of nanotechnology and materials science.

1.2.2.2 Optical properties

Metallic nanoparticles exhibit unique optical properties, such as localized surface plasmon resonance (LSPR), which arise from the interaction of the electric field of an incoming light with the free electrons. The absorption and scattering of light by metallic nanoparticles can be tuned by adjusting their size, shape, and composition. This specific property is the most outstanding property of metallic nanostructures. It started in the early 20^{th} century with Gustav Mie when he published his work explaining the surprising optical properties of metallic colloids in 1908 [32]. However, it is important to note that the utilization of nanoparticles and structures dates back much further. In fact, as early as the fourth century AD, the Romans were employing nanoparticles in their artifacts and creations, although without a comprehensive understanding of the underlying scientific principles at the time. Per example, the Lycurgus cup, despite being created over a thousand years ago, is a remarkable piece of Roman glassware with unique optical properties. It is made of dichroic glass, which means it exhibits different colors depending on the lighting conditions. When lit from the front, it appears green, but when illuminated from behind, it transforms into a vibrant red color [33]. This optical phenomenon confused researchers for centuries until modern scientific techniques allowed them to uncover its secret. In 1990, through analysis using transmission electron microscopy (TEM), it was discovered that the cup contains tiny nanoparticles of gold and silver dispersed within the glass matrix. These nanoparticles are responsible for the cup's color changing properties. The gold nanoparticles produce the red-purple color as a result of light absorption at a wavelength around 520 nm while the green color is attributed to the light scattering by Ag nanoparticles with a size larger than 40 nm. The significance of the Lycurgus cup in the field of nanotechnology lies in its early example of controlling the properties of materials and create nanoscale structures, even without a comprehensive understanding of the scientific principles behind it. In modern times, this concept of manipulating nanoparticles to control light-matter interactions has become a core aspect of nanotechnology [34].

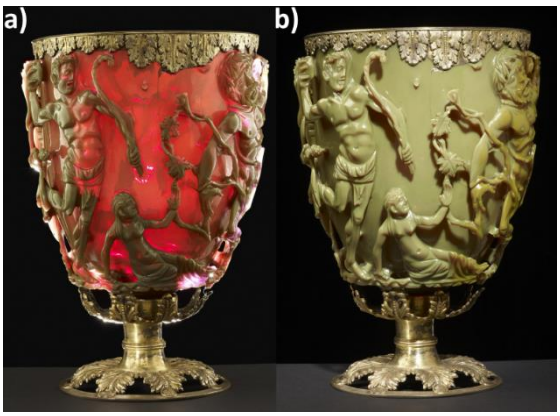

Figure 3. The Lycurgus cup appearing a) red in transmitted light and b) green in reflected light [33].

Having explored the historical utilization of metallic nanoparticles and their intriguing optical properties, we will now explore the scientific signification of localized surface plasmon resonance (LSPR) and its underlying principles. This phenomenon occurs in metallic nanoparticles or nanostructures, where the collective oscillation of free electrons, known as plasmons, is localized to a specific region. Unlike Surface Plasmon Resonance (SPR), which occurs at the interface between a metal and a dielectric medium, LSPR involves the excitation of plasmons within the metal itself. LSPR arises due to the interaction of incident light with the metallic nanostructure (Figure 3). When the electric field of the incident light interact with a particle of a size comparable to the wavelength of light, its electric field will produce a collective electrons oscillation on the metallic particle, leading to the excitation of the plasmons and the generation of a resonant electromagnetic response. One of the key features of LSPR is the strong localization of the electromagnetic field near the nanostructure's surface [35]. This localized field enhancement can significantly amplify the electromagnetic signal, making LSPR a powerful tool for various applications.

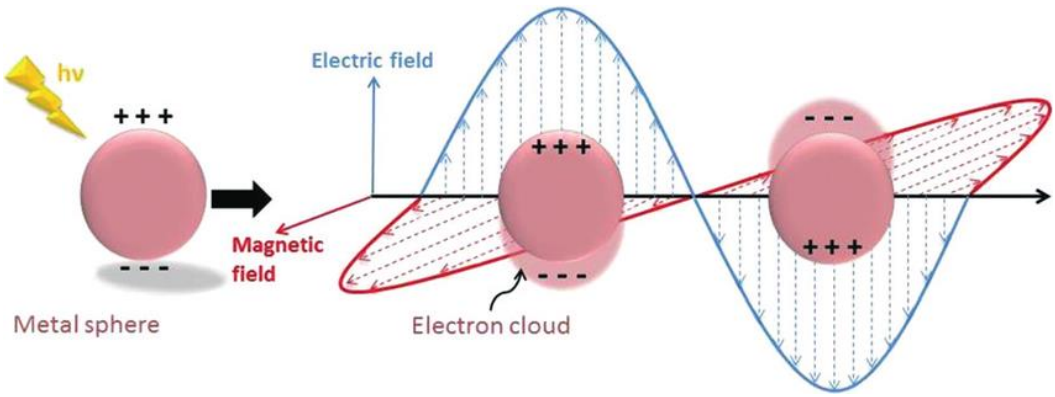

Figure 4. Schematic illustration of the localized surface plasmon resonance (LSPR) of metallic nanoparticles [35].

This resonance is highly dependent on the size, shape, composition of the nanostructure, and extent of the particle agglomeration. Plasmonic metal nanoparticles, such as gold, silver, and platinum, possess excellent light absorption and scattering capabilities. By manipulating factors like nanoparticle size, shape, and composition, their optical response can be precisely adjusted across a broad range from ultraviolet to visible to near-infrared wavelengths as demonstrated in Figure 4 below. This enables control over the color of nanoparticle dispersions. For instance, for spherical gold nanoparticles in solution, the SPR appears around 500-550 nm which corresponds to a purple-red color at visible light resulting from their strong scattering and absorption of green light, while for spherical silver nanoparticles in solution a, the SPR appears around 350-450 nm which corresponds to a yellow color at visible light due to the plasmon resonance occurring in the blue region of the spectrum [36]. This specific property enables various sensing [37] and imaging applications such as catalysis [38], photothermal therapy [39], and biological imaging applications [40].

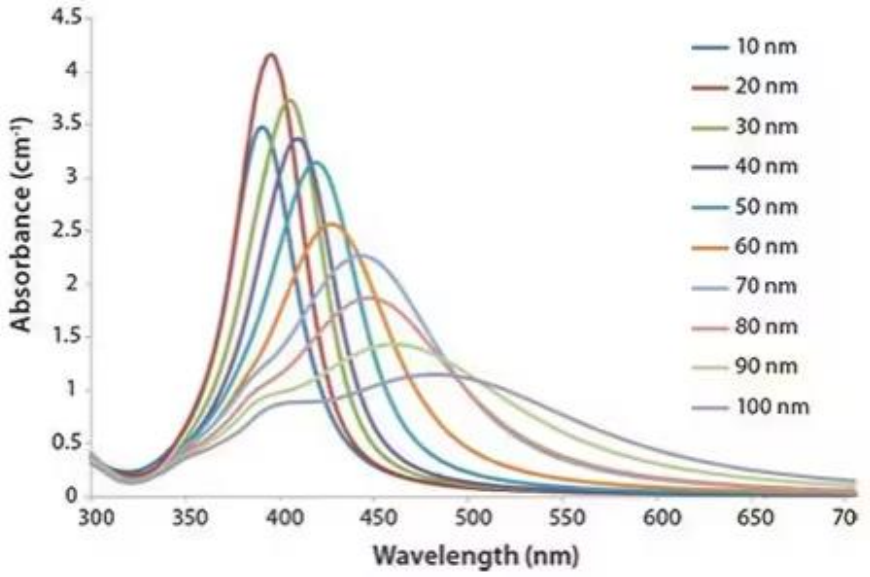

Figure 5. UV-vis absorbance spectra of silver nanoparticles with diameters ranging from 10 to 100 nm with mass concentrations of 0.02 mg/ml [41].

1.2.2.3 Chemical properties

Metallic nanoparticles exhibit distinct chemical parameters that contribute to their unique properties and applications. Firstly, the surface chemistry of metallic nanoparticles can be precisely controlled by functionalizing or modifying their surfaces with ligands, molecules, or polymers [30]. This surface modification enables tailored interactions with other substances, allowing specific applications such as targeted drug delivery and sensing [42]. Secondly, their surface reactivity is significantly enhanced due to the large surface-to-volume ratio. By

precisely engineering the surface chemistry of metallic nanoparticles, their chemical reactivity can be enhanced and harnessed for a wide range of practical applications in fields like medicine, catalysis, and environmental monitoring [43].

1.2.2.4 Electrical properties

Metallic nanoparticles possess notable electrical properties that contribute to their diverse range of applications. Firstly, their metallic nature gives them exceptional electrical conductivity [44], allowing for efficient electron flow. This makes them valuable in various fields, namely in electronics [45], energy storage, and conductive coatings [46]. Secondly, at the nanoscale, metallic nanoparticles can exhibit quantum confinement effects. These effects arise from the restricted movement of electrons within the nanoparticles, resulting in discrete energy levels. Quantum confinement not only impacts their electrical conductivity but also influences their optical behavior [47]. By leveraging these unique electrical properties, metallic nanoparticles hold promise in advancing technologies related to electrical devices, energy conversion, and optoelectronics.

Understanding and harnessing the optical, chemical, and electrical properties of metallic nanoparticles is essential for developing innovative applications in fields such as nanotechnology, catalysis, electronics, photonics, and biomedicine.

1.3 Applications of silver and gold nanoparticles

The properties mentioned above of metallic nanoparticles are the primary reason behind their diverse applications in various fields. Building upon their distinctive characteristics, these nanoparticles find practical utility across a wide range of domains. From healthcare and environmental remediation to electronics and energy, the applications of metallic nanoparticles are continuously expanding. By harnessing their unique optical, chemical, and electrical properties, researchers are unlocking new possibilities for advanced sensing, imaging, drug delivery, catalysis, and more. In this section, we will explore the applications of metallic nanoparticles and explore how their properties are used to address challenges and drive technological advancements [48].

- **Antibacterial applications**

Silver nanoparticles exhibit a unique mechanism of action against bacteria, making them highly effective in inhibiting bacterial growth and preventing infections. The small size and large surface area of silver nanoparticles enhance their interaction with bacterial cells, allowing for efficient penetration and disruption of cell membranes. The antibacterial effect of silver

nanoparticles has been demonstrated against a wide range of bacteria, including both Gram-positive [49] and Gram-negative strains [50].
On the other hand, gold nanoparticles have shown potential antibacterial properties in certain studies, particularly when they possess specific shapes or sizes [51]. Research has indicated that gold nanoparticles with specific geometries can exhibit antibacterial effects against various bacterial strains [52] [53]. However, in other literature, it has been observed that gold nanoparticles alone do not exhibit significant antibacterial activity [54]. Nevertheless, gold nanoparticles can be conjugated with antibiotics, serving as carriers or delivery platforms to enhance the antibacterial efficacy of the drugs [55]. The combination of gold nanoparticles and antibiotics has demonstrated the ability to overcome bacterial resistance to antibiotics, enhance drug penetration into bacterial cells, and improve targeted delivery. This approach has shown promise in addressing the challenges posed by antibiotic-resistant bacteria and could lead to the development of innovative antibacterial strategies.

- **Biomedical applications**

In the field of medicine, as we strive to improve healthcare practices and enhance treatment outcomes, there has been significant focus on finding ways to deliver therapeutic agents in a targeted and precise manner. This has led to extensive exploration of nanoparticles for the development of innovative and improved drug delivery systems. In this pursuit, silver nanoparticle (AgNP)-based nanosystems have emerged as promising candidates for carrying various therapeutic substances, such as those with anti-inflammatory, antioxidant, and anticancer properties. And because of their antimicrobial activity, they are suitable for various applications in wound healing, tissue engineering, and infection control [56].
Also, gold nanoparticles, due to their unique optical properties, have paved the way for applications in biosensing, imaging, and targeted therapy. Gold nanoparticles can be functionalized with biomolecules, including antibodies or ligands, to specifically target cancer cells or disease markers, enabling precise diagnostics and targeted therapies. In biomedical imaging, gold nanoparticles serve as contrast agents for techniques such as computed tomography (CT) and photoacoustic imaging, providing enhanced signal and improved imaging resolution. Additionally, gold nanoparticles possess unique properties that can enhance photothermal therapy, where their ability to convert light into heat is utilized to selectively destroy cancer cells while minimizing damage to healthy tissue [57].

- **Catalysis applications**

Catalysis plays a crucial role in numerous industrial processes, and silver nanoparticles (AgNPs) have garnered significant attention for their catalytic properties [58]. AgNPs exhibit excellent

catalytic activity due to their unique surface properties and high surface-to-volume ratio. The large surface area of AgNPs provides ample active sites for interactions with reactant molecules, promoting efficient catalytic conversion [59]. Additionally, the size and shape of AgNPs can be precisely controlled, allowing for tailoring of their catalytic properties. Gao et al. demonstrated that the catalytic activity of silver nanoparticles (AgNPs) in reducing 4-nitrophenol (4-NP) is significantly enhanced when the AgNPs are carefully controlled in size. This enhancement is attributed to the rapid thermal effect induced by the surface plasmon resonance (SPR) of AgNPs, which promotes the diffusion of reactants near the catalyst surface [60].
Gold nanoparticles are also used as catalysts due to their physicochemical properties. They exhibit remarkable reactivity even under mild conditions, including ambient temperature or lower. The incorporation of these nanoparticles, specifically those with a size below approximately 5 nm, onto base metal oxides or carbon supports yields highly active catalysts [61] [62] [63].

- **Electronics applications**

Metallic thin films play a crucial role in electronic devices by establishing electrical contacts between semiconductors and the associated wiring. Usually, copper, silver, and gold are the preferred metals due to their conductivities. Among these, copper is the most prone to oxidation, which can degrade its performance [64]. On the other hand, silver and gold nanoparticles offer unique electronic properties and high electric conductivity, making them well-suited for a wide range of electronic applications. Silver nanoparticles, for instance, are utilized in conductive inks and printed electronics, enabling the creation of flexible and lightweight electronic circuits [65] [66] [67]. Similarly, gold nanoparticles find utility in various electronic devices, particularly in the form of conductive coatings, due to their exceptional chemical stability and conductivity. Their integration into electronic systems ensures reliable and efficient electrical performance. Furthermore, gold nanoparticles can be functionalized with organic molecules, enabling their integration into electronic devices for sensing, bioelectronics, and molecular electronics applications. The versatility and unique electronic properties of gold nanoparticles make them highly attractive for advancing electronic technologies [64].

- **Sensing applications**

Due to their optical properties, silver and gold nanoparticles proved to be a powerful tool for sensing applications. Despite silver's numerous advantages over gold, such as its higher extinction coefficients, sharper extinction bands, and higher scattering-to-extinction ratio, it has been less commonly used in sensor development, except for sensors based on surface-enhanced spectroscopies. This is mainly due to the lower chemical stability of silver

nanoparticles compared to gold. However, recent advancements have introduced effective protective measures for silver nanoparticles, greatly enhancing their chemical stability. As a result, silver nanoparticles are quickly gaining popularity, and numerous research groups are now exploring alternative approaches to utilize their exceptional optical properties in the creation of optical sensors [68].

1.4 Synthesis methods

As silver and gold nanoparticles have found diverse applications in various fields, the ability to synthesize them with precise control becomes crucial. Several synthesis methods have been developed to achieve this, allowing researchers to tailor the size, shape, and properties of the nanoparticles to suit specific applications and unlock their full potential in different areas [69].

Nanoparticle synthesis methods can be broadly classified into two main approaches: the top-down and bottom-up approach (Figure 6).

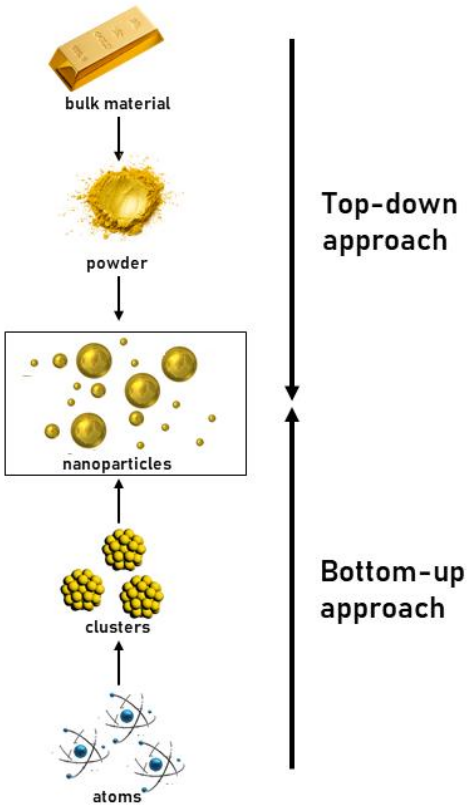

Figure 6. Schematic representation of the top-down and bottom-up approaches for the synthesis of nanoparticles. Reproduced from [69].

1.4.1 Top-down approach

The top-down approach starts with a material on a macroscopic scale, which then undergoes size reduction through physical and chemical processes to produce tiny particles as nanoparticles. Some bottom-up synthesis methods include lithography, mechanical milling, and laser ablation. Lithography utilizes advanced pattering and edging processes to create nanoscale features on a substrate. In particular, electron beam lithography (EBL) uses a focused electron beam to selectively remove or deposit material, enabling the creation of intricate nanopatterns. The creation of nanowires or nanodots using EBL involves several steps. Firstly, an organic resist is spin-coated onto a substrate. Next, the desired pattern is defined using the electron beam. The sample is then immersed in a solvent bath for development. Subsequently, metal is evaporated onto the substrate, and any excess metal is lifted off. This process yields small nanostructures [70]. However, this specific method is a time-consuming and expensive process, and mainly suitable for small-scale production. Another top-down approach is laser ablation, where laser pulses are focused onto a target material, leading to its vaporization and subsequent condensation into nanoparticles. What makes laser ablation synthesis particularly advantageous is that it can be considered an environmentally friendly technique, as it eliminates the need for stabilizing agents or additional chemicals. This method allows for the synthesis of a wide range of nanoparticles, including metal nanoparticles, carbon nanomaterials, etc. By adjusting parameters such as flux, wavelength, and laser salt addition, the properties of the nanoparticles, such as their average size and distribution, can be precisely controlled. Nevertheless, it requires careful optimization of laser parameters and may result in agglomeration or impurities in the synthesized nanoparticles [71]. Another top-down methods used is mechanical milling, this technique is used for the synthesis of nanoparticles through mechanical deformation and energy input. The milling device contains grinding media, such as balls or rods, which collide with the source material, causing it to undergo mechanical deformation and break into smaller particles. During mechanical milling, the impact and friction between the grinding media and the source material result in the reduction of particle size. The high-energy collisions promote the fragmentation and refinement of the material, leading to the formation of nanoparticles. Mechanical milling offers several advantages for nanoparticle synthesis. It is a relatively simple and scalable method that does not require complex equipment or high temperatures. However, there are also some limitations to mechanical milling. The process can induce some deformation in the material, it can also generate high heat leading to potential thermal degradation or unwanted chemical reactions as well as some agglomeration of particles and contamination from the milling media [72].

1.4.2 Bottom-up approach

The bottom-up approach uses individual atoms and builds them up into larger nanomaterials. This approach is widely used for the synthesis of nanoparticles because it offers precise control over size, shape, composition, and surface properties of nanoparticles. One commonly used bottom-up approach is chemical synthesis, where nanoparticles are synthesized through chemical reactions in a controlled environment. This method is widely used and involves two main steps. The first step involves the use of reducing agents such as borohydrides, citric and oxalic acids, polyols, hydrogen peroxide, sulfites, and others [73]. These reducing agents provide electrons to reduce metal ions, leading to the formation of nanoparticles. The second step involves the use of stabilizing agents, namely trisodium citrate dihydrate, sulfur ligands, phosphorus ligands, polymers, surfactants, and others. These stabilization agents prevent nanoparticle aggregation and maintain their stability in solution by creating a repulsive force that controls the growth of nanoparticles in terms of their rate, size, and geometric shape. It is possible for the stabilization agent to also act as the reduction agent in some cases, depending on the intended usage [74]. One of the major advantages of chemical reduction is its simplicity and versatility, as it allows for the production of large quantities of nanoparticles. The choice of reduction agent and reaction conditions can be tailored to achieve specific nanoparticle characteristics. However, there are certain limitations associated with chemical reduction synthesis. One challenge is achieving a narrow size distribution of nanoparticles, as the reduction process may result in a range of particle sizes. Another limitation is the relatively long treatment times associated with chemical reduction. The reduction reaction may proceed slowly, requiring extended reaction times to achieve the desired nanoparticle size and morphology. Furthermore, chemical reduction often involves the use of toxic reagents, such as borohydrides or other reducing agents, which can pose safety and environmental concerns. The purification process after synthesis is also important to remove any unreacted reagents or by-products, which may affect the desired properties of the nanoparticles. Purification steps are necessary to remove unreacted reagents and impurities, which adds complexity and time to the synthesis process [75].

A way to avoid the use of toxic reducing agent is by green reduction method, which offers several advantages over conventional chemical reduction. This technique is environmentally friendly as they utilize sustainable and non-toxic reducing agents, minimizing the release of harmful chemicals or byproducts [76]. Green reduction processes also tend to operate under mild reaction conditions, reducing energy consumption and overall environmental impact. It can be cost-effective, as they often employ readily available and affordable starting materials. However, there are also limitations to consider. Green reduction methods may sometimes exhibit slower reaction rates compared to traditional approaches, leading to longer synthesis

times. The use of milder reaction conditions can also limit the types of materials that can be synthesized, as certain compounds may require higher temperatures or more aggressive reducing agents. Moreover, the scalability of green reduction methods may pose challenges, as maintaining the desired green principles on a larger scale may be more complex. It is important to optimize the green synthesis process to ensure reproducibility and consistency in nanoparticle production [77] [78].

Another bottom-up approach is chemical vapor deposition (CVD), a thin film is formed on the surface of a substrate through the chemical reaction of vapor-phase precursors. A precursor should possess specific characteristics to be suitable for CVD, such as appropriate volatility, high chemical purity, stability during evaporation, affordability, non-hazardous nature, and long shelf-life. It is also important that its decomposition does not leave behind residual impurities. This method offers several advantages. Firstly, it allows precise control over the growth process, enabling the production of nanoparticles with desired sizes, shapes, and compositions. Secondly, CVD offers scalability, making it suitable for large-scale production. The process can be carried out at relatively low temperatures, reducing energy consumption and enabling compatibility with various substrate materials. And finally, CVD provides good uniformity and reproducibility of nanoparticle synthesis. However, there are certain limitations to consider. CVD requires careful selection and handling of precursor materials, which should have specific characteristics as discussed above. The equipment and infrastructure for CVD can be complex and expensive. The growth rate of nanoparticles can be relatively slow, leading to longer processing times [79].

The sol-gel method is a versatile and attractive bottom-up technique for synthesizing nanoparticles. In this method, nanoparticles are synthesized through the controlled hydrolysis and condensation of precursor molecules in a liquid sol, followed by gelation and subsequent drying or calcination. Its advantages are its ability to achieve highly pure and homogeneous nanoparticles with a narrow size distribution as well as the possibility to incorporate dopants or functional groups in order to synthesize nanoparticles with specific properties. This technique offers flexibility in terms of the choice of precursors, allowing for the synthesis of a wide range of materials, including oxides, glasses, and hybrid organic-inorganic compounds [80]. Despite these advantages, the sol-gel method also has some limitations; the synthesis process can be relatively time-consuming, requiring several steps and extended drying or calcination periods. The control of particle size and morphology can be challenging, especially for nanoscale materials, requiring careful optimization of reaction parameters. The potential for agglomeration or particle aggregation during gelation and drying stages may also affect the uniformity of the synthesized nanoparticles [81].

Finally, it is important to highlight the following bottom-up method, plasma for nanoparticle synthesis. Plasma reduction has emerged as a highly promising method for nanoparticle synthesis [82], offering numerous advantages compared to the aforementioned techniques. Its unique characteristics and capabilities position it as a potential solution to the challenges encountered in nanoparticle synthesis. It is referred to the use of plasma, which is a high-energy ionized gas, as a source of energy and reactants in the synthesis process. Plasma can be generated by applying an electric field to a gas flux. In this context, plasma serves as a unique environment for the synthesis of nanoparticles. The high-energy nature of plasma enables the dissociation and activation of precursor molecules, leading to the formation of highly reactive species. These reactive species then participate in chemical reactions, allowing for the controlled synthesis of nanoparticles with desired properties. Unlike traditional chemical reduction methods, plasma reduction enables nanoparticle synthesis under mild conditions, often at ambient temperature. This characteristic allows for the synthesis of nanoparticles on a wide range of substrates, including temperature-sensitive materials. Plasma reduction also offers precise control over nanoparticle size, shape, and composition, leading to enhanced properties and functionalities. Additionally, the use of plasma allows for the synthesis of nanoparticles with high purity and uniformity, minimizing the presence of impurities [83]. Given the remarkable advantages of plasma reduction, we are dedicated to further exploring its potential and continuing our research in this area. We anticipate that this innovative approach will not only address the mentioned problematics but also open up new avenues for advancements in various fields, such as sensing, catalysis, electronics, and biomedical applications, thus driving the progress of nanotechnology.

1.5 Introduction to nanotechnology

Plasma, often referred to as the “fourth state of matter” along with solid, liquid, and gas. It is a distinct physical state in which gas becomes ionized and is characterized by a significant number of free electrically charged particles [84]. Similar to how the application of energy causes a liquid to reach its boiling point and transform into a gas, the heating of a gas leads to the creation of a plasma demonstrated in Figure 7. This plasma can be described as a mixture of charged particles, consisting of positively charged ions and negatively charged electrons. More than 99 % of the visible universe are plasmas of different kinds and are observed as the northern lights, the lightning bolts, the stars, the sun, etc… On the other hand, we are able to engineer plasmas on earth with unique properties that have found numerous practical applications in various fields, namely water treatment, plasma medicine, materials processing, nanoparticle synthesis, and many others [85]. Plasma physicists investigate the collective

behavior of these charged particles, the interactions between them, and the effects of electric and magnetic fields on the plasma. By studying plasma physics, scientists aim to enhance our understanding of the universe and harness the unique properties of plasmas for the mentioned practical applications.

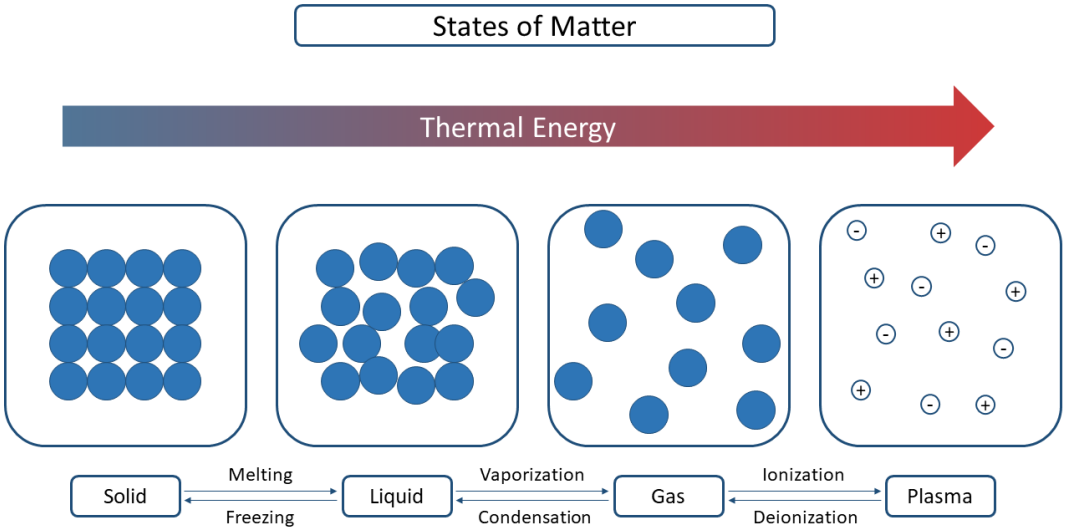

Figure 7. Schematic representation of the four states of matter. Reproduced from [84].

The term "plasma" was derived from the Greek word meaning "moldable substance". It was first introduced in 1927 by Irving Langmuir, an American chemist and physicist to describe this state of matter. Langmuir drew a parallel between the transportation of red and white corpuscles in blood plasma and the movement of electrons and ions in an electrified fluid, which prompted him to make this connections [84].

1.6 Plasmas: classifications and properties

Having explored briefly the fundamental concepts of plasma physics as a distinct state of matter characterized by ionization and the presence of charged particles, we will now investigate their classifications and unique properties. The distinct nature of plasmas sets them apart from other states of matter, exhibiting remarkable behaviors influenced by electric and magnetic fields. Plasmas can be classified into categories and exhibit diverse properties, making them a subject of great scientific interest.

In this section, we will explore the different types of plasmas and explore their properties, shedding light on the unique characteristics that emerge within these highly energetic and complex systems.

1.6.1 Classifications of plasmas

To comprehend the world of plasmas and understand their immense potential, it is essential to classify them. In general, plasmas can be classified based on several factors. Let's explore each category in detail:

Firstly, based on their origin, plasmas can be categorized into natural and engineered plasma discharges [86] [87]:

- **Natural plasmas**

Natural plasmas exist in various forms both in the universe and on Earth. In the vast expanse of the universe, natural plasmas are abundant and play a crucial role in astrophysical phenomena. Stellar plasmas, such as those found in the core of stars like the Sun, are hot and highly ionized. They generate immense energy through nuclear fusion reactions and emit intense electromagnetic radiation. Additionally, natural plasmas can be observed in interstellar space, where they form ionized gas clouds, and plasma jets. These natural plasmas in the universe provide valuable insights into the evolution of stars, galaxies, and the overall structure of the cosmos. On Earth, natural plasmas also occur in the form of atmospheric plasmas, such as lightning discharges and the auroras. Lightning bolts generate plasma channels that carry high electrical currents, while the auroras (northern and southern lights) occur when charged particles from the Sun interact with the Earth's magnetic field, ionizing gases in the upper atmosphere. These natural plasmas on Earth exhibit mesmerizing displays of light and are of great scientific interest, helping us understand atmospheric physics, electrical phenomena, and the interplay between the Sun and our planet.

- **Engineered plasmas**

Engineered plasmas, on the other hand, are intentionally created and controlled by humans for various practical applications. These plasmas are generated under specific conditions and tailored to meet specific requirements. In the field of plasma physics and engineering, researchers employ diverse techniques to create and manipulate engineered plasmas. Usually they are generated when applying a sufficient electric or magnetic energy to ionize a neutral gas. Plasma sources such as dielectric barrier discharges (DBD), radio frequency (RF) discharges, capacitive coupled plasma (CCP), and inductively coupled plasma (ICP) are amongst the commonly used configurations to generate and sustain controlled plasmas in laboratory settings.

Secondly, based on their temperature and degree of ionization, plasma discharges can be broadly categorized into [88]:

- **Temperature**

- Thermodynamic equilibrium plasmas for which all the particles have the same temperature. We denote $T_e = T_i = T_g$ where T_e is the electronic temperature, T_i is the ionic temperature, and T_g is the gas temperature.

- Non-equilibrium plasmas for which the temperature of electrons is between 1000 and 10000 Kelvin, while the temperature of ions and neutral species is around room temperature. We denote $T_e > T_i = T_g$.

These two categories are further divided into subcategories based on the degree of ionization:

When gases are subjected to sufficiently intense electric fields, they become conductive; the complex phenomena that occur are referred to as gas discharges and are caused by the appearance of free electrons and ions. The result of a discharge in a gas is the production of an ionized gas containing n_e electrons, n_i ions, and n_0 neutral atoms or molecules.

The degree of ionization of a gas is defined by the ratio:

$$\boldsymbol{\delta_i = \frac{n_e}{n_e + n_0}}$$

Where:

δ_i is the degree of ionization
n_e is the electronic density
n_0 is the density of neutrals

We can distinguish:

- **Weekly ionized plasmas**

We refer to a plasma as weekly ionized when its degree of ionization is $\delta_i < 10^{-4}$, the electron and ion densities are much lower than the neutral density. The dynamics of these plasmas are governed by binary elastic collisions occurring between neutrals and electrons.

- **Highly ionized plasmas**

We refer to a plasma as highly ionized when its degree of ionization is $\delta_i > 10^{-4}$, this type of plasma is subject to two types of collisional forces: electron-electron and electron-ion.

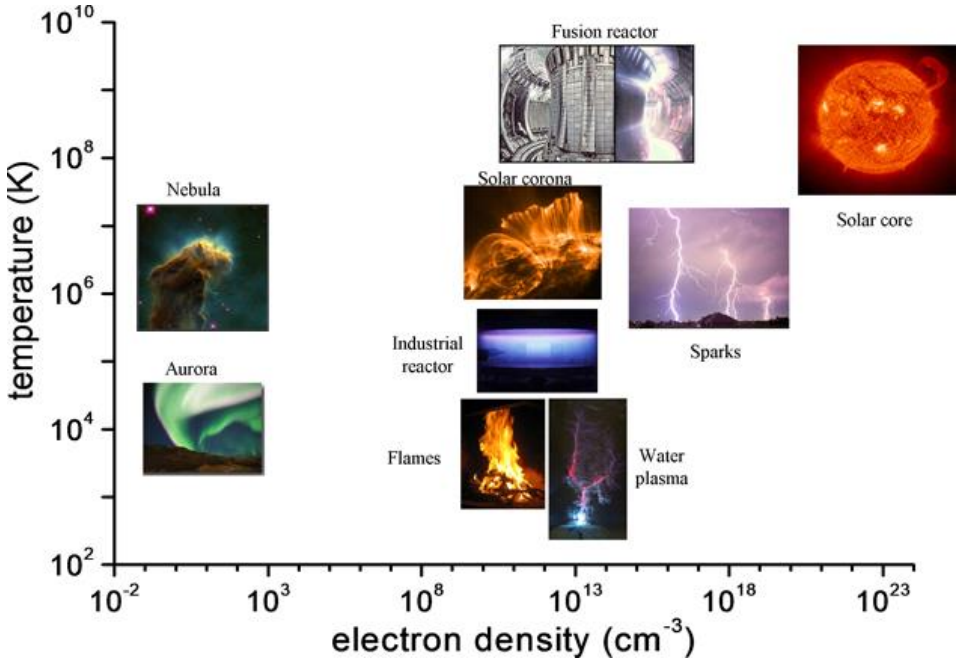

Figure 8. Classification of different plasmas based on their electron density and temperature [89].

Finally, plasmas can also be classified based on their pressure, which plays a crucial role in their behavior and characteristics. Broadly speaking, plasmas can be categorized into three main groups, low-pressure plasmas, atmospheric-pressure plasmas, and high-pressure plasmas [90]:

- **Low-pressure plasmas**

Typically operated below atmospheric pressure, low-pressure plasmas are commonly used in applications such as lighting, etching, deposition in microelectronics, and surface treatment where it involves placing the parts within a vacuum chamber containing partially ionized gas. The gas within the chamber is evacuated using a vacuum pump, and a controlled process gas is introduced to replace it at a specific pressure. The process gas is then energized to create a plasma state, while the vacuum pump continuously removes gas from the chamber to maintain the desired pressure. These plasmas offer excellent uniformity over large volumes, making them suitable for precise and controlled processing and their main advantage is that they provide an ultra-clean surface chemistry over other methods.

- **Atmospheric pressure plasmas**

Atmospheric pressure plasmas are operated at or near atmospheric pressure, which allows for direct interaction with ambient air or surrounding liquids. The system operates by ionizing a continuous flow or gas, creating a stream of partially ionized gas. This stream is then directed towards the material surface to be treated, facilitating the desired interaction between the plasma and the surface. They find applications in water decontamination, sterilization, medical applications, and various chemical processes. Atmospheric pressure plasmas are particularly advantageous due to their ability to operate without the need for vacuum chambers, offering a cost-effective and efficient solution for numerous industrial and biomedical applications.

- **High-pressure plasmas**

High-pressure plasmas exist at gas pressures exceeding atmospheric pressure. These plasmas are encountered in a variety of applications, such as plasma-assisted combustion, and industrial processes. These plasmas exhibit unique behavior due to the increased density of particles, leading to intricate interactions between charged and neutral species. Some examples of high-pressure plasmas are the sun, stars, and fusion reactors where the goal is to recreate the conditions in the core of stars.

By classifying plasma into these categories, we gain a better understanding of their unique characteristics and behavior.

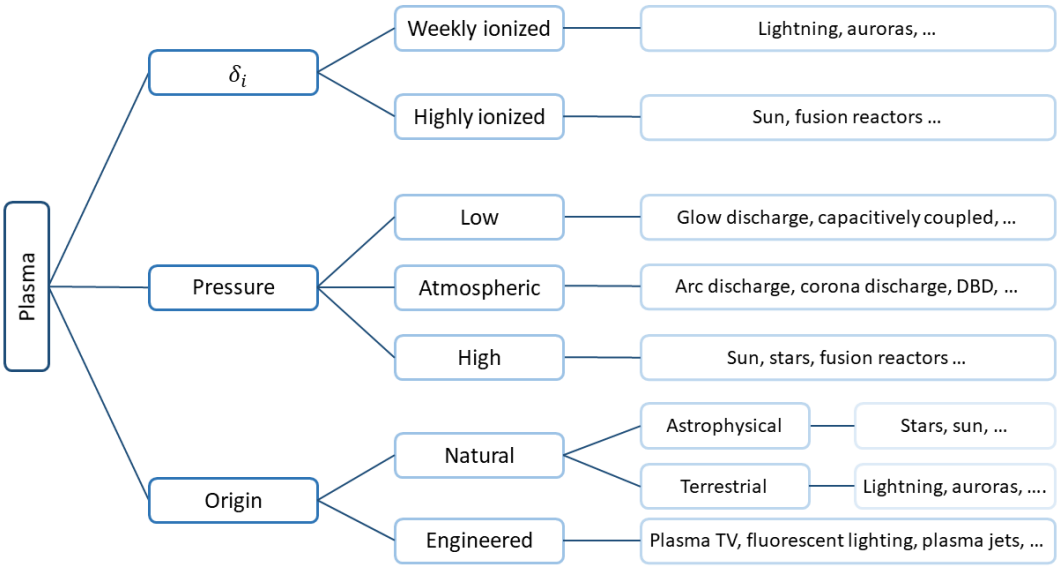

Figure 9. Classification of plasmas based on their degree of ionization, pressure, and origin.

1.6.2 Cold plasmas and their properties

Having examined the various classifications of plasmas based on their pressure, it is evident that each category offers unique characteristics and applications. In this study, we will specifically focus on the exploration of cold atmospheric pressure plasmas due to their distinct advantages over other plasma types. Cold atmospheric pressure plasmas have garnered significant attention in recent years due to their ability to operate at ambient conditions, making them highly accessible and practical for numerous applications [91]. These plasmas offer a range of benefits, including efficient and cost-effective treatment processes, enhanced material surface modifications, and the generation of reactive species for chemical synthesis [92]. Typically, atmospheric pressure cold plasmas are energized and maintained through the application of electrical power with different sources.

One of the key properties of cold plasma is its ability to generate reactive species while maintaining a lower gas temperature. The reactive species, including ions, electrons, radicals, and excited molecules, can interact with materials or biological systems, leading to chemical reactions, surface functionalization, and selective etching. Furthermore, cold plasma demonstrates excellent species selectivity. It can be used to selectively treat specific materials or biological entities without affecting the surrounding environment. The controlled generation of reactive species allows for precise control over the plasma chemistry, making it suitable for targeted treatments, surface functionalization, and nanoparticle synthesis [93].

Another important property of cold plasma is its spatial confinement and high electron energy. This high electron energy in cold plasma enables efficient energy transfer and activation of chemical reactions, making it useful for material processing, thin film deposition, and plasma-assisted synthesis.

Cold plasma also exhibits unique electrical and electromagnetic properties. It can be easily ignited and sustained using various power sources, including radio frequency (RF), microwave (MW), alternating current (AC), and direct current (DC) sources. This flexibility in power sources enables tailored plasma conditions for specific applications. Additionally, the interaction of cold plasma with electric and magnetic fields can be manipulated to control the plasma parameters, such as electron energy distribution and plasma density [87].

In summary, cold plasma exhibits distinct properties that make it a promising tool for a wide range of applications. Its ability to generate reactive species at lower temperatures, spatial confinement, unique electrical and electromagnetic properties, and species selectivity contribute to its versatility and potential.

Having discussed the properties and advantages of cold atmospheric pressure plasmas, we will focus now on exploring the diverse plasma sources employed to generate this form of plasma. There are various techniques available for generating cold atmospheric pressure plasmas using different gases. As shown in the Figure 10 below, these methods include dielectric barrier discharge (DBD), plasma jet, and corona discharge, among others. Commonly used working gases include air, oxygen, nitrogen, helium, argon, and their mixtures. In DBD, a high voltage DC or AC current is applied at high frequency across an adjustable gap between two electrodes separated by an insulating dielectric barrier. The DBD geometry typically consists of two parallel plates or cylindrical arrangements with at least one electrode covered by a dielectric material to prevent electrical arc formation. Atmospheric pressure plasma jets typically comprise two concentric cylindrical electrodes, where the inner electrode is connected to a power source, inducing ionization of the working gas, commonly noble gases like helium or argon. The gas is expelled through a nozzle, creating a characteristic "jet-like" appearance. APPJs can be classified based on their configuration and materials used, including single electrode jets, dielectric-free electrode jets, and DBD jets. Corona discharge involves the application of high voltage between sharp electrodes, creating a weak discharge with low electron and ion densities. These plasma sources can be applied directly or indirectly to the target, either in direct contact with the active plasma region or utilizing plasma afterglow or plasma-activated medium containing various reactive species. In this thesis, the used plasma source is a cold atmospheric pressure plasma jet energized by a current-induced power supply [87].

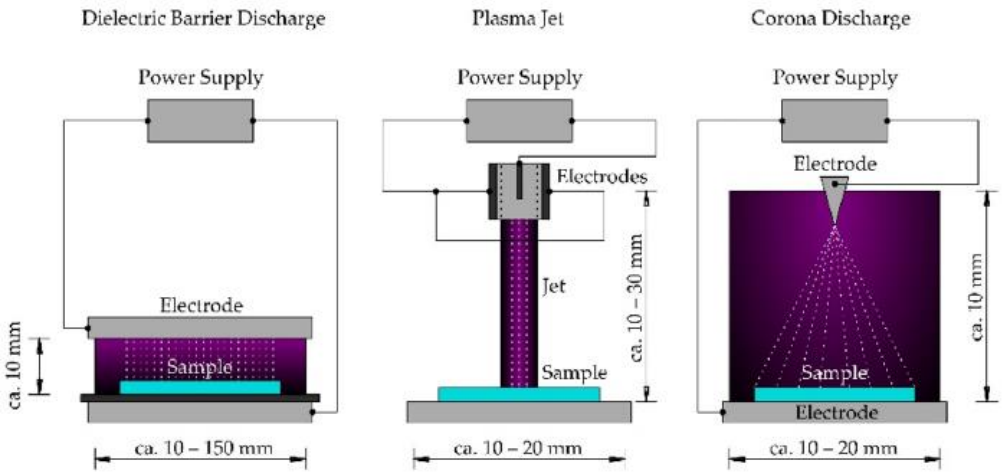

Figure 10. Schematic representation of various cold plasmas at atmospheric pressure [87].

1.7 Applications of plasma discharges

Cold plasmas, with their unique properties and their different experimental configurations, have found numerous applications across various fields:

- **Chemical synthesis**

An important application of cold plasmas is in chemical synthesis, particularly in the synthesis of nanoparticles. Cold plasmas offer a unique environment for controlled nanoparticle formation. By introducing precursor gases into the plasma or by exposing the plasma to a solution containing the precursor. Because of the various chemical reactions induced by the reactive species created by the plasma stream, nanoparticles can be synthesized with precise control over their size, composition, and morphology. This method allows for the production of nanoparticles with tailored properties, making them highly useful in various fields, including electronics, catalysis, and biomedical applications. Sato et al. successfully synthesized silver and platinum nanoparticles without the use of reducing agents by microwave plasma in liquid at atmospheric pressure [92]. Also, Shirai et al. employed an electrolysis technique using two atmospheric pressure glow discharge plasmas as electrodes for the production of metallic nanoparticles in a liquid solution. Silver and gold nanoparticles were synthesized separately as well as Au core covered with a Ag shell using $AgNO_3$ and $HAuCl_4$ only as precursors and sodium dodecyl sulfate as stabilizer [94].

- **Water treatment**

One significant application of cold plasma is water treatment, where reactive species generated by the plasma, such as hydroxyl radicals and ozone, can effectively break down organic contaminants and destroy harmful microorganisms, providing a cost-effective and environmentally friendly method for water purification without the need for external sources of compounds like hydrogen peroxide and ozone. Typically, the application of intense electric fields to water, initiates a combination of chemical and physical reactions that can degrade pollutants and disinfect water. It promotes liquid-phase reactions by absorbing reactive species from the gas phase and transferring volatile reaction products into the liquid phase. These innovative approaches hold promise for addressing environmental challenges. Locke et al. conducted a detailed review on the present research progress concerning the use of plasma discharges in aqueous environments and their applications in water purification [95].

- Medicine

Cold atmospheric plasma can be used for skin, teeth, and wound healing because they are suitable for in situ treatment of live tissues. Also, it has been investigated as a potential for cancer treatments due to its ability to selectively induce apoptosis in cancer cells while sparing healthy cells. This is mainly due to the presence of reactive oxygen and nitrogen species (RONs) in the plasma [96]. This type of plasma also possesses antiseptic characteristics and can promote tissue regeneration, accelerate the healing process, and reduce the risk of infections for wound healing. The antimicrobial properties of the plasma, along with its ability to stimulate cell growth and modulate inflammation, make it a valuable tool in the development of advanced wound care technologies [97]. In addition, it was proven that cold atmospheric plasma has antimicrobial effect. In a study conducted by Jiang et. al, the treatment of E. *faecalis* biofilm for 5 min by a plasma jet resulted in 93.1% kill [98].

In conclusion, the applications of cold plasmas are diverse and rapidly expanding. This offers innovative solutions in several areas. With ongoing research and advancements, the potential for cold plasma technologies to revolutionize various industries and contribute to sustainable development is considerable.

1.8 Plasma-liquid interactions

Plasma-liquid interactions are an interesting area of study that explores the dynamic interplay between plasma and liquid phases. When a plasma comes into contact with a liquid, a range of physical and chemical processes occur, giving rise to unique phenomena. One important aspect of plasma-liquid interactions is the generation of reactive species in the liquid, such as reactive oxygen species and reactive nitrogen species. These species play a crucial role in various chemical reactions, including the degradation of organic pollutants, water disinfection, and the synthesis of functional materials as mentioned before. Additionally, the intense electric fields present in the plasma can induce electrically driven processes in the liquid, leading to effects like electrochemical reactions, electrolysis, and even plasma-induced liquid phase reactions [99].

There are numerous reactor geometries with distinct operational principles, the configuration of the electrodes determines whether the plasma discharges are in direct contact with the liquid phase or are positioned above the liquid and have no direct contact [99].

They can be classified as follows (Figure 11):

- Plasma discharges in liquid phase
- Plasma discharges above liquid phase
- Multiphase plasma discharges

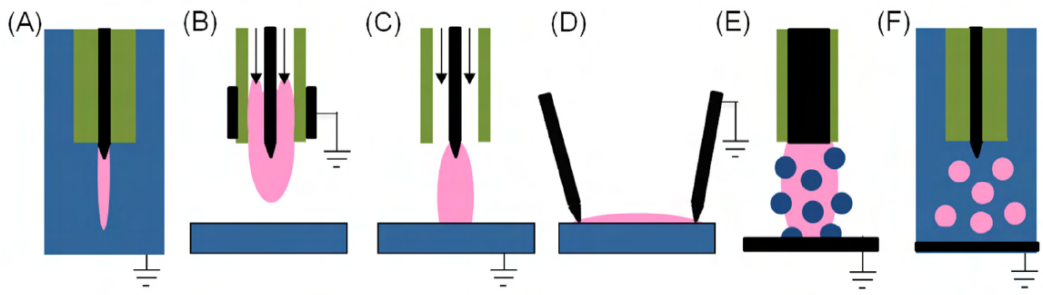

Figure 11. Schematic representation of different discharges: (A) plasma discharge in liquid phase, (B)-(D) plasma discharges above liquid phase, and (E)-(F) multiphase plasma discharges [99].

- **Plasma discharges in liquid phase**

Plasma discharges in the liquid phase refer to the generation of plasma directly within a liquid medium. They require a rapid breakdown processes initiated by strong electric fields. The breakdown can be achieved through various means, such as microsecond voltage pulses, sonoluminescent bubble implosions, or laser pulses. The resulting discharges in the liquid are typically categorized as streamer or corona discharges. They are generated using specific electrode configurations, such as pin-to-pin or pin-to-plate arrangements, and can exhibit unique characteristics [99].

Plasma inside the liquid environment is usually generated through bubbles caused by the gas flow creating thus two interfaces between the plasma and the liquid, the first, plasma-gas interface and the second, gas-liquid interface. Therefore, it enhances the contact between the plasma and the liquid, leading to higher chemical rates.

- **Plasma discharges above liquid phase**

Plasma-liquid interactions above the liquid or in contact with the liquid refer to the dynamic exchange of energy, species, and charge between a plasma and the liquid at close proximity. When a plasma interacts with the liquid surface, several physical and chemical processes take place in different phases. A wide variety of reactive species, namely reactive oxygen and nitrogen species (RONS), can be found in the plasma discharge region due to electron-atom and electron-molecule collisions through ionization, dissociation, and excitation.

The interactions between a plasma jet and the surface of a liquid is divided into three phases, as presented in Figure 12 [100] [101] [102]:

1. **Gas phase**

In the gas phase, the plasma jet is composed of a stream where primary reactive species are formed. These include charged particles (ions and electrons), excited atoms or molecules such as hydroxyl radicals (OH), nitric oxide radicals (ON•), superoxide radicals (O2•-), atomic oxygen (O), singlet oxygen ($^1O_2$), and excited nitrogen (N). Reactive species like OH, O_2^-, and $^1O_2$, are characterized by lifetimes of 2 ns, 1 µs, and 4 µs [103], respectively. These species are directly produced in the discharge region due to the interaction between electrons and molecules of the feeding gas and are propelled towards the liquid surface. They have relatively short lifetimes, and their concentration in the discharge region is very high.

2. **Plasma-liquid interfacial phase**

This phase is where the plasma jet comes in contact with the liquid surface. The chemical reactions occurring at this level result from the interactions between the primary reactive species and molecules present in the surrounding environment. These species are converted into long-lived secondary species such as hydrogen peroxide (H_2O_2), nitrite (NO_2^-), nitrate (NO_3^-), and ozone (O_3). Among these, H_2O_2 is one of the most stable reactive species with a 1 ms lifetime [103]. These species can play a crucial role in subsequent chemical reactions and processes. Upon contact with the liquid surface, they diffuse into the liquid, which corresponds to the third phase.

3. **Liquid phase**

In the liquid phase, the effects initiated at the interfacial phase propagate further into the liquid bulk. The reactive species generated at the liquid-gas interface can diffuse into the liquid and participate in various chemical reactions. These reactions can involve degradation of organic compounds, modification of surface properties, or the generation of new compounds.

The three phases of interaction between a plasma jet and a liquid are interconnected and influence each other. These interactions are also influenced by several factors, including the composition of the plasma, the properties of the liquid, and the distance between the plasma and the liquid surface. The intensity and nature of these interactions can be controlled by adjusting plasma parameters, such as power, gas composition, and flow rate, as well as the properties of the liquid medium.

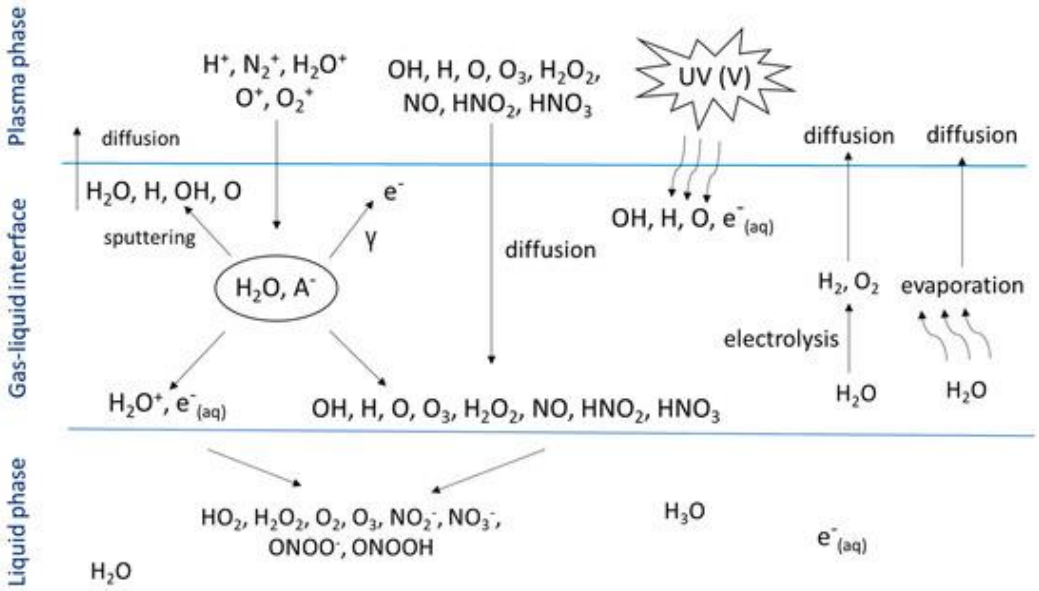

Figure 12. Schematic representation of the main interactions between the plasma and the liquid interface [102].

1.9 Metal nanoparticles synthesis by atmospheric pressure plasma discharge

As already discussed, atmospheric pressure plasmas in contact with a liquid is an advantageous approach for the synthesis of metallic nanoparticles under ambient room conditions and provides several benefits, such as the generation of high quantity of RONS that can induce chemical reactions inside the solutions and reduce the metal ions in the liquid medium to produce metal nanoparticles (NPs) without the need for additional reducing agents that can be considered toxic. The reduction reactions can be initiated by electron transfer or by the transfer of hydrogen atoms from plasma-generated reactive species. Short-lived species such as OH, O_2^-, and $_1O_2$ have a life-time of 2 ns, 1 us, and 4 us respectively [104], they are limited to the surface of the liquid and cannot reach further than the interface region. While long-lived species are present in the bulk liquid and are expected to remain in the liquid after the plasma exposure [105].

The potential reactions occurring in the liquid phase for the reduction of metal salts are as follows [101]:

$$H_2O + e^- \rightarrow H^- + OH^\bullet$$

$$2\ OH^\bullet \rightarrow H_2O_2$$

$$nH_2O_2 + nOH^- + M^{n+} \rightarrow M^0 + nHO_2^- + nH_2O$$

And also it can occur through this reaction:

$$ne^- + M^{n+} \rightarrow M^0$$

The reduction reactions in atmospheric pressure plasma discharge systems are highly dynamic and complex, involving various intermediate species and reaction pathways.
After the reduction of the metal precursor, the next step in the synthesis of metal nanoparticles involves nucleation and growth processes, as already discussed in the bottom-up approach for nanoparticle synthesis in paragraph 1.4.2. Nucleation involves the aggregation of metal atoms to form clusters or nuclei. These nuclei serve as the building blocks for further growth. Through various mechanisms the metal atoms aggregate and accumulate onto the existing nuclei, leading to the growth of nanoparticles. As more metal atoms are added, the nanoparticles increase in size and mass, gradually attaining the desired dimensions (Figure 13).

$$M^0 \text{ growing} \rightarrow M \text{ nanoparticles}$$

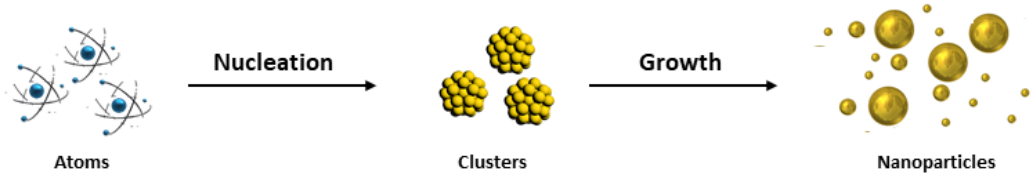

Figure 13. Schematic representation of a controlled nanoparticle nucleation and growth.

The size and shape of nanoparticles formed in atmospheric pressure plasma discharge systems are influenced by both chemical and physical parameters. So, controlling the chemical and physical parameters in atmospheric pressure plasma discharge systems is essential during the synthesis process to obtain the desired results.

1.9.1 Chemical parameters

Chemical parameters include the concentration of metal precursors and capping agents. The concentration of metal precursors determines the availability of metal ions for the reduction process, thereby influencing the size of the resulting nanoparticles. Higher precursor concentrations often lead to larger nanoparticles due to increased nucleation and growth rates. On the other hand, the concentration of capping agents, which are often used to control the size and stability of nanoparticles, can also affect their final size and shape. They can bind to

the nanoparticle surfaces and inhibit further growth, leading to smaller and more uniform nanoparticles.

1.9.2 Physical parameters

Physical parameters, such as the applied plasma current, the distance between the plasma jet and the liquid, and the discharge duration, also play a crucial role in nanoparticle synthesis. The plasma current affects the energy and temperature of the plasma, which in turn influence the reduction reactions and the growth dynamics of nanoparticles affecting the nucleation and growth processes. The distance between the plasma jet and the liquid surface determines the exposure time of the liquid to the plasma, influencing the reaction kinetics and nanoparticle formation. Furthermore, the discharge duration, or the total time of plasma exposure, affects the extent of reduction reactions and nanoparticle growth. Longer discharge durations generally lead to larger nanoparticles due to prolonged reactions.

1.10 Aims and objectives of this thesis

The primary aim of this study is to investigate the avenue that emerges from the convergence of nanotechnology and plasma science, focusing on the precise synthesis and manipulation of metallic nanoparticles, particularly silver and gold nanoparticles. This thesis work will delve into the critical aspect of nanoparticle synthesis within nanotechnology, underlining the importance of understanding and controlling their properties. The first phase of the research is devoted to characterizing the helium atmospheric pressure plasma jet system connected to a pulse power supply, including the examination of reactive species' influence during plasma generation and their impact on liquid physicochemical characteristics. Employing optical characterization, the study intends to trace the evolution of excited species in the plasma jet and discern intensity trends, shedding light on their behavior. Another pivotal objective is the synthesis of silver and gold nanoparticles using the same plasma jet, involving exposure of an aqueous metallic salts solution to the plasma discharge, followed by characterization using UV-vis spectrophotometry, SEM, TEM, EDX, and DLS. The study systematically explores parameters like plasma interaction duration, metal precursor concentration, and capping agent concentration to optimize the synthesis process. A critical goal is to establish an optimal ratio between precursor and capping agent concentrations that yields consistently spherical nanoparticles. Similarly, the next phase is devoted to characterizing a dual-frequency atmospheric pressure plasma jet connected to a pulse power supply and an RF generator. The objective is to unravel the intricate dynamics of nanoparticle formation, especially under varying conditions of process gas (helium or argon) and radiofrequency (RF) power using a dual-frequency atmospheric pressure plasma jet. By characterizing the plasma jet's behavior and understanding the role of RF coupling, the study seeks to elucidate its impact on

nanoparticle size and morphology. To assess the potential applications of the synthesized silver and gold nanoparticles, preliminary tests will be conducted to evaluate their efficacy as antibacterial agents and their suitability for use in photonics.

1.11 Conclusions

This chapter introduces the field of nanotechnology, discussing its emergence and potential to engineer and manipulate materials at the nanoscale. It traces the history of nanotechnology, highlighting key figures and milestones. Then, the classification of nanomaterials based on composition, structure, morphology, and dimension. Metallic nanoparticles are explored, highlighting their unique properties driven by small size and high surface-to-volume ratio, influencing optical, chemical, and electrical behaviors. Applications of silver and gold nanoparticles are detailed across various fields such as antibacterial, biomedical, catalysis, electronics, and sensing. Synthesis methods for nanoparticles are discussed, with a focus on the top-down and bottom-up approaches. The chapter transitions to discussing plasmas, describing them as the fourth state of matter, and their applications in various fields like water treatment, medicine, materials processing, and nanoparticle synthesis. Cold plasmas and their distinct advantages are emphasized, including the ability to generate reactive species at lower temperatures and spatial confinement. Different plasma sources and their applications are explored. Finally, the chapter ends by discussing plasma-liquid interactions and the synthesis of metal nanoparticles using atmospheric pressure plasma discharge.

Chapter 2.
Materials and Methods

2 Materials and Methods

This chapter presents the materials and methods employed for the synthesis and characterization of metallic nanoparticles, specifically silver and gold nanoparticles. The chapter begins with a description of the plasma characterization techniques, including the experimental devices used and the associated diagnostics methods. The investigation focuses on two distinct plasma experimental configurations, each with specific setups to explore their effects on nanoparticle synthesis. We discuss the techniques utilized for plasma characterization, encompassing both electrical diagnostics and optical diagnostics. Following that, we switch into the synthesis of metallic nanoparticles, concentrating on silver and gold nanoparticles, with various concentrations of their respective precursors and stabilizers. Then, the nanoparticle characterization techniques are introduced, categorized based on laser spectroscopy, electron microscopy, particle composition, and elemental analysis.

2.1 Plasma experimental configurations

2.1.1 Plasma experimental devices

In this study, we employed two distinct plasma configurations to investigate their effects on nanoparticle synthesis. The first configuration utilized a power supply system provided by OLISCIE company. This setup consisted of an atmospheric pressure plasma jet, where a high-voltage power supply was connected to the plasma source. The second configuration involved the coupling of the atmospheric pressure plasma jet with two power supplies. In addition to the high-voltage power supply, a radio frequency (RF) generator was incorporated into the system. In this section, we will provide a comprehensive description of the configuration details for both plasma setups.

2.1.1.1 Atmospheric pressure plasma jet

The experimental device used to generate the plasma, presented in Figure 14, consists of an asymmetric source, a power supply and a gas flow. This asymmetric source made of borosilicate glass and composed of a 4 mm diameter tube around which the high voltage electrode is coiled as well as a larger reservoir, with approximately a 35 mm diameter, connected to the ground electrode. The electrodes are located outside the source and are made of aluminum (3M, tape 425, thickness 120 µm). The configuration of the source allows for generating a plasma discharge in the upper part, which then propagates into the smaller tube, forming a plasma jet. At the exit of each tube, the reactive species produced in the discharge interact with the components of the surrounding air, and subsequently with the liquid target. One of the advantages of this configuration is to prevent arcing, due to the glass barrier separating the

electrodes from the plasma. As a result, this discharge is of the double dielectric barrier discharge type. The high voltage power supply from OLISCIE Company (detailed below) is used to generate the discharge [106]. The two electrodes in the experimental setup have a length of 25 mm and are spaced approximately 15 mm apart. The distance between the end of the small tube and the electrode measures 8 mm. The gas used for creating the plasma is helium 99.80% supplied by Linde company. The gas is injected into the upper part of the tube and then diffuses into the tube in the lower part. The helium (He) flow is controlled by a mass flow meter (El-flow Select, Bronkhorst), allowing the flow rate to be set at 3 L.min^{-1}.

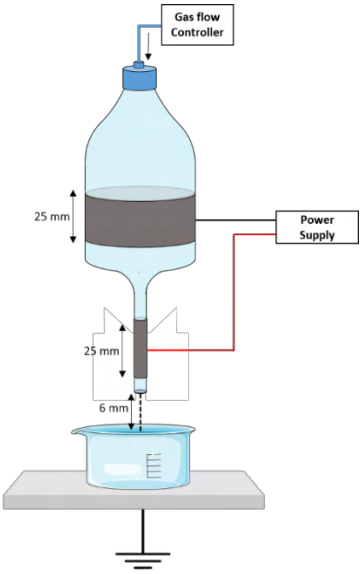

Figure 14. Experimental setup of the atmospheric pressure plasma jet.

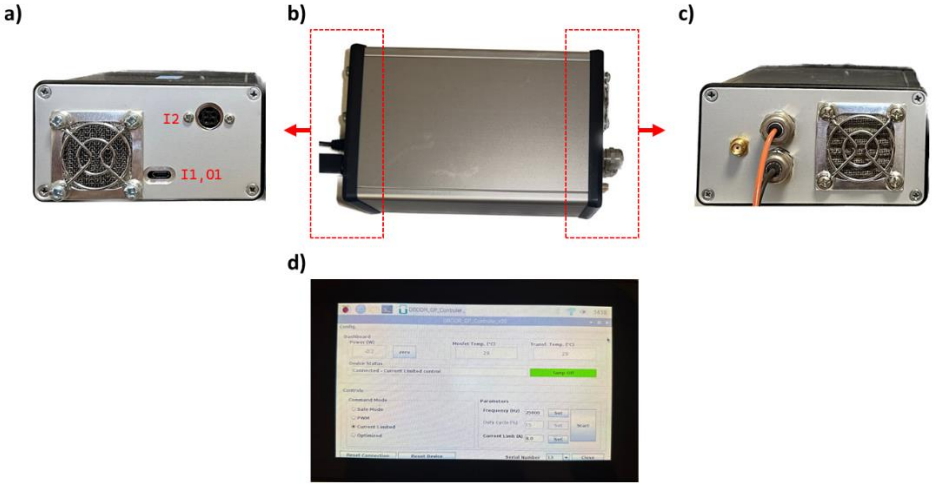

Figure 15. Pictures of the power supply a) left side view, b) top view, c) right side view showing the different input/output outlets and d) control monitor interface.

The power supply, acquired from OLISCIE company, was selected for its portability between France and Brazil. This compact unit measures 15 x 10 cm, making it convenient for transportation (Figure 15-b). Firstly, it is equipped with a versatile wire, which can function as both input and output (I1 – O1) (Figure 15-a). This wire not only controls the voltage and current passing through to the source but also transmits temperature information from both the source and the power supply to the control monitor also connected to this wire. Secondly, it is equipped with an input wire I2 (Figure 15-a) that provides power using an alternating current source. And finally, the power supply features two outlets, each corresponding to the red and black wires (Figure 15-c). These wires are connected respectively to the high voltage and ground electrodes of the system enabling the generation of the plasma discharge.
The monitor connected to the power supply allows the adjustment of the control power applied to the supply (Figure 15-d). The monitor's interface offers the ability to select the operating mode and choose the input parameters including the frequency (Hz) and the current limit (A). The different options of operating modes include safe mode, Pulse Width Modulation (PMW) mode, current limited mode, and optimized mode. The operating mode used in this study is the current limited where the current is limited to a specific value which is used to protect sensitive electronic components by limiting the current passing through them, thereby preventing potential damage caused by electrical overload.

2.1.1.2 Dual-frequency atmospheric pressure plasma jet

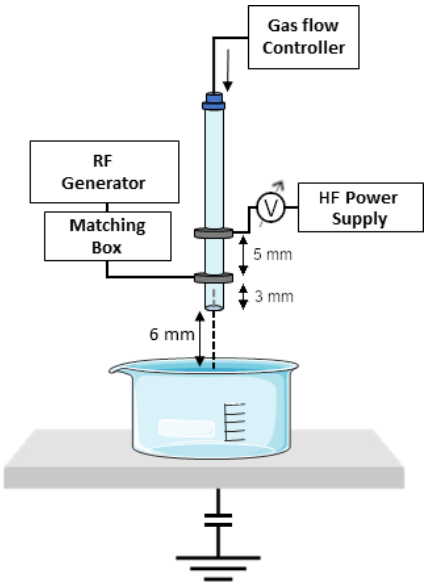

Figure 16. Experimental setup of the plasma jet coupled with two power supplies.

A schematic representation of the experimental device used to generate the plasma jet is shown in Figure 16 and consists of two sets of ring electrodes separated by approximately 5 mm, each one of these sets of electrodes connected to a different power supply. The plasma tube is composed of Alumina and has an outer diameter of 1 cm and an inner diameter of 9 mm. A power supply purchased from OLISCIE company which uses a patented technology to apply fast voltage pulses on a capacitive load [106]. The second consists of a ring-shaped electrode that is coupled to an RF generator (27.12 MHz, Seren R301) over a matching network [107]. A gas flux is supplied through the tube to the source impinging into ambient air. The gases utilized included helium (He) with a purity of 99.999% and argon (Ar) with a purity of 99.995%. The gas inlet is equipped by a mass flow controller. Air was fluxed to cool the electrodes and to control the atmosphere around the plasma plume.

2.1.2 Plasma characterization techniques

Various measurement tools were used to characterize the plasma from both electrical and optical perspectives. In this study, we employed a range of measurement tools to gain a deeper understanding of the plasma's behavior. The electrical aspect was investigated through the use of an oscilloscope and voltage and current probes, enabling us to analyze the electrical properties of the plasma. On the other hand, optical characterization was carried out using a dedicated setup for optical emission spectroscopy, providing valuable insights into the emission spectrum of the plasma. The following sections will provide detailed descriptions of the various plasma diagnostic tools employed.

2.1.2.1 Electrical diagnostics

Electrical measurements are conducted to obtain information about the generation and dynamics of the discharge. These measurements allow for the calculation of the power and energy deposited by the discharge. All electrical signals are simultaneously visualized and recorded using a digital oscilloscope (Rohde & Schwarz) with a bandwidth of 2 GHz and a sampling rate of 5 GSa/s.

The current probe is connected to the high-voltage electrode. It is a Pearson Electronics 6585 model with a frequency range from 40 Hz to 250 MHz and a sensitivity of 1 V/A. Figure 17 illustrates a representative example of the plasma's discharge current measurement. Notably, it is essential to highlight that the input current of the power supply is 8 A, while the measured current delivered by the power supply amounts to approximately 1.2 A.

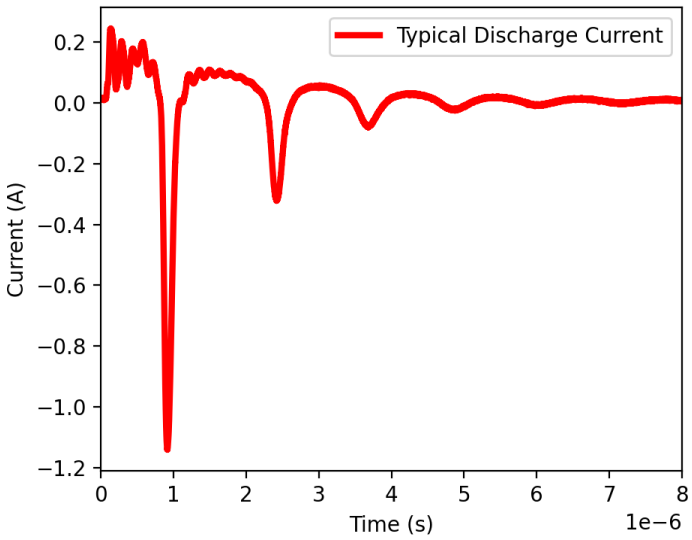

Figure 17. The typical discharge current of the plasma as a function of time.

2.1.2.2 Optical diagnostics - Optical emission spectroscopy (OES)

Optical emission spectroscopy (OES) is a powerful technique used to analyze the optical emission spectrum of a plasma jet. The principle behind this method lies in the fact that excited atoms and ions in the plasma emit characteristic photons at specific wavelengths when they return to their ground state. During the plasma discharge, electrons are excited to higher energy levels, and as they de-excite, they emit photons. By dispersing the emitted light through a spectrometer, the emitted wavelengths can be separated and measured, revealing valuable information about the elemental composition and excitation states of the plasma. OES allows for the identification of various species present in the plasma and can provide insights into the plasma temperature and electron density. This non-intrusive and versatile technique plays a crucial role in understanding the plasma's behavior and is widely employed in the field of plasma diagnostics and nanoparticle synthesis research.

The experimental setup used for optical diagnostics consists of a 600 µm diameter optical fiber connected to a high-resolution monochromator (Princeton Instrument, HRS-750) with a focal length of 75 mm. The monochromator is equipped with three diffraction gratings: 300 lines.mm^{-1}, 2400 lines.mm^{-1}, and 3600 lines.mm^{-1}, along with an intensified CCD camera (iCCD Pi-MAX4, Princeton Instruments). The spectrum was recorded at the point where the plasma jet exits from the source, as well as at intervals of 1 mm along the axial direction up to 6 mm, where the distance between the jet's exit and the samples was fixed at 6 mm. This systematic 1 mm interval measurement was performed to investigate the spatial evolution of specific

reactive species. This approach was adopted for three different targets, illustrated in Figure 18. First, measurements were taken with a free plasma jet, second, with a non-conductive flat surface as a target positioned at 6 mm away from the exit, and third, a solution also positioned at 6 mm from the surface. This investigation allowed for a detailed comparison of the optical emission characteristics and the spatial evolution of the reactive species under different experimental conditions.

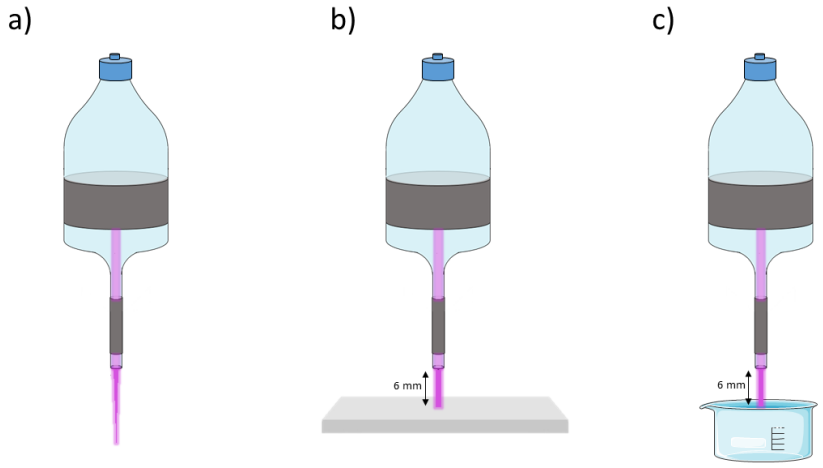

Figure 18. Experimental setup with three different targets: a) free plasma jet, b) flat surface, and c) solution.

The light emitted by the plasma passes through a first convergent lens with a focal length of 200 mm and then reaches a second convergent lens with a 100 mm focal length. The light is directed towards the optical fiber and reaches the monochromator's entrance slit. Figure 19 illustrates the optical setup installed for the optical emission spectroscopy measurements. The integration time is adjusted to avoid camera saturation. Through spectroscopy, we were able to identify the species produced by the plasma and track their intensity variations along the jet.

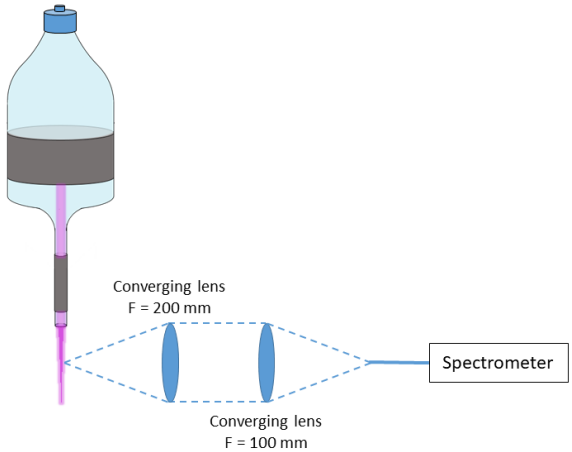

Figure 19. Schematic representation of the optical setup for optical emission spectroscopy measurements.

2.2 Plasma treated target

A liquid target, contained in a crystallizer, is positioned under the plasma jet. This crystallizer can hold ultra-pure water (Millipore Direct-Q 3 UV Water Purification System, Thermo Fisher Scientific) and unless stated otherwise, the distance between the source outlet and the liquid surface is fixed at 6 mm. This parameter is also set to maximize the production of reactive species in the liquid phase. Two Pyrex crystallizers were used depending on the availability in the laboratory of study. Tests have been made to ensure that the two different crystallizers shapes do not alter the resulted solution and let to the same results. One has an internal diameter of 40 mm and a height of 25 mm. And the other has an internal diameter of 22 mm and a height of 30 mm. The volume of the treated liquid is set at 10 mL, except for measurements with laser absorption, optical emission spectroscopy, and imaging, where the liquid volume completely fills the crystallizer. This precaution is taken to prevent the plasma light or laser beam (as applicable) from propagating through the crystallizer.

2.3 Liquid chemical characterization

Hydrogen peroxide (H_2O_2) is considered one of the main oxygen radical species generated by plasma and it can be measured due to its long lifetime. Its concentration in the plasma-treated distilled water was quantified using a colorimetric technique, a widely used method for determining the concentration of chemical compounds based on their absorption of light. The Einsenberg method [108] is based on the formation of titanium ions, H_2TiO^{4+}, a yellow colored compound resulting from the reaction of hydrogen peroxide H_2O_2 and titanium oxysulfate ($TiSO_4$). The reaction equation is as follows:

$$\mathbf{Ti}^{4+} + \mathbf{H_2O_2} + 2\ \mathbf{H_2O} \rightarrow \mathbf{H_2TiO}^{4} + 4\ \mathbf{H}^{+}$$

In this study, 10 ml volume of ultra-pure water was subjected to the plasma discharge, and immediately after the treatment, 100 µl from the sample was mixed with 5 µl of sodium azide (NaN_3). The purpose of this addition was to effectively quench the reactive nitrogen species (nitrite, nitrate) that could potentially interfere with the measurement of H_2O_2 concentration. After that, 50 µl of titanium oxysulfate ($TiSO_4$) was subsequently added to the solution. This reagent helps in forming a colored complex with H_2O_2 as previously mentioned, allowing for its quantitative determination. The absorbance of the resulting solution was measured at 407 nm using Tecan, Infinite 200 Pro plate reader.

Through a series of measurements and analysis, a linear relationship was established between the absorbance and the corresponding H_2O_2 concentration. Known concentrations of H_2O_2 were

utilized, covering a range of values from 0 to 2 mM. The calibration curve obtained in this manner followed the equation y = 0.2614 x + 0.0143, and is shown in Figure 20 below.
To ensure the accuracy and precision of the measurements, each sample was analyzed in triplicate, and the mean value was calculated. This reduces potential errors and improves the reliability of the obtained results.

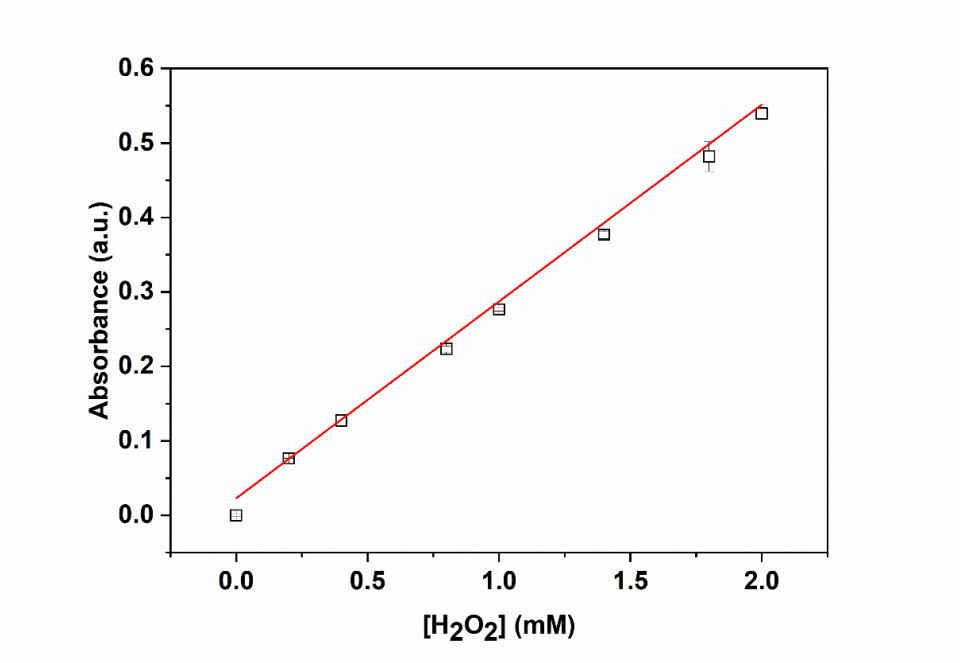

Figure 20. Calibration curve of hydrogen peroxide in liquid phase.

2.4 Metallic nanoparticles

2.4.1 Synthesis of silver nanoparticles

The synthesis of silver nanoparticles begins with the preparation of the metal precursor solution. $AgNO_3$ (99+% A.C.S reagent, Sigma-Aldrich) was dissolved in filtrated deionized water. Trisodium citrate dihydrate (Sigma-Aldrich) is subsequently added into the solution as a stabilizing agent. The inclusion of citrate in the synthesis process is of paramount importance as it serves as both a reducing agent and a stabilizer. Citrate is widely acknowledged as the preferred capping agent for silver colloids, ensuring homogeneous dispersion and preventing agglomeration in the treated medium. To examine the impact of precursor and stabilizer concentrations on the resulting nanoparticles, a systematic variation of their respective concentrations was employed.

Table 1. Table summarizing the concentrations of silver nitrate and citrate concentrations used in this study.

[AgNO$_3$] (mM)	*[cit] (mM)*
1	0.05, 0.1, 0.2, 0.3, 0.4, 0.5, 1, 1.5, 3, 6.3
2	0.5, 1.5, 3, 6.3
3	0.5, 1.5, 3, 6.3
4	0.5, 1.5, 3, 6.3
5	0.5, 1.5, 3, 6.3

Subsequently, 10 ml of each prepared solution underwent treatment utilizing a plasma jet at atmospheric pressure and ambient temperature, employing a defined duration and fixed operating parameters, encompassing a power supply current of 8 A, a frequency of 25 kHz, a gas flow rate of 3 l.min^{-1}, and a controlled plasma-liquid distance of 6 mm.

2.4.2 Synthesis of gold nanoparticles

The synthesis of gold nanoparticles follows a similar methodology, commencing with the preparation of the metal precursor solution. Gold (III) chloride hydrate (HAuCl4 · xH2O, 99.995%, MW: 339.79 g.mol^{-1}, Sigma-Aldrich) was dissolved in Ultrapure water (Direct-Q UV, Millipore). Polyvinylpyrrolidone (PVP, MW: 40 000 g.mol^{-1}) was also purchased from Sigma-Aldrich and used as a capping agent for the nanoparticles. These two products were used as purchased with no further purification. By varying the concentrations of the gold precursor and PVP, the influence of these parameters on the resultant nanoparticles was investigated (Table 2).

Table 2. Table summarizing the concentrations of chloroauric acid and PVP concentrations used in this study.

[HAuCl$_4$] (mM)	*[PVP] (mM)*
0.1	0.0005, 0.005, 0.01, 0.05, 0.08, 0.1
0.2	0.05
0.5	0.05
1	0.05
1.5	0.05

Subsequently, similarly to silver nanoparticles synthesis, 10 ml of each prepared solution underwent treatment utilizing the atmospheric pressure plasma jet, employing a specific duration and fixed operational parameters as already mentioned in the previous section.

2.4.3 Nanoparticles characterization techniques

Numerous characterization techniques have been developed to analyze the properties of nanoparticles, providing valuable information about their physical and chemical characteristics. In this section, we will focus on the techniques utilized for the analysis of metallic nanoparticles. We can categorize these techniques into the following divisions based on the nature of the techniques:

Spectroscopic techniques:

- Ultraviolet-visible spectroscopy (UV-vis)
- Dynamic light scattering (DLS)

Electron microscopy techniques:

- Scanning electron microscopy (SEM)
- Transmission electron microscopy (TEM)

Surface analysis techniques:

- Atomic force microscopy (AFM)

Structural analysis techniques:

- X-ray diffraction (XRD)
- Electron dispersive X-ray spectroscopy (EDX)

2.4.3.1 Ultraviolet-visible spectroscopy (UV-vis)

UV-vis spectroscopy is a non-invasive and non-destructive analytical technique used to measure the absorbed and scattered light in the ultraviolet (UV) and visible (vis) regions by a sample, which is referred to as the extinction. In general, the basic setup involves placing the sample between a light source that emits a broad range of wavelengths and a photodetector that measures the intensity of light transmitted through or absorbed by the sample as shown in Figure 21 below. The intensity of the beam is measured before (I_0) and after (I) passing through the sample. To ensure accuracy, each spectrum is corrected by subtracting the background signal obtained from a "blank" cuvette filled solely with the dispersing medium, thereby eliminating any spectral features originating from the solvent. By comparing these

measurements at different wavelengths, the sample's absorbance spectrum can be determined. The resulting absorption spectrum provides insights into the electronic structure, concentration, and optical properties of the sample. Additionally, it enables the study of stability, and structural changes in nanoparticles, providing valuable information for research, and process optimization as the resulted spectra depends on factors related to particle characteristics such as size, shape, and agglomeration status. The wavelength at which the particles exhibit maximum light absorption (λ_{max}) is determined by the nature of the compound and its size. Additionally, the intensity of absorption is influenced by the quantity of particles present in the measured sample.

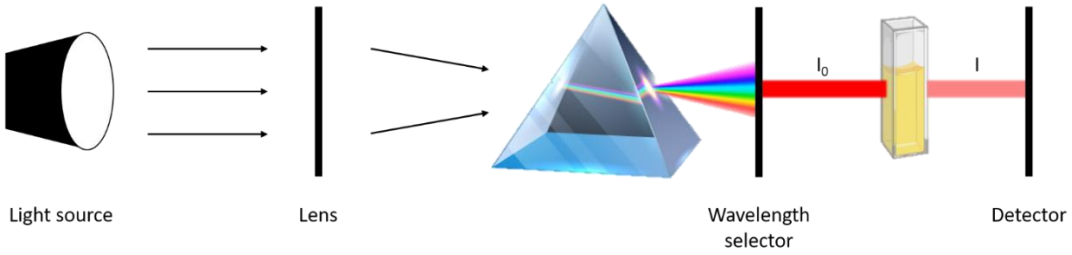

Figure 21. Schematic representation of the instrumentation of a UV-vis spectrophotometer.

The Beer-Lambert law states that the absorbance of a sample is directly proportional to the concentration of the absorbing species and the path length of the sample cell. This relationship allows for quantitative analysis, as the absorbance can be used to determine the concentration of a specific compound in a sample when the molar absorptivity and path length are known.

$$\mathbf{A = \varepsilon\ c\ L}$$

Where:

ε is the molar extinction coefficient

c is the concentration of the absorbing species in moles per liter

L is the path length of the sample cell in centimeters

The transmittance (T) is the ratio of the intensity of light transmitted through the sample (I) to the intensity of incident light (I_0):

$$\mathbf{T = I\ /\ I_0}$$

The formula used to calculate the absorbance (A) in UV-vis spectroscopy is as follows:

$$\mathbf{A = - \log_{10} (T)}$$

Where:

A is the absorbance

T is the transmittance

In our study, several UV-vis spectrophotometric instruments were utilized to obtain the absorbance spectra, taking into consideration the available instrumentations in the laboratory and country of stay. The Evolution 60S from Thermo Scientific and the V-670 from Jasco UV-vis Spectrophotometers were used. Prior to analysis, around 2 ml of the treated samples are transferred into a 10 mm x 10 mm quartz cuvette and placed in the sample holder. The Infinite 200 Pro from Tecan and the Synergy H1 from BioTek Instruments SAS multifunctional microplate readers were also used. 200 µl of the treated samples are transferred into the microplate's wells and placed for analysis. The samples were analyzed immediately following plasma treatment to prevent potential agglomeration, which could occur over time, within the wavelength range of 300-800 nm.

2.4.3.2 Dynamic light scattering (DLS)

Dynamic Light Scattering (DLS) is a technique for measuring the hydrodynamic size of nanoparticles, their size distribution and their agglomeration status within a liquid medium. It is a non-destructive, non-invasive technique and offers many advantages. It requires minimal sample preparation and provides immediate results. When a laser beam is directed at the nanoparticle suspension, the particles scatter the light in different directions. The scattered light is collected and measured by a detector at a certain detection angle (Figure 22).
Due to the Brownian motion, particles undergo random motion in various directions due to constant collisions with solvent molecules. These collisions transfer energy to the particles, prompting their movement. As the energy transfer remains relatively constant, it has a more significant impact on smaller particles, causing them to move at higher velocities compared to larger particles which results in a fluctuation of the intensity of scattered light over time. By analyzing the autocorrelation function of the scattered light, DLS determines the rate at which the intensity fluctuations occur. This information is then used to calculate the hydrodynamic diameter of the nanoparticles. Additionally, DLS provides insights into the polydispersity index, which indicates the distribution of particle sizes within the sample.

The instrument that was used in the characterization of the nanoparticles solutions is a Zetasizer Nano from Malvern Instruments equipped with a He-Ne laser at 633 nm wavelength. The data was collected at a fixed angle of 90°. Prior to the analysis, the colloidal solution was transferred to an ultrasonic bath during 10 min in order to eliminate possible agglomeration of the synthesized nanoparticles. 100 µl of the sample is diluted with 1 ml of ultra-pure water and then transferred into a 10 mm x 10 mm cuvette and placed in the DLS sample chamber.

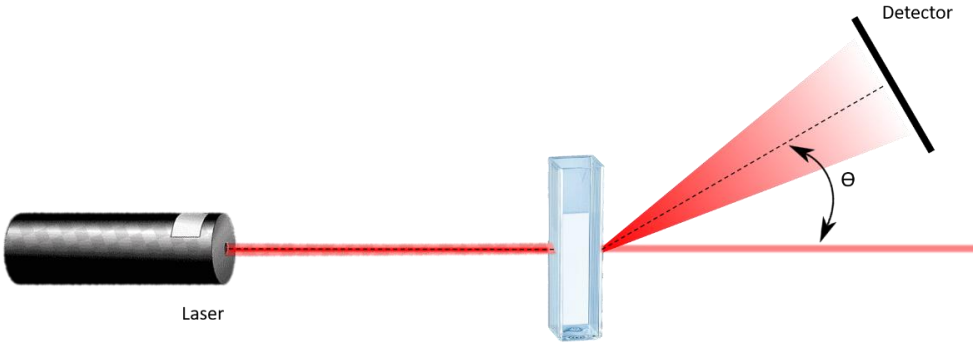

Figure 22. Schematic representation of a DLS measurement system. Reproduced from [109].

2.4.3.3 Scanning electron microscopy (SEM)

Scanning Electron Microscopy (SEM) is a characterization technique that provides high-resolution images and detailed surface information by scanning a sample with a focused electron beam. Its principle involves the interaction of the electron beam with the sample, which leads to the emission of secondary electrons, backscattered electrons, and characteristics X-rays. When the electron beam scans the surface of the sample, the emitted signals are detected and converted into an image. For effective imaging, the sample must exhibit conductivity; otherwise, it is usually coated with a thin layer of conductive material in order to prevent static electric charge accumulation on the surface. Figure 23 illustrates the standard configuration of a scanning electron microscope, consisting of an electron gun (electron source and accelerating anode), electromagnetic lenses responsible for electron focusing, a vacuum chamber where the samples are held and several detectors to collect emitted signals from the sample.

SEM offers several advantages for nanoparticle characterization. It allows for high magnification imaging with high resolution, enabling the visualization of nanoparticles at nanoscale resolution. Additionally, SEM provides information about the surface topography and can reveal details such as surface roughness, porosity, and agglomeration state of nanoparticles. However, this technique has some disadvantages such as the charge effects of some materials caused by the accumulation of static electric fields leading to the destruction of the sample. Additionally, SEM requires a high-vacuum environment, which limits the analysis of samples in their native liquid or gas states.

It is also important to note that SEM is an imaging technique and cannot directly provide information about the internal structure or chemical state of nanoparticles. Elemental analysis of nanoparticles can also be performed using Energy-Dispersive X-ray Spectroscopy (EDX) coupled with SEM, which provides information about the elemental composition of the sample. This technique will be discussed in a later section.

In this study, the SEM employed to capture high-resolution images of the synthesized nanoparticles is the ZEISS Sigma HD model. Sample preparation involved placing a drop of the plasma-treated solution onto a silicon (100) wafer and spin-coating it for 30 seconds. Beforehand, the silicon surface underwent cleaning through a base piranha etch.

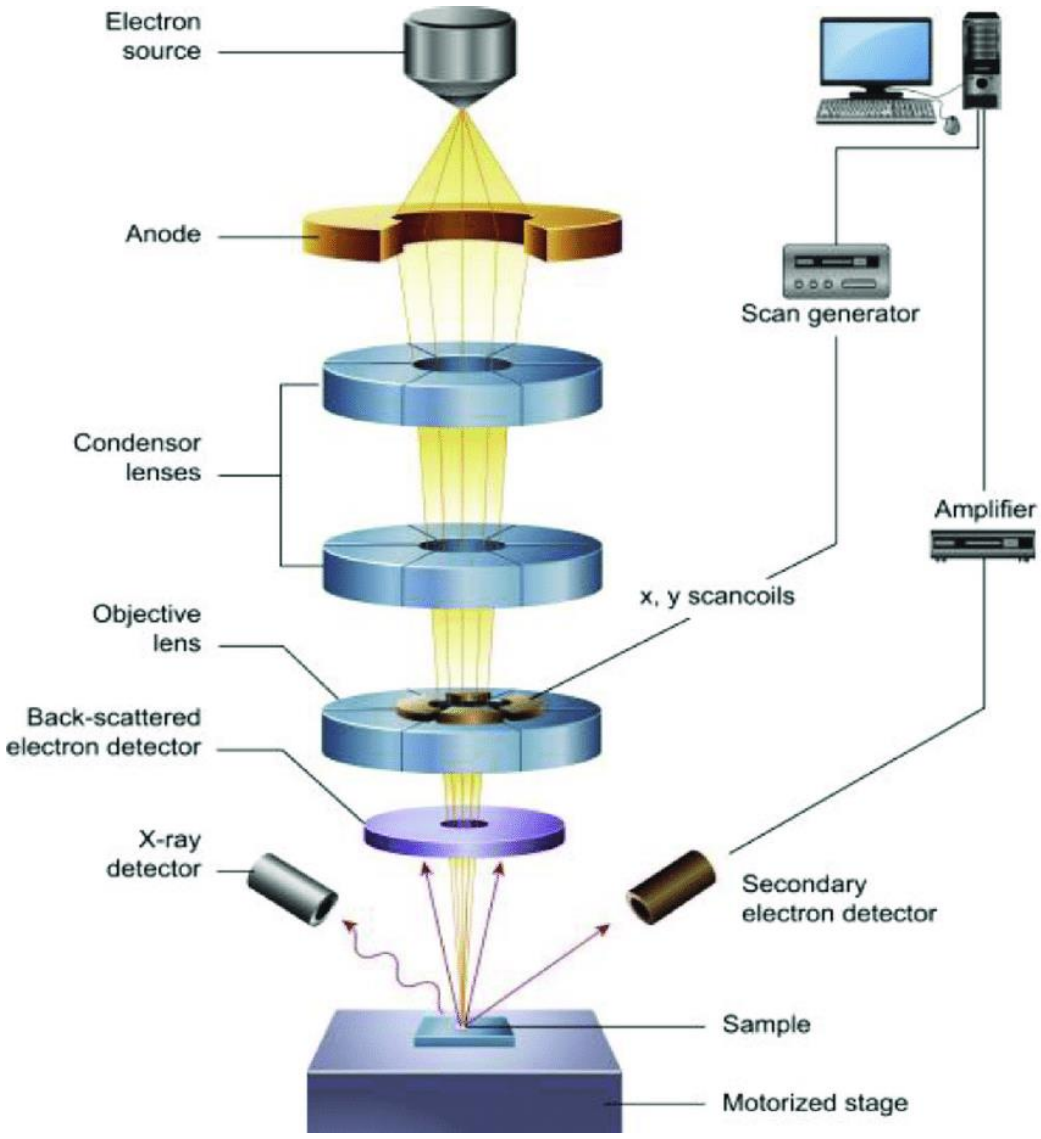

Figure 23. Schematic representation of the core components of a scanning electron microscope [110].

2.4.3.4 Electron dispersive X-ray spectroscopy (EDX)

Energy dispersive X-ray Spectroscopy (EDX), is used for elemental analysis of materials. It provides information about the elemental composition within a sample. This technique works in conjunction with scanning electron microscopy (SEM). The process is illustrated in Figure 24. The primary electron beam from the microscope interacts with the sample, causing the emission of characteristic X-rays from the atoms within the sample. When the electrons interact with the atoms in the sample, inner-shell electrons are displaced, creating vacancies. To fill these vacancies, outer-shell electrons transition to the lower energy levels, releasing characteristic X-rays in the process. The emitted X-rays have unique energies associated with specific elements. EDX analysis can be used to confirm the presence of specific elements in nanoparticles, and investigate impurities or contaminants. The intensity of the peaks in an EDX spectrum is directly proportional to the concentration of the corresponding element present in the sample. It is particularly useful in nanoparticle research for verifying the elemental identity of synthesized nanoparticles and assessing the elemental purity of samples.

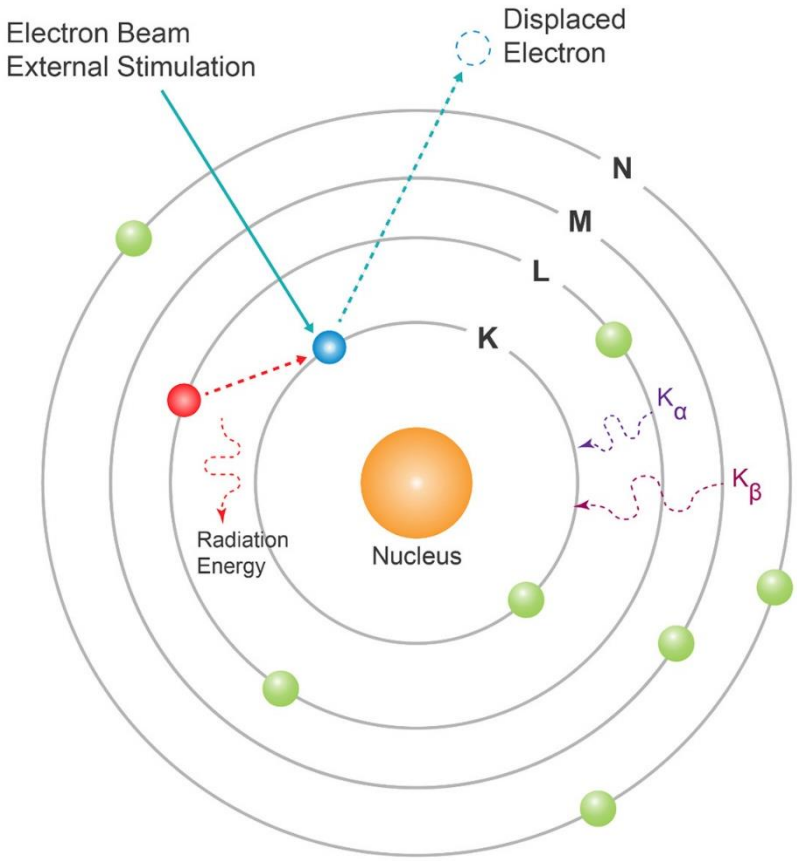

Figure 24. Schematic representation of X-ray generation principle [111].

2.4.3.5 Transmission electron microscopy (TEM)

Transmission Electron Microscopy (TEM) is an advanced imaging technique for analyzing the internal microstructure of a sample. It involves the transmission of a high-energy electron beam through an ultra-thin specimen. This technique requires the preparation of thin samples, typically in the form of ultra-thin sections or nanoparticles dispersed on a supporting grid in order to let the electron beam pass through it. The electrons interact with the sample, leading to elastic scattering, inelastic scattering, and diffraction. Figure 25 illustrates the standard configuration of a transmission electron microscope, consisting of an electron gun (electron source and accelerating anode), electrostatic lenses to focus the electrons before and after the specimen, and a transmitted electron detection system.

In TEM, a highly focused electron beam is generated and directed towards the specimen. The electron beam passes through the sample, and the transmitted electrons are collected by a detector to form an image. The resulting images provide extremely high resolution, enabling the visualization of nanoparticles and their internal structures, such as crystal lattice planes, defects, and interfaces. Also, it allows for the determination of nanoparticle size using image analysis techniques by measuring their average diameter from the micrographs.
Additionally, high-resolution electron microscopy (HR-TEM) provides details about the crystallographic structures. High-resolution imaging has the capability to identify specific crystalline defects, enabling the determination of lattice spacing and crystallographic parameters.

One of the major advantages of TEM is its high magnification capability and direct observations of detailed nanostructures. Also, it can be coupled with Energy-Dispersive X-ray Spectroscopy (EDX) to perform elemental analysis, providing information about the composition of nanoparticles. However, TEM also comes with several limitations. One significant disadvantage is its high-vacuum requirement. Operating in a high-vacuum environment restricts the analysis of samples in their native liquid or gas states. Furthermore, the intense electron beam used in TEM can cause electron beam damage to sensitive samples, leading to structural changes or damage.

The TEM instrument used in this study is the JEM 100CX – II from JEOL SAS. Prior to sample preparation, the nanoparticles solution was transferred into an ultrasonic bath for 10 min to eliminate possible agglomeration. The sample was prepared by placing a drop of the solution after treatment on a carbon coated copper mesh grid and dried at ambient pressure and room temperature.

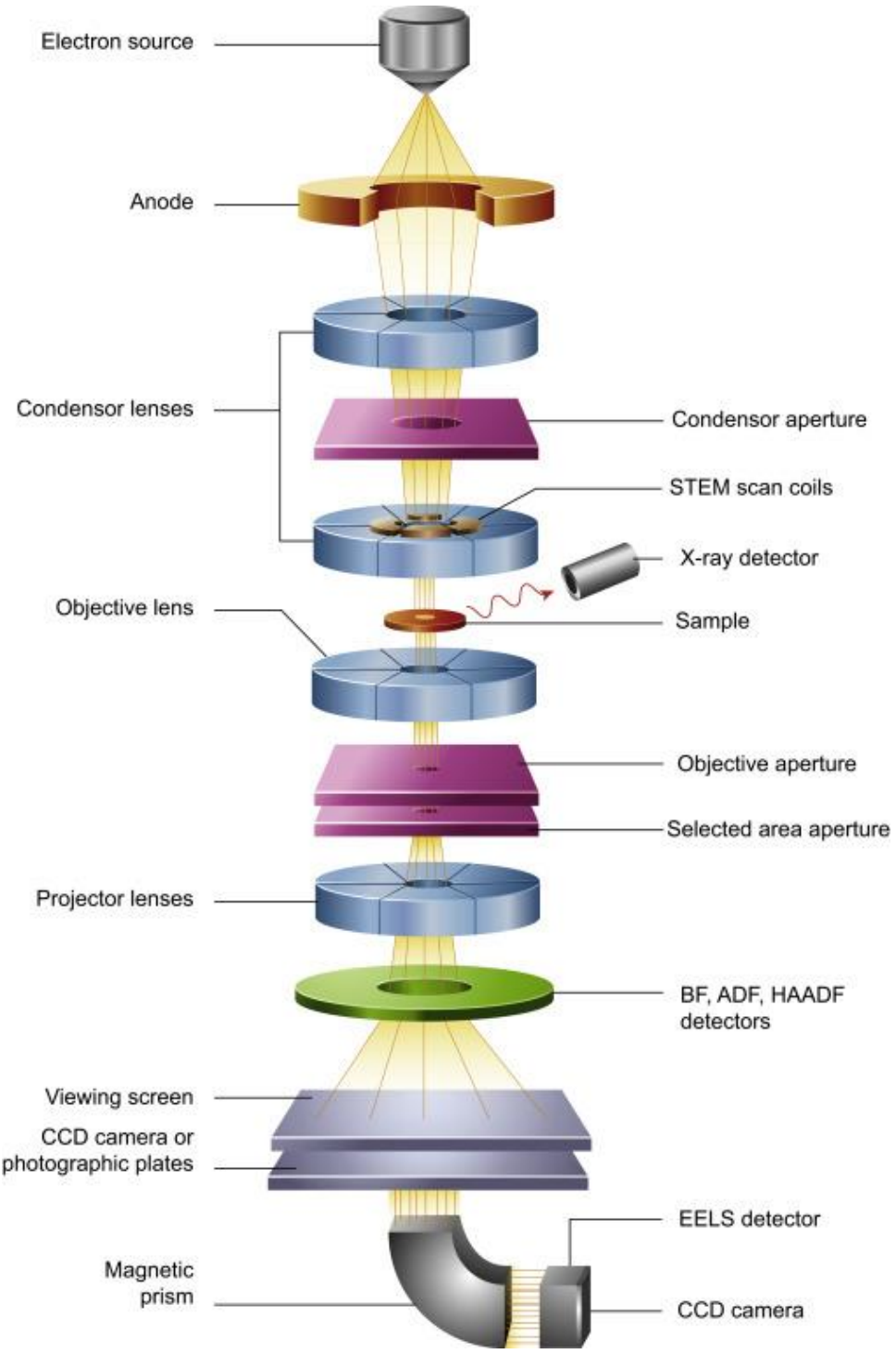

Figure 25. Schematic representation of the core components of a transmission electron microscope [110].

2.4.3.6 Atomic force microscopy (AFM)

Atomic Force Microscopy (AFM) is a versatile technique that provides information about the surface topography and morphology of nanoparticles. This instrument consists of a sharp and delicate head attached to an elastic probe known as a cantilever. This cantilever is connected to a piezoelectric arm, and its back is coated with a metallic thin layer to enhance the reflection of a laser beam used to determine the cantilever's orientation in 3D space. Figure 26 below is a representation of the atomic force microscopy instrument. By applying precise voltages to the piezoelectric in the x, y, and z directions, the cantilever attachment spot can be shifted to any desired point in space with angstrom precision. Once the AFM head touches the sample surface, a force is exerted on the head, which depends on the distance and type of the surface. This force induces bending and displacement of the laser beam in a plane perpendicular to the horizon. Using optical diodes to measure the amount of cantilever bending and knowing the final position of the cantilever, the spatial position of the AFM head is determined. By continuously changing the voltage differences applied to the piezoelectric, the AFM head scans the sample surface, determining surface points one by one, which are then plotted on a computer screen as a 3D surface [112].

This technique offers several advantages, its versatility allows it to be used across various scientific disciplines, examining solid surfaces, soft materials, and biological specimens. Additionally, AFM is non-destructive, preserving the integrity of samples during analysis. However, AFM does have some limitations to consider. It is time consuming especially for acquiring high-resolution images, which may hinder large-scale studies. Also, the tip can experience wear or damage during scanning, affecting image quality and posing a risk to delicate samples.

In this study, the atomic force microscope employed to capture high-resolution images of the synthesized nanoparticles is the Solver Nano model from NT-MDT Spectrum Instruments. Sample preparation involved placing a drop of the plasma-treated solution onto a silicon (100) wafer and spin-coating it for 30 seconds. Beforehand, the silicon surface underwent cleaning through a base piranha etch.

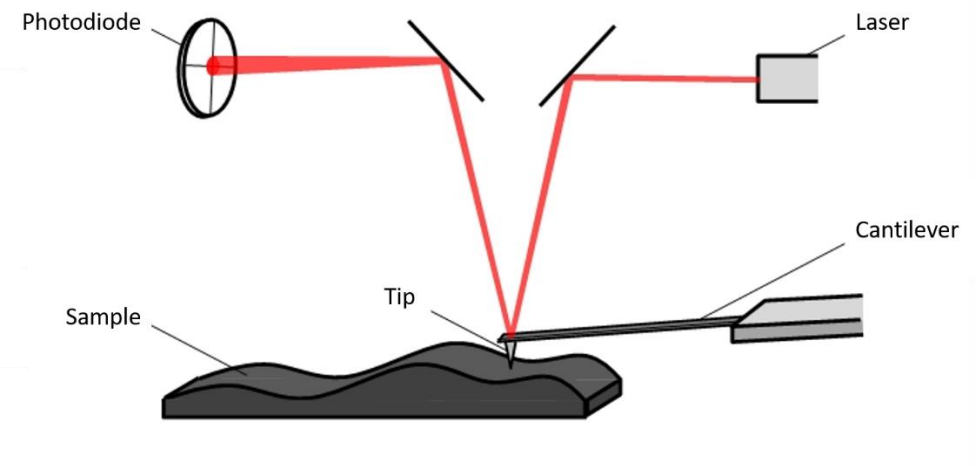

Figure 26. Schematic representation of an atomic force microscope set-up [112].

2.4.3.7 X-ray diffraction (XRD)

X-ray diffraction (XRD) is a widely used technique providing information about the crystal structure, phase composition, and lattice parameters of nanoparticles. This technique is based on Bragg's law, which allows the determination of the arrangement of atoms within a crystal lattice (Figure 27). A monochromatic X-ray beam is directed towards the sample, and the X-rays interact with the crystal lattice. The X-rays are diffracted at specific angles determined by the arrangement of atoms in the crystal structure. The diffracted X-rays are collected by a detector placed on the opposite direction, and the resulting diffraction pattern, known as a diffraction spectrum or X-ray diffractogram, is obtained. The diffraction pattern contains a series of peaks that correspond to the diffraction angles and intensities of the diffracted X-rays. By analyzing the positions and intensities of these peaks, valuable information about the crystal structure and phase composition of the sample can be obtained. Each crystalline phase has a unique diffraction pattern, allowing for identification and quantification of different phases present in the sample. For nanoparticle characterization, XRD can provide information about the crystalline nature of the nanoparticles, their crystal size, lattice strain, and preferred crystallographic orientations. XRD is a non-destructive technique that does not require extensive sample preparation. It is applicable to a wide range of materials, including metals, ceramics, minerals, and organic compounds. The technique is highly sensitive to changes in crystal structure and can detect even small variations in phase composition. However, XRD also has certain limitations. It requires samples to be in crystalline form, which may not always be feasible for certain nanoparticle materials. Additionally, XRD is not suitable for analyzing

nanoparticles with extremely small sizes or when the nanoparticles are amorphous or poorly crystalline.

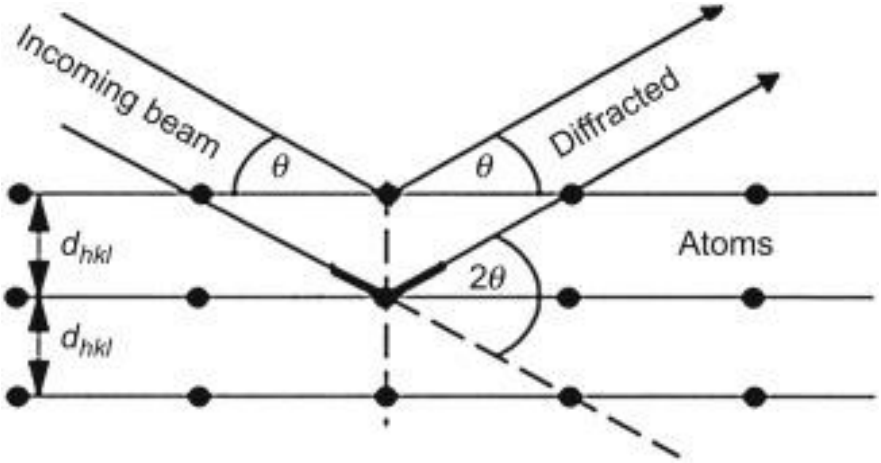

Figure 27 Schematic representation of X-ray diffraction principle.

Bragg's law is a fundamental principle in X-ray crystallography that describes the scattering of X-rays by crystal lattices, leading to the formation of diffraction patterns. It relates the angles of incidence and diffraction of X-rays with the spacing of crystal planes in a crystal lattice.

The mathematical expression of Bragg's law is given as:

$$\mathbf{n\lambda = 2d\ sin\theta}$$

Where:

n is an integer (the order of the diffraction peak)
λ is the wavelength of the incident X-ray radiation
d is the interplanar spacing of the crystal lattice planes
θ is the angle of incidence or diffraction of the X-ray beam

Elemental analysis, crystallinity and phase of the silver nanoparticles were determined by XRD. Preparation of the samples for analysis was as follows: 50 ml of the treated silver colloids solution was dried at 50 ° C overnight, then the particles were collected and analyzed.

2.5 Conclusions

The experimental set-up presented in this chapter is aimed for the synthesis of metallic nanoparticles using a technique based on the generation of plasma discharge in contact with a liquid solution. The synthesis of nanoparticles is realized through the reduction of metal ions without the addition of any reducing agent. This chapter has provided a comprehensive overview of the materials and methods utilized for the synthesis and characterization of silver and gold nanoparticles. The plasma characterization techniques, including the plasma experimental devices and associated diagnostics methods, were discussed, emphasizing their importance in understanding the plasma treatment process. Furthermore, the liquid chemical characterization techniques were presented, highlighting their role in analyzing the nanoparticle solutions. The synthesis methods for silver and gold nanoparticles were described. Lastly, a range of nanoparticle characterization techniques, including UV-vis spectroscopy, dynamic light scattering, scanning electron microscopy, transmission electron microscopy, atomic force microscopy, X-ray diffraction, and energy dispersive X-ray spectroscopy, were introduced, showcasing their significance in investigating the structural, morphological, and compositional properties of the nanoparticles. These materials and methods lay the foundation for the subsequent chapters, where the results and findings obtained from the nanoparticle synthesis and characterization will be presented and discussed in detail.

Chapter 3.
Synthesis of Metallic Nanoparticles by Atmospheric Pressure Plasma Jet

3 Synthesis of Metallic Nanoparticles by Atmospheric Pressure Plasma Jet

Divided into three separate sections, this chapter explores the synthesis of metallic nanoparticles using an atmospheric pressure plasma jet (APPJ).

In the first section, the initial focus is on the characterization of the helium plasma jet itself, serving as the main tool for nanoparticle synthesis. With the use of optical emission spectroscopy (OES) analysis, we gain more information on the plasma's dynamic nature as well as the reactive species present in the plasma which have a direct effect on nanoparticle synthesis. This section also examines the intricacies of the interaction dynamics of the plasma jet with liquid solutions, and subsequent effects on nanoparticle synthesis.

The second section focuses on the silver nanoparticles synthesis and their characterizations. The synthesis protocol is presents and detailed analyses on the effects of different chemical parameters on the optical properties, size distribution, and surface properties of the synthesized silver nanoparticles. This section presents a comprehensive investigation, including diverse aspects such as spectroscopic characterization, crystalline structure determination, and shape homogeneity assessment.

In the third and final section, the study continues with the synthesis of gold nanoparticles where the protocols employed are presented. Through characterization techniques such as X-ray diffraction, transmission electron microscopy, and dynamic light scattering, this section highlights the role of parameters such as precursor concentration and capping agents in tailoring the nanoparticles' size, shape, and homogeneity.

In this comprehensive investigation, we aim to study the underlying mechanisms that govern the formation of nanoparticles within the context of a helium atmospheric pressure plasma jet. It is worth noting that parts of this chapter have been previously published in the international journal "Nanotechnology" by IOP Publishing, titled "Synthesis of silver nanoparticles by atmospheric pressure plasma jet" [113]. The corresponding Digital Object Identifier (DOI) for this publication is 10.1088/1361-6528/ac6528.

3.1 Plasma characterization

3.1.1 Optical emission spectroscopy (OES)

The investigation of optical emission spectroscopy (OES) offers valuable insights into the dynamics of plasma generated reactive species. In this section, we present a comprehensive analysis of the optical emission spectrum ranging from 200 to 750 nm, illustrating the excited species generated by the plasma setup under different plasma process parameters. The initial spectral overview showcases the species generated by this plasma discharge (power supply current= 8 A, frequency= 25 kHz, He gas flux= 3 L.min^{-1}, jet-target distance= 6 mm). After that, we investigated the spatial evolution of some excited species within the plasma plume, covering distances from 0 mm to 6 mm. By systematically varying parameters such as the target that comes in contact with the plasma jet (free jet, plane surface and solution), as well as manipulating the input current of the plasma jet, we aim to understand the influence of these factors on the distribution and concentration of excited species. This investigation into the generation and special evolution of excited species through OES is essential for comprehending the mechanisms driving plasma-solution interactions.

3.1.1.1 Optical emission spectrum of the plasma jet

We used an optical emission spectrometer placed perpendicular to the source to identify the species present in the jet. The light emission of the plasma plume is characteristic of these species. This allowed for a study of the distribution of light emission as a function of wavelength, across the entire plume, thus offering insights into the induced chemistry in the liquid phase following treatment by the plasma. The spectrum is shown in Figure 28 and is representative of the emissions observed for plasma jets in the presence of helium as process gas [114] [115] [116]. Within the source, the plasma is predominantly composed of helium species from the gas. The emissions from OH, N_2 and N_2^+ are induced mainly by the air impurities diffused into the helium gas stream from the ambient air. No intensity calibration has been performed, which prevents us from comparing the intensity values of different excited species among themselves.

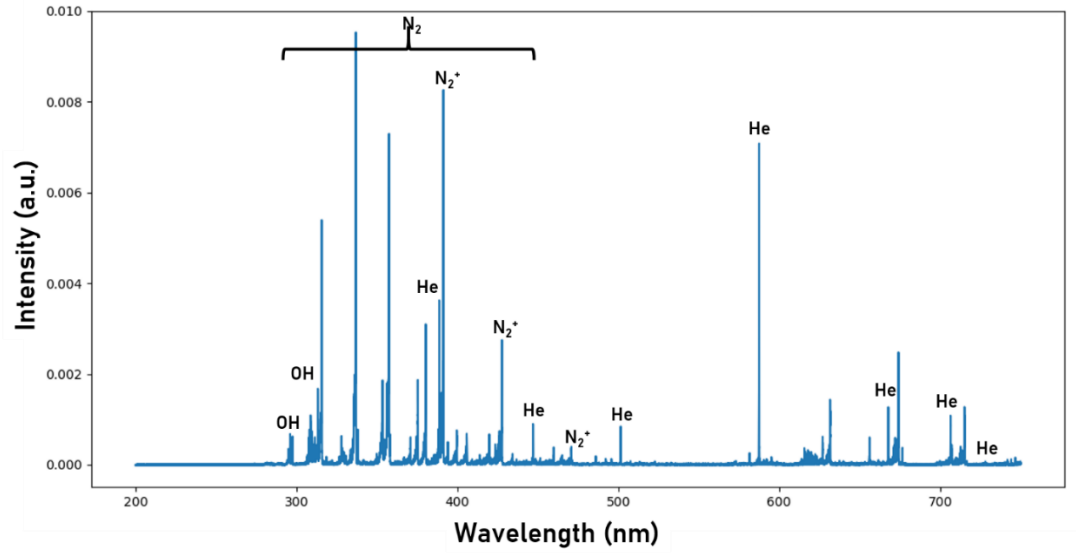

Figure 28. Optical emission spectrum of the atmospheric pressure plasma jet at a power supply current of 8 A, frequency at 25 kHz and helium gas flux at 3 L.min^{-1}.

The observed lines and their corresponding transitions are listed in Table 3. The excited species are identified based on the work of Pearse and Gaydon for molecular band transitions (Book, The Identification of Molecular Spectra) [117] and from the National Institute of Standards and Technology (NIST) website for atomic transitions. For helium, the transitions involve electron movement between different energy levels, such as 3p to 2s and 4d to 2p. The hydroxyl radical exhibits transitions at different vibrational and rotational levels. Nitrogen displays transitions in its Second Positive System (SPS), including C 3Πu to B 3Πg with varying vibrational and rotational quantum numbers. The nitrogen cation, N_2^+, demonstrates transitions in its First Negative System (FNS), such as B 2∑u + to X 2∑g + with different vibrational states. These transitions, characterized by specific wavelengths, provide valuable insights into the electronic structure and energy transitions within these molecular species.

Table 3. Species identified based on the lines observed in the optical emission spectrum obtained with their corresponding transitions.

Specie	***Wavelength (nm)***	***Transition***
He	388	$3p\ ^3P^\circ_{1,2} - 2s\ ^1S_1$
	447	$4d\ ^1D1_{,2} - 2p\ ^3P^\circ\ 0_{,1}$
	501	$3p\ ^1P^\circ_{\ 1} - 2s\ ^1S_0$
	587	$3d\ ^3D_{1,2,3} - 2p\ ^3P^\circ_{\ 0,1,2}$
	667	$3d\ ^1D_2 - 2p\ ^1P^\circ_{\ 1}$
	706	$3s\ ^3S_1 - 2p\ ^3P^\circ_{\ 0,1,2}$
	728	$3s\ ^1S_0 - 2p\ ^1P^\circ_{\ 1}$
OH	295	$A\ ^2\sum^+ - X\ ^2\Pi\ (3,2)$
	308	$A\ ^2\sum^+ - X\ ^2\Pi\ (0,0)$
N_2 (Second Positive System SPS)	313	$C\ ^3\Pi_u - B\ ^3\Pi_g\ (2,1)$
	315	$C\ ^3\Pi_u - B\ ^3\Pi_g\ (1,0)$
	337	$C\ ^3\Pi_u - B\ ^3\Pi_g\ (0,0)$
	353	$C\ ^3\Pi_u - B\ ^3\Pi_g\ (1,2)$
	357	$C\ ^3\Pi_u - B\ ^3\Pi_g\ (0,1)$
	371	$C\ ^3\Pi_u - B\ ^3\Pi_g\ (2,4)$
	375	$C\ ^3\Pi_u - B\ ^3\Pi_g\ (1,3)$
	380	$C\ ^3\Pi_u - B\ ^3\Pi_g\ (0,2)$
	399	$C\ ^3\Pi_u - B\ ^3\Pi_g\ (1,4)$
	405	$C\ ^3\Pi_u - B\ ^3\Pi_g\ (0,3)$
	414	$C\ ^3\Pi_u - B\ ^3\Pi_g\ (3,7)$
	420	$C\ ^3\Pi_u - B\ ^3\Pi_g\ (2,6)$
	434	$C\ ^3\Pi_u - B\ ^3\Pi_g\ (0,4)$
	449	$C\ ^3\Pi_u - B\ ^3\Pi_g\ (2,7)$
N_2^+ (First Negative System FNS)	391	$B\ ^2\sum_u{}^+ - X\ ^2\sum_g{}^+\ (0,0)$
	427	$B\ ^2\sum_u{}^+ - X\ ^2\sum_g{}^+\ (0,1)$
	470	$B\ ^2\sum_u{}^+ - X\ ^2\sum_g{}^+\ (0,2)$

3.1.1.2 Intensity of reactive species along the plasma jet

Figure 29 illustrates the spatial distribution of reactive species (OH, N_2, N_2^+, and He) along the plasma jet. Measurements were conducted along the plasma jet (Y-axis) with a length of 6 mm with three different targets: a) free jet, b) in contact with a solution, and c) in contact with a non-conductive flat surface.

It is evident from the graphs that the spatial distribution of species emissions is not uniform along the plasma jet. In Figure 29(a), two trends emerge from these curves. The first to OH (308 nm) and He (706 nm), where both species exhibit high emission intensities at the tube's exit, which then gradually decrease along the plasma jet. This suggests that the discharge loses energy as it moves away from the tube exit, explaining the decrease in emissions.

The second trend is observed for N_2 (337 nm) and N_2^+ (391 nm) profiles where their intensities increase from the tube's exit, reach their maximum at Y= 3 mm of distance from the exit, and then progressively decrease along the jet. This phenomenon can be attributed to the mixture of plasma gas and the surrounding atmospheric air. At the discharge tube exit, the presence of air is minimal, leading to reduced emissions of these spectral bands. Nevertheless, as one moves farther from the exit, the influx of air into the plasma intensifies, resulting in elevated emissions. After that, the quantity of air within the mixture reaches a level where it becomes substantial enough to hinder the continuation of plasma propagation and this is evident by the decrease in emissions.

The proximity of a solution situated at 6 mm from the tube and in contact with the plasma had a subtle impact on the spatial distribution of species emissions. As evidenced in Figure 29, two distinct trends also emerged, with N_2 (337 nm) and N_2^+ (391 nm) profiles also displaying heightened intensities at Y = 4 mm and Y = 5 mm, respectively. While OH (308 nm) and He (706 nm) exhibited peak emission intensities at the tube exit, they then experienced a slight increase at Y = 4 mm and Y = 3 mm, respectively, before diminishing.

Moreover, a more pronounced and notable shift in the spectral distribution of species emissions was observed when a non-conductive planar surface served as a target in contact with the plasma at a distance of 6 mm from the tube (Figure 29(c)). In this scenario, OH (308 nm) displayed an opposing trend, while He (706 nm) exhibited minimal intensity until reaching Y = 5 mm, where it increased to reach its maximum. The introduction of the flat surface significantly augmented He emission near the target.

Hence, the selection and presence of a target in contact with the plasma possess the potential to reshape both the distribution and intensities of the species generated by the plasma jet.

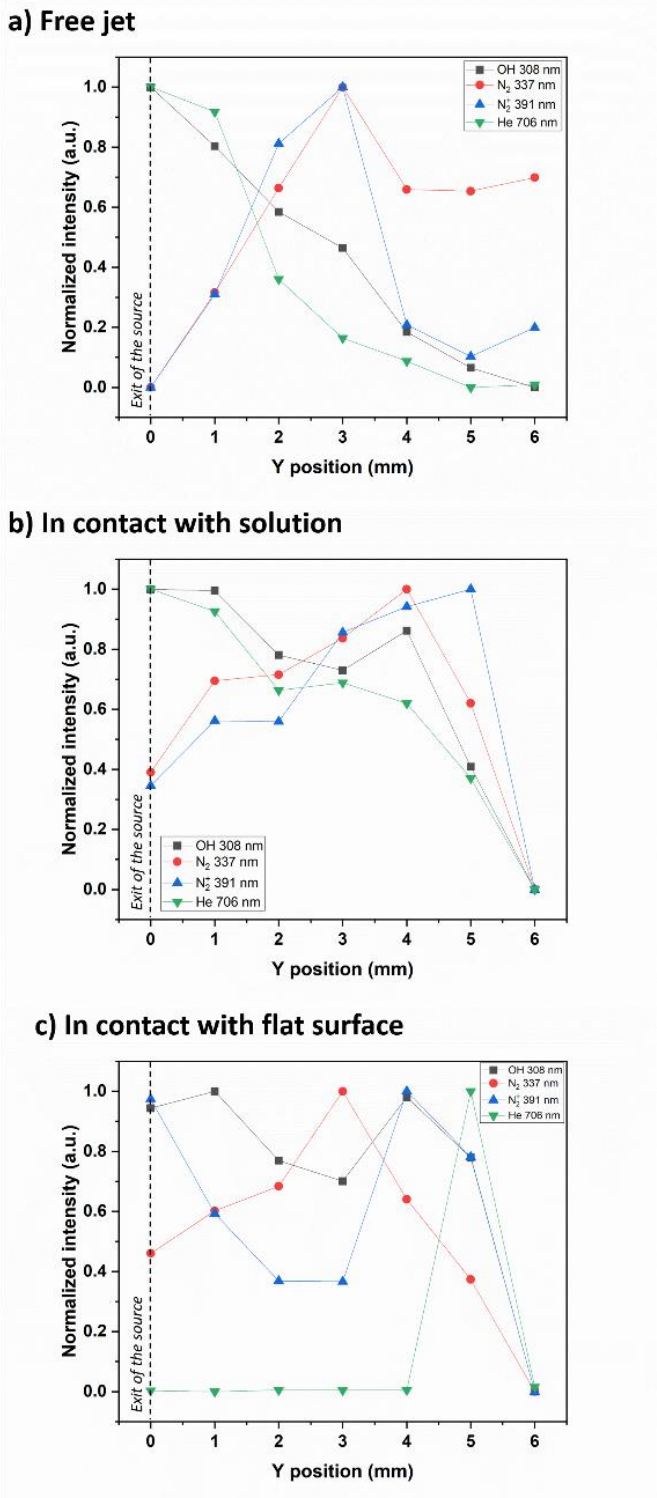

Figure 29. Distribution of the intensity of reactive species along the plasma jet when it's a) free plasma jet, b) in contact with a solution, and c) in contact with a non-conductive flat surface. The plasma is generated at an input power supply current of 8 A, a frequency of 25 kHz, and a helium flow rate of 3 L.min^{-1}.

3.2 Liquid chemical characterization

The impact of plasma-generated reactive species on the nanoparticle synthesis within the treated solution is multifaceted, as detailed by Kaushik et. al [118]. While certain reactive species exert a direct influence and contribute to the chemical reactions in the solution, others display an indirect role by participating in reactions that produce stable, enduring reactive species within the aqueous medium. Reactive species like OH, O_2^-, and $^1O_2$, characterized by lifetimes of 2 ns, 1 µs, and 4 µs [103], respectively, remain confined to the liquid's surface, unable to extend beyond the interface region. While long-lived species are present in the bulk liquid and are expected to remain in the liquid after the plasma exposure [119]. Among these, H_2O_2 is one of the most stable reactive species [120] [121] with a 1 ms lifetime [103]. Hence, measuring its concentration in the liquid phase is very important to understand the chemical effects of the plasma jet on the treated solution. The interaction between water vapor released by the plasma jet when touching the liquid solution and the electrons leads to the breakdown of water molecules into hydroxyl radicals. Subsequent to this reaction, the formation of H_2O_2 emerges from the recombination of two hydrogen radicals and follows the equation [122] [123]:

$$HO \bullet + HO \bullet \rightarrow H_2O_2$$

The concentration of H_2O_2 in the liquid solution, determined through experiments as described in chapter 2, are visualized in Figure 30. To minimize measurement uncertainty, each measurement was replicated three times, and the mean values are summarized in Table 4. This revealed an increase in H_2O_2 production with prolonged plasma exposure duration.

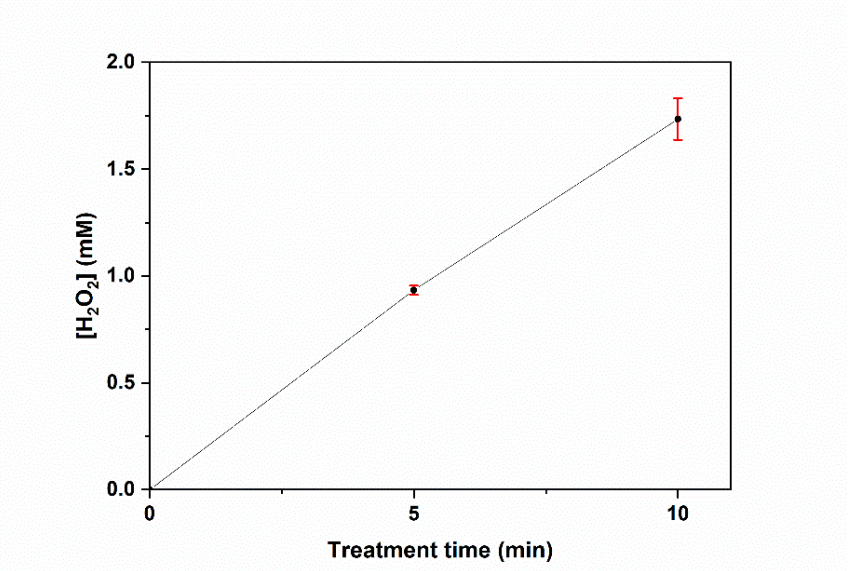

Figure 30. Concentration of hydrogen peroxide in water solution treated with a helium atmospheric pressure plasma jet at different exposure durations (0, 5 and 10 min).

Table 4. Table summarizing the concentration of hydrogen peroxide in water solution treated with a helium atmospheric pressure plasma jet at different exposure durations (5 and 10 min).

Treatment time (min)	***[H_2O_2] (mM)***	***Error (mM)***
0	-	-
5	0.93	0.02
10	1.73	0.09

According to Judée et al., achieving an H_2O_2 concentration of 1.8 mM in water necessitated a 30-minute plasma exposure [124]. However, our study employing the APPJ showcased a remarkable contrast, as this concentration was attained within 10 minutes of the solution plasma exposure. It is difficult to compare the measured concentration of hydrogen peroxide due to the many different types of plasma jets and wide range of solutions of biological interest that are used. Many parameters in the experimental setup (for example, the nature of the gas, the gas flow, the applied voltage, the distance between the plasma and the solution, the composition of the solution, the volume of the solution, etc.) play a role in the amount of plasma-induced RONS in solution. In order to contextualize our findings, a comparative assessment was conducted by referring to literature and is summarized in Table 5 [125]:

Table 5. Table summarizing the concentration of hydrogen peroxide in distilled water after treatment by APPJ from different studies.

Gas	***Flow rate ($L.min^{-1}$)***	***Conditions***	***Time (min)***	***Method***	***[H_2O_2] (mM)***	***Reference***
He	0.1	U= 8 kV f= 15 kHz P= 5 W	2	fluorimetric assay Kit	0.026	[126]
He	3	U= 10 kV f= 9.69 kHz	2.5	fluorimetric assay Kit	1.75	[127]
Air	-	U= 12 kV f= 500 Hz	30	Colorimetric	1.85	[124]
He (present study)	3	I(power supply) = 8A f= 25 kHz	10	Colorimetric	1.73	-

3.3 Synthesis of silver nanoparticles

The synthesis of silver nanoparticles was carried out using a helium atmospheric pressure plasma jet in contact with a liquid solution. The preliminary process for particle synthesis and sample preparation is detailed as follows: A 10 ml aqueous silver solution containing 1 mM of silver nitrate and 0.2 mM of citrate was prepared without the addition of any other chemical compounds. Subsequently, the solution was exposed to the plasma discharge for 5 minutes at specific operating conditions, including an input power discharge current of 8 A, frequency of 25 KHz, and helium gas flux set at 3 $L.min^{-1}$ at a distance of approximately 6 mm from the exit of the plasma jet. The plasma discharge was generated by applying a high voltage between the two electrodes, and the plasma jet exiting the source interacted with the solution. During the exposure, a notable change in the solution's color was observed as seen in Figure 31, transforming it from transparent to brownish-yellow. This distinctive color of the sample served as a distinctive spectroscopic indication of the nanoparticle formation process.

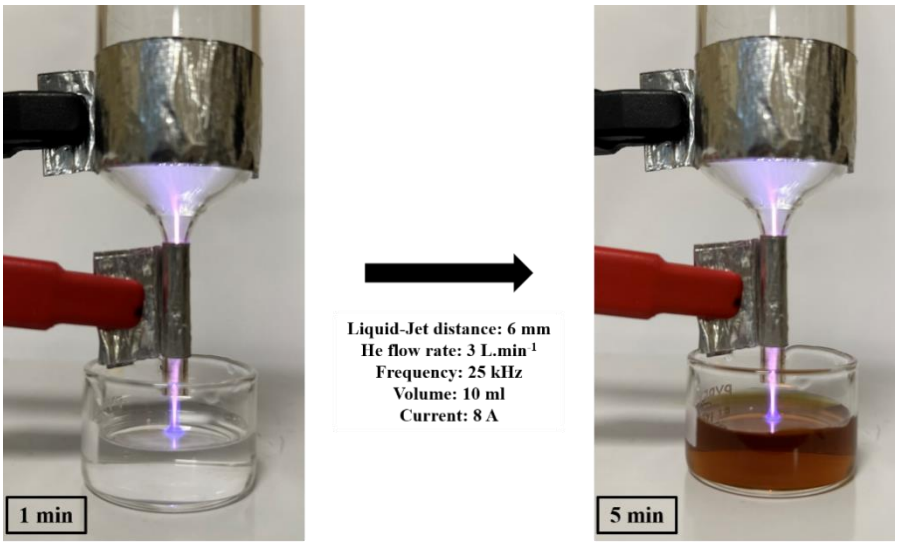

Figure 31. Pictures showing the silver sample before and after the plasma jet treatment: (left) 1 min of plasma exposure (right) 5 min of plasma exposure.

However, at this stage, the exact composition of the resulting product remains partially unknown. To determine the nature and composition of the synthesized nanoparticles, preliminary particle characterization and elemental analysis were conducted. For an initial characterization test and to closely observe the obtained particles, Scanning Electron Microscopy (SEM) and Energy-Dispersive X-ray Spectroscopy (EDX) were performed to study the elemental composition of the nanoparticles. A drop of the solution, immediately after treatment, was deposited onto an Aluminum sample holder and dried at room temperature for the analysis.

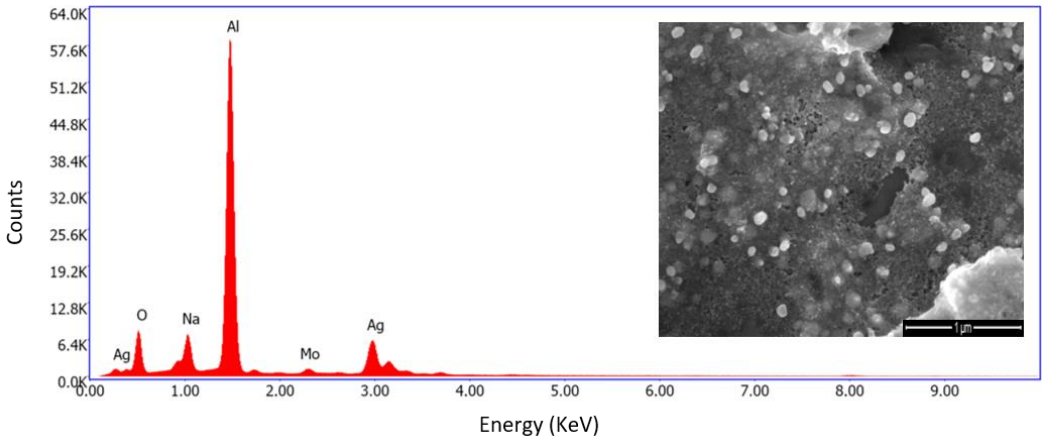

Figure 32. EDX analysis graph, (inserted) SEM micrograph of silver nanoparticles.

Table 6. Elements identified in the measured sample via SEM-EDX analysis with their weight and atomic percentage.

Element	***Weight %***	***Atomic %***
O K	20.22	33.42
Na K	11.26	12.95
Al K	50.04	49.03
Mo L	2.23	0.61
Ag L	16.24	3.98

The Energy Dispersive X-ray Spectroscopy (EDX) technique was employed to conduct qualitative and quantitative analysis of the chemical composition in the nanoparticle samples. Figure 32 displays the EDX analysis measurements, presenting varying signal intensities on the X-axis corresponding to different binding energies (keV), confirming the presence of diverse elements in the sample. Notably, a strong signal at 3 keV indicates the existence of metallic silver in the synthesized nanoparticles. In addition to the aforementioned signals, other weak to moderate signals were observed, attributed to oxygen, molybdenum, and aluminum, originating from sample preparation and the aluminum sample holder used. Also, the presence of sodium is the result of the capping agent molecule residues in the solution. Table 6 presents the elemental composition identified in the sample, with silver being one of the major elements, accounting for 16.24% of the total composition, confirming the formation of AgNPs. These obtained findings align with the characteristic outcomes of elemental nanosilver at 3 keV,

which are consistent with the surface plasmon resonance effects reported in scientific literature [128], [129], [130], [131]. The SEM image inserted in Figure 32 also showcases the visual evidence of the synthesized nanoparticles in the sample.

It is thus concluded that the preliminary tests conducted to investigate the synthesis of silver nanoparticles using our plasma dispositive have shown promising results, confirming the feasibility of nanoparticle formation.

An investigation into existing literature concerning various methods for synthesizing silver nanoparticles using different reduction techniques was done to establish a comparative framework for our findings. A summary of this study is presented in

Table 7 for reference. Notably, chemical reduction processes are recognized for their prolonged duration and the subsequent need for additional steps to eliminate residual toxic chemicals and reducing agents from the final solution. Similarly, sonochemical method also requires extended treatment periods and has yielded non-monodisperse nanoparticles according to the literature. In contrast, our plasma-based setup emerged as highly efficient, with a 5-minute treatment time for nanoparticle elaboration, coupled with an approximate 5-minute solution preparation time. Moreover, these nanoparticles exhibit monodispersity, homogeneity, and an absence of agglomeration within samples prepared with the optimized process parameters.

Table 7. Table summarizing different reduction methods for the synthesis of silver nanoparticles and the used chemical products, treatment time and the shape and size of the obtained nanoparticles.

Reduction method	*Precursor*	*Capping agent*	*Other products*	*Treatment time (min)*	*Shape*	*Size (nm)*	*Ref*
Chemical	$AgNO_3$	CTAB	Anilin (reducing agent)	120	Spherical aggregated	10-30	[132]
Chemical	$AgNO_3$	PVP	Glucose (reducing agent)	-	Spherical aggregated	20-80	[133]
Chemical	$AgNO_3$	sodium dodecyl sulfate (SDS)	$NaBH_4$ (reducing agent)	90	Spherical aggregated	30-40	[134]
Sonochemical	$AgNO_3$	-	-	60	Amorphous	20	[135]
Sonochemical	$AgNO_3$	-	Ammonia	90	Amorphous	5	[136]
Sonochemical	$AgNO_3$	-	Starch	20	Spherical aggregated	23-97	[137]
Plasma	$AgNO_3$	CTAB	-	5, 10, 20	Spherical, dendrite shaped	10-50	[138]
`Plasma	$AgNO_3$	-	-	5	Spherical	36-60	[139]
Plasma (present study)	$AgNO_3$	Trisodium citrate dihydrate	-	5 min	Spheres	13 ± 2	[113]

As we progress in investigating the potential of silver nanoparticles for various applications, it becomes essential to gain a deeper understanding of the effects of different parameters on their size and morphology. Each specific application of silver nanoparticles demands unique characteristics [140], and thus, our future studies will focus on systematically exploring and optimizing these parameters to have a precise control over the size, shape, and properties of the synthesized nanoparticles. By doing so, we aim to tailor the silver nanoparticles to meet the

requirements of various applications, unlocking their potential in diverse fields ranging from biomedicine to catalysis and beyond.

3.3.1 Effect of the plasma interaction duration

With the initial characterization of silver nanoparticles, our attention turns towards exploring how the duration of plasma discharge influences the process of nanoparticle synthesis. To understand and investigate the potential influence of plasma discharge duration on the kinetics of nanoparticle formation and growth, our approach involves systematically altering the plasma discharge duration while maintaining other parameters constant, aiming to study the interplay between the synthesis process and the properties of the nanoparticles produced.
A series of experiments were conducted using five different discharge time durations, ranging from 0 to 10 minutes (with 0 indicating no plasma exposure). For these experiments, we maintained the concentrations of $AgNO_3$ and citrate to 1 mM and 1.5 mM, respectively.

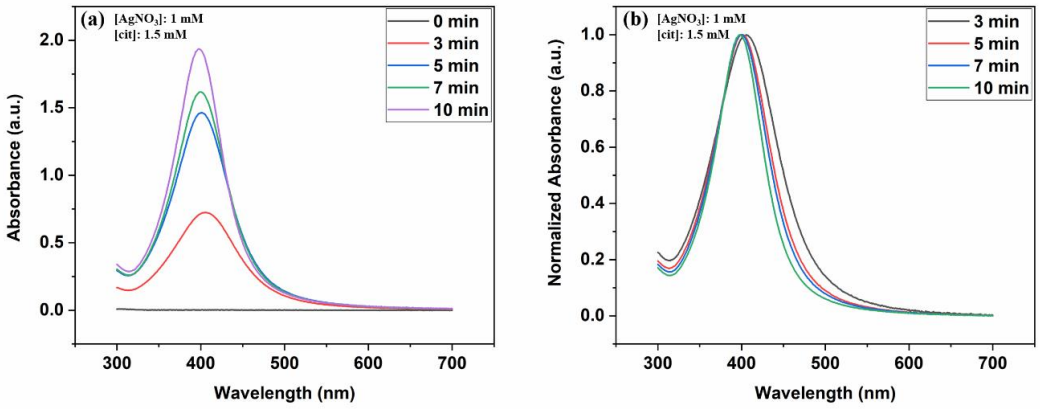

Figure 33. UV-vis (a) absorbance (b) normalized absorbance spectra of the solutions with 1 mM of $AgNO_3$ and 1.5 mM of citrate at different plasma exposure durations ranging from 0 (considering 0 as no plasma treatment) to 10 min.

The UV-vis absorption spectra were recorded to ascertain the presence of absorbance bands, with an observable appearance of a band at 406 nm after a 3-minute duration, providing further validation of the successful synthesis of AgNPs. Notably, in the absence of plasma discharge, no corresponding absorbance band was observed, confirming the absence of silver nanoparticles. Examining Figure 33(a), it is evident that prolonged plasma interaction led to an augmentation in the intensity of the absorption band, an outcome anticipated due to the higher concentration of silver nanoparticles formed. Moreover, a slight decrease in the wavelength of the maximum absorption band, shifting to shorter wavelengths, was noticeable, as highlighted more vividly in Figure 33(b) and documented in Table 8. However, the spectral profile remained unaltered, signifying that plasma duration primarily impacted nanoparticle

concentration, leaving their shape unaffected. The presence of narrow and symmetric bands implies that the nanoparticles shared a uniform shape and size, with no indication of agglomerated particles within the samples. It is important also to note that, beyond a 7-minute duration, the solution exhibited a reduction in volume, attributed to the partial evaporation caused by an increase of temperature generated during plasma exposure.

Table 8. Table summarizing the band max intensity and wavelengths of the treated solutions with 1 mM of $AgNO_3$ and 1.5 mM of citrate concentrations at different plasma exposure durations.

Plasma discharge duration (min)	λ_{max} ***(nm)***	***Abs (a.u.)***
0	-	-
3	406	0.725
5	400	1.463
7	399	1.616
10	398	1.936

3.3.2 Effect of the metal precursor's concentration

The next parameter that has been investigated is the precursor concentration, which has proven to have a significant impact on the size and morphology of the nanoparticles during their synthesis. In this study, silver nitrate ($AgNO_3$), a solid metal salt, was chosen as the precursor for silver nanoparticle synthesis. It is common to work within the mM concentration unit in plasma processes [141] [142] [143]. In accordance with existing literature, the selected precursor concentration is in the range of 1 - 5 mM $AgNO_3$. Process parameters applied in this study are presented in Table 9:

Table 9. Table summarizing the experimental process parameters applied.

Experimental parameters	
Pressure	atmospheric
Gas	Helium
Power supply current	8 A
Frequency	25 kHz
Gas flow rate	3 $L.min^{-1}$
Plasma-Solution distance	6 mm

Five samples with varying precursor concentrations and a constant 3 mM of citrate were subjected to a 5 min plasma treatment. The observation of yellow coloration in the solutions during the plasma exposure served as an initial indicator of silver nanoparticle formation. This was further corroborated by the presence of an absorption band in the visible range, resulting from the surface plasmon resonance (SPR), as seen in the UV-vis spectra. The maximum position of the surface plasmon resonance is usually recognized as an indicator of the size of Ag nanoparticles [144] [145]. It has been emphasized in the works of Skiba et al. and Guidelli et al. that a characteristic feature of silver nanoparticles is the presence of a maximum absorption band within the 350-450 nm range [139] [146]. **Figure 34** presents the normalized UV-vis absorption spectra of the silver solutions with different silver nitrate concentrations. The spectra were normalized in order to facilitate the comparison between the different curves. Notably, as the precursor concentration increases, the bands become broader. A gradual appearance of a shoulder at higher wavelengths is observed, eventually leading to the emergence of a second broad band, indicating either an increase in the size of the formed nanoparticles or the presence of two distinct sizes of silver nanoparticles in the treated solution [147].

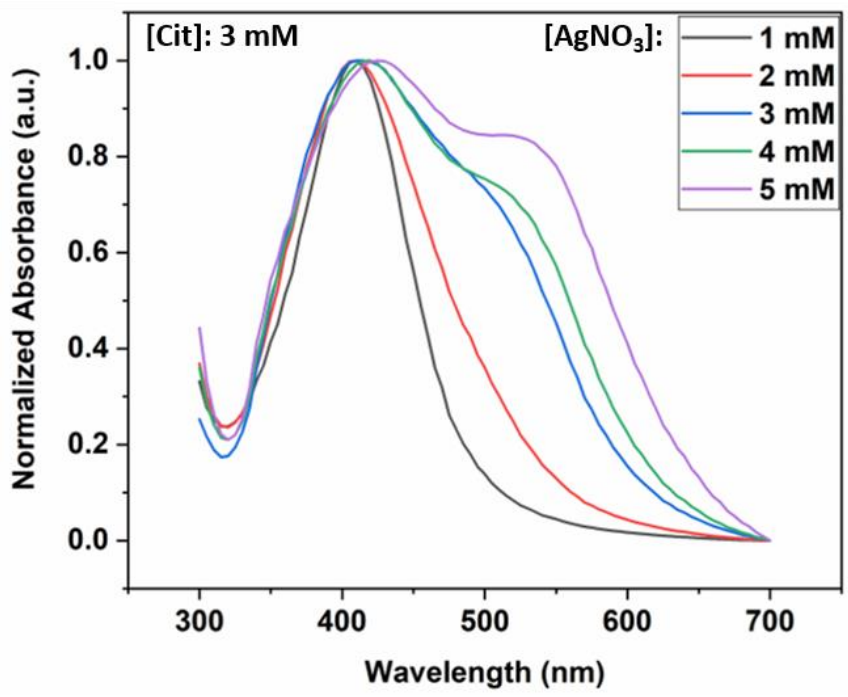

Figure 34. Normalized UV-vis absorbance spectra of different silver concentrations ranging from 1 to 5 mM and at 3 mM of citrate concentration.

When nanoparticles are synthesized, their size and shape influence the position and intensity of the LSPR peak in the UV-vis spectra. Smaller nanoparticles typically exhibit LSPR peaks at shorter wavelengths, while larger nanoparticles show peaks at longer wavelengths. Additionally, the shape of the nanoparticles can lead to different spectral profiles. Understanding the LSPR peak position and shape helps to determine the average size and size distribution of the nanoparticles, providing crucial information about their morphology [148].
In our spectra, a noticeable trend emerges as we increase the silver nitrate concentration: the absorbance band gradually shifts towards higher wavelengths, indicating an increase in nanoparticle size. Specifically, the maximum absorbance bands were observed at 405, 410, 415, 420, and 425 nm for silver nitrate concentrations of 1, 2, 3, 4, and 5 mM, respectively. Additionally, the appearance of a second band in some samples suggests the presence of anisotropic shapes of silver nanoparticles. This observation highlights the possibility of varying morphologies within the synthesized nanoparticles, contributing to the overall complexity of the nanoparticle structure in the samples.

We then proceeded to investigate the deconvolution of these UV-vis spectra. This involves mathematically separating overlapping peaks or contributions from different components in a UV-visible absorption spectrum into individual component bands. In the context of silver nanoparticles, the deconvolution of the UV-vis spectra allows us to distinguish and quantify the contributions of different-sized nanoparticles present in the sample. By analyzing the deconvoluted spectra, it is possible to assess the homogeneity of the nanoparticle size distribution and identify the presence of multiple particle populations with distinct sizes. The deconvoluted spectra of the UV-vis spectra of each precursor concentration is presented below in **Figure 35**.
The deconvolution analysis of the UV-vis spectra provided valuable insights into the spectral aspects and band positions of our synthesized silver nanoparticles. **Figure 35**(a) displays a single, highly symmetric, and narrow plasmon band, indicating a sample with minimal agglomeration [149]. While at higher silver salt concentrations (**Figure 35**(b), (c), (d), and (e)), the deconvoluted spectra exhibit multiple plasmon bands, suggesting the presence of different particle sizes resulting from either agglomeration or larger particles. This observation suggests that higher silver nitrate concentration may promote particle growth. This deconvolution analysis revealed that the second band at lower energy corresponds to larger particles in the sample, supporting the notion that distinct particle sizes and agglomerations coexist in the system.

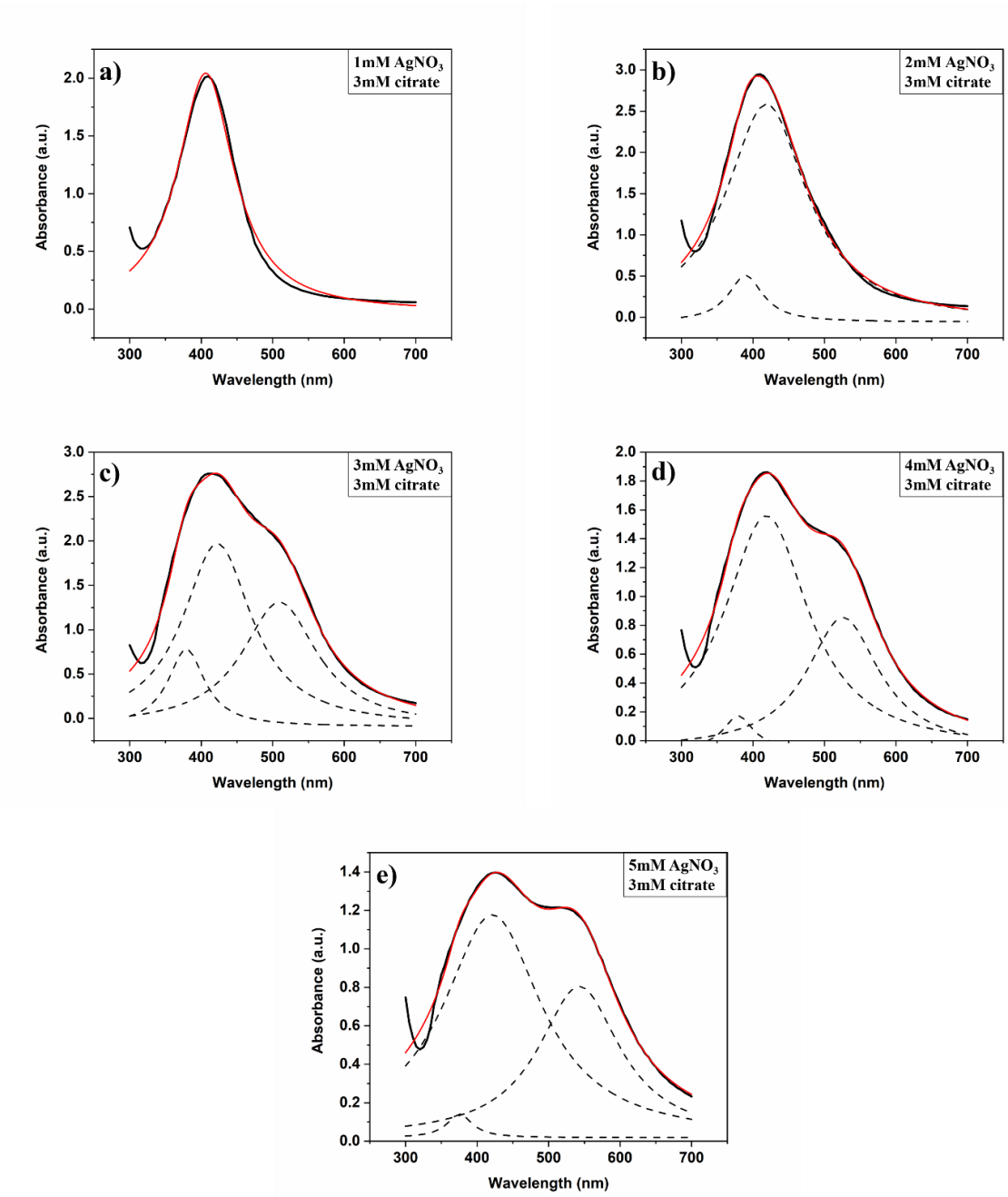

Figure 35. The UV-vis deconvoluted absorption spectra with 3 mM citrate concentration at different silver nitrate concentrations: (a) 1 mM, (b) 2 mM, (c) 3 mM, (d) 4 mM, and (e) 5 mM (The black lines represent the original curves, the black dashed lines represent the deconvoluted curves and the red lines represent the cumulative fit).

3.3.3 Effect of the capping agent's concentration

In the previous section, it was determined that increasing the $AgNO_3$ concentration resulted in an increase in the average particle size and lead to irregular shaped nanoparticles in the sample. This can be due to the aggregation and coalescence of smaller sized nanoparticles. The presence of agglomerated nanoparticles hinders the enhancement of nanoparticle properties and diminishes their reactivity, posing challenges for their application in specialized fields. To overcome this limitation, it became imperative to investigate the impact of incorporating a stabilizing agent during the synthesis of silver nanoparticles. By studying the influence of a stabilizing agent, we aim to prevent nanoparticle agglomeration, thus ensuring the production of well-dispersed and stable silver nanoparticles.

The stabilizing agent used in this study is trisodium citrate dihydrate which is a compound with the chemical formula $Na_3C_6H_5O_7 \cdot 2H_2O$. Due to its ability to bind metal ions and stabilize solutions, trisodium citrate dihydrate is particularly useful in nanoparticle synthesis, including the production of silver nanoparticles, where it acts as a reducing agent and stabilizing agent to prevent particle agglomeration [150] [151]. The stabilizing effect of citrate is attributed to its ability to adsorb onto the surface of the silver nanoparticles through its functional groups, forming a protective layer. This layer, often referred to as a "capping layer", acts as a barrier between the nanoparticles, preventing them from coming into close contact and aggregating [152]. By stabilizing the nanoparticles, citrate helps maintain their individual, discrete nature, ensuring they remain dispersed and well-separated in the solution. The stabilization also leads to better control over the size and shape of the nanoparticles, which is vital for tailoring their properties. This is especially important in applications where uniform dispersion and stability of nanoparticles are critical, such as in medical, catalytic, or optical applications.

In addition to this role, citrate also is a reducing agent. It can be responsible for the conversion of silver ions (Ag^+) present in the precursor solution (e.g. silver nitrate) into metallic silver (Ag^0), leading to the formation of nanoparticles. The mechanism of reaction could be expressed as follows [153]:

$$4\ Ag^+ + C_6H_5O_7Na_3 + 2\ H_2O \rightarrow 4\ Ag^0 + C_6H_5O_7H_3 + 3\ Na^+ + H^+ + O_2$$

The simultaneous action of trisodium citrate dihydrate as a reducing agent and capping agent is what makes it a valuable component in the synthesis of silver nanoparticles. Its dual role allows for the efficient reduction of silver ions into nanoparticles while simultaneously stabilizing and controlling their size and shape.

Depending on the component and structure of the stabilizing agent used, the amount required to stabilize nanoparticles may vary. In literature, it is common to apply a low concentration of stabilizing agent. The chosen trisodium citrate dihydrate concentration is in the working range of 0.05 – 6 mM. In this part of the study, silver nanoparticles were synthesized using the same method as described in previous sections. The process involved a 5-minute treatment with a helium plasma under the identical plasma conditions specified in Table 9. Various solutions were prepared with citrate concentrations ranging from 0.5 to 6.3 mM, and for each of these, different silver nitrate concentrations ranging from 1 to 5 mM were used. The UV-vis absorbance spectra for each treated solution medium were measured and are presented in Figure 36. The impact of citrate concentration on the position of the maximum absorbance band wavelength is clearly negligible, as evidenced in Table 10. However, it significantly influenced the intensity of the band. With higher concentrations, we observe a gradual increase in intensity, signifying the formation of a greater number of silver nanoparticles [154].

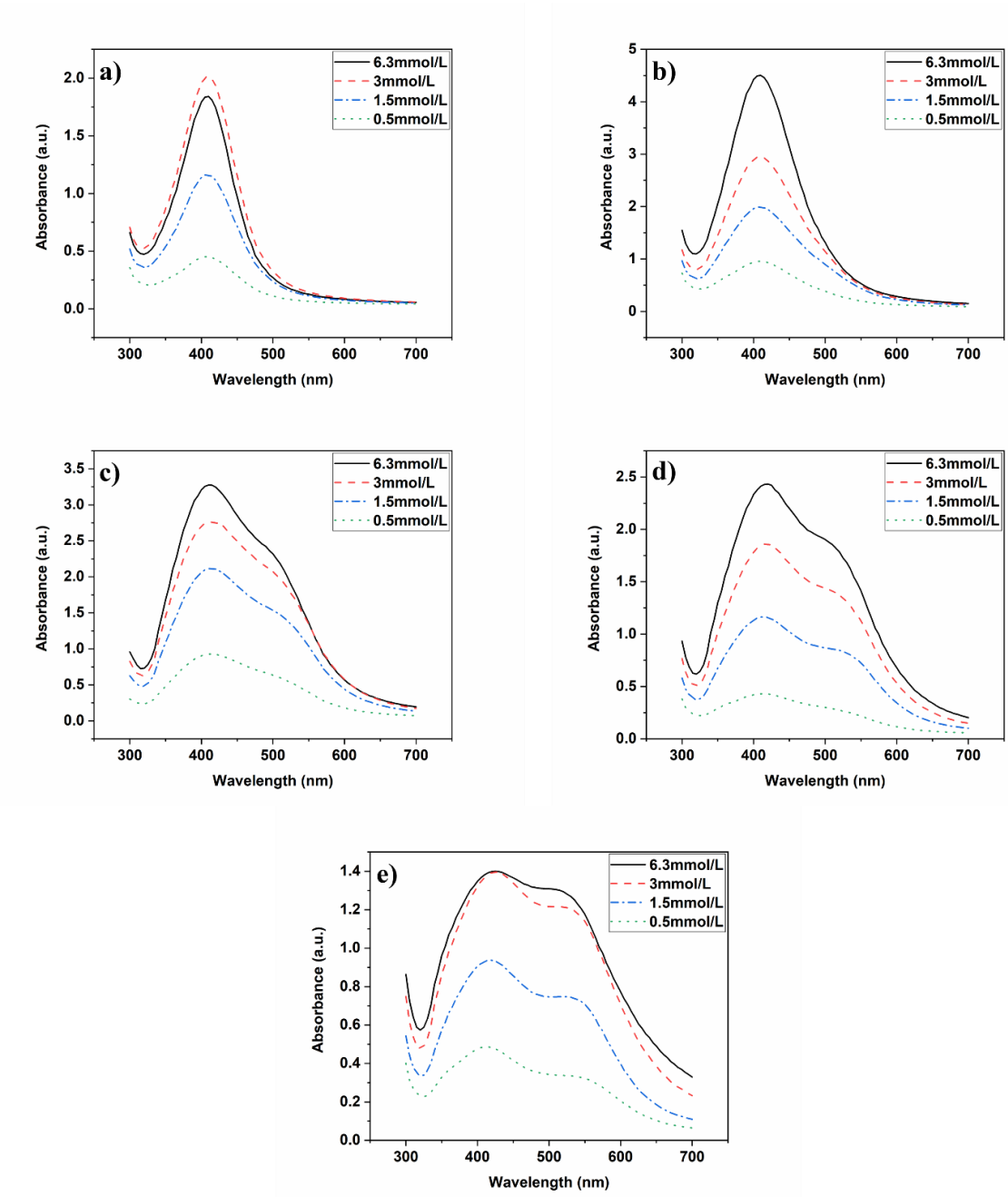

Figure 36. The UV-vis absorption spectra at different citrate concentrations of 0.5 mM (green dot line), 1.5 mM (blue dash-dot line), 3 mM (red dash line), and 6.3 mM (black line) for various initial $AgNO_3$ concentrations: (a) 1 mM, (b) 2 mM, (c) 3 mM, (d) 4 mM, and (e) 5 mM.

Table 10. Effect of Silver Nitrate and Citrate Concentrations on Max Wavelength and Intensity of Silver Nanoparticles.

		$[AgNO_3]$ mM									
		1		2		3		4		5	
		λ_{max} nm	Abs au	λ_{max} nm	Abs au	λ_{max} nm	Abs au	λ_{max} nm	Abs au	λ_{max} nm	Abs au
[cit] mM	0.5	405	0.45	410	0.95	415	0.92	420	0.43	425	0.48
	1.5	405	1.16	410	1.99	415	2.11	420	1.16	425	0.93
	3	405	2.01	410	2.94	415	2.75	420	1.86	425	1.39
	6.3	405	1.84	410	4.50	415	3.27	420	2.43	420	1.40

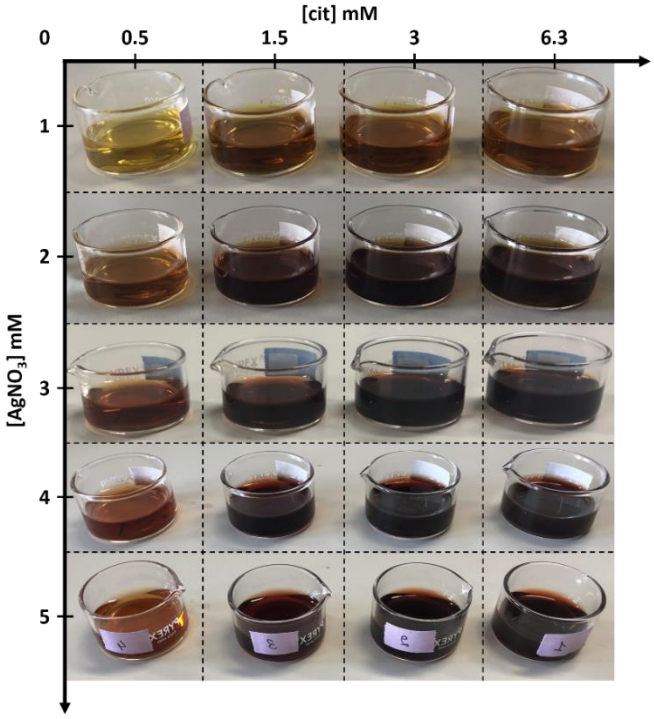

Figure 37. Images graph showing the variations in color observed in the treated solutions with different concentrations of both the precursor and capping agent.

The images presented in Figure 37 showcase the variations in color observed in the treated solutions with different concentrations of both the precursor and capping agent. It is evident from the pictures that as the concentrations of both the precursor and trisodium citrate dihydrate increase, the color of the solutions becomes darker. This change in color is attributed to the role of trisodium citrate dihydrate as a reducing agent, facilitating the more efficient reduction of silver ions and resulting in the formation of a higher number of silver nanoparticles. Consequently, the UV-vis intensity increases as a greater number of nanoparticles are present in the solution, contributing to the overall absorption intensity. The darkening of the solutions is also influenced by the increased nanoparticle concentration, which leads to enhanced scattering and absorption of light, giving rise to the darker appearance. To demonstrate the significance of the plasma jet in the reduction process, control tests were conducted. When a solution containing both the precursor and capping agent was left untreated for one week, no change in color or observable absorbance band was noticed in the UV-vis measurements presented in Figure 38. Similarly, subjecting the same solution to stirring and high temperature for two hours yielded no evidence of nanoparticle formation. This reinforces the critical role of the plasma jet in facilitating the reduction process, which complements the function of the trisodium citrate dihydrate as a capping agent in the synthesis of silver nanoparticles.

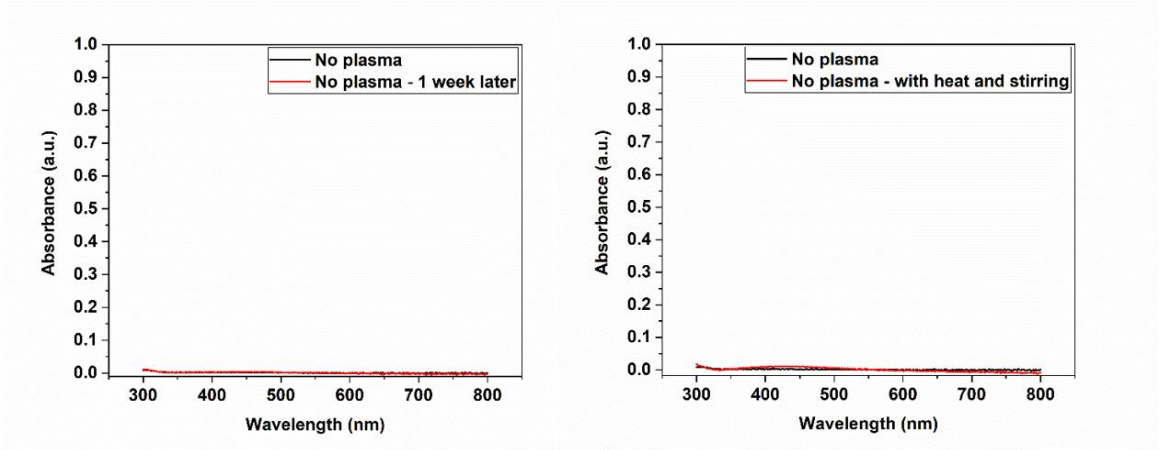

Figure 38. UV-vis absorbance spectra of silver/citrate solution before and after (left) one week at room temperature, and (right) 2 hours at high temperature and vigorous stirring.

Building upon the findings presented in Section 3.3.2, where a 1 mM concentration of silver nitrate demonstrated a uniform and narrow absorption band typically associated with nanoparticles of uniform size and shape distribution, we decided to further investigate the effect of varying citrate concentrations at this specific silver nitrate concentration. A series of solutions containing 1 mM silver nitrate and varying citrate concentrations ranging from 0.05

to 6 mM were prepared, treated, and analyzed using UV-vis spectroscopy. Figure 39(a) presents an image showing the color degradation of the treated solutions in function of citrate concentrations and Figure 39(b) presents their measured absorbance. As expected, the absorption band's wavelength remained unchanged at 405 nm with varying citrate concentrations, while the intensity of the band increased proportionally with higher citrate concentrations, as depicted in Figure 39(c).

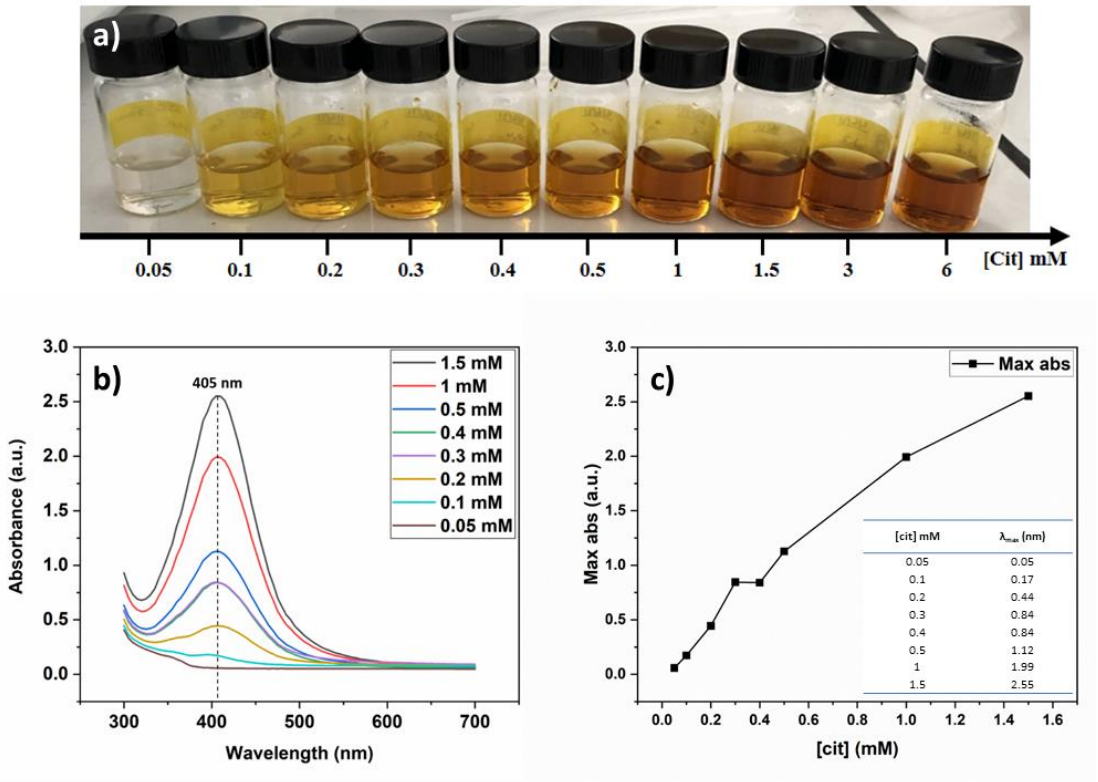

Figure 39. (a) The color change of the solutions with 1 mM $AgNO_3$ concentration for several citrate concentrations, from 0.05 mM (left) to 6 mM (right) at fixed plasma parameters. (b) The UV-vis absorption spectra of the solutions at 1 mM of silver nitrate concentration and citrate concentrations ranging from 0.05 mM to 1.5 mM at fixed plasma parameters. (c) Graph illustrating the relationship between citrate concentration and the maximum absorbance band intensity at 405 nm of the treated solutions. Inserted is a table presenting the corresponding values for each data point.

To confirm our observations and gain visual insights into the nanoparticles, microscopy analysis was subsequently conducted, allowing us to validate our explanations and further understand the impact of citrate concentration on nanoparticle formation and stability. The microscopy results are detailed in the following sections.

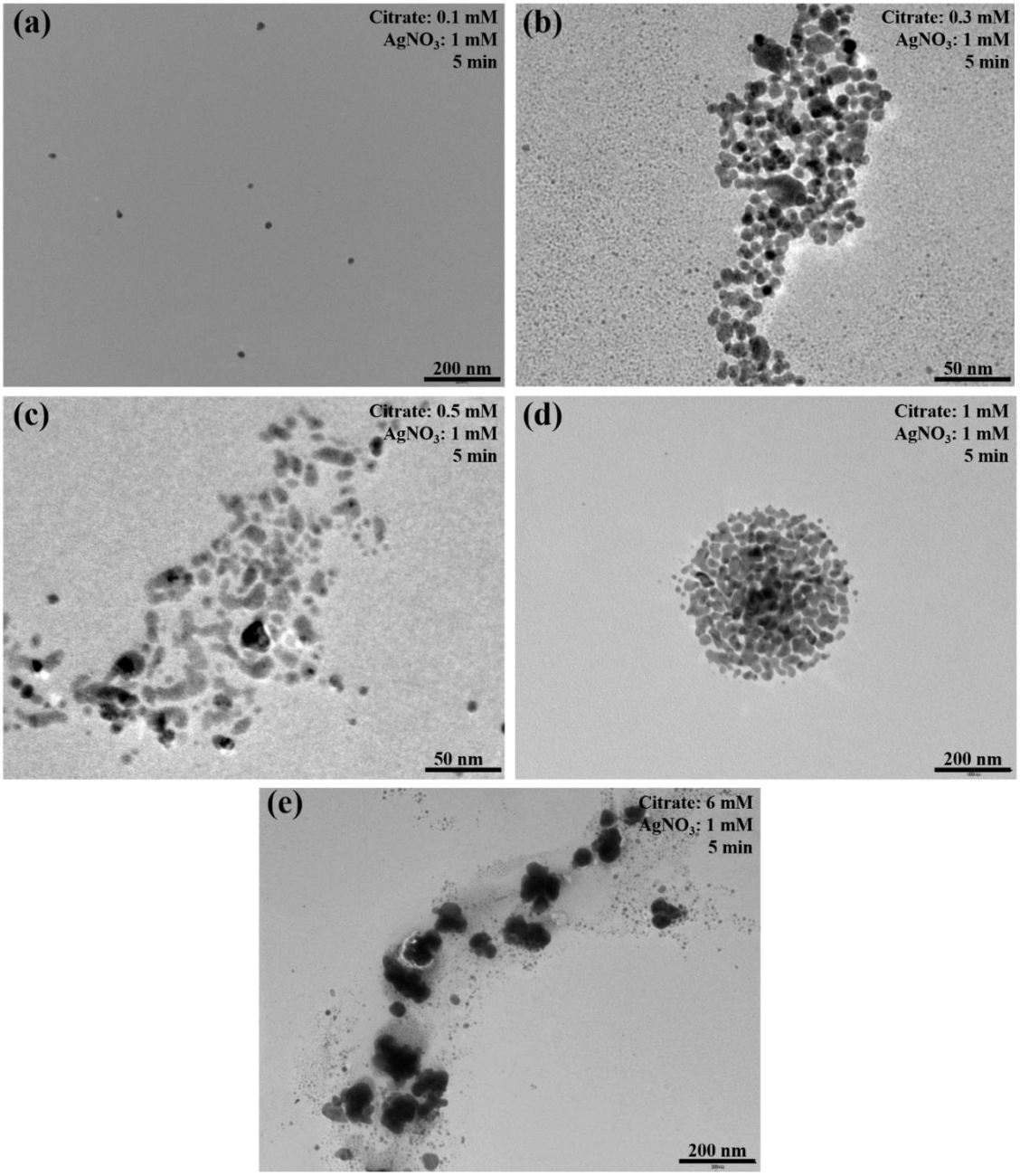

Figure 40. TEM micrographs of the silver nanoparticle solutions after 5 min of plasma exposure with 1 mM of $AgNO_3$ at (a) 0.1 mM, (b) 0.3 mM, (c) 0.5 mM, (d) 1 mM, and (e) 6 mM of $HAuCl_4$ concentration.

Figure 40 presents the transmission electron microscopy (TEM) micrographs of five distinct samples, each prepared with a silver nitrate concentration of 1 mM and varying citrate concentrations. The micrographs illustrate the influence of citrate concentration on the morphology and dispersion of the synthesized silver nanoparticles. The sample with the lowest citrate concentration (0.1 mM) exhibits well-dispersed spherical nanoparticles, characterized by an average diameter of 13 ± 2 nm, as determined by measuring 200 randomly selected nanoparticles. In contrast, an increase in citrate concentration leads to a visible change in the sample's appearance, with nanoparticles exhibiting a tendency to aggregate and form larger clusters. This phenomenon can be attributed to the higher nanoparticle production rate in solutions with increased citrate concentrations, as discussed previously. With an increased number of nanoparticles in the solution, the likelihood of particle collisions and subsequent agglomeration rises. This mechanism is commonly observed in nanoparticle synthesis processes. The intricate interplay between citrate concentration, nanoparticle production, and agglomeration dynamics is essential to comprehend. The balance between stabilization and nucleation that the capping agent, citrate, provides significantly influences the overall outcome. It is noteworthy that finding the optimal citrate concentration is important in obtaining well-dispersed nanoparticles. For our study, the optimal ratio of silver nitrate to citrate concentration was determined to be 1 mM and 0.1 mM, respectively. This ratio ensured the production of separated and uniformly shaped silver nanoparticles.

3.4 Synthesis of gold nanoparticles

The synthesis of gold nanoparticles was carried out using a helium atmospheric pressure plasma jet in contact with a liquid solution. The preliminary process for particle synthesis and sample preparation is detailed as follows: 10 ml aqueous gold solution containing 1 mM of $HAuCl_4$ and 0.05 mM of PVP was prepared without the addition of any other chemical compounds. Subsequently, the solution was exposed to the plasma discharge for 5 minutes at specific operating conditions, including an input power discharge current of 8 A, frequency of 25 KHz, and helium gas flux set at 3 $L.min^{-1}$ at a distance of approximately 6 mm from the exit of the plasma jet. The plasma discharge was generated by applying a high voltage between the two electrodes, and the plasma jet exiting the source interacted with the solution. During the exposure, a notable change in the solution's color was observed transforming it from light yellow to purple, as demonstrated in Figure 41. This distinctive color of the sample served as a distinctive spectroscopic indication of the nanoparticle formation process.

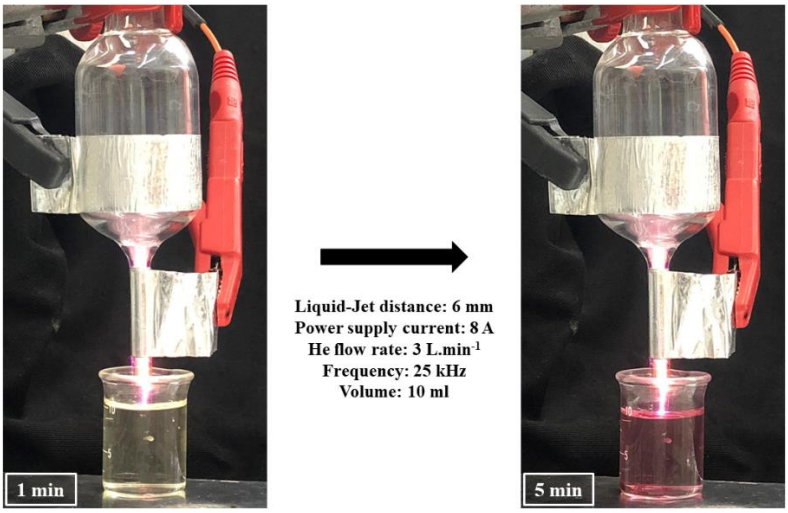

Figure 41. Pictures showing the gold sample before and after the plasma jet treatment: (left) 1 min of plasma exposure (right) 5 min of plasma exposure.

However, at this stage, the exact composition of the resulting product remains partially unknown. To determine the nature and composition of the synthesized nanoparticles, preliminary particle characterization and elemental analysis were conducted. For an initial characterization test, we employed X-ray diffraction (XRD) analysis. XRD is a powerful technique used to elucidate the crystalline structure of materials, providing valuable insights into the phase and composition of the nanoparticles. The XRD measurements were carried out using an X-ray diffractometer, and the data collected is presented in Figure 42. The sample was dried at 50 degrees Celsius overnight and the powder was collected and analyzed.

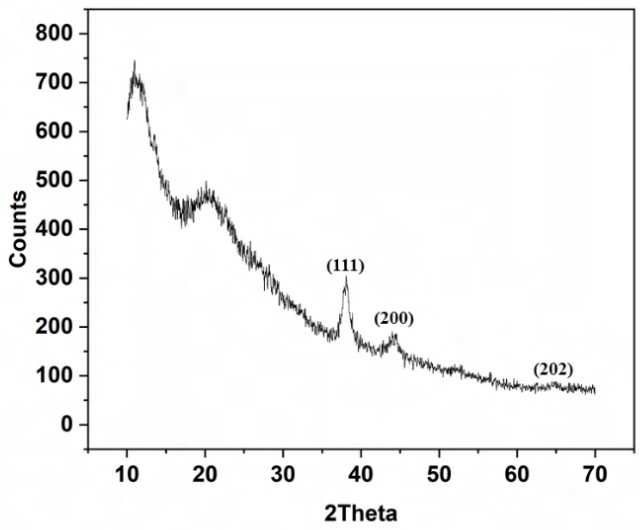

Figure 42. X-ray diffraction pattern of the synthesized AuNPs after 5 min of plasma exposure with 1 mM of $HAuCl_4$ and 0.05 mM of PVP.

The resulting XRD demonstrate the formation of crystalline gold nanoparticles in the sample, confirming their purity and identity. The diffraction peaks obtained in the entire 2 theta region from 0 to 70 degrees showed a cubic diffraction pattern (JCPD file number no.04-0784). The peaks at 38.24°, 44.45°, 64.67° correspond to the standard Bragg reflections (111), (200), and (220) of face center cubic lattice, respectively. In addition, the peak width is in agreement with the nanostructured sample.

It is thus concluded that the preliminary tests conducted to investigate the synthesis of gold nanoparticles using our plasma dispositive have shown promising results, confirming the feasibility of nanoparticle formation.

Research amongst some of the literature synthesizing gold nanoparticles with different reduction techniques was conducted in order to compare our results and is summarized in Table 11. The chemical reduction is known to be a very long process and additional steps are required in order to remove all the toxic chemicals and reducing agents from the final solution. The sonochemical and electrochemical techniques also require long treatment times and in some of the literature they did not result in monodisperse nanoparticles. We found that our plasma setup is the most efficient in terms of treatment time as it takes only 5 min to elaborate the nanoparticles, the solution preparation time is also around 5 min and in terms of the results obtained, our nanoparticles are the most monodisperse, homogeneous and no agglomeration is found in the samples.

Table 11. Table summarizing different reduction methods for the synthesis of gold nanoparticles and the used chemical products, treatment time and the shape and size of the obtained nanoparticles.

Reduction method	***Precursor***	***Capping agent***	***Other products***	***Treatment time (min)***	***Shape***	***Size (nm)***	***Ref***
Chemical	$HAuCl_4.3H_2O$	-	Sodium citrate (Reducing agent)	30	spheres	12 ± 2	[155]
Chemical	$HAuCl_4$	-	Chitosan (Reducing agent)	3 hours	Spheres but not monodisperse	< 20	[156]
Chemical	$HAuCl_4$	Sodium citrate	$NaBH_4$ (reducing agent)	24 hours	spheres	7 ± 2	[157]
Sonochemical	$HAuCl_4$	PVP	1-propanol	120	Spheres, triangles, ellipse...	15-25	[158]
Sonochemical	$AuCl_4^-$	-	Ethanol	10	Spheres, triangle, rods...	23 ± 7	[159]
Sonochemical	$HAuCl_4$	-	Silica spheres, ammoniac	45	Spheres	8	[160]
Electrochemical	$HAuCl_4$	PVP	KNO_3, SDBS	5-40	Spheres but not monodisperse	11.3 ± 2.3	[161]
Electrochemical	$HAuCl_4.4H_2O$	-	KCl	5 electrodeposition cylcles	Spheres	35 ± 5	[162]
Plasma	$HAuCl_4$	Chitosan	-	15 (3h preparation time before)	Spheres	4	[163]
Plasma	$HAuCl_4.4H_2O$	SDS	-	5 45	Triangles, pentagons, hexagons...	50 20	[164]
Plasma	$HAuCl_4.3H_2O$	CTAB	NaOH	30	Spheres	2 (pH12), 4 (pH 6), 10 (pH 3)	[165]
Plasma (present study)	$HAuCl_4 \cdot xH_2O$	PVP	-	5	Monodispersed spheres	13 ± 4 nm	-

Similar to the study of silver nanoparticles, our research extends towards harnessing the full potential of gold nanoparticles for a diverse range of applications. In order to effectively utilize gold nanoparticles for specific purposes, it is important to gain an understanding of the impact of various parameters on their size and morphology. Each distinct application of gold nanoparticles necessitates unique characteristics, prompting us to undertake systematic

exploration and optimization of these parameters. The main objective is to attain precise control over the size, shape, and properties of the synthesized gold nanoparticles. Through this concerted effort, we aim to tailor gold nanoparticles to cater to the specific requirements of various applications, thus unlocking their vast potential across various fields.

3.4.1 Effect of the plasma interaction duration

Having established the initial characterization of gold nanoparticles, our focus now shifts to investigating the effect of plasma discharge duration on the nanoparticle synthesis process. The plasma discharge duration has been identified as a significant factor that can potentially impact the kinetics of nanoparticle formation and growth. By systematically varying the plasma discharge duration while keeping other parameters constant, we aim to understand the relationship between the synthesis process and the resulting nanoparticles' characteristics.

A series of experiments were conducted using six different discharge time durations, ranging from 0 to 15 minutes (with 0 indicating no plasma exposure). For these experiments, we maintained a fixed concentration of 1 mM $HAuCl_4$ and 0.05 mM of PVP. As seen in Figure 43, the treated solutions revealed a color change after plasma exposure, indicative of the formation of gold nanoparticles.

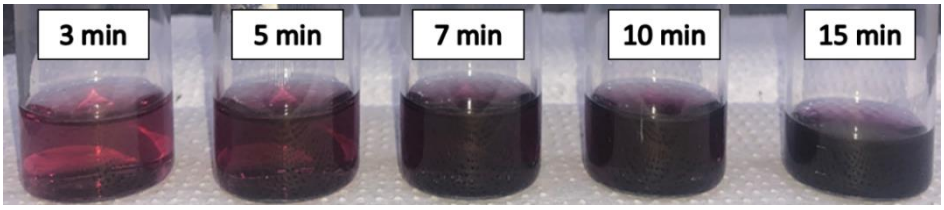

Figure 43. Picture of the samples with 1 mM of HAuCl4 and 0.05 mM of PVP concentrations after treatment at different plasma exposure durations.

The UV-vis absorption of the solutions was measured where an appearance of a detectable absorbance band at 533 nm after 3 minutes further confirmed the successful synthesis of AuNPs. In Figure 44(a), we observed that the intensity of the absorption band increased with longer plasma interaction, suggesting a higher concentration of gold nanoparticles formed while the max band remained unchanged at 533 nm. At the 15-minute interaction mark, the spectrophotometer reached its saturation point, and we obtained the highest nanoparticle concentration, which was also visually evident from the deepest color amongst the samples, as seen in the picture in Figure 43. It is worth noting that, in addition to the increased nanoparticle concentration, the solution experienced a slight decrease in volume at this

duration. This decrease was caused by the partial evaporation of the solution due to the high temperature generated during the 15-minute plasma exposure.

To investigate the morphology of the formed nanoparticles and facilitate comparison, Figure 44(b) displays the normalized absorbance of the different samples. With increasing plasma exposure duration, a shoulder gradually emerged at a higher wavelength, indicating the presence of two different nanoparticle sizes and some agglomerations [166]. However, at 3 and 5 minutes of exposure, the plasmon bands exhibited a high degree of symmetry and narrowness, with a full width at half maximum (FWHM) of 54 and 56 nm, respectively (as indicated in Table 12). This suggests that the nanoparticles were primarily of the same shape and size, and the samples did not contain agglomerated particles [148].

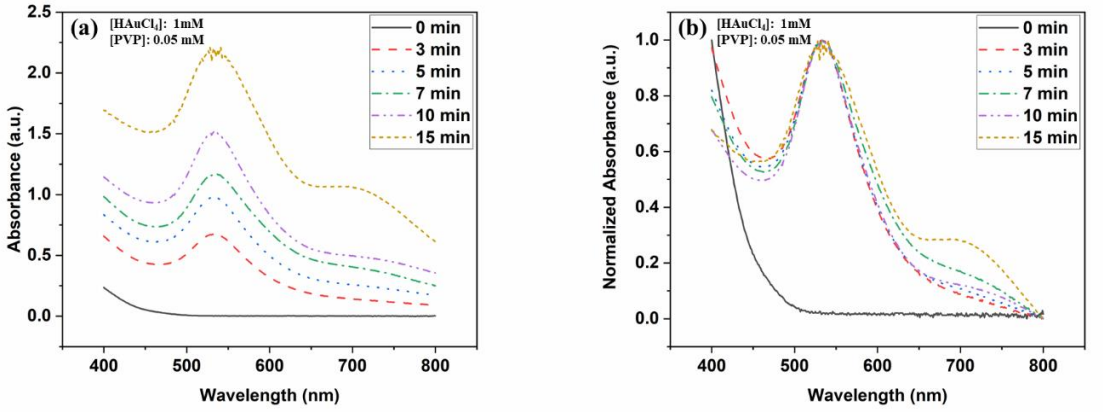

Figure 44. UV-vis (a) absorbance (b) normalized absorbance spectra of the solutions with 1 mM of $HAuCl_4$ and 0.05 mM of PVP at different plasma exposure durations (from 0 to 15 min).

Table 12. Table summarizing the FWHM and the max intensity band wavelength of the treated solutions at different plasma exposure durations.

Plasma discharge duration (min)	***FWHM (nm)***	$\boldsymbol{\lambda_{max}}$ ***(nm)***
0	-	-
3	54	533
5	56	533
7	62	533
10	60	533
15	69	533

As the polydispersity of particles can be determined by the width of the absorption band, and is thus represented by the full width half maximum (FWHM) value. Based on these observations, we chose 5 minutes as the optimal plasma exposure duration for further studies. While 3 minutes appeared insufficient for efficient synthesis, as evidenced by the low absorbance band intensity compared to the other samples, 5 minutes allowed for an efficient and uniform synthesis rate of gold nanoparticles.

3.4.2 Effect of the metal precursor's concentration

With the identification of the optimal plasma duration for nanoparticle synthesis, our attention shifted to investigating the impact of varying precursor concentrations on the synthesis process. This study aimed to investigate the influence of various $HAuCl_4$ concentrations on the morphology and size distribution of Au nanoparticles while maintaining a fixed concentration of the capping agent, PVP, at 0.05 mM. Figure 46 displays the UV-vis absorbance spectra and the normalized spectra of five different solutions with $HAuCl_4$ concentrations ranging from 0.1 to 1.5 mM, after 5 minutes of plasma discharge exposure. Interestingly, as the $HAuCl_4$ concentration increased, a noticeable red shift in the position of the plasmon band was observed, shifting from 525 nm to 536 nm. This red shift is typically associated with an increase in nanoparticle size [167]. Additionally, the uniformity of the Au nanoparticles was characterized by studying the full width at half maximum (FWHM) of the absorption spectra [168]. Notably, the precursor's concentration of 0.1 mM exhibited the most symmetric and narrowest absorbance band at 525 nm with an FWHM of 50 nm as summarized in Table 13, suggesting a more uniform and consistent nanoparticle size and shape at this specific concentration. A decrease in the FWHM value is associated with a decrease in polydispersity and agglomeration of the nanoparticles. These findings indicate the importance of precursor concentration in tailoring the size and uniformity of the synthesized Au nanoparticles.

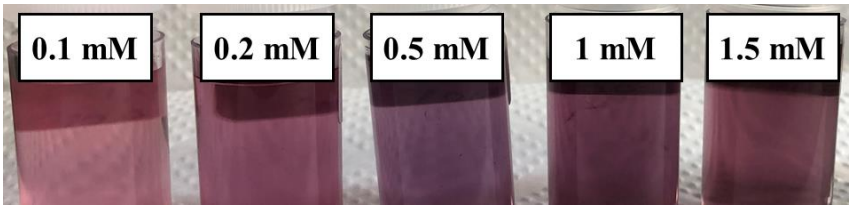

Figure 45. Picture of the samples after 5 min of plasma treatment with 0.05 mM of PVP concentration at different $HAuCl_4$ concentrations ranging from 0.1 to 1.5 mM.

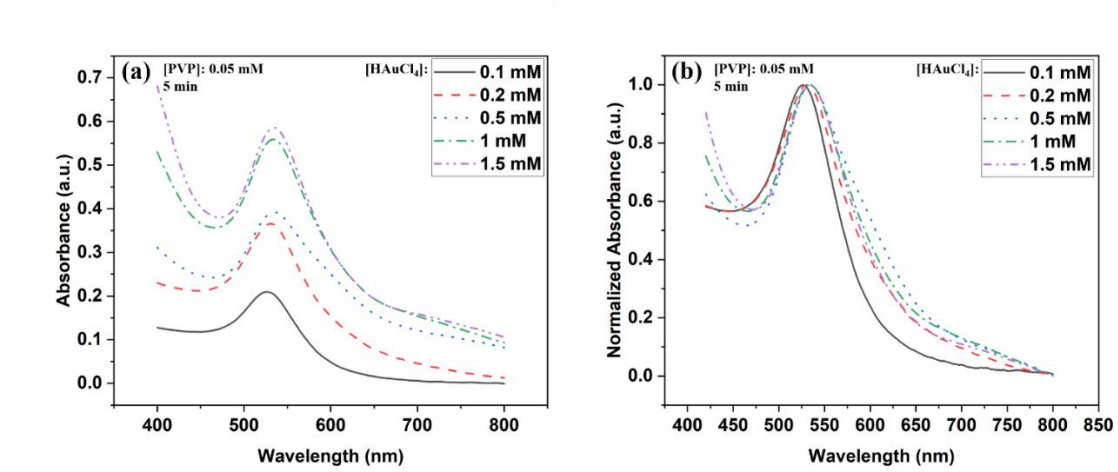

Figure 46. (a) UV-vis absorbance spectra (b) normalized UV-vis absorbance spectra of the solutions after 5 min of plasma exposure with 0.05 mM of PVP at $HAuCl_4$ concentrations ranging from 0.1 to 1.5 mM.

Table 13. Table summarizing the FWHM and the max intensity band wavelength of the treated solutions at different $HAuCl_4$ concentrations.

[$HAuCl_4$] (mM)	*FWHM (nm)*	*λ_{max} (nm)*
0.1	50	525
0.2	56	532
0.5	62	533
1	57	534
1.5	54	536

Further insight into the influence of $HAuCl_4$ concentration was pursued through transmission electron microscopy (TEM), allowing a detailed exploration of the nanoparticles' morphological changes (Figure 47). The TEM images offer a clear difference of how both the average size and shape of gold nanoparticles are strongly impacted by variations in the precursor's concentration. For instance, at an $HAuCl_4$ concentration of 0.1 mM (Figure 47(a)), the nanoparticles exhibited a uniform spherical geometry, marked by dispersion and homogeneity. Measuring 200 random nanoparticles in TEM micrographs yielded an average diameter of 13 ± 4 nm. At 0.2 $mmol.L^{-1}$ (Figure 47(b)), the nanoparticles displayed a larger average diameter of 27 ± 7 nm, with a diverse array of shapes, including triangles, rods, pentagons, and more. While the TEM images at 0.5, 1, and 1.5 mM in Figure 47(c), (d), and (e), respectively exhibited nanoparticle aggregation. These visual observations emphasize the relationship between precursor concentration and nanoparticle morphology. Notably, the optimal precursor concentration for obtaining uniform and spherical gold nanoparticles emerged as 0.1 mM. The present TEM analysis reinforces the significance of precursor concentration control in shaping nanoparticles.

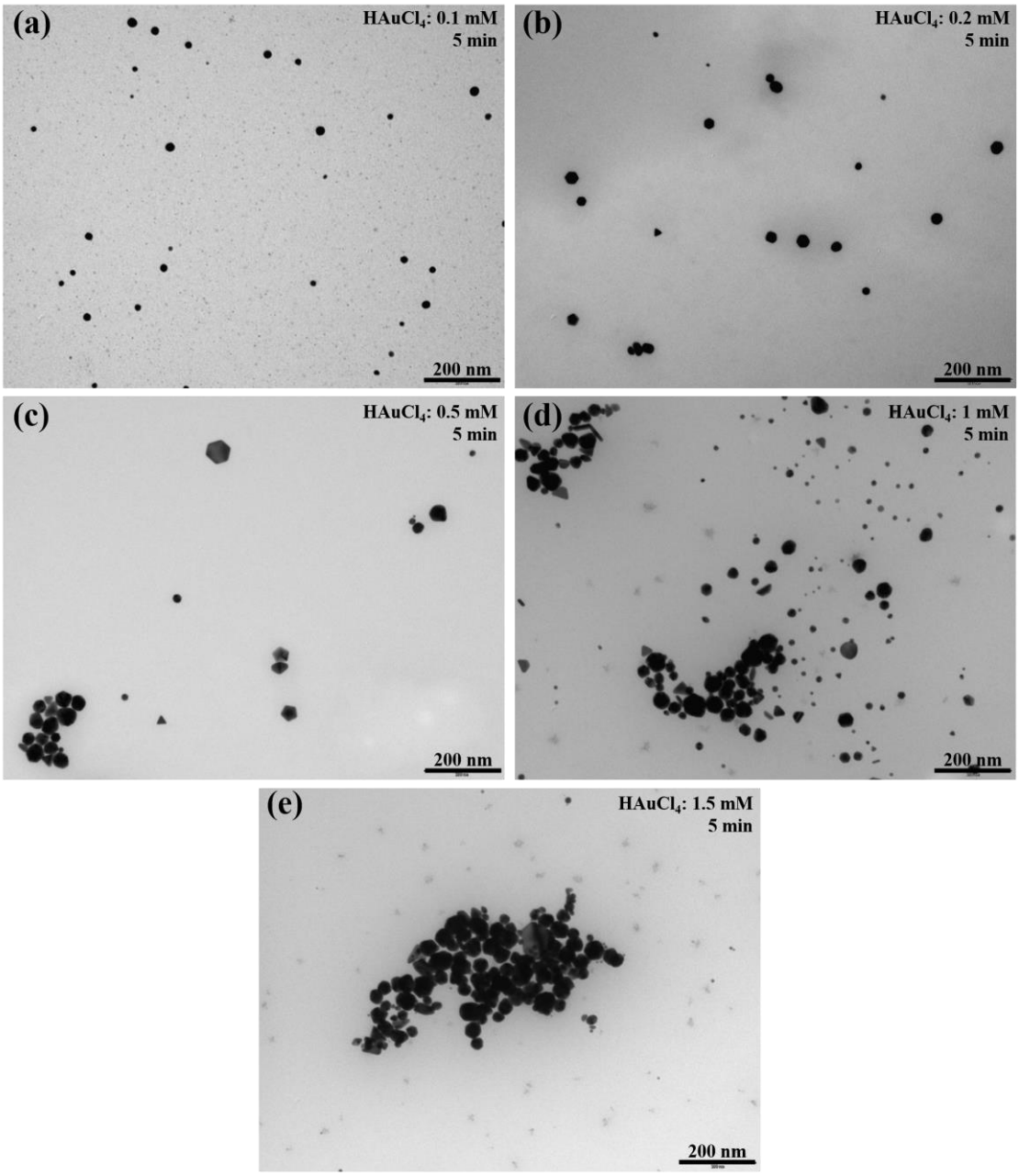

Figure 47. TEM micrographs of the gold nanoparticle solutions after 5 min of plasma exposure with 0.05 mM of PVP at (a) 0.1 mM, (b) 0.2 mM, (c) 0.5 mM, (d) 1 mM, and (e) 1.5 mM of $HAuCl_4$ concentration.

3.4.3 Effect of the capping agent's concentration

Building upon the findings from the preceding section, our investigation continued by focusing on a $HAuCl_4$ concentration of 0.1 mM. As agglomerated nanoparticles can cause a problem in their applications for specific fields. In order to further avoid agglomerations, it is therefore necessary to study the influence of the presence of a capping agent during gold nanoparticle synthesis. The influence of PVP concentrations on nanoparticle size and shape is recognized to be substantial [169].

Polyvinylpyrrolidone (PVP) is a non-toxic, non-ionic polymer with CO, CN and CH_2 functional groups, which functions as a stabilizing agent in nanoparticle synthesis, effectively preventing agglomeration through its unique molecular properties. It serves as a capping agent that binds to the nanoparticle surface, creating a protective layer. This layer of PVP molecules forms a barrier that hinders the direct contact and interaction between individual nanoparticles, mitigating the attractive forces that drive agglomeration. PVP molecules possess both hydrophilic and hydrophobic segments within their structure. Its hydrophobic carbon chains extend into the solvent and prevent the aggregation of the nanoparticle via their repulsive forces [170]. This steric stabilization provided by PVP molecules is particularly crucial during the early stages of nanoparticle formation when the nanoparticles are most susceptible to agglomeration due to their high surface energy. PVP is available in various molecular weight grades, each with its own specific properties and applications. Some common molecular weight grades of PVP include 10 000 $g.mol^{-1}$, 40 000 $g.mol^{-1}$, 360 000 $g.mol^{-1}$. They have different solubility characteristics, viscosities, and abilities to stabilize nanoparticles. PVP 10 000 $g.mol^{-1}$ was used in this study and for all the samples. In literature, it is generally common to use a low concentration of capping agents.

Employing consistent plasma parameters as usual and maintaining 0.1 mM of $HAuCl_4$, distinct solutions were subjected to a 5-minute plasma jet exposure, encompassing PVP concentrations ranging from 0 (considering 0 as no PVP was added to the solution) to 0.1 mM (Figure 48). The UV-vis spectra and the normalized spectra of these seven distinct samples are depicted in Figure 49.

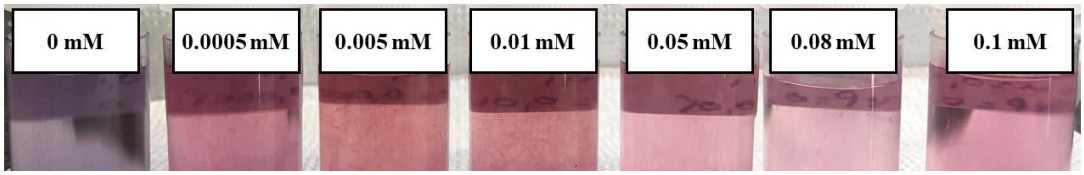

Figure 48. Picture of the samples after 5 min of plasma treatment with 0.1 mM of $HAuCl_4$ concentration at different PVP concentrations.

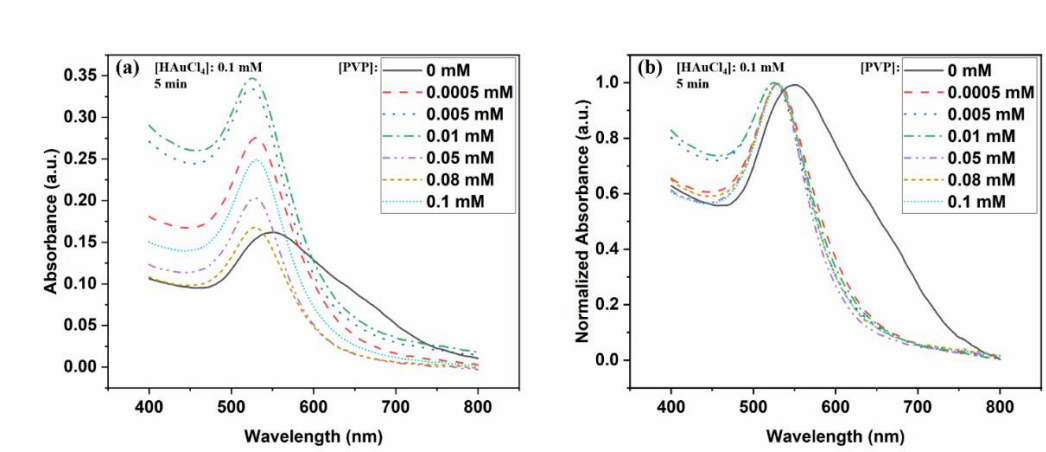

Figure 49. (a) UV-vis absorbance spectra (b) normalized UV-vis absorbance spectra of the solutions after 5 min of plasma exposure with 0.1 mM of $HAuCl_4$ at PVP concentrations ranging from 0 to 0.1 mM.

The crucial role played by PVP became evident, especially in the sample lacking the capping agent, which exhibited a noticeable distinct absorbance band. This broad band shifted from approximately 525 nm to around 550 nm. This signifies the presence of larger particles and extensive agglomeration within the solution. Notably, this optical behavior was corroborated by the TEM analysis presented in Figure 50(a), presenting the uncontrolled nucleation and growth that led to the presence of sizable and aggregated gold particles. As PVP concentration was incrementally increased, the λ_{max} exhibited a slight shift towards shorter wavelengths, a phenomenon known as a blue shift in the plasmon band, attributed to the reduction in the size of the formed nanoparticles [171]. Complementing these insights, transmission electron microscopy results in Figure 50(b)-(c)-(d) confirmed the formation of smaller-sized gold nanoparticles, showcasing diverse shapes beyond spheres, including triangles, rods, and hexagons. When PVP is absent from the solution, significant agglomeration occurs among the nanoparticles due to the lack of a stabilizing agent. As PVP is gradually introduced, aggregation diminishes, leading to the formation of well-separated nanoparticles, with the process continuing until a certain concentration threshold is reached. At 0.05 mM (Figure 50(e)), the resultant particle size was consistently maintained. TEM imaging revealed that these nanoparticles uniformly exhibited an average diameter of 13 ± 4 nm, determined from measurements of 200 randomly selected nanoparticles, with the majority displaying spherical, well-dispersed, and separated characteristics. Beyond this concentration, when PVP concentration is further increased in Figure 50(f)-(g), we can see a different behavior as the small nanoparticles start to agglomerate. It was reported by Guo et al., that an excess amount of PVP in gold nanoparticle synthesis can lead to aggregation of small nanoparticles until an equilibrium between the precursor and PVP is reached [172]. So the molar ratio of PVP to $HAuCl_4$ is a key factor to easily control the diameter of gold nanoparticles. Accordingly, PVP

emerged as a pivotal factor for the synthesis process of gold nanoparticles, effectively preventing agglomeration and yielding spherical, homogeneous nanoparticles.

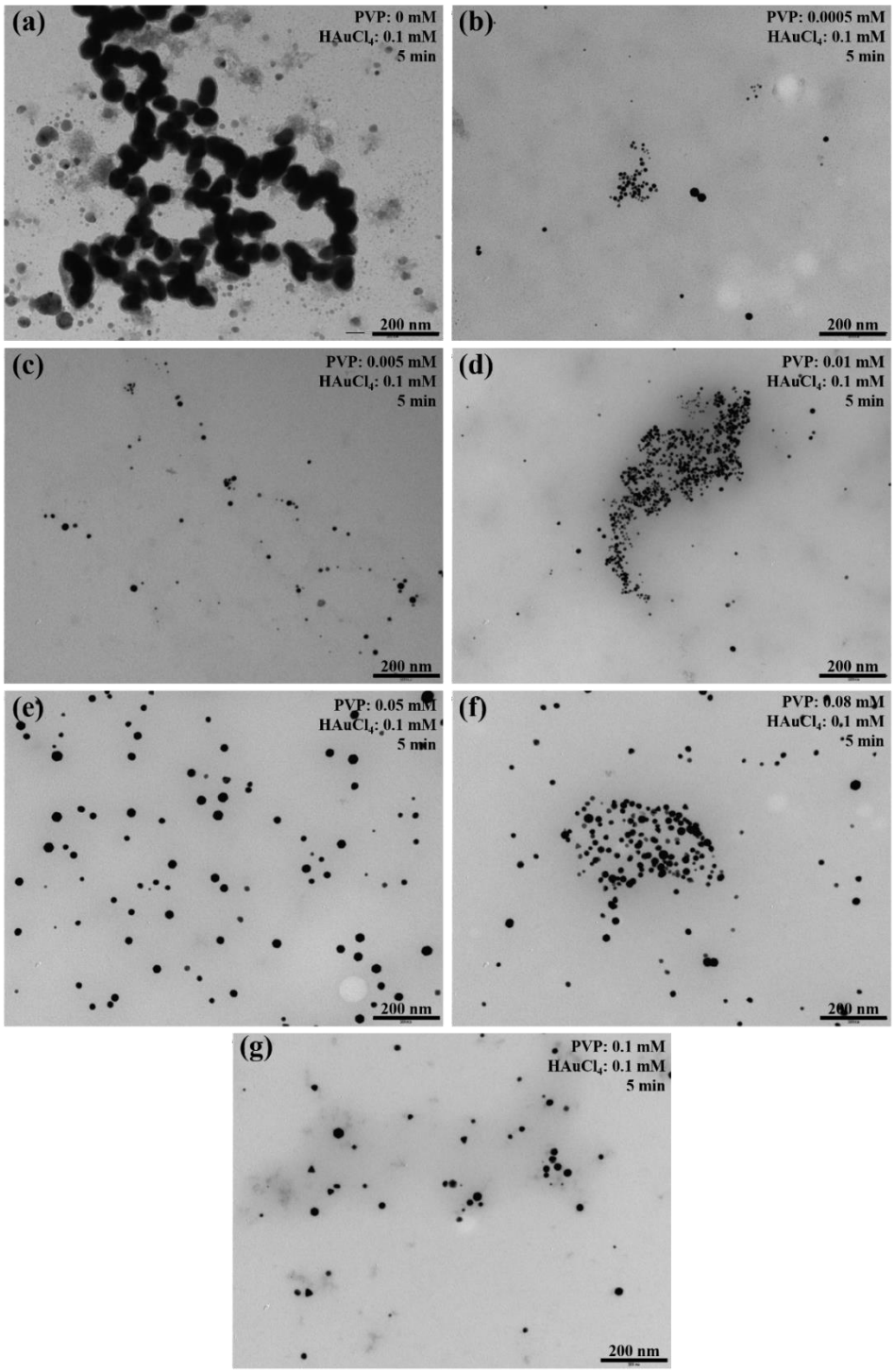

Figure 50. TEM micrographs of the solutions after 5 min of plasma exposure with 0.1 mM of $HAuCl_4$ at (a) 0 mM, (b) 0.0005 mM, (c) 0.005 mM, (d) 0.01 mM, (e) 0.05 mM, (f) 0.08 mM, and (g) 0.1 mM of PVP concentration.

The sample gold nanoparticles obtained after 5 min of plasma discharge with 0.1 mM of $HAuCl_4$ and 0.05 mM concentrations was analyzed by dynamic light scattering (DLS) to obtain their size distribution. As demonstrated in Figure 51, the average size was 23 ± 7 nm which matches with the size calculated by measuring 200 random nanoparticles in the TEM images (13 ± 4 nm). The size obtained is slightly higher than with TEM because DLS measures the hydrodynamic diameter of nanoparticles in a liquid solution, accounting for the surrounding solvent molecules and their movement, resulting in a slightly larger apparent size. In contrast, TEM provides a direct observation of the nanoparticles in their solid state, offering a more accurate representation of their intrinsic size without the influence of solvent molecules. Therefore, the slightly higher size obtained by DLS is attributed to the inclusion of the solvent shell around the nanoparticles during measurement.

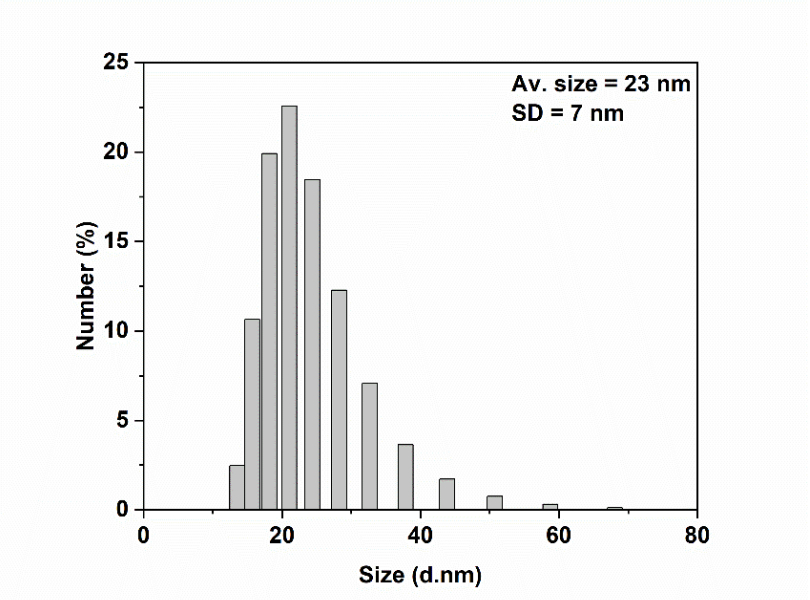

Figure 51. Size distribution measured by DLS of the synthesized AuNPs after 5 min of plasma exposure with 0.1 mM of $HAuCl_4$ and 0.05 mM of PVP concentrations.

3.5 Conclusions

In conclusion, this chapter is an exploration of nanoparticle synthesis using a helium atmospheric pressure plasma jet, composed of an asymmetric borosilicate glass source and a micropulse power supply. The initial phase of the study involved characterizing the plasma jet's generation of reactive species and their influence on the physicochemical properties of the liquid. Through optical characterization, key excited species in the plasma were identified, with their evolution observed over the plasma jet's length. Furthermore, the concentration of long-lived reactive species, particularly H2O2, was found to increase with plasma treatment time.

The second part of the chapter, the focus shifted to synthesizing silver nanoparticles using the characterized plasma jet. The nanoparticle synthesis process was systematically tuned and investigated. Key parameters included plasma interaction duration, metal precursor concentration, and capping agent concentration. An optimal ratio of precursor and capping agent concentrations was identified to achieve uniformly spherical silver nanoparticles with an average diameter of 13 nm. The plasma treatment duration of 5 minutes was determined as the optimal timeframe for efficient nanoparticle generation.

Continuing with gold nanoparticle synthesis, a similar approach was employed. The influence of plasma interaction duration, metal precursor concentration, and capping agent concentration were explored. An optimal ratio of precursor and capping agent concentrations was found, resulting in uniformly spherical gold nanoparticles with an average diameter of 13. Again, a 5-minute plasma treatment duration was established as optimal for nanoparticle synthesis.

The research underlines the significance of optimizing various parameters in nanoparticle synthesis to achieve desired properties. The interaction between plasma discharge duration, precursor concentration, and capping agent concentration played a critical role in controlling nanoparticle size, shape, and distribution. The efficiency and quality of the plasma-based approach were demonstrated through comparisons with literature methods.

Chapter 4. Synthesis of Metallic Nanoparticles by Dual-Frequency Atmospheric Pressure Plasma Jet

4 Synthesis of Metallic Nanoparticles by Dual-Frequency Atmospheric Pressure Plasma Jet

In this chapter, we initiate an exploration using an alternative plasma setup configuration, incorporating a dual-frequency source to refine nanoparticle synthesis. The primary objective of this chapter is to investigate the relationship between process gas choice, radiofrequency (RF) power, and plasma dynamics, and their consequential impact on gold nanoparticle production.

The incorporation of a dual-frequency source, achieved through an alumina tube connected to both a micropulse power supply employed previously and an additional RF generator, adds a novel dimension to the conventional plasma setup. This setup paves the way for investigating how the introduction of RF power affects plasma behavior, influencing the nanoparticle formation process. This investigation includes maintaining a consistent geometric configuration of the apparatus (detailed in chapter 2), micropulse APPJ input parameters (power supply current = 8 A, frequency = 25 kHz), and the flow rates (3 $L.min^{-1}$) of the gases involved. The variables subjected to alteration were the RF power levels, ranging from a minimum of 0 W (as to no RF power was added) to a maximum of 30 W, the duration of the treatment, set at either 10 minutes or 20 minutes, and the selection of process gas species, encompassing both helium (He) and argon (Ar).

Our study starts by the characterization of the dual-frequency atmospheric pressure plasma jet. This entails an analysis of the instrumental setup, with a focus on the observed changes in the optical emission spectrum that arise due to the choice of the process gas. This initial phase provides an essential understanding of how the dual-frequency source implementation influences the plasma's behavior, its interactions with the gases, and the overall environment within this setup. The distinct emission spectra, gas temperature variations, and the intriguing behavior of charge collection under RF coupling all contribute to the plasma's transformation from a self-propagating mode to a capacitive coupled configuration. This characterization serves as the foundation for the subsequent phase of our study, which centers on the production of gold nanoparticles.

Focusing on gold nanoparticle synthesis, this chapter goes through the consequences of employing the dual-frequency source with helium and argon as process gases on the nanoparticles' characteristics. The spectral changes observed through UV-vis spectrophotometry offer a visual

into the interplay of parameters. This visual is further confirmed by SEM and AFM micrographs, which capture the modifications in nanoparticle size and shape by systematically varying the RF power, treatment duration, and process gas species.

4.1 Plasma characterization

This section presents a characterization of the dual-frequency atmospheric pressure plasma jet (DF-APPJ) employed in this study. The geometric configuration of the setup, as detailed in chapter 2, was maintained constant, as were the micropulse APPJ input parameters (power supply current = 8 A, frequency = 25 kHz), and the flow rates of the gases (3 $L.min^{-1}$).
The primary focus of this characterization is to examine the influence of process gas and RF power on the plasma jet behavior. In Figure 52 below, images of the plasma jet are presented at different RF power levels, both for helium and argon as process gases. The upper images correspond to helium, while the lower ones depict argon. Clearly, the plasma jets exhibit distinct visual characteristics based on the process gas utilized. As anticipated, the plasma color differs between helium and argon, indicating their individual emission spectra. It is noteworthy that the plasma generated with argon demonstrates a more filamentary structure appearance compared to the helium-generated plasma where it appeared to be uniform within the time exposure of 30 ms considered. With argon as process gas the filaments moves randomly following the anular outlet of the dielectric tube. Due to this plasma instability the OES was carried out collecting the light from 5 mm circular parallel beam including all the plasma area from the jet outlet to the liquid surface. This observation aligns with the differing behavior of these gases under the plasma's influence. In both cases, the plasma seems to propagate on the liquid surface. Additionally, the impact of RF power is evident in the images. With the augmentation of RF power, the brightness of the plasma jet increases.

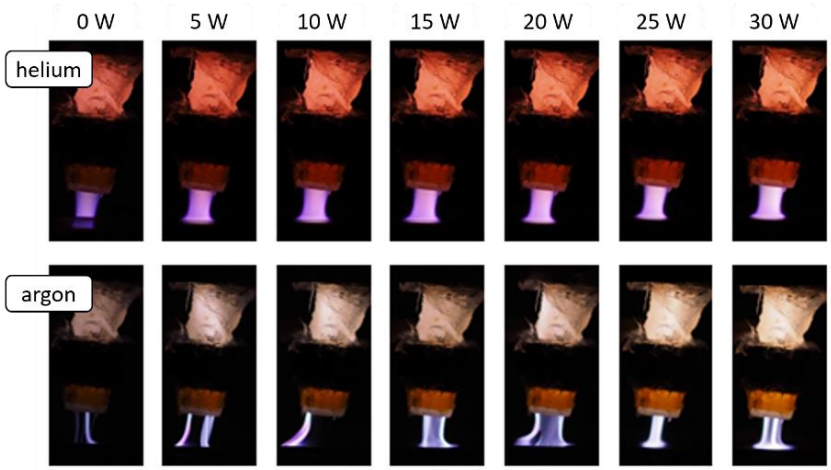

Figure 52. Images of the dual frequency atmospheric pressure plasma jet at different RF power levels with (upper) helium, and (bottom) argon as process gases.

In the subsequent section we will examine the optical emission spectroscopy of the plasma with both gases to characterize the emission spectra and investigate the variations in reactive species emissions between helium and argon.

4.1.1 Optical emission spectroscopy (OES)

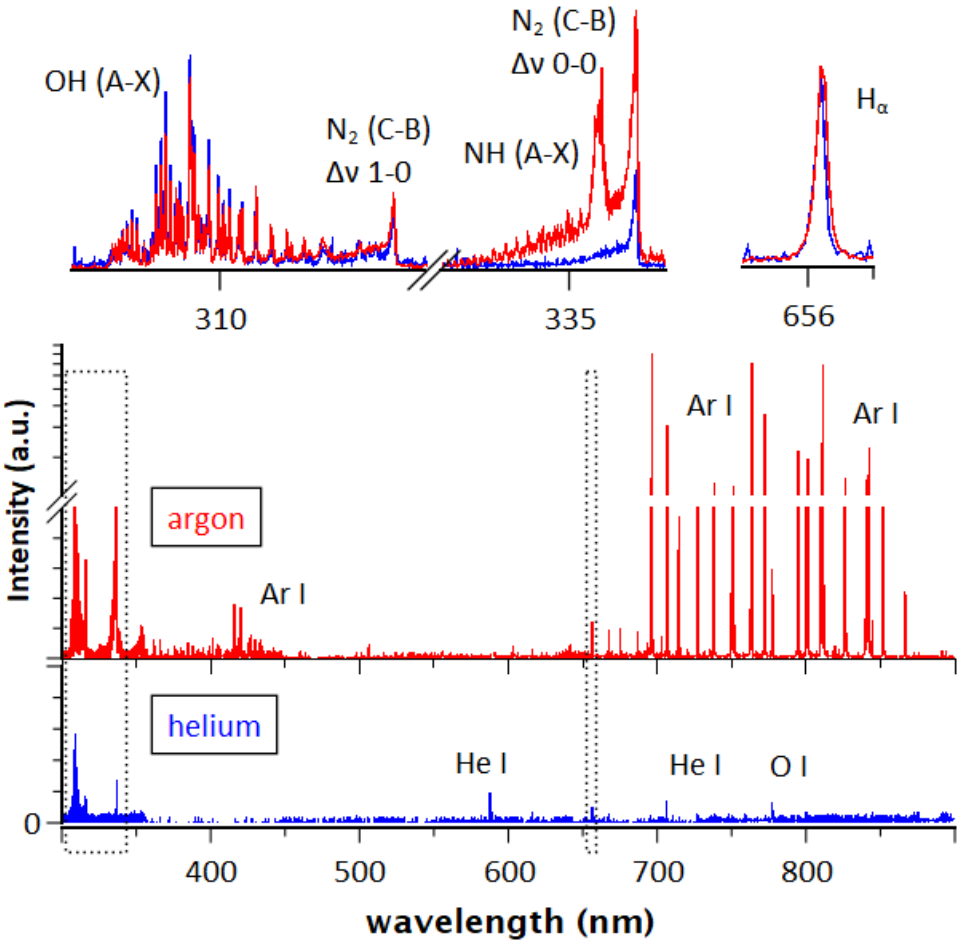

Figure 53. Optical emission spectra of the helium and argon plasma jet at 30 W RF power. In the upper part are shown the spectral zoom of the signals relative to the OH(A-X), NH(A-X), N_2(C-B) and H_α emissions.

A multi-channel spectrometer AvaSpec from Avantes was used to measure the plasma optical emission spectrum [173]. A fiber optic cable with a parallel beam condensing lens was placed perpendicular to the plasma at a 10 cm distance. The diameter of the parallel beam was about 5 mm therefore the fiber was collecting a spatially integrated signal of the whole plasma plume between the liquid surface and the outlet of the jet. Integration time was 200 ms. In Figure 53, the optical emission spectra corresponding to the condition of 30 W of RF power for the two gas species are presented. The principal spectral lines are indicated in the figure.

The spectra of helium and argon exhibit distinct fingerprints, consistent with existing literature references [174], [175], [176]. The argon plasma demonstrates a significantly higher overall emission intensity compared to helium. In both cases, alongside the process gas lines, we identified distinct features including the nitrogen second positive system (N_2 SPS), the OH molecular band, as well as prominent atomic oxygen and hydrogen emission lines.

Table 14. Species identified based on the lines observed in the optical emission spectrum obtained using the dual frequency atmospheric pressure plasma jet for helium and argon as process gases.

Specie	***Wavelength (nm)***
He I	587
	667
	706
	728
Ar I	696
	706
	714
	727
	738
	750
	763
	772
	795
	800
	810
	811
	826
	840
	842
	852
	866
OH	295
	308
N_2 (Second Positive System SPS)	315
	337
NH	336
H_α	656

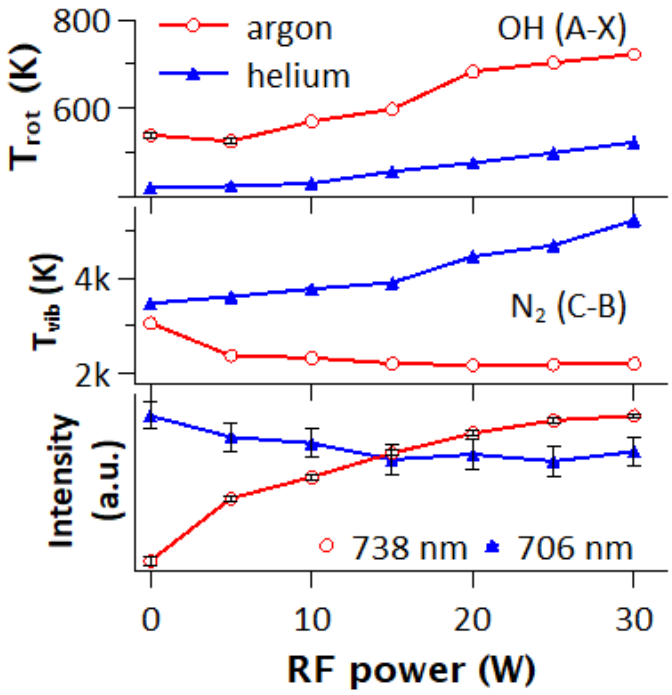

Figure 54. OES analysis results as a function of the RF power for (blue) helium and (red) argon gases: (top) rotational temperature of OH from OH (A-H) band; (center) vibrational temperature of N_2 from N_2 SPS; and (bottom) optical emission intensity of He I 706 nm and Ar I 738 nm lines.

With the alteration of RF power levels, the features and overall emission characteristics of the spectra remained consistent. However, there were changes in the intensities of some specific emission lines. Figure 54 depicts the trends of He I and Ar I lines intensities along with the variation in the rotational and vibrational temperatures. The emissions at wavelengths 706 nm for helium and 738 nm for argon have been chosen as representatives of the He I and Ar I lines, respectively. It can be seen in the figure above that the emission intensity in argon demonstrates a consistent increase with the augmentation of RF power supplied to the discharge. Conversely, for helium, the emission remains relatively constant.

The upper part of
Figure 53 illustrates the OH (A-X) transition and the N_2 (C-B) bands for argon and helium under 30 W RF conditions. Derived by these OH and N_2 SPS bands are the results of the rotational temperature (T_{rot}) and the vibrational temperature (T_{vib}), respectively, presented as a function of RF power levels in Figure 54. Plasma gas temperature parameters was obtained fitting OH, N_2 and NH spectral bands by means of MassiveOES code. The OH (A-X) transition was used to determine the rotational temperature, the fitting was performed in the 303 – 320 nm interval, with a Lorentzian HWHM of 0.03 nm. The vibrational temperature was obtained

by the N_2 (C-B) bands fitting in the interval 300 – 355 nm considering in the fitting also the OH (A-X) and the NH (A-X) bands. An increase in the rotational temperature is present in both discharges even if for helium the variation is limited within 100 K. The rotational temperature in the helium-process gas scenario consistently remains below 500 K, as expected, positioned 100 – 200 K lower than that observed with argon [177]. The lower temperature is additionally highlighted by the absence of NH emissions at 336 nm [178]. The increase of NH formation for the argon gas plasma may be due also to a higher solution evaporation as featured by a stronger increase in the OH band, O I, and H_α emissions. The higher temperature in argon is also due to its lower thermal conductivity, which also contributes to its filamentary structure formation [179]. The argon-produced plasma may potentially exhibit greater density, as suggested by the heightened Stark broadening of the H_α line in comparison to helium conditions
(
Figure 53). While the T_{rot} can be linked usually to gas temperature and therefore also to the power delivered in the discharge, the T_{vib} is more linked to a direct electron energy transfer to the molecules. In the helium discharge, the increase of the T_{vib} as a function of the RF power applied is clearly visible and higher than in argon, which is consistent with its outer equilibrium condition. The increase may be due to the higher power dissipated in the discharge but can also suggest an enhanced electron heating or to a change in the plasma regime. The plasma generated in argon does not show the same trend but this information may be affected by the filamentary structure, since the recorded signal integrated spatially all the area between the jet outlet and the liquid surface. Nonetheless, the overarching consequence of augmenting RF power levels is a heightened intensity of OH radicals' emissions, both in helium and argon setups.

4.1.2 Charge collected

The information obtained by the OES are spatially and temporally integrated and the main differences among the plasma conditions are mainly related to the gas species and to the RF power applied. In order to highlight further differences related to the dual frequency concept applied to the micropulse, a temporally resolved characterization is required. So, the charge collected is recorded in three RF power conditions 0 W, 15 W and 30 W. The voltage of the pulsed electrode was measured by means of a capacitive voltage divider (Le Croy PPE6KV-A) and the charge through the sample was measured with a 22 pF capacitor in series to the ground below the beaker containing the solution

Figure 55 (bottom) illustrates the pulse voltage applied to the upper electrode. The pulse is distinguished by a brief pre-pulse negative bias lasting a few microseconds. The pulse originates from impulse current charging an RLC network, with its peak exhibiting a rise time on the

order of 100 ns. The oscillations last few tens of microseconds, and therefore do not overlap between the 25 kHz cycles.
In Figure 55 (top and center), the charge collected beneath the solution to the ground is also presented for both process gases at various RF power levels. When RF was not applied and only the micropulse was active, the plasma plume reached the liquid surface, and the corresponding charge could therefore be collected in the capacitor below the solution.

It can be observed that during the pre-pulse, no charge is collected indicating the absence of residual ionization between pulse repetitions. As the upper electrode became positive the electrons migrate towards it, leaving a positive spatial charge behind. These positive charges subsequently drift toward the liquid, giving rise to a rapidly propagating self-propagating head, which is quite fast within the order of few tens of nanoseconds. This progression forms an ionized channel linking the liquid and the micropulse electrode. Consequently, the following oscillations led to a capacitive coupling, as signified by the similar shape of the voltage and charge oscillations. The charge collected using helium is roughly half that of argon, aligning coherently with the differences in plasma density observed through OES measurements. In essence, the primary phase of plasma generation is predominantly concentrated within the initial pulse, a part that is magnified in Figure 55.

The introduction of RF power yields a noticeable augmentation in the maximum charge collected by the liquid. This augmentation displays a minimal dependence on the RF power levels, even when varying the levels of RF power added, the maximum charge collected remains consistent. This increase in the collected maximum charge is most likely attributed to the shift of a denser plasma region from within the alumina tube towards the outlet, where the RF electrode is positioned. This shift bears a resemblance to bringing the micropulse electrode closer to the liquid's surface. As a consequence, the resultant electric fields are intensified. Moreover, this effect is more evident in the case of use of argon due to its higher plasma density and filamentary structure. This higher plasma density also allows the persistence of the plasma channel between two consecutive micropulses. This stable electrical connection between the HF and the liquid surface improves the capacitive coupled character of the discharge, and the surface charge on the liquid matches more closely the supplied voltage at HF.

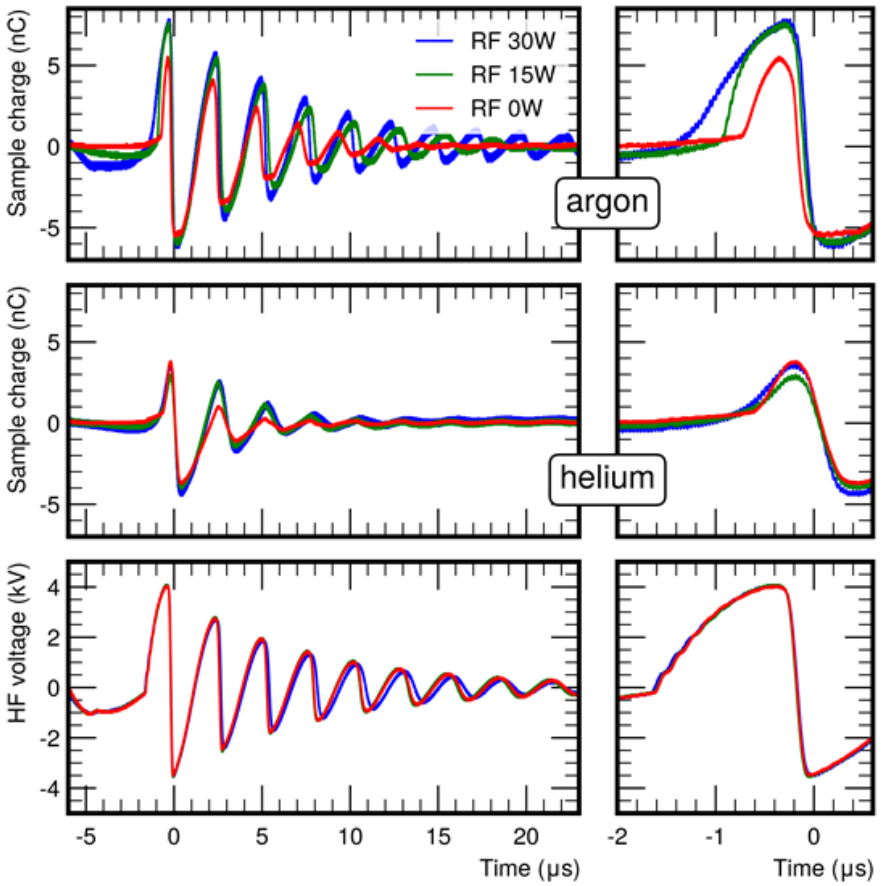

Figure 55 Charge collected by the sample in (top) argon and in (center) helium as a function of the (bottom) electrode pulse polarization. Charge is recorded in three RF power conditions 0 W, 15 W and 30 W, and on the right is a time zoom of the pulse.

4.2 Influence of helium as process gas on gold nanoparticles morphology

Having established the significant influence of process gas on the plasma's behavior, we will now try to investigate its profound impact on the dynamics of gold nanoparticles production. In the preceding chapter, we successfully determined the optimized parameters for gold nanoparticle synthesis through an exploration of varying the precursor and capping agent concentrations. Our findings identified that employing 0.1 mM $HAuCl_4$ and 0.05 mM PVP concentrations yielded nanoparticles with good homogeneity, narrow size distribution, and negligible agglomeration. Building upon these results, we have chosen to proceed with these parameter settings for the ongoing study. With the plasma configuration characterized in the prior section featuring a dual-frequency source, we now aim to investigate the influence of helium as process gas and RF power levels on the production of gold nanoparticles.

To initiate this investigation, we prepared six separate samples, each comprising 10 ml of a solution containing 0.1 mM $HAuCl_4$ as a precursor and 0.05 mM PVP as a capping agent. These samples were then subjected to plasma treatment in a helium environment, while varying key operational conditions. Specifically, we explored different RF power levels (0, 15, 30 W) and plasma exposure durations (10, 20 min). The resulting samples were characterized firstly by UV-vis spectrophotometry and the results were compared to determine the influence of these conditions on the size and shape of the obtained nanoparticles.

In Figure 56, the absorbance spectra of the treated gold nanoparticle solutions are presented for different RF powers and treatment durations. The spectra are normalized to the interband gold transition to allow an easier comparison of the plasmon absorption. However, as expected, longer treatment time leads to higher particle density. No relevant variation of particle density is observed as a function of the RF power, in line with the conclusions drawn by the plasma electrical characterization. As increasing the treatment duration from 10 to 20 min did not significantly alter the band profile or maximum plasmon band wavelength position, but led to an increase in the band intensity as shown in Figure 57.

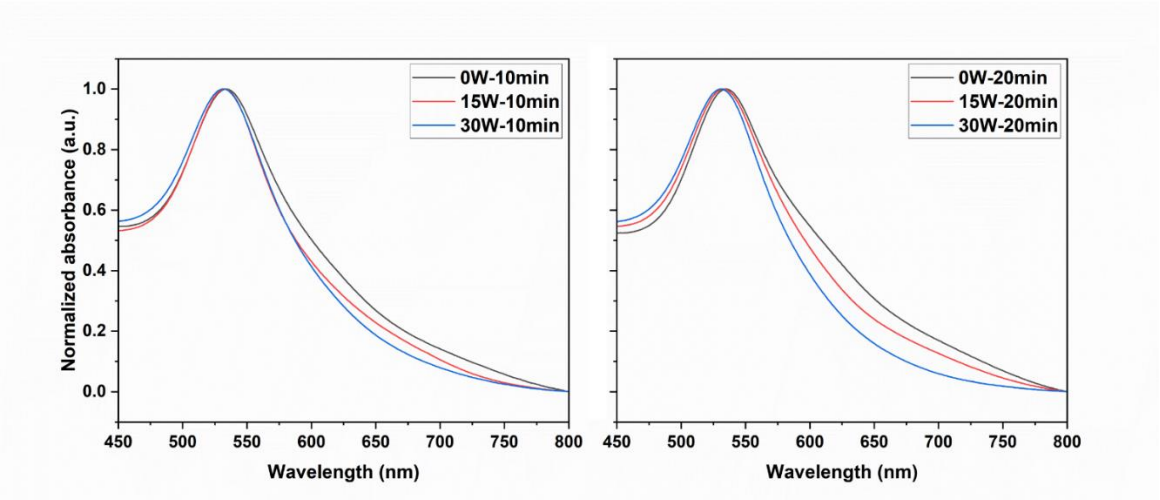

Figure 56. UV-vis absorbance spectra of the obtained gold nanoparticles after (left) 10 min and (right) 20 min of helium plasma treatment at different RF power 0 W, 15 W and 30 W. The spectra have been normalized to the interband gold transitions.

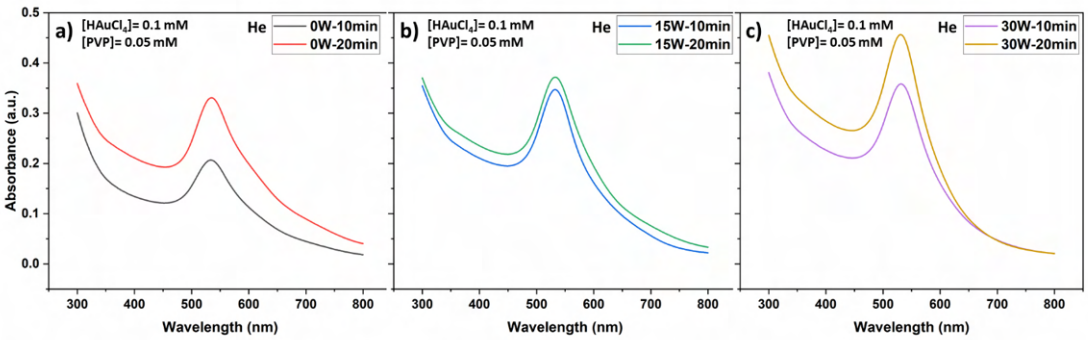

Figure 57. UV-vis absorbance spectra of the obtained gold nanoparticles after 10 and 20 min of helium plasma treatment at a) 0 W, b) 15 W and c) 30 W of RF power.

Table 15. Table summarizing the absorbance band max wavelength as a function of RF power levels and plasma treatment duration using helium-DFAPPJ.

RF power (W)	***Treatment time (min)***	λ_{max} ***(nm)***
0	10	534
	20	531
15	10	533
	20	533
30	10	532
	20	535

The samples produced with no RF power showed a slight higher intensity at longer wavelengths than with the addition of RF, which could be associated with different particle size or shape [180]. As the RF power levels increased, this intensity at higher wavelengths gradually decreased. Particularly, the spectra observed at 30 W RF power for both treatment duration, showcased the narrowest band among the three RF power conditions. The deconvolution of the particle size and shape profile from the plasmon band feature is challenging since additional preliminary information on particles distribution are required.

The maximum band shifted to lower wavelengths when RF power was introduced, decreasing from 535 nm without RF power to 531 nm with a 30 W RF power. While this shift could potentially be the result of a decrease in the nanoparticles size [181], it might also be resulting from the addition of RF power causing a transition from asymmetric shapes.
To further confirm this analysis, scanning electron microscopy (SEM) was used to visualize the formed nanoparticles. The resulting images are presented below and are in agreement with

our previous analysis. In fact, Figure 58(a) shows the nanoparticles synthesized with 8 A of power supply current without the addition of an RF power for 10 min and reveals some exotic shapes other than spheres such as rods, triangles, and pentagons with an average diameter of 28 ± 3 nm. Also, Figure 58(b) with an added 15 W of RF power presents nanoparticles of different shapes but with less variation than the previous samples. While in Figure 58(c), the particles are spherical and well separated with no agglomerations seen in the images with an average diameter of 22 nm and a 3 nm standard deviation calculated measuring random nanoparticles in the SEM images. We employed ImageJ software to calculate the particle diameters using the SEM images. The reported diameters were averaged from measurements of approximately 50-100 nanoparticles observed in the SEM images.

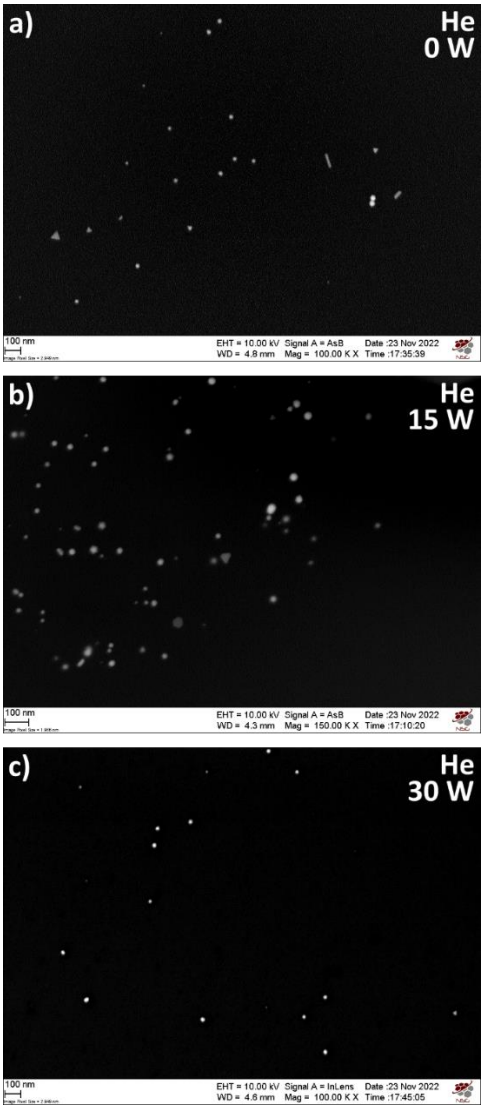

Figure 58. SEM micrographs of the synthesized gold nanoparticles with a 10 min helium plasma jet exposure at a) 0 W, b) 15 W, and c) 30 W RF power.

Recognizing that SEM data might not yield the precision needed, we conducted Atomic Force Microscopy (AFM) analysis as an additional step to validate the obtained sizes. Our AFM images only covers around 10 µm of the silicon wafer sample holder; therefore, multiple measurements were recorded for each sample to ensure reliable and accurate results [182]. Figure 59 presents the topographical images in 2D and 3D measured with the AFM technique of the samples treated for 10 min with the helium plasma jet, one without RF and the other with an added 30 W RF power. These results supported the SEM data by confirming the particle sizes and reinforced the previously reported data. Our results clearly demonstrate and further confirm that the addition of RF leads to a reduction in the size of the gold nanoparticles.

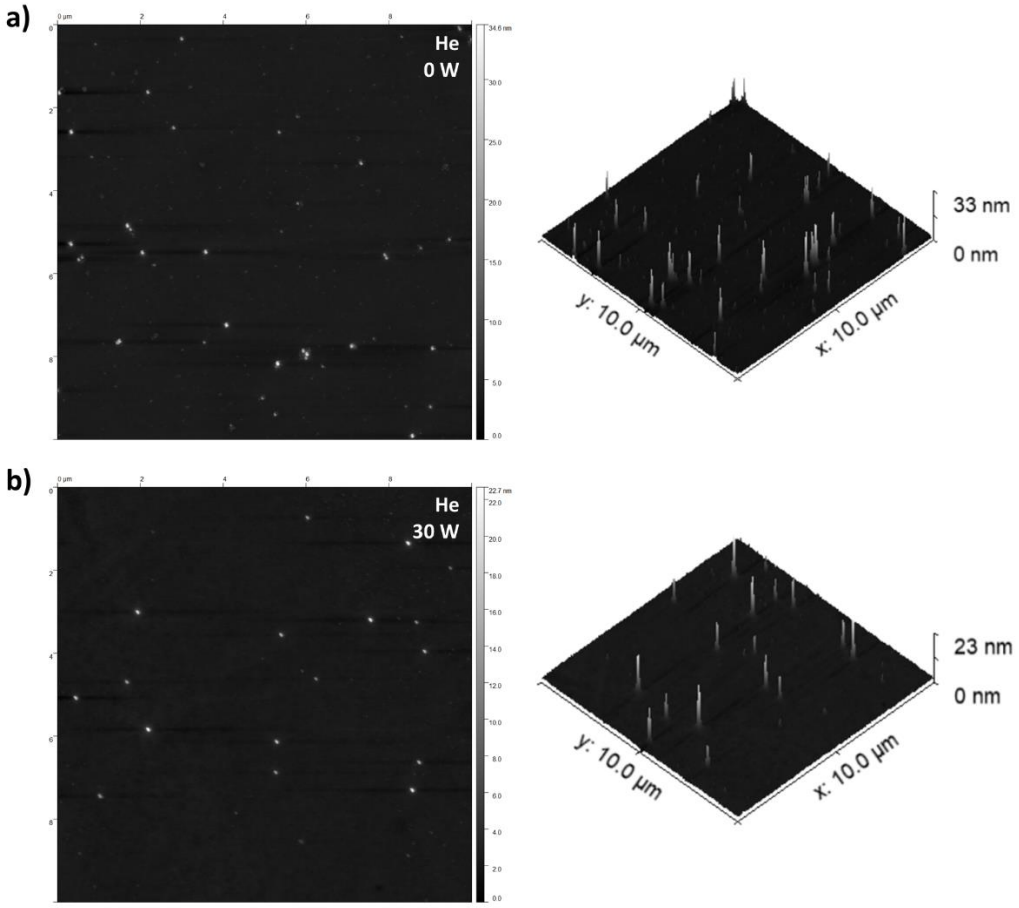

Figure 59. AFM topographical images in 2D and 3D of the synthesized gold nanoparticles with a 10 min helium plasma jet exposure at a) 0 W, and b) 30 W RF power.

4.3 Influence of argon as process gas on nanoparticles morphology

In this section, our focus will shift towards investigating the impact of argon as the process gas and RF power levels on gold nanoparticle production. Mirroring the methodology employed previously, we will prepare six samples utilizing a consistent concentration of 0.1 mM of $HAuCl_4$ and 0.05 mM of PVP concentrations. Subsequently, these samples will undergo plasma treatment within the argon environment each one with a different RF power level addition ranging from 0 W to 30 W and with different plasma exposure durations (10, 20 min) as well. The resulting samples were as well characterized by UV-vis spectrophotometry and the results were compared to determine the influence of the conditions on the size and shape of the obtained gold nanoparticles.

Figure 60 presents the absorbance spectra of the plasma treated gold nanoparticles solutions for different RF powers and treatment durations. The spectra are normalized to the interband gold transition to allow an easier comparison of the plasmon absorption. These results reveals distinctions in the behavior of nanoparticles when argon is employed as the process gas. We observe that the spectral characteristics exhibit minimal change between the samples of RF power addition at both 15 W and 30 W, suggesting that RF power level doesn't have a strong effect on the shape and size of the gold nanoparticles. The substantial contrast, however, becomes apparent when comparing no RF addition to RF addition scenarios and at 20 min of plasma exposure. This difference emerged in the form of a blue shift from 538 nm without the addition of RF power and only the micropulse he-APPJ working to 533 nm when 30 W RF power was added for the treatment, as shown in Figure 60 (right) and summarized in Table 16. This phenomenon could be attributed to the formation of smaller nanoparticles within the samples, contributing to this pronounced shift.

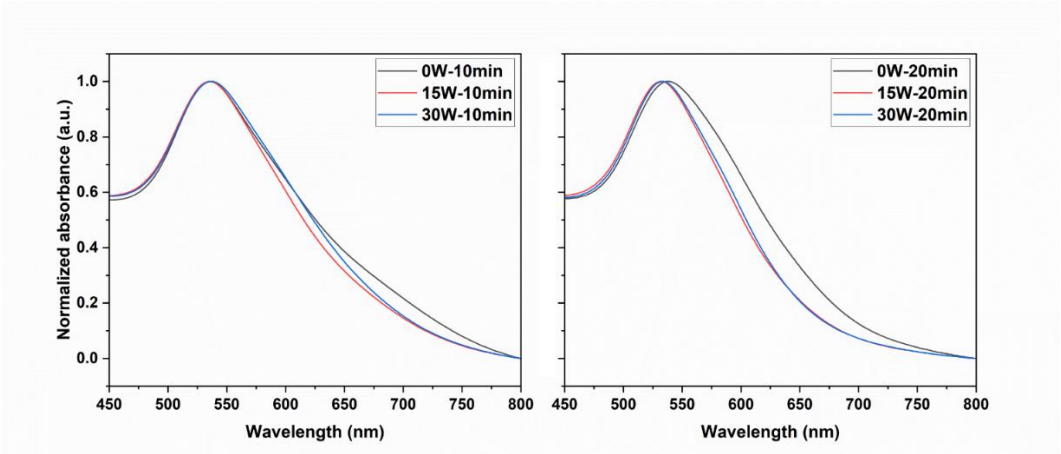

Figure 60. UV-vis absorbance spectra of the obtained gold nanoparticles after (left) 10 min and (right) 20 min of argon plasma treatment at different RF power 0 W, 15 W and 30 W. The spectra have been normalized to the interband gold transitions.

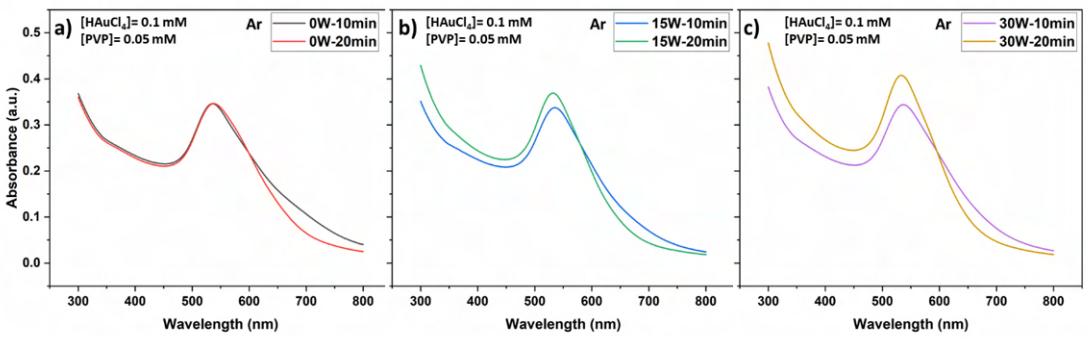

Figure 61. UV-vis absorbance spectra of the obtained gold nanoparticles after 10 and 20 min of argon plasma treatment at a) 0 W, b) 15 W and c) 30 W of RF power.

Table 16. Table summarizing the absorbance band max wavelength as a function of RF power levels and plasma treatment duration using argon-DFAPPJ.

RF power (W)	***Treatment time (min)***	λ_{max} ***(nm)***
0	10	536
	20	538
15	10	535
	20	532
30	10	537
	20	533

SEM micrographs were recorded across the samples in order to visualize the nanoparticles' morphology and validating the UV-vis results. As illustrated in the micrographs in Figure 62, each portraying an individual gold nanoparticle, the spherical nature of the nanoparticles is apparent across different RF powers and treatment durations. A distinct observation emerges in the samples treated with 30 W RF power, in comparison to the sample without RF power addition, the nanoparticles display a notable reduction in size. For instance, the nanoparticle dimension decreased from 22 nm in Figure 62(a) to 15 nm in Figure 62(b) during a 10-minute plasma exposure. Similarly, for a 20-minute exposure, the size reduces from 23 nm in Figure 62(c) to 18 nm in Figure 62(d). This reduction aligns with our earlier analysis, which indicated a blue shift in the absorbance spectra. These size values were also determined through averaging measurements across a certain number of nanoparticles using ImageJ software. These results suggest that the addition of an RF plasma plays a crucial role in determining the size of the nanoparticles synthesized through the argon plasma DF-APPJ process.

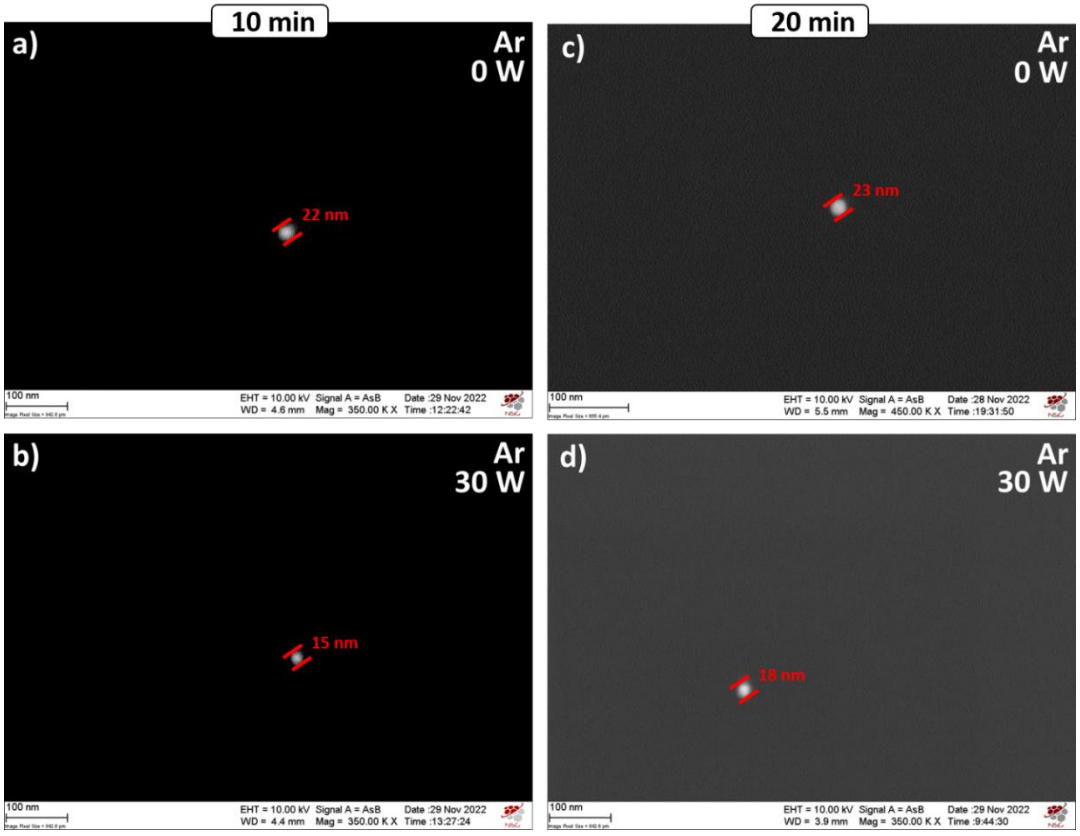

Figure 62. SEM micrographs of one gold nanoparticles synthesized at (left) 10 min and (right) 20 min of argon DF-APPJ exposure at a) and c) 0 W, and b) and d) 30 W RF power.

To provide further validation of the previous findings, we employed the AFM technique to capture 2D and 3D topographical images of two distinct samples subjected to 10-minute treatment using the argon plasma jet, as showcased in Figure 63. In the first sample presented in Figure 63(a), RF power was not utilized, while the second sample in Figure 63(b) was subjected to an additional 30 W RF power. The outcomes not only corroborate our earlier analyses but also reinforce the conclusion that plasma treatment supplemented with RF power yields the formation of smaller-sized gold nanoparticles. This assertion is supported by the reduction in the maximum nanoparticle size observed in the samples, decreasing from 25 nm to 19 nm.

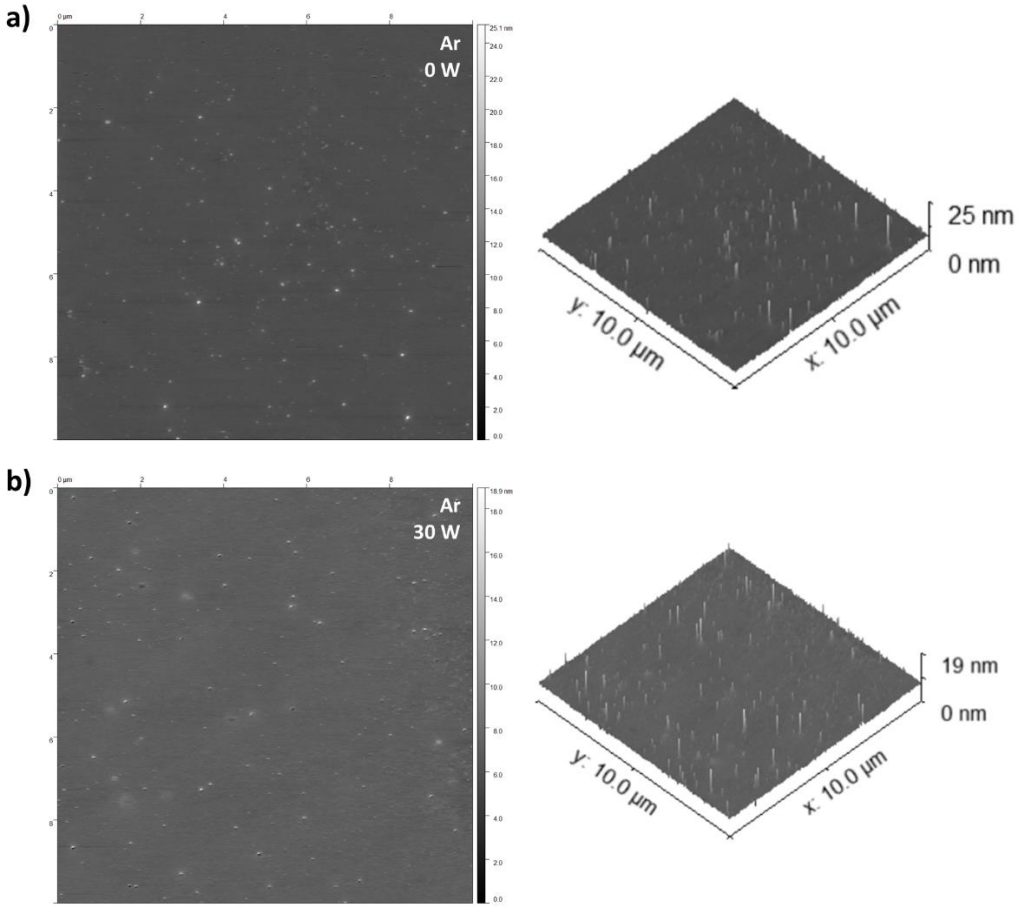

Figure 63. AFM topographical images in 2D and 3D of the synthesized gold nanoparticles with a 10 min argon plasma jet exposure at a) 0 W, and b) 30 W RF power.

4.4 Implications of dual-frequency plasma configuration on gold nanoparticles production

The characteristics of synthesized gold nanoparticles, particularly their shape and size, are influenced by many factors, among which the choice of process gas employed in the plasma synthesis. When considering helium as the process gas, a range of effects comes into play, including lower processing temperatures, decreased plasma density, and consequently reduced current density [183]. These factors, even in the absence of additional RF power and when relying only on the micropulse plasma source, lead to the generation of gold nanoparticles characterized by diverse shapes and sizes. While the exact origins of such variation needs further exploration, what remains consistent is the impact of RF coupling. For both helium and argon as process gases, the introduction of RF coupling triggers a noticeable reduction in the intensity of higher wavelength shoulders. This reduction favors the production of spherical nanoparticles and also induces a decrease in nanoparticle size [184], [185]. Interestingly, the rate of nanoparticle production does not exhibit a linear relationship with RF power levels,

aligning with the observation that the processes catalyzing nanoparticle formation come predominantly from the interplay at the plasma-liquid interface, rather than within the plasma itself.

In order to understand such phenomena, we have to consider how the generator coupling may affect the production process. We showed that the coupling of the RF is mainly changing the plasma from a self-propagating regime to a capacitive coupled configuration. When the plasma is coupled with RF, it can influence the movement of charged particles (ions and electrons) within the plasma. The total ion flux into the surrounding liquid remains relatively constant. However, what changes is the way these charges are delivered to the liquid. In the self-propagating regime, the energy release can be more sudden and intense, potentially leading to higher current densities. When RF coupling is introduced, this process becomes more gradual, resulting in a reduction of the current density. This change in the way charges are transferred to the liquid can have a significant impact on the synthesis process. A more gradual release of charges, as induced by RF coupling, could lead to more controlled and stable conditions for the creation of nanoparticles. The sudden release of charges in the self-propagating regime might lead to more unpredictable outcomes, potentially causing agglomeration or uneven particle growth. In contrast, the more controlled release in the capacitive coupled configuration could provide greater precision and control over the synthesis process, resulting in nanoparticles with more uniform sizes and characteristics.

4.5 Conclusions

In conclusion, this chapter is an investigation of an alternative plasma setup configuration involving a dual-frequency source, specifically an alumina tube coupled to both a micropulse power supply and an additional RF generator. The central focus remained the investigation of the effects of this unique plasma configuration on the synthesis of gold nanoparticles. A systematic approach was adopted to evaluate the impact of incorporating dual-frequency capabilities on the nanoparticle production process.

This study started by characterizing the dual-frequency atmospheric pressure plasma jet (DF-APPJ), in order to understanding how the plasma's behavior changes with the choice of process gas and the application of RF power. Through detailed optical emission spectroscopy (OES) analysis, we presented the differences in the plasma's behavior when employing helium and argon as process gases. The emission spectra, gas temperatures, and charge collection behavior highlighted how RF coupling transformed the plasma from a self-propagating mode to a capacitive coupled configuration. This shift was accompanied by variations in emission intensity and temperature, affecting the plasma's dynamics.

Focusing on gold nanoparticle synthesis, our study provided valuable insights into the impact of helium and argon as process gases coupled with RF power on the nanoparticles' characteristics. UV-vis spectrophotometry analysis revealed that the addition of RF power induced significant changes in absorbance spectra, with blue shifts in maximum plasmon band wavelengths and alterations in intensity. SEM and AFM micrographs confirmed these findings, displaying pronounced variations in nanoparticle size and shape under different conditions. The results particularly emphasized that the incorporation of RF power led to the formation of smaller nanoparticles, ultimately attributed to the modulation of plasma behavior and the dynamics of charge transfer to the liquid phase.

Furthermore, the relationship between RF power, process gas choice, and nanoparticle properties was depicted. The observations found that the dual-frequency configuration and the introduction of RF power had a substantial influence on nanoparticle synthesis, primarily by shifting the plasma's behavior towards more controlled and gradual energy release to the liquid. This control not only contributed to the production of nanoparticles with uniform sizes but also highlighted the potential for tuning their properties based on the process parameters.

Conclusions and Perspectives

Conclusions

The convergence of nanotechnology and plasma science presents an exciting avenue for the controlled synthesis and manipulation of nanomaterials with tailored properties. The journey through the chapters of this study has unveiled a comprehensive exploration of plasma-assisted synthesis of metallic nanoparticles, particularly silver and gold nanoparticles. In this concluding section, we reflect on the key findings, their implications, and the potential future directions that emerge from this thesis.

The historical timeline revealed the pivotal contributions of visionaries such as Richard Zsigmondy, Richard Feynman, and Norio Taniguchi. The emergence of metallic nanoparticles as versatile building blocks for various applications was emphasized, driven by their unique properties arising from their nanoscale dimensions. The synthesis of these nanoparticles, a critical aspect of nanotechnology, was highlighted, underscoring the significance of understanding and controlling their properties.

The first part of this thesis was dedicated to the study and characterization of nanoparticle synthesis using a helium atmospheric pressure plasma jet composed of an asymmetric borosilicate glass source and a micropulse power supply. The production of reactive species in the plasma generation phase and their influence on the physicochemical characteristics of the liquid was examined. Optical characterization of the discharge allowed us to identify the main excited species produced in the plasma jet (OH, N_2, N_2^+, and He), associated with molecular emission bands and atomic emission lines, with a predominance of molecular emission bands. We were also able to track the evolution of these species in the plasma jet over a length of 6 mm and noticed two different intensity trends: The first to OH (308 nm) and He (706 nm), where both species exhibited high emission intensities at the tube's exit, which then gradually decreased along the plasma jet. This suggested that the discharge loses energy as it moves away from the tube exit, explaining the decrease in emissions. The second trend was observed for N_2 (337 nm) and N_2^+ (391 nm) profiles where their intensities increased from the tube's exit, reach their maximum at Y= 3 mm of distance from the exit, and then progressively decreased along the jet. This phenomenon can be attributed to the mixture of plasma gas and the surrounding atmospheric air. At the exit of the discharge tube, the existence of air was minimal, which caused a decrease in emissions of these spectral bands. However, as distance increased from the exit, the influx of air into the plasma grew stronger, causing emissions to rise. Subsequently, the volume of air within the mixture reached a point where it became significant enough to impede the further propagation of the plasma, as evidenced by the reduction in emissions.

After the characterization of the plasma jet, particularly during interaction with a liquid surface, we turned our attention to the evolution of long-lived reactive species concentrations generated in the liquid after plasma treatment. The results showed that the concentration of H_2O_2 increased with treatment time.

This part was divided into two separate sections. In the first section, we were interested in investigating the synthesis of silver nanoparticles using the helium atmospheric pressure plasma jet characterized previously. The method involved exposing an aqueous silver salts solution containing silver nitrate and citrate to the plasma discharge for a specific duration while maintaining the plasma's operating conditions. The color of the solution changed to yellow during exposure, indicating silver nanoparticle formation. The UV-vis absorbance spectra showed a plasmon resonance band in the 400 - 450 nm range which is specific for silver nanoparticles. The composition of the synthesized nanoparticles was analyzed using Scanning Electron Microscopy (SEM) and Energy-Dispersive X-ray Spectroscopy (EDX). Silver was identified as a major element in the nanoparticles, confirming their formation. Our study continued by tuning the synthesis process and investigating the effect of different parameters that can influence the synthesis process:

- *Effect of plasma interaction duration* - By varying exposure times from 0 to 10 minutes, it was observed that a 5-minute exposure duration was optimal for nanoparticle synthesis. Longer exposure durations resulted in higher nanoparticle concentrations without affecting their shape. And beyond beyond a 7-minute duration, the solution exhibited a reduction in volume, attributed to the partial evaporation caused by an increase of temperature generated during plasma exposure.

- *Effect of metal precursor concentration* - The concentration of silver nitrate ($AgNO_3$) as a precursor was varied from 1 mM to 5 mM while maintaining a constant citrate concentration at 3 mM and after 5 minutes of plasma discharge. Increasing the silver nitrate concentration led to broader absorption bands in UV-vis spectra and a shoulder band at higher wavelengths, indicating larger nanoparticle sizes. Deconvolution of the spectra revealed multiple plasmon bands, suggesting the presence of nanoparticles with varying sizes and shapes.

- *Effect of capping agent concentration* - Trisodium citrate dihydrate was used as a capping agent to stabilize and control the nanoparticle synthesis process. Its concentration was varied from 0.05 mM to 6 mM while maintaining the silver nitrate concentration at 1 mM and with a treatment duration of 5 minutes. Higher concentrations of trisodium citrate dihydrate led to darker solution colors and increased UV-vis intensity due to the formation of more nanoparticles. TEM analysis showed that low citrate concentrations resulted in well-dispersed nanoparticles, while

higher concentrations caused agglomeration likely caused by particle collisions and subsequent agglomeration due to the increased number of nanoparticles in the solution.

It was ultimately concluded that achieving uniformly spherical silver nanoparticles, characterized by an average diameter of 13 ± 2 nm, hinged upon establishing an optimal ratio between silver nitrate and citrate concentrations. This optimal ratio was found to be 1 mM for silver nitrate and 0.1 mM for citrate. A plasma treatment duration of 5 minutes was identified as the optimal timeframe for generating a substantial yield of nanoparticles.

In the second section, our study continued with the synthesis of gold nanoparticles. Same as with the silver, the method involved exposing an aqueous gold salts solution containing Chloroauric acid and PVP to the plasma discharge for 5 min while maintaining the plasma's operating conditions fix. The color of the solution changed to purple/red during exposure, indicating gold nanoparticle formation. The UV-vis absorbance spectra showed a plasmon resonance band in the 500 - 550 nm range which is specific for gold nanoparticles. X-ray diffraction (XRD) analysis was employed to characterize the synthesized nanoparticles. The resulting XRD pattern demonstrates the formation of crystalline gold nanoparticles, confirming their purity and identity. Our study continued by exploring the impact of various parameters on gold nanoparticles synthesis:

- *Effect of plasma interaction duration* - By varying exposure times from 0 to 15 minutes, it was observed that a 5-minute exposure duration yielded optimal results for nanoparticle synthesis. An increase in interaction duration resulted in higher absorption band intensity, indicating a higher nanoparticle concentration. At the 15-minute mark, the highest nanoparticle concentration was achieved, although the solution experienced slight evaporation due to the generated high temperature. The normalized absorbance spectra demonstrated evolving nanoparticle sizes and some agglomeration with extended plasma exposure times. However, symmetry and narrowness in the plasmon bands at 3 and 5 minutes suggested uniformity in size and shape.

- *Effect of metal precursor concentration* - The concentration of chloroauric acid ($HAuCl_4$) as a precursor was varied from 0.1 mM to 1.5 mM while maintaining a constant PVP concentration at 0.05 mM and after 5 minutes of plasma discharge. As $HAuCl_4$ concentration increased, a red shift in the plasmon band position was noted from 536 nm to 525 nm, indicating larger nanoparticle sizes at high $HAuCl_4$ concentrations. The uniformity of the Au nanoparticles was assessed using the full width at half maximum (FWHM) of the absorption spectra. The concentration of 0.1 mM ex-

hibited the most symmetric and narrowest absorbance band, signifying reduced polydispersity and agglomeration. Visualizing the formed nanoparticles with TEM analysis reinforced this analysis.

- *Effect of capping agent concentration* - Polyvinylpyrrolidone (PVP) was used as a capping agent to stabilize and control the nanoparticle synthesis process. Its concentration was varied from 0 mM (as to no PVP was used during the synthesis process) to 0.1 mM maintaining 0.1 mM concentration of the gold precursor and a treatment duration of 5 minutes. The role of PVP became evident, as samples without PVP exhibited distinct absorbance bands indicative of larger particles and extensive agglomeration. The TEM analysis confirmed this uncontrolled nucleation and growth. As PVP concentration increased, a blue shift in the plasmon band and changes in nanoparticle morphology were observed. The addition of PVP reduced aggregation, yielding well-separated nanoparticles until a concentration threshold was reached. An optimal PVP concentration of 0.05 mM resulted in consistent spherical, well-dispersed nanoparticles. Dynamic light scattering (DLS) analysis further validated the nanoparticle size distribution results.

It was ultimately concluded that achieving uniformly spherical gold nanoparticles, characterized by an average diameter of 13 ± 4 nm, hinged upon establishing an optimal ratio between chloroauric acid and PVP concentrations. This optimal ratio was found to be 0.1 mM for chloroauric acid and 0.05 mM for PVP. A plasma treatment duration of 5 minutes was identified as the optimal timeframe for generating a substantial yield of nanoparticles.

This study showed the importance of optimizing parameters to achieve desired nanoparticle properties for specific applications. The interaction between plasma discharge duration, precursor, and capping agent played a crucial role in controlling nanoparticle size, shape, and distribution. Our results for silver and gold synthesis were compared with literature in terms of the methods employed, the products used, treatment duration, nanoparticles morphology and agglomeration status, highliting the efficiency and wuality of our plasma-based approach.

The second part of this thesis was dedicated to the study and characterization of gold nanoparticles synthesis using a dual-frequency atmospheric pressure plasma jet composed of an alumina tube connected to both micropulse power supply and an additional RF generator with variation of the process gases used. The main objective of this part revolved around deciphering the impact of process gas selection (helium or argon) and radiofrequency (RF) power application on plasma dynamics and their effects on nanoparticle formation. The study began by

characterizing the dual-frequency atmospheric pressure plasma jet (DF-APPJ) configuration adopted in our study. The setup maintained a constant geometric configuration, micropulse APPJ input parameters, and gas flow rates. Our primary focus was to investigate the influence of process gas and RF power on the plasma jet's behavior. The optical emission spectroscopy (OES) analysis results showed the differences in emission spectra between helium and argon plasmas. The analysis included spectral features, rotational temperature, vibrational temperature, and emission intensity trends of He and Ar lines with the variation of RF power levels. The introduction of RF power displayed notable effects on emission intensities, with argon showing consistent increases. The emission spectra, gas temperatures, and charge collection behavior highlighted how RF coupling transformed the plasma from a self-propagating mode to a capacitive coupled configuration. This shift was accompanied by variations in emission intensity and temperature, affecting the plasma's dynamics.

The impact of helium as process gas and RF power levels on gold nanoparticle synthesis was then explored. Employing 0.1 mM $HAuCl_4$ and 0.05 mM PVP concentrations as established in earlier chapters, we systematically explored different RF power levels varied from 0 W (as no RF power was added) to 30 W and plasma exposure durations (10 min and 20 min). UV-vis spectrophotometry revealed spectral changes indicating shifts in nanoparticle characteristics, with blue shifts in absorbance spectra and alterations in intensity due to the addition of RF power and change in the plasma exposure durations. The addition of RF power demonstrated a role in reducing nanoparticle size, yielding a narrowing of absorbance bands. This was substantiated through SEM and AFM imaging, which visually confirmed the size reduction.

The impact of argon as process gas and RF power levels on gold nanoparticle synthesis was also explored. Employing the same precursor and capping agent concentrations, we conducted a similar analysis, systematically varying RF power levels and plasma exposure durations. UV-vis spectrophotometry indicated spectral shifts, corroborated by SEM and AFM micrographs. These results confirmed the role of RF power in inducing a reduction in nanoparticle size, consistent with spectral blue shifts.

The controlled and gradual release of energy induced by RF coupling emerged as a pivotal factor influencing nanoparticle properties, offering enhanced precision in shaping both nanoparticle size and morphology. The intricate interplay between plasma behavior, process gases, and RF power revealed non-linear relationships and intricate dynamics. Through the transition from self-propagating to capacitive coupled configurations, induced by the introduction of RF coupling, a regime of controlled and stable conditions for nanoparticle synthesis was established. This transition manifested in a notable reduction in the size of gold nanoparticles.

These findings highlighted that the dual-frequency configuration, in conjunction with the incorporation of RF power and the choice of process gas, presented a versatile avenue for tailoring nanoparticle characteristics based on the modulation of key process parameters.

These findings lay the foundation for controlled and application-specific synthesis strategies in the field of nanotechnology.

Perspectives

The results presented in this thesis demonstrate the feasibility of utilizing an atmospheric pressure plasma jet for the synthesis of metallic nanoparticles, with the added capability of tuning their morphology through specific processing parameter adjustments. Silver and gold nanoparticles, known for their widespread applications, have been the focus of this study. Although this thesis did not focus on a specific application for the synthesized nanoparticles, it laid the groundwork for understanding how processing parameters can be fine-tuned to tailor nanoparticles for specific applications that demand distinct shapes and sizes. Our approach aims to pave the way for practical utilization:

- **Antibacterial activity of silver nanoparticles**

To explore the potential applications of the synthesized nanoparticles, preliminary tests were conducted to assess their usability. In particular, the antibacterial activity of silver nanoparticles was examined. This particular property of silver nanoparticles is well-documented in the literature [186] [187] [188] [189]. It is associated with electronic effects arising from alterations in the local electronic configurations of their surfaces, which result from their reduced dimensions. These effects are believed to play a role in augmenting the surface reactivity of silver nanoparticles.

In this section, two strains of bacteria, *Escherichia coli* and *Staphylococcus aureus*, representing gram-negative and gram-positive strains respectively, were chosen as test subjects. The antibacterial activity and mechanism of action of the silver nanoparticles were investigated by analyzing the growth of bacterial cells following treatment with nanoparticles. The growth curves of *E. coli* and *S. aureus* mixed with silver nanoparticles synthesized with a helium atmospheric pressure plasma jet at an input power supply current of 8 A, a frequency at 25 kHz, gas flow rate of 3 L.min^{-1}, and the distance between the exit of the tube and the solution is 6 mm, were shown in Figure 64. Optical densities of the control and solutions containing different concentrations of silver nanoparticles comprising 0.84, 1.68, 3.37, 6.75, 13.5, 27, 54, and 108 µg/ml were measured at 600 nm every 30 min for both bacteria strains. To calculate the silver concentrations in the solution, we considered that the entire quantity of silver nitrate was reduced during the plasma treatment. It is shown that for the two strains of bacteria, when the concentration of silver nanoparticles rises, the optical density of the growth curve decreases in intensity and also initiates after the timeframe of the control curve, where no silver nanoparticles were added. This decrease can be attributed to the reduced growth of bacterial cells. When exposed to 108, 54, and 27 µg/ml, *E. coli* did not show any growth. For 13.5 µg/ml of silver nanoparticles, the delay in bacterial growth was obvious

compared to the control curve. Now for *S. aureus*, silver nanoparticles at 108 µg/ml was found to be effective as there was visibly no bacterial growth. When the concentration of silver nanoparticles decreased, the curves did show growth but are delayed in comparison to the control curve. With concentrations lower than 6.75 µg/ml, silver nanoparticles didn't exert any antibacterial effect on *S. aureus*.

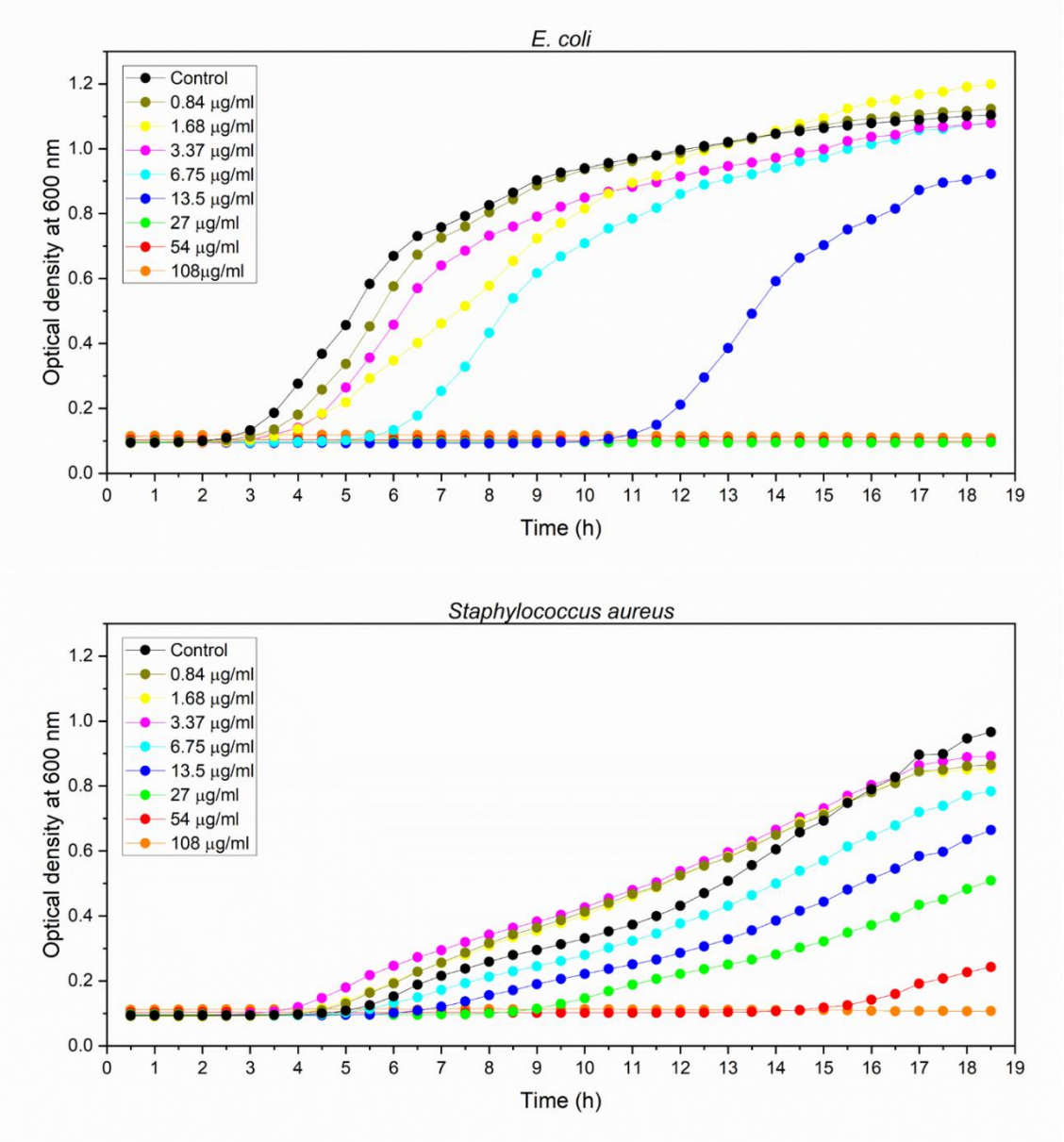

Figure 64. Growth curves of (top) E. coli and (bottom) Staphylococcus aureus cells exposed to different concentrations of silver nanoparticles synthesized by plasma.

It is important to emphasize that while these preliminary tests provide a valuable idea of the potential applications, they represent only the initial step. To fully realize the capabilities of these nanoparticles in different practical contexts, more in-depth investigations are required. The complex interactions between nanoparticles and biological systems demand extensive exploration, including further studies on the mechanisms of nanoparticle-bacteria interaction, potential toxicity, and long-term effects.

- **Anti-Stokes excitation enhancement**

By the action of an atmospheric pressure plasma jet, metallic nanoparticles were synthesized directly on the surface of inorganic particles. That allowed us to explore another interesting application of the metallic nanoparticles produced. The enhancement of anti-stokes excitation of trivalent neodymium ions (Nd^{3+}) in crystalline particles by decorating them with metallic nanoparticles (Figure 65). In these TEM micrographs, it is observed that spherical silver and gold nanoparticles were deposited on the surface of the particles. The silver nanoparticles have an average diameter of 5 nm and the gold nanoparticles have an average diameter of 13 nm. The study used inherent heating through laser light interaction with metallic nanoparticles (Ag or Au) on submicrometric $Y_{1-x}Nd_xAl_3(BO_3)_4$ (x = 0.10, 0.20, and 1.00) particles to enhance anti-Stokes excitation at 1064 nm. Significant enhancements, surpassing undecorated particles, demonstrate the technique's potential. The primary interaction revolves around the conversion of light into heat through the absorption of excitation light by the vibrational transitions of MNPs. Consequently, this raises the temperature of the dielectric particles, subsequently influencing several temperature-dependent processes occurring within the material. The anti-Stokes excitation of Nd^{3+} at 1064 nm initiates through two temperature-dependent processes: nonresonant GSA ($^4I_{9/2} \rightarrow {}^4F_{3/2}$) and resonant ESA ($^4I_{11/2} \rightarrow {}^4F_{3/2}$), facilitated by the population of the $^4I_{11/2}$ state via thermal coupling with the ground state ($^4I_{9/2}$). Consequently, the further increase in temperature due to the interaction between the excitation beam and MNPs promotes both excitation pathways. As a result, the observed Nd^{3+} transitions exhibit higher PL intensity in Ag and Au decorated $Nd_xY_{1.00-x}Al_3(BO_3)_4$ particles compared to undecorated ones (Figure 66).

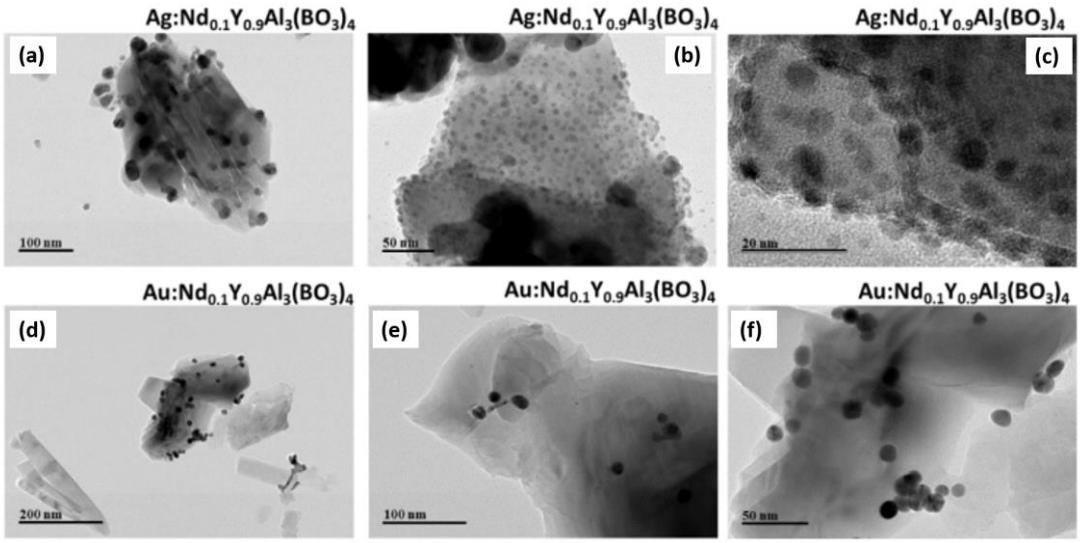

Figure 65. (a-c) TEM of the Ag:$Nd_xY_{1.00-x}Al_3(BO_3)_4$ ($x = 0.1$) and (d-f) TEM of the Au: $Nd_xY_{1.00-x}Al_3(BO_3)_4$ ($x = 0.1$).

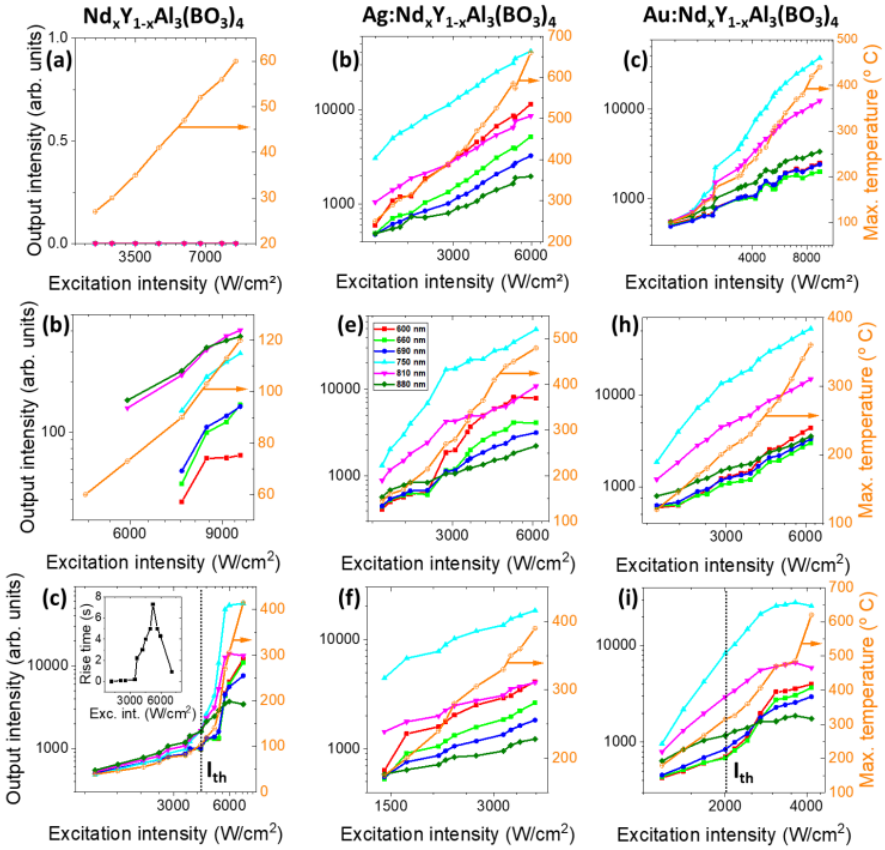

Figure 66. Photoluminescence characterization by the input-output power dependences for the $Nd_xY_{1.00-x}Al_3(BO_3)_4$ powders ($x = 0.10$ (first row), 0.20 (second row), and 1.00 (third row)) without (first column) and with Ag (second column) and Au (third column) metallic nanoparticles on the surfaces of the crystalline particles.

The detailed investigation is presented and published in Optical Materials Journal - Elsevier, DOI: 10.1016/j.omx.2023.100254 [190]. These findings may extend to other luminescent materials, trivalent rare-earth ions, hosting media, and excitation wavelengths.

- **Silver/Gold core-shell nanoparticles**

While this thesis primarily focused on the separate synthesis of silver and gold nanoparticles, it opens the door to an intriguing avenue of research: the synthesis of core-shell silver-gold nanoparticles. Combining these two noble metals within core-shell nanostructures presents an opportunity to fine-tune the localized surface plasmon resonance (LSPR) by controlling not only the size of the core but also the thickness of the external shell [191]. Such bimetallic nanoparticles hold the potential to exhibit unique optical and catalytic properties. Investigating the synthesis and characterization of core-shell silver-gold nanoparticles could represent an exciting future direction for research, offering insights into the synergistic effects and enhanced functionalities achievable through controlled nanoscale engineering. To explore this process, an initial test was conducted, but further characterization is required to confirm its success. High-resolution transmission electron microscopy (HRTEM) was employed to visualize the obtained nanoparticles (Figure 67), the shell does not resemble the corresponding core shape. A spherical shell is formed around a prism core. These initial experiments demonstrated the feasibility of plasma-assisted synthesis and formation of well-defined core-shell bimetallic nanoparticles. Additional comprehensive studies are still needed to provide a more thorough understanding of this research direction.

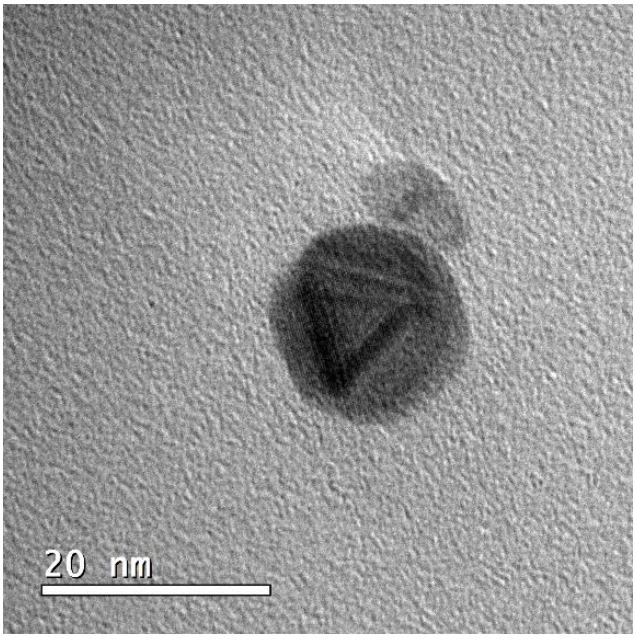

Figure 67. HRTEM images of the nanoparticles obtained.

- **Avenues for future research**

In this thesis, our primary focus was on investigating the chemical parameters of the solution exposed to the plasma, such as exposure time and varying chemical concentrations. However, it is important to acknowledge that we did not delve into the impact of crucial input parameters of the plasma setup, such as the variations in input power supply current, frequency, and gas flow rate. These parameters remained constant throughout the study. Exploring the influence of these plasma input parameters is a significant avenue for future research, as they undoubtedly play a substantial role in nanoparticle synthesis. Variations in these parameters can lead to differences in the generation and concentration of reactive species, which are the key drivers for the reduction of metallic salts in the treated solution.

Additionally, we recognize the potential for further investigation into different precursors and capping agents to expand our repertoire of synthesized nanoparticles. Comparative studies on the selection of precursors and capping agents can shed light on their impact on the properties of the resulting nanoparticles. The stability of the nanoparticles synthesized during this thesis was a concern, and the choice of a different capping agent may offer a solution for prolonging their stability.

Lastly, our thesis did not address the quantification of the produced nanoparticles, indicating the need for future studies to develop methods for separating and quantifying these nanoparticles accurately. These avenues of research hold great promise for advancing our understanding of plasma-based nanoparticle synthesis.

Appendix

Materials and Methods

- **Antibacterial activity of silver nanoparticles**

In order to assess the antibacterial effect of silver nanoparticles, a silver solution of a silver nitrate concentration of 1 mM and 0.1 mM of citrate was prepared and exposed to the helium plasma jet for 5 minutes. Subsequently, 1 mL of the solution was transferred to 1.5 mL tubes and centrifuged for 20 minutes at 14,000 g. The supernatant was gently removed, and the nanoparticles were resuspended in 1 mL of Mueller-Hinton (MH) culture medium. The solutions were diluted at a (1:1) ratio to obtain nanoparticle concentrations ranging from 108 µg/ml to 0.84 µg/ml.

We selected *Escherichia coli* (ATCC 10536) and *Staphylococcus aureus* (ATCC 6538) as model strains. These bacterial strains were cultured in tryptone soy broth (TSB) medium and incubated overnight at 37°C. From these cultures, the strains were streaked for isolation on tryptic soy agar (TSA) plates and incubated overnight at 37°C. The bacteria were washed and diluted in fresh Mueller-Hinton (MH) broth to achieve a final concentration of 105 CFU/mL. Then, 2 µL of bacterial suspension and 200 µL of medium (MH) containing different nanoparticle dilutions were transferred to multi-well plates. For the positive control, wells were prepared by inoculating bacteria without nanoparticles. An uninoculated well was used as a negative control. The plate was sealed, incubated, and read using a microplate reader at an absorbance of 600 nm (BioTeK) for 20 hours, with a reading interval of 30 minutes.

- **Anti-Stokes excitation enhancement**

The $Y_{1-x}Nd_xAl_3(BO_3)_4$ powders were synthesized via the Pechini method. Initially, $Y(NO_3)_3$ at a concentration of 0.48 M and $Nd(NO_3)_3$ at 0.12 M were introduced into 50 mL of ultrapure water. These metal ions were then complexed with citric acid in a 3:1 molar ratio of citric acid to metals (including boron). Following this, $Al(NO_3)_3 \cdot 9H_2O$, diluted in 20 mL of water, was added, and the mixture was heated and stirred at 75°C for 30 minutes. Subsequently, a solution containing boric acid and D-sorbitol, in a mass ratio of 3:2 citric acid to D-sorbitol, was incorporated. The temperature was raised to 100 °C, and the solution was heated for 1 hour to yield a resin. This resin was then subjected to overnight drying in an oven at 120 °C. Lastly, the material underwent heat treatment under an O_2 atmosphere using a heating stage program of 400 °C/24h, 700 °C/24h, and 1100 °C/5min.

Silver decoration involved dispersing 0.1 g of $Y_{1-x}Nd_xAl_3(BO_3)_4$ particles in a 10 mL aqueous solution containing a silver nitrate ($AgNO_3$) concentration of $5x10^{-3}$ M and trisodium citrate concentration of 0.05 M while stirring. The mixture underwent 5 minutes of treatment with the He APPJ, followed by particle isolation through centrifugation at 14500 rpm for 5 minutes.

For gold decoration, 0.1 g of $Nd_xY_{1.00-x}Al_3(BO_3)_4$ particles were dispersed in a 10 mL aqueous solution containing a chloroauric acid ($HAuCl_4$) concentration of 0.1 x 10^{-3} M and Polyvinylpyrrolidone (PVP 40) concentration of 0.05 x 10^{-3} M while stirring. Similar to silver decoration, this mixture also received 5 minutes of He APPJ treatment, followed by particle isolation through centrifugation at 14500 rpm for 5 minutes.

- **Silver/Gold core-shell nanoparticles**

Initially, silver nanoparticles were synthesized after 5 minutes of plasma exposure with helium as process gas (plasma parameters constant as mentioned previously) with 1 mM of silver nitrate and 0.1 of citrate concentrations. 7 ml of the obtained solution was then mixed with 3 ml of an untreated gold salt solution with 0.1 mM of choloauric acid and 0.05 mM of PVP concentrations. And after that, the resulting solution was exposed to the plasma jet for 5 minutes.

Bibliography

[1] A. Gnach, T. Lipinski, A. Bednarkiewicz, J. Rybka, and J. A. Capobianco, "Upconverting nanoparticles: assessing the toxicity," *Chem. Soc. Rev.*, vol. 44, no. 6, pp. 1561–1584, 2015, doi: 10.1039/C4CS00177J.

[2] S. Bayda, M. Adeel, T. Tuccinardi, M. Cordani, and F. Rizzolio, "The History of Nanoscience and Nanotechnology: From Chemical–Physical Applications to Nanomedicine," *Molecules*, vol. 25, no. 1, p. 112, Dec. 2019, doi: 10.3390/molecules25010112.

[3] B. Bhushan, *Springer Handbook of Nanotechnology*. Springer, 2017.

[4] J. Hulla, S. Sahu, and A. Hayes, "Nanotechnology: History and future," *Hum Exp Toxicol*, vol. 34, no. 12, pp. 1318–1321, Dec. 2015, doi: 10.1177/0960327115603588.

[5] N. Taniguchi, "On the basic concept of'nano-technology'," in *Proc. Intl. Conf. Prod. Eng. Tokyo, Part II, 1974*, Japan Society of Precision Engineering, 1974.

[6] A. Rondags, W. Y. Yuen, M. F. Jonkman, and B. Horváth, "Fullerene C $_{60}$ with cytoprotective and cytotoxic potential: prospects as a novel treatment agent in Dermatology?," *Exp Dermatol*, vol. 26, no. 3, pp. 220–224, Mar. 2017, doi: 10.1111/exd.13172.

[7] E. Drexler, *Engines of creation: the coming era of nanotechnology*. Anchor, 1987.

[8] N. K. Tolochko, "History of nanotechnology," *Encyclopedia of Life Support Systems (EOLSS)*, 2009.

[9] "Home | National Nanotechnology Initiative." Accessed: Jul. 03, 2023. [Online]. Available: https://www.nano.gov/

[10] T. A. Saleh, "Nanomaterials: Classification, properties, and environmental toxicities," *Environmental Technology & Innovation*, vol. 20, p. 101067, Nov. 2020, doi: 10.1016/j.eti.2020.101067.

[11] M. Vassal, S. Rebelo, and M. D. L. Pereira, "Metal Oxide Nanoparticles: Evidence of Adverse Effects on the Male Reproductive System," *IJMS*, vol. 22, no. 15, p. 8061, Jul. 2021, doi: 10.3390/ijms22158061.

[12] K. M. Kadish and R. S. Ruoff, *Fullerenes: chemistry, physics, and technology*. John Wiley & Sons, 2000.

[13] B. C. Yadav and R. Kumar, "Structure, properties and applications of fullerenes," *International Journal of Nanotechnology and Applications*, vol. 2, no. 1, pp. 15–24, 2008.

[14] A. K. Geim, "Graphene: Status and Prospects," *Science*, vol. 324, no. 5934, pp. 1530–1534, Jun. 2009, doi: 10.1126/science.1158877.

[15] I. N. Kholmanov *et al.*, "Improved electrical conductivity of graphene films integrated with metal nanowires," *Nano letters*, vol. 12, no. 11, pp. 5679–5683, 2012.

[16] J. Che, T. Cagin, and W. A. Goddard III, "Thermal conductivity of carbon nanotubes," *Nanotechnology*, vol. 11, no. 2, p. 65, 2000.

[17] E. L. Wolf, *Applications of graphene: an overview*. Springer, 2014.

[18] M. M. Telkar, C. V. Rode, R. V. Chaudhari, S. S. Joshi, and A. M. Nalawade, "Shape-controlled preparation and catalytic activity of metal nanoparticles for hydrogenation of

2-butyne-1, 4-diol and styrene oxide," *Applied Catalysis A: General*, vol. 273, no. 1–2, pp. 11–19, 2004.

[19] S. Chen, R. Yuan, Y. Chai, and F. Hu, "Electrochemical sensing of hydrogen peroxide using metal nanoparticles: a review," *Microchimica Acta*, vol. 180, pp. 15–32, 2013.

[20] Y. Wu, M. R. Ali, K. Chen, N. Fang, and M. A. El-Sayed, "Gold nanoparticles in biological optical imaging," *Nano Today*, vol. 24, pp. 120–140, 2019.

[21] T. G. Schaaff and R. L. Whetten, "Giant gold− glutathione cluster compounds: intense optical activity in metal-based transitions," *The Journal of Physical Chemistry B*, vol. 104, no. 12, pp. 2630–2641, 2000.

[22] R. Saravanan, V. K. Gupta, V. Narayanan, and A. Stephen, "Comparative study on photocatalytic activity of ZnO prepared by different methods," *Journal of Molecular Liquids*, vol. 181, pp. 133–141, 2013.

[23] S. Kumar, A. Dhiman, P. Sudhagar, and V. Krishnan, "ZnO-graphene quantum dots heterojunctions for natural sunlight-driven photocatalytic environmental remediation," *Applied Surface Science*, vol. 447, pp. 802–815, 2018.

[24] C. Zhou, Z. Xi, D. J. Stacchiola, and M. Liu, "Application of ultrathin TiO2 layers in solar energy conversion devices," *Energy Science & Engineering*, vol. 10, no. 5, pp. 1614–1629, 2022.

[25] D. Bederak, D. N. Dirin, N. Sukharevska, J. Momand, M. V. Kovalenko, and M. A. Loi, "S-Rich PbS quantum dots: A promising p-type material for optoelectronic devices," *Chemistry of Materials*, vol. 33, no. 1, pp. 320–326, 2020.

[26] A. Nazarov, J. P. Colinge, F. Balestra, J.-P. Raskin, F. Gamiz, and V. S. Lysenko, *Semiconductor-on-insulator materials for nanoelectronics applications*. Springer, 2011.

[27] C. Yuan *et al.*, "Polymer/molecular semiconductor all-organic composites for high-temperature dielectric energy storage," *Nature communications*, vol. 11, no. 1, p. 3919, 2020.

[28] V. Mody, R. Siwale, A. Singh, and H. Mody, "Introduction to metallic nanoparticles," *J Pharm Bioall Sci*, vol. 2, no. 4, p. 282, 2010, doi: 10.4103/0975-7406.72127.

[29] S. Gharpure, A. Akash, and B. Ankamwar, "A Review on Antimicrobial Properties of Metal Nanoparticles," *j nanosci nanotechnol*, vol. 20, no. 6, pp. 3303–3339, Jun. 2020, doi: 10.1166/jnn.2020.17677.

[30] G. Cao, *Nanostructures & nanomaterials: synthesis, properties & applications*. Imperial college press, 2004.

[31] Z.-Y. Zhou, N. Tian, J.-T. Li, I. Broadwell, and S.-G. Sun, "Nanomaterials of high surface energy with exceptional properties in catalysis and energy storage," *Chemical Society Reviews*, vol. 40, no. 7, pp. 4167–4185, 2011.

[32] M. A. Garcia, "Surface plasmons in metallic nanoparticles: fundamentals and applications," *J. Phys. D: Appl. Phys.*, vol. 45, no. 38, p. 389501, Sep. 2012, doi: 10.1088/0022-3727/45/38/389501.

[33] "drinking-cup | British Museum," The British Museum. Accessed: Jul. 03, 2023. [Online]. Available: https://www.britishmuseum.org/collection/object/H_1958-1202-1

[34] N. Venkatesh, "Metallic Nanoparticle: A Review," *BJSTR*, vol. 4, no. 2, Apr. 2018, doi: 10.26717/BJSTR.2018.04.0001011.

[35] S. Peiris, J. McMurtrie, and H.-Y. Zhu, "Metal nanoparticle photocatalysts: emerging processes for green organic synthesis," *Catal. Sci. Technol.*, vol. 6, no. 2, pp. 320–338, 2016, doi: 10.1039/C5CY02048D.

[36] nanoComposix, "Plasmonics," nanoComposix. Accessed: Jul. 03, 2023. [Online]. Available: https://nanocomposix.com/pages/plasmonics

[37] M. S. Rodrigues *et al.*, "Optimization of nanocomposite Au/TiO2 thin films towards LSPR optical-sensing," *Applied surface science*, vol. 438, pp. 74–83, 2018.

[38] T. P. Araujo, J. Quiroz, E. C. Barbosa, and P. H. Camargo, "Understanding plasmonic catalysis with controlled nanomaterials based on catalytic and plasmonic metals," *Current Opinion in Colloid & Interface Science*, vol. 39, pp. 110–122, 2019.

[39] Y. Zhan *et al.*, "Phase-controlled synthesis of molybdenum oxide nanoparticles for surface enhanced Raman scattering and photothermal therapy," *Nanoscale*, vol. 10, no. 13, pp. 5997–6004, 2018.

[40] Y. Jin, "Multifunctional compact hybrid Au nanoshells: a new generation of nanoplasmonic probes for biosensing, imaging, and controlled release," *Accounts of chemical research*, vol. 47, no. 1, pp. 138–148, 2014.

[41] "Silver nanoparticles different sizes | Sigma-Aldrich." Accessed: Jul. 03, 2023. [Online]. Available: https://www.sigmaaldrich.com/FR/fr/search/silver-nanoparticles-different-sizes?focus=products&page=1&perpage=30&sort=relevance&term=silver%20nanoparticles%20different%20sizes&type=product

[42] L. A. Austin, M. A. Mackey, E. C. Dreaden, and M. A. El-Sayed, "The optical, photothermal, and facile surface chemical properties of gold and silver nanoparticles in biodiagnostics, therapy, and drug delivery," *Archives of toxicology*, vol. 88, pp. 1391–1417, 2014.

[43] L. Castilla-Amorós, D. Stoian, J. R. Pankhurst, S. B. Varandili, and R. Buonsanti, "Exploring the chemical reactivity of gallium liquid metal nanoparticles in galvanic replacement," *Journal of the American Chemical Society*, vol. 142, no. 45, pp. 19283–19290, 2020.

[44] D. Greshnykh, A. Fromsdorf, H. Weller, and C. Klinke, "On the electric conductivity of highly ordered monolayers of monodisperse metal nanoparticles," *Nano Letters*, vol. 9, no. 1, pp. 473–478, 2009.

[45] H. W. Tan, J. An, C. K. Chua, and T. Tran, "Metallic nanoparticle inks for 3D printing of electronics," *Advanced Electronic Materials*, vol. 5, no. 5, p. 1800831, 2019.

[46] J.-T. Lue, "A review of characterization and physical property studies of metallic nanoparticles," *Journal of physics and chemistry of solids*, vol. 62, no. 9–10, pp. 1599–1612, 2001.

[47] I. Aruna, B. R. Mehta, L. K. Malhotra, and S. M. Shivaprasad, "Size dependence of core and valence binding energies in Pd nanoparticles: Interplay of quantum confinement and coordination reduction," *Journal of Applied Physics*, vol. 104, no. 6, 2008.

[48] S. Gharpure, A. Akash, and B. Ankamwar, "A Review on Antimicrobial Properties of Metal Nanoparticles," *j nanosci nanotechnol*, vol. 20, no. 6, pp. 3303–3339, Jun. 2020, doi: 10.1166/jnn.2020.17677.

[49] W.-R. Li, X.-B. Xie, Q.-S. Shi, S.-S. Duan, Y.-S. Ouyang, and Y.-B. Chen, "Antibacterial effect of silver nanoparticles on Staphylococcus aureus," *Biometals*, vol. 24, no. 1, pp. 135–141, Feb. 2011, doi: 10.1007/s10534-010-9381-6.

[50] I. Sondi and B. Salopek-Sondi, "Silver nanoparticles as antimicrobial agent: a case study on E. coli as a model for Gram-negative bacteria," *Journal of Colloid and Interface Science*, vol. 275, no. 1, pp. 177–182, Jul. 2004, doi: 10.1016/j.jcis.2004.02.012.

[51] M. R. Bindhu and M. Umadevi, "Antibacterial activities of green synthesized gold nanoparticles," *Materials Letters*, vol. 120, pp. 122–125, Apr. 2014, doi: 10.1016/j.matlet.2014.01.108.

[52] E. Piktel *et al.*, "Varied-shaped gold nanoparticles with nanogram killing efficiency as potential antimicrobial surface coatings for the medical devices," *Sci Rep*, vol. 11, no. 1, Art. no. 1, Jun. 2021, doi: 10.1038/s41598-021-91847-3.

[53] S. Sathiyaraj *et al.*, "Biosynthesis, characterization, and antibacterial activity of gold nanoparticles," *Journal of Infection and Public Health*, vol. 14, no. 12, pp. 1842–1847, Dec. 2021, doi: 10.1016/j.jiph.2021.10.007.

[54] S. Dasari Tp and Z. Y, "Antibacterial Activity and Cytotoxicity of Gold (I) and (III) Ions and Gold Nanoparticles," *Biochem Pharmacol (Los Angel)*, vol. 04, no. 06, 2015, doi: 10.4172/2167-0501.1000199.

[55] J. N. Payne *et al.*, "Novel Synthesis of Kanamycin Conjugated Gold Nanoparticles with Potent Antibacterial Activity," *Front. Microbiol.*, vol. 7, May 2016, doi: 10.3389/fmicb.2016.00607.

[56] A.-C. Burdușel, O. Gherasim, A. M. Grumezescu, L. Mogoantă, A. Ficai, and E. Andronescu, "Biomedical Applications of Silver Nanoparticles: An Up-to-Date Overview," *Nanomaterials*, vol. 8, no. 9, p. 681, Aug. 2018, doi: 10.3390/nano8090681.

[57] N. Elahi, M. Kamali, and M. H. Baghersad, "Recent biomedical applications of gold nanoparticles: A review," *Talanta*, vol. 184, pp. 537–556, Jul. 2018, doi: 10.1016/j.talanta.2018.02.088.

[58] V. K. Vidhu and D. Philip, "Catalytic degradation of organic dyes using biosynthesized silver nanoparticles," *Micron*, vol. 56, pp. 54–62, Jan. 2014, doi: 10.1016/j.micron.2013.10.006.

[59] Z.-J. Jiang, C.-Y. Liu, and L.-W. Sun, "Catalytic Properties of Silver Nanoparticles Supported on Silica Spheres," *J. Phys. Chem. B*, vol. 109, no. 5, pp. 1730–1735, Feb. 2005, doi: 10.1021/jp046032g.

[60] S. Gao, Z. Zhang, K. Liu, and B. Dong, "Direct evidence of plasmonic enhancement on catalytic reduction of 4-nitrophenol over silver nanoparticles supported on flexible fibrous networks," *Applied Catalysis B: Environmental*, vol. 188, pp. 245–252, Jul. 2016, doi: 10.1016/j.apcatb.2016.01.074.

[61] G. J. Hutchings and J. K. Edwards, "Application of Gold Nanoparticles in Catalysis," in *Frontiers of Nanoscience*, vol. 3, Elsevier, 2012, pp. 249–293. doi: 10.1016/B978-0-08-096357-0.00001-7.

[62] A. Corma and H. Garcia, "Supported gold nanoparticles as catalysts for organic reactions," *Chem. Soc. Rev.*, vol. 37, no. 9, p. 2096, 2008, doi: 10.1039/b707314n.

[63] D. T. Thompson, "Using gold nanoparticles for catalysis," *Nano Today*, vol. 2, no. 4, pp. 40–43, Aug. 2007, doi: 10.1016/S1748-0132(07)70116-0.

[64] P. T. Bishop *et al.*, "Printed gold for electronic applications," *Gold Bull*, vol. 43, no. 3, pp. 181–188, Sep. 2010, doi: 10.1007/BF03214985.

[65] S. Park, D. Seo, and J. Lee, "Preparation of Pb-free silver paste containing nanoparticles," *Colloids and Surfaces A: Physicochemical and Engineering Aspects*, vol. 313–314, pp. 197–201, Feb. 2008, doi: 10.1016/j.colsurfa.2007.04.092.

[66] D. Chen, X. Qiao, X. Qiu, and J. Chen, "Synthesis and electrical properties of uniform silver nanoparticles for electronic applications," *J Mater Sci*, vol. 44, no. 4, pp. 1076–1081, Feb. 2009, doi: 10.1007/s10853-008-3204-y.

[67] A. Bouafia *et al.*, "The Recent Progress on Silver Nanoparticles: Synthesis and Electronic Applications," *Nanomaterials*, vol. 11, no. 9, p. 2318, Sep. 2021, doi: 10.3390/nano11092318.

[68] K.-S. Lee and M. A. El-Sayed, "Gold and Silver Nanoparticles in Sensing and Imaging: Sensitivity of Plasmon Response to Size, Shape, and Metal Composition," *J. Phys. Chem. B*, vol. 110, no. 39, pp. 19220–19225, Oct. 2006, doi: 10.1021/jp062536y.

[69] M. Huston, M. DeBella, M. DiBella, and A. Gupta, "Green Synthesis of Nanomaterials," *Nanomaterials*, vol. 11, no. 8, p. 2130, Aug. 2021, doi: 10.3390/nano11082130.

[70] M. K. Corbierre, J. Beerens, and R. B. Lennox, "Gold Nanoparticles Generated by Electron Beam Lithography of Gold(I)−Thiolate Thin Films," *Chem. Mater.*, vol. 17, no. 23, pp. 5774–5779, Nov. 2005, doi: 10.1021/cm051085b.

[71] N. Baig, I. Kammakakam, and W. Falath, "Nanomaterials: a review of synthesis methods, properties, recent progress, and challenges," *Mater. Adv.*, vol. 2, no. 6, pp. 1821–1871, 2021, doi: 10.1039/D0MA00807A.

[72] T. Prasad Yadav, R. Manohar Yadav, and D. Pratap Singh, "Mechanical Milling: a Top Down Approach for the Synthesis of Nanomaterials and Nanocomposites," *NN*, vol. 2, no. 3, pp. 22–48, Aug. 2012, doi: 10.5923/j.nn.20120203.01.

[73] C. Daruich De Souza, B. Ribeiro Nogueira, and M. E. C. M. Rostelato, "Review of the methodologies used in the synthesis gold nanoparticles by chemical reduction," *Journal of Alloys and Compounds*, vol. 798, pp. 714–740, Aug. 2019, doi: 10.1016/j.jallcom.2019.05.153.

[74] S. V. Kumar and S. Ganesan, "Preparation and characterization of gold nanoparticles with different capping agents," *International Journal of Green Nanotechnology*, vol. 3, no. 1, pp. 47–55, 2011.

[75] C. Daruich De Souza, B. Ribeiro Nogueira, and M. E. C. M. Rostelato, "Review of the methodologies used in the synthesis gold nanoparticles by chemical reduction," *Journal of Alloys and Compounds*, vol. 798, pp. 714–740, Aug. 2019, doi: 10.1016/j.jallcom.2019.05.153.

[76] M. T. H. Aunkor, I. M. Mahbubul, R. Saidur, and H. S. C. Metselaar, "The green reduction of graphene oxide," *Rsc Advances*, vol. 6, no. 33, pp. 27807–27828, 2016.

[77] A. I. Usman, A. Abdul Aziz, and O. Abu Noqta, "APPLICATION OF GREEN SYNTHESIS OF GOLD NANOPARTICLES: A REVIEW," *Jurnal Teknologi*, vol. 81, no. 1, Dec. 2018, doi: 10.11113/jt.v81.11409.

[78] S. Ahmad *et al.*, "Green nanotechnology: a review on green synthesis of silver nanoparticles — an ecofriendly approach," *IJN*, vol. Volume 14, pp. 5087–5107, Jul. 2019, doi: 10.2147/IJN.S200254.

[79] N. Rajput, "METHODS OF PREPARATION OF NANOPARTICLES – A REVIEW," vol. 7, no. 4.

[80] M. Niederberger, "Nonaqueous sol–gel routes to metal oxide nanoparticles," *Accounts of chemical research*, vol. 40, no. 9, pp. 793–800, 2007.

[81] D. Bokov *et al.*, "Nanomaterial by Sol-Gel Method: Synthesis and Application," *Advances in Materials Science and Engineering*, vol. 2021, pp. 1–21, Dec. 2021, doi: 10.1155/2021/5102014.

[82] K. C. Sabat, P. Rajput, R. K. Paramguru, B. Bhoi, and B. K. Mishra, "Reduction of oxide minerals by hydrogen plasma: an overview," *Plasma Chemistry and Plasma Processing*, vol. 34, pp. 1–23, 2014.

[83] M. Skiba, A. Pivovarov, A. Makarova, and V. Vorobyova, "Plasma-chemical Synthesis of Silver Nanoparticles in the Presence of Citrate," *ChemJMold*, vol. 13, no. 1, pp. 7–14, Apr. 2018, doi: 10.19261/cjm.2018.475.

[84] S. S. Golazari, M. Khalily, F. Entezami, and P. Xiao, "Perfomance Analysis of the Loop-Shaped Plasma Antenna Under Different Pressure Conditions," in *2018 International Symposium on Networks, Computers and Communications (ISNCC)*, Rome: IEEE, Jun. 2018, pp. 1–4. doi: 10.1109/ISNCC.2018.8530993.

[85] M. Laroussi *et al.*, "Low-Temperature Plasma for Biology, Hygiene, and Medicine: Perspective and Roadmap," *IEEE Transactions on Radiation and Plasma Medical Sciences*, vol. 6, no. 2, pp. 127–157, Feb. 2022, doi: 10.1109/TRPMS.2021.3135118.

[86] H. Conrads and M. Schmidt, "Plasma generation and plasma sources," *Plasma Sources Sci. Technol.*, vol. 9, no. 4, pp. 441–454, Nov. 2000, doi: 10.1088/0963-0252/9/4/301.

[87] M. Domonkos, P. Tichá, J. Trejbal, and P. Demo, "Applications of Cold Atmospheric Pressure Plasma Technology in Medicine, Agriculture and Food Industry," *Applied Sciences*, vol. 11, no. 11, p. 4809, May 2021, doi: 10.3390/app11114809.

[88] J.-L. Delcroix and A. Bers, *Physique des plasmas*, vol. 1. Dunod Paris, 1963.

[89] "LPP - Laboratoire de Physique des Plasmas - UMR 7648 - LPP studies all aspects of plasma physics and technology from space to the laboratory, from theory to experiments." Accessed: Jul. 03, 2023. [Online]. Available: https://www.lpp.polytechnique.fr/Our-research-in-a-few-words

[90] G. Osenga, "Atmospheric Plasma vs Low Pressure Plasma." Accessed: Jul. 03, 2023. [Online]. Available: https://www.thierry-corp.com/plasma-knowledgebase/atmospheric-plasma-vs-low-pressure-plasma

[91] S.-P. Lin *et al.*, "Applications of atmospheric cold plasma in agricultural, medical, and bioprocessing industries," *Appl Microbiol Biotechnol*, vol. 106, no. 23, pp. 7737–7750, Dec. 2022, doi: 10.1007/s00253-022-12252-y.

[92] S. Sato, K. Mori, O. Ariyada, H. Atsushi, and T. Yonezawa, "Synthesis of nanoparticles of silver and platinum by microwave-induced plasma in liquid," *Surface and Coatings Technology*, vol. 206, no. 5, pp. 955–958, Nov. 2011, doi: 10.1016/j.surfcoat.2011.03.110.

[93] F. L. Tabares and I. Junkar, "Cold Plasma Systems and Their Application in Surface Treatments for Medicine," *Molecules*, vol. 26, no. 7, p. 1903, Mar. 2021, doi: 10.3390/molecules26071903.

[94] N. Shirai, S. Uchida, and F. Tochikubo, "Synthesis of metal nanoparticles by dual plasma electrolysis using atmospheric dc glow discharge in contact with liquid," *Jpn. J. Appl. Phys.*, vol. 53, no. 4, p. 046202, Apr. 2014, doi: 10.7567/JJAP.53.046202.

[95] B. R. Locke, M. Sato, P. Sunka, M. R. Hoffmann, and J.-S. Chang, "Electrohydraulic Discharge and Nonthermal Plasma for Water Treatment," *Ind. Eng. Chem. Res.*, vol. 45, no. 3, pp. 882–905, Feb. 2006, doi: 10.1021/ie050981u.

[96] S. N. Zucker *et al.*, "Preferential induction of apoptotic cell death in melanoma cells as compared with normal keratinocytes using a non-thermal plasma torch," *Cancer Biology & Therapy*, vol. 13, no. 13, pp. 1299–1306, Nov. 2012, doi: 10.4161/cbt.21787.

[97] C. Duchesne, S. Banzet, J. Lataillade, A. Rousseau, and N. Frescaline, "Cold atmospheric plasma modulates endothelial nitric oxide synthase signalling and enhances burn wound neovascularisation," *J. Pathol.*, vol. 249, no. 3, pp. 368–380, Nov. 2019, doi: 10.1002/path.5323.

[98] C. Jiang, C. Schaudinn, D. E. Jaramillo, P. Webster, and J. W. Costerton, "*In Vitro* Antimicrobial Effect of a Cold Plasma Jet against *Enterococcus faecalis* Biofilms," *ISRN Dentistry*, vol. 2012, pp. 1–6, Jan. 2012, doi: 10.5402/2012/295736.

[99] P. J. Bruggeman *et al.*, "Plasma–liquid interactions: a review and roadmap," *Plasma Sources Sci. Technol.*, vol. 25, no. 5, p. 053002, Sep. 2016, doi: 10.1088/0963-0252/25/5/053002.

[100] N. K. Kaushik *et al.*, "Biological and medical applications of plasma-activated media, water and solutions," *Biological Chemistry*, vol. 400, no. 1, pp. 39–62, Dec. 2018, doi: 10.1515/hsz-2018-0226.

[101] N. Kaushik *et al.*, "Plasma and Nanomaterials: Fabrication and Biomedical Applications," *Nanomaterials*, vol. 9, no. 1, p. 98, Jan. 2019, doi: 10.3390/nano9010098.

[102] J. Małajowicz, K. Khachatryan, and M. Kozłowska, "Properties of Water Activated with Low-Temperature Plasma in the Context of Microbial Activity," *Beverages*, vol. 8, no. 4, p. 63, Oct. 2022, doi: 10.3390/beverages8040063.

[103] S. Wu *et al.*, "Reactive radical-driven bacterial inactivation by hydrogen-peroxide-enhanced plasma-activated-water," *Eur. Phys. J. Spec. Top.*, vol. 226, no. 13, pp. 2887–2899, Aug. 2017, doi: 10.1140/epjst/e2016-60330-y.

[104] S. Wu *et al.*, "Reactive radical-driven bacterial inactivation by hydrogen-peroxide-enhanced plasma-activated-water," *Eur. Phys. J. Spec. Top.*, vol. 226, no. 13, pp. 2887–2899, Aug. 2017, doi: 10.1140/epjst/e2016-60330-y.

[105] Y. Morabit, M. I. Hasan, R. D. Whalley, E. Robert, M. Modic, and J. L. Walsh, "A review of the gas and liquid phase interactions in low-temperature plasma jets used for biomedical applications," *Eur. Phys. J. D*, vol. 75, no. 1, p. 32, Jan. 2021, doi: 10.1140/epjd/s10053-020-00004-4.

[106] S. BHOSLE, "Generateur d'impulsions electriques," FR3055494B1, Sep. 21, 2018 Accessed: Sep. 02, 2023. [Online]. Available:

https://patents.google.com/patent/FR3055494B1/en?q=(electrical+pulse+generator+S.+Bhosle%2c)&oq=electrical+pulse+generator+S.+Bhosle%2c+

[107] A. PATELLI, E. V. FALZACAPPA, P. SCOPECE, R. PIEROBON, and S. Vezzu', "Method for generating an atmospheric plasma jet and atmospheric plasma minitorch device," WO2015071746A1, May 21, 2015 Accessed: Aug. 22, 2023. [Online]. Available: https://patents.google.com/patent/WO2015071746A1/en

[108] G. Eisenberg, "Colorimetric Determination of Hydrogen Peroxide".

[109] "The principles of dynamic light scattering | Anton Paar Wiki," Anton Paar. Accessed: Jul. 19, 2023. [Online]. Available: https://wiki.anton-paar.com/ch-fr/les-principes-de-la-diffusion-dynamique-de-la-lumiere/

[110] B. J. Inkson, "Scanning electron microscopy (SEM) and transmission electron microscopy (TEM) for materials characterization," in *Materials Characterization Using Nondestructive Evaluation (NDE) Methods*, Elsevier, 2016, pp. 17–43. doi: 10.1016/B978-0-08-100040-3.00002-X.

[111] "Energy Dispersive X-Ray Spectroscopy (EDS/EDX)," Particle Technology Labs. Accessed: Jul. 21, 2023. [Online]. Available: https://particletechlabs.com/analytical-testing/energy-dispersive-x-ray-spectroscopy-eds-edx/

[112] M. Aliofkhazraei and N. Ali, "AFM Applications in Micro/Nanostructured Coatings," in *Comprehensive Materials Processing*, Elsevier, 2014, pp. 191–241. doi: 10.1016/B978-0-08-096532-1.00712-3.

[113] T. Habib, J. M. A. Caiut, and B. Caillier, "Synthesis of silver nanoparticles by atmospheric pressure plasma jet," *Nanotechnology*, vol. 33, no. 32, p. 325603, May 2022, doi: 10.1088/1361-6528/ac6528.

[114] R. Wang, Y. Shen, C. Zhang, P. Yan, and T. Shao, "Comparison between helium and argon plasma jets on improving the hydrophilic property of PMMA surface," *Applied Surface Science*, vol. 367, pp. 401–406, Mar. 2016, doi: 10.1016/j.apsusc.2016.01.199.

[115] Q. Xiong, A. Y. Nikiforov, M. Á. González, C. Leys, and X. P. Lu, "Characterization of an atmospheric helium plasma jet by relative and absolute optical emission spectroscopy," *Plasma Sources Sci. Technol.*, vol. 22, no. 1, p. 015011, Dec. 2012, doi: 10.1088/0963-0252/22/1/015011.

[116] A. Kone, F. P. Sainct, C. Muja, B. Caillier, and P. Guillot, "Investigation of the Interaction between a Helium Plasma Jet and Conductive (Metal)/ Non-Conductive (Dielectric) Targets," *Plasma Med*, vol. 7, no. 4, pp. 333–346, 2017, doi: 10.1615/PlasmaMed.2018019503.

[117] *The identification of molecular spectra*, vol. 297. 1976.

[118] N. Kaushik *et al.*, "Plasma and Nanomaterials: Fabrication and Biomedical Applications," *Nanomaterials*, vol. 9, no. 1, p. 98, Jan. 2019, doi: 10.3390/nano9010098.

[119] Y. Morabit, M. I. Hasan, R. D. Whalley, E. Robert, M. Modic, and J. L. Walsh, "A review of the gas and liquid phase interactions in low-temperature plasma jets used for biomedical applications," *Eur. Phys. J. D*, vol. 75, no. 1, p. 32, Jan. 2021, doi: 10.1140/epjd/s10053-020-00004-4.

[120] T. Takamatsu *et al.*, "Investigation of reactive species using various gas plasmas," *RSC Adv.*, vol. 4, no. 75, pp. 39901–39905, Sep. 2014, doi: 10.1039/C4RA05936K.

[121] P. Lukes, E. Dolezalova, I. Sisrova, and M. Clupek, "Aqueous-phase chemistry and bactericidal effects from an air discharge plasma in contact with water: evidence for the formation of peroxynitrite through a pseudo-second-order post-discharge reaction of H2O2 and HNO2," *Plasma Sources Sci. Technol.*, vol. 23, no. 1, p. 015019, Feb. 2014, doi: 10.1088/0963-0252/23/1/015019.

[122] T. Desmet, R. Morent, N. De Geyter, C. Leys, E. Schacht, and P. Dubruel, "Nonthermal Plasma Technology as a Versatile Strategy for Polymeric Biomaterials Surface Modification: A Review," *Biomacromolecules*, vol. 10, no. 9, pp. 2351–2378, Sep. 2009, doi: 10.1021/bm900186s.

[123] B. He *et al.*, "Simultaneous quantification of aqueous peroxide, nitrate, and nitrite during the plasma–liquid interactions by derivative absorption spectrophotometry," *J. Phys. D: Appl. Phys.*, vol. 50, no. 44, p. 445207, Oct. 2017, doi: 10.1088/1361-6463/aa8819.

[124] F. Judée, S. Simon, C. Bailly, and T. Dufour, "Plasma-activation of tap water using DBD for agronomy applications: Identification and quantification of long lifetime chemical species and production/consumption mechanisms," *Water Research*, vol. 133, pp. 47–59, Apr. 2018, doi: 10.1016/j.watres.2017.12.035.

[125] A. Khlyustova, C. Labay, Z. Machala, M.-P. Ginebra, and C. Canal, "Important parameters in plasma jets for the production of RONS in liquids for plasma medicine: A brief review," *Front. Chem. Sci. Eng.*, vol. 13, no. 2, pp. 238–252, Jun. 2019, doi: 10.1007/s11705-019-1801-8.

[126] Z. Chen *et al.*, "A Novel Micro Cold Atmospheric Plasma Device for Glioblastoma Both In Vitro and In Vivo," *Cancers*, vol. 9, no. 6, Art. no. 6, Jun. 2017, doi: 10.3390/cancers9060061.

[127] J. Chauvin, F. Judée, M. Yousfi, P. Vicendo, and N. Merbahi, "Analysis of reactive oxygen and nitrogen species generated in three liquid media by low temperature helium plasma jet," *Sci Rep*, vol. 7, no. 1, Art. no. 1, Jul. 2017, doi: 10.1038/s41598-017-04650-4.

[128] B. Syed, N. P. M.N., D. B.L., M. K. K., Y. S., and S. S., "Synthesis of silver nanoparticles by endosymbiont Pseudomonas fluorescens CA 417 and their bactericidal activity," *Enzyme and Microbial Technology*, vol. 95, pp. 128–136, Dec. 2016, doi: 10.1016/j.enzmictec.2016.10.004.

[129] H. M. M. Ibrahim, "Green synthesis and characterization of silver nanoparticles using banana peel extract and their antimicrobial activity against representative microorganisms," *Journal of Radiation Research and Applied Sciences*, vol. 8, no. 3, pp. 265–275, Jul. 2015, doi: 10.1016/j.jrras.2015.01.007.

[130] H. Padalia, P. Moteriya, and S. Chanda, "Green synthesis of silver nanoparticles from marigold flower and its synergistic antimicrobial potential," *Arabian Journal of Chemistry*, vol. 8, no. 5, pp. 732–741, Sep. 2015, doi: 10.1016/j.arabjc.2014.11.015.

[131] J. S. Devi, B. V. Bhimba, and D. M. Peter, "Production of biogenic Silver nanoparticles using Sargassum longifolium and its applications," *INDIAN J. MAR. SCI.*, no. 1, 2013.

[132] Z. Khan, S. A. Al-Thabaiti, A. Y. Obaid, and A. O. Al-Youbi, "Preparation and characterization of silver nanoparticles by chemical reduction method," *Colloids and Surfaces B: Biointerfaces*, vol. 82, no. 2, pp. 513–517, Feb. 2011, doi: 10.1016/j.colsurfb.2010.10.008.

[133] H. Wang, X. Qiao, J. Chen, and S. Ding, "Preparation of silver nanoparticles by chemical reduction method," *Colloids and Surfaces A: Physicochemical and Engineering Aspects*, vol. 256, no. 2, pp. 111–115, Apr. 2005, doi: 10.1016/j.colsurfa.2004.12.058.

[134] K. C. Song, S. M. Lee, T. S. Park, and B. S. Lee, "Preparation of colloidal silver nanoparticles by chemical reduction method," *Korean J. Chem. Eng.*, vol. 26, no. 1, pp. 153–155, Jan. 2009, doi: 10.1007/s11814-009-0024-y.

[135] R. A. Salkar, P. Jeevanandam, S. T. Aruna, Y. Koltypin, and A. Gedanken, "The sonochemical preparation of amorphous silver nanoparticles," *Journal of Materials Chemistry*, vol. 9, no. 6, pp. 1333–1335, 1999, doi: 10.1039/A900568D.

[136] V. G. Pol *et al.*, "Sonochemical Deposition of Silver Nanoparticles on Silica Spheres," *Langmuir*, vol. 18, no. 8, pp. 3352–3357, Apr. 2002, doi: 10.1021/la0155552.

[137] B. Kumar, K. Smita, L. Cumbal, A. Debut, and R. N. Pathak, "Sonochemical Synthesis of Silver Nanoparticles Using Starch: A Comparison," *Bioinorganic Chemistry and Applications*, vol. 2014, pp. 1–8, 2014, doi: 10.1155/2014/784268.

[138] H. Lee, S. H. Park, S.-C. Jung, J.-J. Yun, S.-J. Kim, and D.-H. Kim, "Preparation of nonaggregated silver nanoparticles by the liquid phase plasma reduction method," *Journal of Materials Research*, vol. 28, no. 8, pp. 1105–1110, Apr. 2013, doi: 10.1557/jmr.2013.59.

[139] M. Skiba, A. Pivovarov, V. Vorobyova, T. Derkach, and I. Kurmakova, "PLASMA-CHEMICAL FORMATION OF SILVER NANOPARTICLES: THE SILVER IONS CONCENTRATION EFFECT ON THE PARTICLE SIZE AND THEIR ANTIMICROBIAL PROPERTIES," 2019.

[140] C. M. Cobley, S. E. Skrabalak, D. J. Campbell, and Y. Xia, "Shape-Controlled Synthesis of Silver Nanoparticles for Plasmonic and Sensing Applications," *Plasmonics*, vol. 4, no. 2, pp. 171–179, Jun. 2009, doi: 10.1007/s11468-009-9088-0.

[141] J. Weerasinghe *et al.*, "Bactericidal Silver Nanoparticles by Atmospheric Pressure Solution Plasma Processing," *Nanomaterials*, vol. 10, no. 5, p. 874, May 2020, doi: 10.3390/nano10050874.

[142] A. Treshchalov, "Stabilizer-free silver nanoparticles as efficient catalysts for electrochemical reduction of oxygen," *Journal of Colloid and Interface Science*, vol. 491, p. 9, 2017.

[143] G. Suriati, M. Mariatti, and A. Azizan, "Synthesis of silver nanoparticles by chemical reduction method: effect of reducing agent and surfactant concentration," *Int. J. Automot. Mech. Eng.*, vol. 10, pp. 1920–1927, Dec. 2014, doi: 10.15282/ijame.10.2014.9.0160.

[144] Y. Xia and N. J. Halas, "Shape-Controlled Synthesis and Surface Plasmonic Properties of Metallic Nanostructures," *MRS Bulletin*, vol. 30, no. 5, pp. 338–348, May 2005, doi: 10.1557/mrs2005.96.

[145] Y. Xia and N. J. Halas, "Shape-Controlled Synthesis and Surface Plasmonic Properties of Metallic Nanostructures," *MRS Bull.*, vol. 30, no. 5, pp. 338–348, May 2005, doi: 10.1557/mrs2005.96.

[146] E. J. Guidelli, A. P. Ramos, M. E. D. Zaniquelli, and O. Baffa, "Green synthesis of colloidal silver nanoparticles using natural rubber latex extracted from Hevea brasiliensis," *Spectrochimica Acta Part A: Molecular and Biomolecular Spectroscopy*, vol. 82, no. 1, pp. 140–145, Nov. 2011, doi: 10.1016/j.saa.2011.07.024.

[147] J. J. Mock, M. Barbic, D. R. Smith, D. A. Schultz, and S. Schultz, "Shape effects in plasmon resonance of individual colloidal silver nanoparticles," *The Journal of Chemical Physics*, vol. 116, no. 15, pp. 6755–6759, Apr. 2002, doi: 10.1063/1.1462610.

[148] L. T. Q. Xuan, L. N. Nguyen, and N. T. Dao, "Synthesis of stabilizer-free, homogeneous gold nanoparticles by cold atmospheric-pressure plasma jet and their optical sensing property," *Nanotechnology*, vol. 33, no. 10, p. 105603, Mar. 2022, doi: 10.1088/1361-6528/ac3c7f.

[149] A. Henglein and M. Giersig, "Formation of Colloidal Silver Nanoparticles: Capping Action of Citrate," *J. Phys. Chem. B*, vol. 103, no. 44, pp. 9533–9539, Nov. 1999, doi: 10.1021/jp9925334.

[150] Moh. S. Arif, R. Ulfiya, Erwin, and A. S. Panggabean, "Synthesis silver nanoparticles using trisodium citrate and development in analysis method," presented at the INTERNATIONAL CONFERENCE ON ENERGY AND ENVIRONMENT (ICEE 2021), Thrissur, India, 2021, p. 050007. doi: 10.1063/5.0059493.

[151] G. Suriati, M. Mariatti, and A. Azizan, "SYNTHESIS OF SILVER NANOPARTICLES BY CHEMICAL REDUCTION METHOD: EFFECT OF REDUCING AGENT AND SURFACTANT CONCENTRATION," *Int. J. Automot. Mech. Eng.*, vol. 10, pp. 1920–1927, Dec. 2014, doi: 10.15282/ijame.10.2014.9.0160.

[152] Q. Zhang, N. Li, J. Goebl, Z. Lu, and Y. Yin, "A Systematic Study of the Synthesis of Silver Nanoplates: Is Citrate a 'Magic' Reagent?," *J. Am. Chem. Soc.*, vol. 133, no. 46, pp. 18931–18939, Nov. 2011, doi: 10.1021/ja2080345.

[153] A. Šileikait, I. Prosy, J. Puišo, A. Juraitis, and A. Guobien, "Analysis of Silver Nanoparticles Produced by Chemical Reduction of Silver Salt Solution".

[154] S. L. Smitha, K. M. Nissamudeen, D. Philip, and K. G. Gopchandran, "Studies on surface plasmon resonance and photoluminescence of silver nanoparticles," *Spectrochimica Acta Part A: Molecular and Biomolecular Spectroscopy*, vol. 71, no. 1, pp. 186–190, Nov. 2008, doi: 10.1016/j.saa.2007.12.002.

[155] N. R. Jana, L. Gearheart, and C. J. Murphy, "Evidence for Seed-Mediated Nucleation in the Chemical Reduction of Gold Salts to Gold Nanoparticles," *Chem. Mater.*, vol. 13, no. 7, pp. 2313–2322, Jul. 2001, doi: 10.1021/cm000662n.

[156] D. Wei and W. Qian, "Facile synthesis of Ag and Au nanoparticles utilizing chitosan as a mediator agent," *Colloids and Surfaces B: Biointerfaces*, vol. 62, no. 1, pp. 136–142, Mar. 2008, doi: 10.1016/j.colsurfb.2007.09.030.

[157] A. Chaudhary and S. Garg, "siRNA delivery using polyelectrolyte-gold nanoassemblies in neuronal cells for BACE1 gene silencing," *Materials Science and Engineering: C*, vol. 80, pp. 18–28, Nov. 2017, doi: 10.1016/j.msec.2017.05.101.

[158] K. Okitsu, M. Ashokkumar, and F. Grieser, "Sonochemical Synthesis of Gold Nanoparticles: Effects of Ultrasound Frequency," *J. Phys. Chem. B*, vol. 109, no. 44, pp. 20673–20675, Nov. 2005, doi: 10.1021/jp0549374.

[159] R. A. Caruso, M. Ashokkumar, and F. Grieser, "Sonochemical Formation of Gold Sols," *Langmuir*, vol. 18, no. 21, pp. 7831–7836, Oct. 2002, doi: 10.1021/la020276f.

[160] V. G. Pol, A. Gedanken, and J. Calderon-Moreno, "Deposition of Gold Nanoparticles on Silica Spheres: A Sonochemical Approach," *Chem. Mater.*, vol. 15, no. 5, pp. 1111–1118, Mar. 2003, doi: 10.1021/cm021013+.

[161] H. Ma *et al.*, "Synthesis of Silver and Gold Nanoparticles by a Novel Electrochemical Method," *ChemPhysChem*, vol. 5, no. 1, pp. 68–75, Jan. 2004, doi: 10.1002/cphc.200300900.

[162] Y. Hu, Y. Song, Y. Wang, and J. Di, "Electrochemical synthesis of gold nanoparticles onto indium tin oxide glass and application in biosensors," *Thin Solid Films*, vol. 519, no. 19, pp. 6605–6609, Jul. 2011, doi: 10.1016/j.tsf.2011.04.211.

[163] Y. Jin, Z. Li, L. Hu, X. Shi, W. Guan, and Y. Du, "Synthesis of chitosan-stabilized gold nanoparticles by atmospheric plasma," *Carbohydrate Polymers*, vol. 91, no. 1, pp. 152–156, Jan. 2013, doi: 10.1016/j.carbpol.2012.08.018.

[164] J. Hieda, N. Saito, and O. Takai, "Exotic shapes of gold nanoparticles synthesized using plasma in aqueous solution," *Journal of Vacuum Science & Technology A: Vacuum, Surfaces, and Films*, vol. 26, no. 4, pp. 854–856, Jul. 2008, doi: 10.1116/1.2919139.

[165] M. A. Bratescu, S.-P. Cho, O. Takai, and N. Saito, "Size-Controlled Gold Nanoparticles Synthesized in Solution Plasma," *J. Phys. Chem. C*, vol. 115, no. 50, pp. 24569–24576, Dec. 2011, doi: 10.1021/jp207447c.

[166] S. M. Kim, G. S. Kim, and S. Y. Lee, "Effects of PVP and KCl concentrations on the synthesis of gold nanoparticles using a solution plasma processing," *Materials Letters*, vol. 62, no. 28, pp. 4354–4356, Nov. 2008, doi: 10.1016/j.matlet.2008.07.025.

[167] P. Pimpang and S. Choopun, "Monodispersity and Stability of Gold Nanoparticles Stabilized by Using Polyvinyl Alcohol," *Chiang Mai J. Sci.*, p. 8.

[168] V. Amendola and M. Meneghetti, "Size Evaluation of Gold Nanoparticles by UV−vis Spectroscopy," *J. Phys. Chem. C*, vol. 113, no. 11, pp. 4277–4285, Mar. 2009, doi: 10.1021/jp8082425.

[169] K. M. Koczkur, S. Mourdikoudis, L. Polavarapu, and S. E. Skrabalak, "Polyvinylpyrrolidone (PVP) in nanoparticle synthesis," *Dalton Trans.*, vol. 44, no. 41, pp. 17883–17905, 2015, doi: 10.1039/C5DT02964C.

[170] R. Si, Y.-W. Zhang, L.-P. You, and C.-H. Yan, "Self-Organized Monolayer of Nanosized Ceria Colloids Stabilized by Poly(vinylpyrrolidone)," *J. Phys. Chem. B*, vol. 110, no. 12, pp. 5994–6000, Mar. 2006, doi: 10.1021/jp057501x.

[171] U. Kreibig, "OPTICAL ABSORPTION OF SMALL METALLIC PARTICLES," p. 23.

[172] S. Guo and E. Wang, "One-Pot, High-Yield Synthesis of Size-Controlled Gold Particles with Narrow Size Distribution," *Inorg. Chem.*, vol. 46, no. 16, pp. 6740–6743, Aug. 2007, doi: 10.1021/ic700662j.

[173] J. Voráč, P. Synek, L. Potočňáková, J. Hnilica, and V. Kudrle, "Batch processing of overlapping molecular spectra as a tool for spatio-temporal diagnostics of power modulated microwave plasma jet," *Plasma Sources Sci. Technol.*, vol. 26, no. 2, p. 025010, Jan. 2017, doi: 10.1088/1361-6595/aa51f0.

[174] R. Wang, Y. Shen, C. Zhang, P. Yan, and T. Shao, "Comparison between helium and argon plasma jets on improving the hydrophilic property of PMMA surface," *Applied Surface Science*, vol. 367, pp. 401–406, Mar. 2016, doi: 10.1016/j.apsusc.2016.01.199.

[175] F. Rezaei *et al.*, "Investigation of plasma-induced chemistry in organic solutions for enhanced electrospun PLA nanofibers," *Plasma Process Polym*, vol. 15, no. 6, p. 1700226, Jun. 2018, doi: 10.1002/ppap.201700226.

[176] Q. Xiong, A. Y. Nikiforov, M. Á. González, C. Leys, and X. P. Lu, "Characterization of an atmospheric helium plasma jet by relative and absolute optical emission spectroscopy," *Plasma Sources Sci. Technol.*, vol. 22, no. 1, p. 015011, Dec. 2012, doi: 10.1088/0963-0252/22/1/015011.

[177] F. do Nascimento, K. G. Kostov, M. Machida, and A. Flacker, "Properties of DBD Plasma Jets Using Powered Electrode With and Without Contact With the Plasma," *IEEE Transactions on Plasma Science*, vol. 49, no. 4, pp. 1293–1301, Apr. 2021, doi: 10.1109/TPS.2021.3067159.

[178] J. Nakajima and H. Sekiguchi, "Synthesis of ammonia using microwave discharge at atmospheric pressure," *Thin Solid Films*, vol. 516, no. 13, pp. 4446–4451, May 2008, doi: 10.1016/j.tsf.2007.10.053.

[179] P. J. Bruggeman, F. Iza, and R. Brandenburg, "Foundations of atmospheric pressure non-equilibrium plasmas," *Plasma Sources Sci. Technol.*, vol. 26, no. 12, p. 123002, Nov. 2017, doi: 10.1088/1361-6595/aa97af.

[180] S. M. Kim, G. S. Kim, and S. Y. Lee, "Effects of PVP and KCl concentrations on the synthesis of gold nanoparticles using a solution plasma processing," *Materials Letters*, vol. 62, no. 28, pp. 4354–4356, Nov. 2008, doi: 10.1016/j.matlet.2008.07.025.

[181] P. Pimpang and S. Choopun, "Monodispersity and stability of gold nanoparticles stabilized by using polyvinyl alcohol," *Chiang Mai Journal of Science*, vol. 38, no. 1, pp. 31–38, 2011.

[182] O. Couteau and G. Roebben, "Measurement of the size of spherical nanoparticles by means of atomic force microscopy," *Meas. Sci. Technol.*, vol. 22, no. 6, p. 065101, Jun. 2011, doi: 10.1088/0957-0233/22/6/065101.

[183] T. R. Acharya, G. J. Lee, and E. H. Choi, "Influences of Plasma Plume Length on Structural, Optical and Dye Degradation Properties of Citrate-Stabilized Silver Nanoparticles Synthesized by Plasma-Assisted Reduction," *Nanomaterials*, vol. 12, no. 14, p. 2367, Jul. 2022, doi: 10.3390/nano12142367.

[184] M. Moravej, X. Yang, G. R. Nowling, J. P. Chang, R. F. Hicks, and S. E. Babayan, "Physics of high-pressure helium and argon radio-frequency plasmas," *Journal of Applied Physics*, vol. 96, no. 12, pp. 7011–7017, Dec. 2004, doi: 10.1063/1.1815047.

[185] J. Jonkers, M. V. D. Sande, A. Sola, A. Gamero, and J. V. D. Mullen, "On the differences between ionizing helium and argon plasmas at atmospheric pressure," *Plasma Sources Sci. Technol.*, vol. 12, no. 1, pp. 30–38, Feb. 2003, doi: 10.1088/0963-0252/12/1/304.

[186] W.-R. Li, X.-B. Xie, Q.-S. Shi, H.-Y. Zeng, Y.-S. OU-Yang, and Y.-B. Chen, "Antibacterial activity and mechanism of silver nanoparticles on Escherichia coli," *Appl Microbiol Biotechnol*, vol. 85, no. 4, pp. 1115–1122, Jan. 2010, doi: 10.1007/s00253-009-2159-5.

[187] M. Raffi, F. Hussain, T. Bhatti, J. Akhter, A. Hameed, and M. Hassan, "Antibacterial Characterization of Silver Nanoparticles against E. Coli ATCC-15224," *JOURNAL OF MATERIALS SCIENCE & TECHNOLOGY*, vol. 24, pp. 192–196, Nov. 2007.

[188] W.-R. Li, X.-B. Xie, Q.-S. Shi, S.-S. Duan, Y.-S. Ouyang, and Y.-B. Chen, "Antibacterial effect of silver nanoparticles on Staphylococcus aureus," *Biometals*, vol. 24, no. 1, pp. 135–141, Feb. 2011, doi: 10.1007/s10534-010-9381-6.

[189] F. Mirzajani, A. Ghassempour, A. Aliahmadi, and M. A. Esmaeili, "Antibacterial effect of silver nanoparticles on Staphylococcus aureus," *Research in Microbiology*, vol. 162, no. 5, pp. 542–549, Jun. 2011, doi: 10.1016/j.resmic.2011.04.009.

[190] E. G. Hilário *et al.*, "Metallic nanoparticles-decorated NdxY1-xAl3(BO3)4 sub-micrometric particles to enhance anti-Stokes excitation performance," *Optical Materials: X*, vol. 19, p. 100254, Jul. 2023, doi: 10.1016/j.omx.2023.100254.

[191] L. Lu, G. Burkey, I. Halaciuga, and D. V. Goia, "Core–shell gold/silver nanoparticles: Synthesis and optical properties," *Journal of Colloid and Interface Science*, vol. 392, pp. 90–95, Feb. 2013, doi: 10.1016/j.jcis.2012.09.057.

Résumé Substantiel

Résumé Substantiel

Introduction

Les plasmas sont des gaz ionisés globalement neutres comprenant à la fois des particules chargées (ions et électrons) et neutres (atomes, molécules et radicaux). Les progrès de l'ingénierie des plasmas offrent de nouvelles applications pour les plasmas non thermiques dans divers domaines. Si le traitement et la modification de surface de matériaux sensibles à la chaleur constituaient les premières applications des plasmas froids, de récentes avancées ont élargi leur portée. Par exemple, le plasma non thermique est désormais exploité dans l'industrie alimentaire pour concevoir des surfaces recouvertes d'agents antibactériens afin de limiter la formation de biofilm. Son utilisation s'est étendue au domaine biomédical, notamment dans la régénération des tissus, la cicatrisation des plaies, le traitement du cancer et la décontamination microbiologique des surfaces et des liquides. Il est important de noter que les plasmas sont devenus un outil puissant pour la synthèse de nanoparticules avec un contrôle possible sur la taille, la morphologie et d'autres caractéristiques des nanoparticules.

La nanotechnologie est devenue un domaine large avec des applications couvrant diverses industries. La synthèse de nanoparticules, notamment en phase liquide, offre des avantages significatifs, notamment la possibilité d'adapter les propriétés de surface des nanoparticules à des applications spécifiques. Parmi les nanoparticules métalliques les plus étudiées figurent les nanoparticules d'argent et d'or en raison de leurs nombreuses applications en photonique, électronique, biomédecine, capteurs et cosmétiques. En chimie conventionnelle des solutions, les ions métalliques sont généralement exposés à une source d'énergie telle que la chaleur ou la lumière UV, ainsi qu'à un agent réducteur, pour convertir les ions métalliques en nanoparticules métalliques. Ces méthodes de synthèse présentent des limites en terme de processus respectueux de l'environnement et d'efficacités. La synthèse de nanoparticules par plasma appliqué à un liquide, quant à elle, génère des électrons hautement énergétiques à partir de décharges plasma. Ces espèces énergétiques dissocient les molécules d'eau en radicaux (O, H, OH) et en ions (H_2O^+, O_2^-), qui participent à la réduction des ions métalliques en nanoparticules. Cela nous amène à la présente étude, qui introduit une méthode de réduction plasma pour la synthèse de nanoparticules métalliques qui respecte les critères de processus suivants :

Processus en une seule étape - Un procédé simple, qui nécessite le moins d'étapes de synthèse possible

L'approche est un processus simple, caractérisé par sa simplicité et son efficacité, n'impliquant qu'un nombre minimal d'étapes de synthèse. Le processus commence par la préparation de la solution échantillon, une opération qui demande peu de temps et d'efforts. Cette préparation implique la dissolution du précurseur et de l'agent stabilisant dans l'eau. Une fois cette solution préparée, elle sera ensuite exposée au jet de plasma, initiant une séquence de réactions responsables de la formation de nanoparticules.

Gain de temps - Un procédé à temps de réaction court pour la synthèse de nanoparticules

Un aspect particulièrement notable de cette méthode est la création quasiment instantanée de nanoparticules, mettant en évidence l'efficacité remarquable de notre approche. La durée du traitement occupe un rôle central dans le cadre de cette enquête, où son influence sur la morphologie et la taille des nanoparticules est examinée.

Écologique - Un procédé qui n'utilise pas de réactifs nocifs et dangereux

Cette approche offre des avantages distincts par rapport aux méthodologies conventionnelles, qui impliquent souvent l'utilisation de réactifs dangereux, entraînant la génération de sous-produits nocifs et de résidus inutiles. Notamment, la synthèse pilotée par plasma réduit avec succès les sels métalliques présents dans la solution, ceci est rendu possible par les espèces réactives créées par le plasma.

Cette thèse est structurée en deux parties principales, chacune employant une configuration distincte de jet de plasma pour la synthèse de nanoparticules métalliques. La première partie s'articule autour de l'utilisation d'un jet de plasma d'hélium à pression atmosphérique, doté d'une source asymétrique en verre borosilicaté connectée à une alimentation pulsée. Cette section aborde séparément la production de nanoparticules d'argent et d'or. Une enquête approfondie est menée, explorant l'impact de la durée d'exposition au plasma, de la concentration en précurseur et de la concentration en agent stabilisant sur les caractéristiques des nanoparticules synthétisées.

Dans la deuxième partie de cette thèse, une configuration différente du plasma est étudiée. Ici, un jet de plasma à pression atmosphérique à double fréquence, composé d'un tube d'alumine connecté à la fois à l'alimentation impulsionnelle et à un générateur de puissance RF, est utilisé. Cette configuration est exploitée pour étudier la synthèse de nanoparticules d'or. L'enquête dans cette partie se concentre sur la compréhension des effets et des implications des

paramètres physiques clés du processus, y compris le choix du gaz de traitement et l'ajout de niveaux de puissance RF sur les caractéristiques des nanoparticules d'or synthétisées.

L'objectif principal de cette étude est d'étudier la synthèse de nanoparticules d'argent et d'or en utilisant un jet de plasma à pression atmosphérique en contact avec une solution aqueuse de sel métallique au travers d'études paramétriques.

La présente thèse se compose de quatre chapitres divisés en sections :

Le chapitre 1 est destiné à fournir une revue de la littérature : les concepts fondamentaux de la nanotechnologie, les caractéristiques optiques, chimiques et électriques, les applications des nanoparticules d'argent et d'or, les méthodes de synthèse (approches top-down et bottom-up), les plasmas froids.

Le chapitre 2 fournit des détails sur le matériel et les méthodes expérimentales utilisées tout au long de ce travail : configurations expérimentales des dispositifs à plasma les outils de diagnostic (électriques et optiques), quantification de la concentration du peroxyde d'hydrogène en solution, préparation et caractérisation des nanoparticules métalliques d'argent et d'or (taille, morphologie, etc.).

Le chapitre 3 présente les résultats de la synthèse de nanoparticules d'argent et d'or par jet de plasma à pression atmosphérique utilisant une alimentation impulsionnelles avec l'hélium comme gaz de traitement pour la génération de la décharge : spectroscopie d'émission optique (OES), distribution spatiale des espèces réactives, caractérisation chimique de la solution liquide, effets de la durée de l'interaction plasma, de la concentration en précurseur métallique et de la concentration en agent stabilisant sur le processus de synthèse, effet sur leur forme et leur taille.

Le chapitre 4 présente les résultats de la synthèse de nanoparticules d'or par jet de plasma à pression atmosphérique à double fréquence utilisant à la fois une alimentation à micro-impulsions et un générateur de puissance RF pour la génération de la décharge de plasma : spectroscopie d'émission optique avec l'hélium ou et l'argon, les températures, niveaux de puissance sur les caractéristiques des nanoparticules.

Enfin, le présent travail se termine par une conclusion générale présentant les résultats de notre recherche, ainsi que les perspectives.

1 Revue de la Litérature

1.1 Introduction à la nanotechnologie

La nanotechnologie est devenue un domaine révolutionnaire de recherche et de progrès technologique, offrant de nouvelles opportunités pour concevoir et manipuler des matériaux à l'échelle nanométrique. La nanotechnologie est définie comme la conception, la synthèse, la manipulation et la caractérisation de matériaux dont les dimensions varient de 1 à 100 nanomètres. Or, à cette échelle, le comportement de la matière peut s'écarter considérablement de celui observé dans les matériaux massifs, donnant lieu à de nouvelles applications. La capacité de concevoir des matériaux aux niveaux atomique et moléculaire offre un énorme potentiel pour développer des matériaux avancés dotés de fonctionnalités sur mesure et de performances améliorées, ouvrant la voie à une nouvelle ère de découverte scientifique et d'innovation technologique. La prochaine révolution industrielle pourrait venir de la nanotechnologie. L'histoire de la nanotechnologie remonte à l'Antiquité, lorsque les humains interagissaient sans le savoir avec des matériaux à l'échelle nanométrique. Cependant, l'étude formelle et le développement de la nanotechnologie en tant que domaine distinct ont commencé au XXe siècle.

1.2 Nanomatériaux : classements et propriétés

En général, les nanomatériaux peuvent être classés en fonction de leur composition, structure, morphologie et dimension. En catégorisant les nanomatériaux en fonction de leur composition, cela donne un aperçu des types de matériaux qui existent à l'échelle nanométrique et de leurs propriétés distinctes. De plus, comprendre la dimensionnalité des nanomatériaux nous permet d'explorer leurs caractéristiques structurelles et leurs implications dans diverses applications. Premièrement, en fonction de leur composition, les nanomatériaux peuvent être largement classés en matériaux organiques et inorganiques. Deuxièmement, les nanomatériaux peuvent également être classés en fonction de leur dimensionnalité, qui fait référence au nombre de dimensions confinées à l'échelle nanométrique.

Les nanomatériaux possèdent une gamme de propriétés uniques qui les distinguent de leurs homologues en vrac. Ces propriétés sont dues à leur petite taille et à leur rapport surface/volume élevé, conduisant à une réactivité améliorée et à un comportement nouveau. Certaines propriétés clés des nanomatériaux métalliques comprennent les propriétés optiques, chimiques et électriques qui seront détaillées ci-dessous.
Les nanoparticules métalliques présentent des propriétés optiques uniques, telles que la résonance plasmonique de surface localisée (LSPR), qui résultent de l'interaction de la lumière

avec les électrons libres présents à leur surface. L'absorption et la diffusion de la lumière par les nanoparticules métalliques peuvent être ajustées en ajustant leur taille, leur forme et leur composition. Cette propriété spécifique est la propriété la plus remarquable des nanostructures métalliques. Tout a commencé au début du XXe siècle avec Gustav Mie lorsqu'il a publié en 1908 son ouvrage expliquant les surprenantes propriétés optiques des colloïdes métalliques.

Les nanoparticules métalliques présentent des paramètres chimiques distincts qui contribuent à leurs propriétés et applications uniques. Premièrement, la chimie de surface des nanoparticules métalliques peut être contrôlée avec précision en fonctionnalisant ou en modifiant leurs surfaces avec des ligands, des molécules ou des polymères. Cette modification de surface permet des interactions personnalisées avec d'autres substances, permettant des applications spécifiques telles que l'administration et la détection ciblées de médicaments. Deuxièmement, leur réactivité de surface est considérablement améliorée en raison du rapport surface/volume élevé. Cette réactivité accrue en fait d'excellents catalyseurs dans diverses réactions chimiques, où leur présence accélère la vitesse de réaction.

Les nanoparticules métalliques possèdent des propriétés électriques remarquables qui contribuent à leur large gamme d'applications. Premièrement, leur nature métallique leur confère une conductivité électrique exceptionnelle, permettant un flux électronique efficace. Cela les rend précieux dans divers domaines, notamment dans l'électronique, le stockage d'énergie et les revêtements conducteurs. Deuxièmement, à l'échelle nanométrique, les nanoparticules métalliques peuvent présenter des effets de confinement quantique. Ces effets résultent du mouvement restreint des électrons au sein des nanoparticules, entraînant des niveaux d'énergie discrets.

1.3 Applications des nanoparticules d'argent et d'or

Les propriétés mentionnées ci-dessus des nanoparticules métalliques sont la principale raison de leurs diverses applications dans divers domaines. S'appuyant sur leurs caractéristiques distinctives, ces nanoparticules trouvent une utilité pratique dans un large éventail de domaines :

- **Applications antibactériennes**

Les nanoparticules d'argent présentent un mécanisme d'action unique contre les bactéries, ce qui les rend très efficaces pour inhiber la croissance bactérienne et prévenir les infections. La petite taille et la grande surface des nanoparticules d'argent améliorent leur interaction avec

les cellules bactériennes, permettant une pénétration et une perturbation efficaces des membranes cellulaires.

- **Applications biomédicales**

Les nanosystèmes basés sur des nanoparticules d'argent (AgNP) sont apparus comme des candidats prometteurs pour transporter diverses substances thérapeutiques, telles que celles ayant des propriétés anti-inflammatoires, antioxydantes et anticancéreuses. Et en raison de leur activité antimicrobienne, ils conviennent à diverses applications dans la cicatrisation des plaies, l'ingénierie tissulaire et le contrôle des infections. De plus, les nanoparticules d'or, en raison de leurs propriétés optiques uniques, ont ouvert la voie à des applications en biodétection, en imagerie et en thérapie ciblée.

- **Applications de catalyse**

Les AgNP présentent une excellente activité catalytique en raison de leurs propriétés de surface uniques et de leur rapport surface/volume élevé. La grande surface des AgNP fournit de nombreux sites actifs pour les interactions avec les molécules réactives, favorisant ainsi une conversion catalytique efficace. Les nanoparticules d'or sont également utilisées comme catalyseurs en raison de leurs propriétés physico-chimiques. Ils présentent une réactivité remarquable même dans des conditions douces, notamment à température ambiante ou inférieure.

- **Applications électroniques**

Les nanoparticules d'argent, par exemple, sont utilisées dans les encres conductrices et les produits électroniques imprimés, permettant la création de circuits électroniques flexibles et légers. De même, les nanoparticules d'or trouvent leur utilité dans divers appareils électroniques, notamment sous forme de revêtements conducteurs, en raison de leur stabilité chimique et de leur conductivité exceptionnelle. Leur intégration dans les systèmes électroniques garantit des performances électriques fiables et efficaces.

- **Applications de détection**

Malgré les nombreux avantages de l'argent par rapport à l'or, tels que ses coefficients d'extinction plus élevés, ses bandes d'extinction plus nettes et son rapport diffusion/extinction plus élevé, il a été moins couramment utilisé dans le développement de capteurs, à l'exception

des capteurs basés sur des spectroscopies améliorées en surface. Cela est principalement dû à la moindre stabilité chimique des nanoparticules d'argent par rapport à l'or.

1.4 Méthodes de synthèses

Plusieurs méthodes de synthèse ont été développées pour y parvenir, permettant aux chercheurs d'adapter la taille, la forme et les propriétés des nanoparticules à des applications spécifiques et de libérer leur plein potentiel dans différents domaines. Les méthodes de synthèse de nanoparticules peuvent être globalement classées en deux approches principales : l'approche top-down et l'approche bottom-up.

L'approche top-down commence avec un matériau à l'échelle macroscopique, qui subit ensuite une réduction de taille grâce à des processus physiques et chimiques pour produire de minuscules particules sous forme de nanoparticules. Certaines méthodes de synthèse top-down incluent la lithographie, le fraisage mécanique et l'ablation laser.

L'approche bottom-up utilise des atomes individuels et les transforme en nanomatériaux plus gros. Cette approche est largement utilisée pour la synthèse de nanoparticules car elle offre un contrôle précis de la taille, de la forme, de la composition et des propriétés de surface des nanoparticules. Les approches bottom-up couramment utilisées sont la synthèse chimique, le dépôt chimique en phase vapeur (CVD), la méthode sol-gel et la réduction plasma.

1.5 Introduction auc plasmas

Le plasma, souvent appelé le « quatrième état de la matière » avec le solide, le liquide et le gaz. Il s'agit d'un état physique distinct dans lequel le gaz devient ionisé et se caractérise par un nombre important de particules libres chargées. De la même manière que l'application d'énergie amène un liquide à atteindre son point d'ébullition et à se transformer en gaz, l'apport d'énergie au gaz peut conduire à la création d'un plasma. Ce plasma peut être décrit comme un mélange de particules chargées, constituées d'ions chargés positivement et d'électrons chargés négativement. Nous sommes capables de concevoir sur Terre des plasmas aux propriétés uniques qui ont trouvé de nombreuses applications pratiques dans divers domaines.

1.6 Plasmas : classements et propriétés

En général, les plasmas peuvent être classés en fonction de plusieurs facteurs. Premièrement, en fonction de leur origine, les plasmas peuvent être classés en décharges de plasma naturelles et artificielles. Deuxièmement, les décharges de plasma peuvent être largement classées en fonction de leur température et de leur degré d'ionisation. Les plasmas peuvent également être classés en fonction de leur pression, qui joue un rôle crucial dans leur comportement et leurs

caractéristiques. D'une manière générale, les plasmas peuvent être classés en trois groupes principaux : les plasmas à basse pression, les plasmas à pression atmosphérique et les plasmas à haute pression.

Les plasmas froids à pression atmosphérique ont suscité une attention considérable ces dernières années en raison de leur capacité à fonctionner dans des conditions ambiantes, ce qui les rend très accessibles et pratiques pour de nombreuses applications. Ces plasmas offrent de nombreux avantages, notamment des processus de traitement efficaces et rentables, des modifications améliorées de la surface des matériaux et la génération d'espèces réactives pour la synthèse chimique. Généralement, les plasmas froids à pression atmosphérique sont alimentés et entretenus grâce à l'application d'énergie électrique provenant de différentes sources. L'une des propriétés clés du plasma froid est sa capacité à générer des espèces réactives tout en maintenant une température de gaz plus basse. Les espèces réactives, notamment les ions, les électrons, les radicaux et les molécules excitées, peuvent interagir avec des matériaux ou des systèmes biologiques, conduisant à des réactions chimiques, fonctionnalisation de surface et gravure sélective. Une autre propriété importante du plasma froid est son confinement spatial et sa haute énergie électronique. Cette énergie électronique élevée dans le plasma froid permet un transfert d'énergie efficace et l'activation de réactions chimiques, ce qui la rend utile pour le traitement des matériaux, le dépôt de couches minces et la synthèse assistée par plasma. Le plasma froid présente également des propriétés électriques et électromagnétiques uniques. Il peut être facilement allumé et entretenu à l'aide de diverses sources d'énergie.

1.7 Applications des décharges plasma

Les plasmas froids, avec leurs propriétés uniques et leurs différentes configurations expérimentales, ont trouvé de nombreuses applications dans des domaines variés :

- **Synthèse chimique**

Les plasmas froids offrent un environnement unique pour la formation contrôlée de nanoparticules. En introduisant des gaz précurseurs dans le plasma ou en exposant le plasma à une solution contenant le précurseur. Grâce aux diverses réactions chimiques induites par les espèces réactives créées par le flux de plasma, les nanoparticules peuvent être synthétisées avec un contrôle précis de leur taille, de leur composition et de leur morphologie. Cette méthode permet la production de nanoparticules aux propriétés adaptées.

- **Traitement de l'eau**

Une application importante du plasma froid est le traitement de l'eau, où les espèces réactives générées par le plasma, telles que les radicaux hydroxyles et l'ozone, peuvent décomposer efficacement les contaminants organiques et détruire les micro-organismes nuisibles, offrant ainsi une méthode rentable et respectueuse de l'environnement pour la purification de l'eau sans besoin de sources externes de composés comme le peroxyde d'hydrogène et l'ozone.

- **Médecine**

Le plasma atmosphérique froid peut être utilisé pour la cicatrisation de la peau, des dents et des plaies, car il convient au traitement in situ des tissus vivants. En outre, il a été étudié comme potentiel pour les traitements contre le cancer en raison de sa capacité à induire sélectivement l'apoptose des cellules cancéreuses tout en épargnant les cellules saines. Ceci est principalement dû à la présence de RON dans le plasma.

1.8 Interactions plasma-liquid

Lorsqu'un plasma entre en contact avec un liquide, toute une série de processus physiques et chimiques se produisent, donnant lieu à des phénomènes uniques. Un aspect important des interactions plasma-liquide est la génération d'espèces réactives dans le liquide, telles que les espèces réactives de l'oxygène et les espèces réactives de l'azote. Il existe de nombreuses géométries de réacteurs avec des principes de fonctionnement distincts, la configuration des électrodes détermine si les décharges plasma sont en contact direct avec la phase liquide ou sont positionnées au-dessus du liquide et n'ont pas de contact direct.

Dans les décharges de plasma au-dessus de la phase liquide, les interactions entre le jet de plasma et la surface d'un liquide sont divisées en trois phases :

- **Phase gazeuse**

En phase gazeuse, le jet de plasma est composé d'un flux où se forment des espèces réactives primaires. Ceux-ci incluent des particules chargées (ions et électrons), des atomes ou des molécules excitées. Les espèces réactives comme OH, O_2^- et $^1O_2$, caractérisées respectivement par des durées de vie de 2 ns, 1 µs et 4 µs, sont directement produites dans la région de décharge en raison de l'interaction entre les électrons et les molécules du gaz d'alimentation et sont propulsées vers le surface liquide.

- **Phase interfaciale plasma-liquide**

Cette phase est celle où le jet de plasma entre en contact avec la surface du liquide. Les réactions chimiques se produisant à ce niveau résultent des interactions entre les espèces réactives primaires et les molécules présentes dans le milieu environnant. Ces espèces sont converties en espèces secondaires à longue durée de vie telles que le peroxyde d'hydrogène (H_2O_2), le nitrate (NO_2), le nitrite (NO_3) et l'ozone (O_3). Au contact de la surface du liquide, ils diffusent dans le liquide, ce qui correspond à la troisième phase.

- **Phase liquide**

Dans la phase liquide, les effets initiés au niveau de la phase interfaciale se propagent plus loin dans la masse liquide. Les espèces réactives générées à l'interface liquide-gaz peuvent diffuser dans le liquide et participer à diverses réactions chimiques. Ces réactions peuvent impliquer une dégradation des composés organiques, une modification des propriétés de surface ou la génération de nouveaux composés.

1.9 Synthèse de nanoparticules métalliques par plasma jet à pression atmosphérique

Les plasmas à pression atmosphérique en contact avec un liquide constituent une approche avantageuse pour la synthèse de nanoparticules métalliques dans des conditions ambiantes et offrent plusieurs avantages, tels que la génération d'une grande quantité de RONS qui peuvent induire des réactions chimiques à l'intérieur des solutions et réduire les ions métalliques dans le milieu liquide pour produire des nanoparticules métalliques sans avoir recours à des agents réducteurs supplémentaires pouvant être considérés comme toxiques. Les réactions de réduction peuvent être initiées par transfert d'électrons ou par transfert d'atomes d'hydrogène à partir d'espèces réactives générées par plasma. Après la réduction du précurseur métallique, la prochaine étape de la synthèse des nanoparticules métalliques implique des processus de nucléation et de croissance, comme déjà évoqué dans l'approche ascendante de la synthèse des nanoparticules. La nucléation implique l'agrégation d'atomes métalliques pour former des amas ou des noyaux. Ces noyaux servent de base à une croissance future. Par divers mécanismes, les atomes métalliques s'agrègent et s'accumulent sur les noyaux existants, conduisant à la croissance de nanoparticules. À mesure que d'autres atomes métalliques sont ajoutés, les nanoparticules augmentent en taille et en masse, atteignant progressivement les dimensions souhaitées.

La taille et la forme des nanoparticules formées dans les systèmes de décharge plasma à pression atmosphérique sont influencées par des paramètres chimiques et physiques. Ainsi, le contrôle des paramètres chimiques et physiques dans les systèmes de décharge plasma à pression atmosphérique est essentiel pendant le processus de synthèse pour obtenir les résultats souhaités.

Les paramètres chimiques incluent la concentration de précurseurs métalliques et d'agents stabilisant. La concentration de précurseurs métalliques détermine la disponibilité des ions métalliques pour le processus de réduction, influençant ainsi la taille des nanoparticules résultantes. Des concentrations plus élevées de précurseurs conduisent souvent à des nanoparticules plus grosses en raison de l'augmentation des taux de nucléation et de croissance. D'un autre côté, la concentration des agents stabilisant, souvent utilisés pour contrôler la taille et la stabilité des nanoparticules, peut également affecter leur taille et leur forme finales. Ils peuvent se lier aux surfaces des nanoparticules et inhiber leur croissance ultérieure, conduisant à des nanoparticules plus petites et plus uniformes.

Les paramètres physiques, tels que le courant appliqué, la distance entre le jet de plasma et le liquide et la durée de la décharge, jouent également un rôle crucial dans la synthèse des nanoparticules. Le courant affecte l'énergie et la température du plasma, qui à leur tour influencent les réactions de réduction et la dynamique de croissance des nanoparticules affectant les processus de nucléation et de croissance. La distance entre le jet de plasma et la surface du liquide détermine le temps d'exposition du liquide au plasma, influençant la cinétique de réaction et la formation de nanoparticules. De plus, la durée de la décharge, ou la durée totale d'exposition au plasma, affecte l'ampleur des réactions de réduction et la croissance des nanoparticules. Des durées de décharge plus longues conduisent généralement à des nanoparticules plus grosses en raison de réactions prolongées.

1.10 Buts et objectifs de cette thèse

L'objectif principal de cette étude est d'étudier la voie qui émerge de la convergence des nanotechnologies et de la science des plasmas, en se concentrant sur la synthèse et la manipulation précises de nanoparticules métalliques, en particulier de nanoparticules d'argent et d'or. Ce travail de thèse approfondira l'aspect critique de la synthèse des nanoparticules au sein des nanotechnologies, soulignant l'importance de comprendre et de contrôler leurs propriétés. La première phase de la recherche est consacrée à la caractérisation du système de jet de plasma d'hélium à pression atmosphérique connecté à une alimentation pulsée. Un autre objectif central est la synthèse de nanoparticules d'argent et d'or à l'aide du même jet de plasma, impliquant l'exposition d'une solution aqueuse de sels métalliques à la décharge plasma,

suivie d'une caractérisation. De la même manière, la phase suivante est consacrée à la caractérisation d'un jet de plasma à pression atmosphérique bi-fréquence connecté à une alimentation impulsionnelle et à un générateur RF. L'objectif est de comprendre la dynamique complexe de la formation des nanoparticules, en particulier dans des conditions variables de gaz de traitement (hélium ou argon) et de puissance radiofréquence (RF), à l'aide d'un jet de plasma à pression atmosphérique à double fréquence.

2 Matériels et Méthodes

2.1 Configurations expérimentaux plasma

Dans cette étude, nous avons utilisé deux configurations de plasma distinctes pour étudier leurs effets sur la synthèse des nanoparticules.

Le jet de plasma à pression atmosphérique utilisé pour générer le plasma est constitué d'une source asymétrique, d'une alimentation électrique et d'un flux de gaz. Cette source asymétrique est réalisée en verre borosilicaté et composée d'un tube de 4 mm de diamètre autour duquel s'enroule l'électrode haute tension ainsi que d'un réservoir plus grand, d'environ 35 mm de diamètre, relié à l'électrode de masse. Les électrodes sont situées à l'extérieur de la source et sont en aluminium (3M, ruban 425, épaisseur 120 µm). La configuration de la source permet de générer une décharge plasma dans la partie supérieure, qui se propage ensuite dans le tube plus petit, formant un jet de plasma. A la sortie de chaque tube, les espèces réactives produites lors de la décharge interagissent avec les composants de l'air ambiant, puis avec la cible liquide. L'alimentation haute tension de la société OLISCIE est utilisée pour générer la décharge. Les deux électrodes de la configuration expérimentale ont une longueur de 25 mm et sont espacées d'environ 15 mm. La distance entre l'extrémité du petit tube et l'électrode mesure 8 mm. Le gaz utilisé pour créer le plasma est de l'hélium à 99,80 % fourni par la société Linde. Le gaz est injecté dans la partie supérieure du tube puis diffuse dans le tube en partie inférieure.

Le jet de plasma à pression atmosphérique à double fréquence comprend deux ensembles d'électrodes annulaires positionnées à environ 5 mm l'une de l'autre, chaque ensemble étant connecté à des alimentations distinctes. La première alimentation, acquise auprès de la société OLISCIE, utilise une technologie brevetée qui applique des impulsions de tension rapides sur une charge capacitive. La deuxième alimentation est connectée à une électrode en forme d'anneau couplée à un générateur RF fonctionnant à 27,12 MHz (Seren R301) via un réseau d'adaptation. Un flux contrôlé de gaz est introduit à travers un tube dans la source de plasma et pénètre dans l'air ambiant. L'air était fluxé pour refroidir les électrodes et contrôler l'atmosphère autour du jet plasma.

Divers outils de mesure ont été utilisés pour caractériser le plasma du point de vue électrique et optique.

Des mesures électriques sont effectuées pour obtenir des informations sur la génération et la dynamique de la décharge. Ces mesures permettent de calculer la puissance et l'énergie déposées par la décharge. Tous les signaux électriques sont simultanément visualisés et

enregistrés à l'aide d'un oscilloscope numérique (Rohde & Schwarz) avec une bande passante de 2 GHz et un taux d'échantillonnage de 5 GSa/s. La sonde de courant est connectée à l'électrode haute tension. Il s'agit d'un modèle Pearson Electronics 6585 avec une plage de fréquence de 40 Hz à 250 MHz et une sensibilité de 1 V/A. Il est essentiel de souligner que le courant d'entrée de l'alimentation est de 8 A, tandis que le courant mesuré délivré par l'alimentation s'élève à environ 1,2 A.

La spectroscopie d'émission optique (OES) est une technique puissante utilisée pour analyser le spectre d'émission optique d'un jet de plasma. Le principe de cette méthode réside dans le fait que les atomes et les ions excités du plasma émettent une lumière caractéristique à des longueurs d'onde spécifiques lorsqu'ils reviennent à leur état fondamental. Pendant la décharge plasma, les électrons sont excités à des niveaux d'énergie plus élevés et, lorsqu'ils se désexcitent, ils émettent des photons. En dispersant la lumière émise à travers un spectromètre, les longueurs d'onde émises peuvent être séparées et mesurées, révélant des informations précieuses sur la composition élémentaire et les états d'excitation du plasma. OES permet l'identification de diverses espèces présentes dans le plasma et peut fournir des informations sur la température du plasma et la densité électronique.

La configuration expérimentale utilisée pour le diagnostic optique consiste en une fibre optique de 600 µm de diamètre connectée à un monochromateur haute résolution (Princeton Instrument, HRS-750) avec une distance focale de 75 mm. Le monochromateur est équipé de trois réseaux de diffraction : 300 lignes.mm^{-1}, 2400 lignes.mm^{-1} et 3600 lignes.mm^{-1}. Le spectre a été enregistré au point de sortie du jet de plasma de la source, ainsi qu'à des intervalles de 1 mm dans la direction axiale jusqu'à 6 mm, où la distance entre la sortie du jet et les échantillons a été fixée à 6 mm.

2.2 Cible traitée par plasma

Une cible liquide, contenue dans un cristalliseur, est positionnée sous le jet de plasma. Ce cristalliseur peut contenir de l'eau ultra pure (Millipore Direct-Q 3 UV Water Purification System, Thermo Fisher Scientific) et sauf indication contraire, la distance entre la sortie de la source et la surface du liquide est fixée à 6 mm. Le volume de liquide traité est fixé à 10 mL, sauf pour les mesures par absorption laser, spectroscopie d'émission optique, où le volume de liquide remplit entièrement le cristalliseur. Cette précaution est prise pour empêcher la lumière plasma ou le faisceau laser de se propager à travers le cristalliseur.

2.3 Caractérisation chimique du liquide

Le peroxyde d'hydrogène (H_2O_2) est considéré comme l'une des principales espèces de radicaux oxygénés générés par le plasma et peut être mesuré en raison de sa longue durée de vie. Sa concentration dans l'eau distillée traitée au plasma a été quantifiée à l'aide d'une technique colorimétrique. Dans cette étude, un volume de 10 ml d'eau ultra-pure a été soumis à la décharge plasma et immédiatement après le traitement, 100 µl de l'échantillon ont été mélangés à 5 µl d'azoture de sodium (NaN_3). Le but de cet ajout était d'éteindre efficacement les espèces réactives de l'azote (nitrite, nitrate) qui pourraient potentiellement interférer avec la mesure de la concentration en H_2O_2. Après cela, 50 µl d'oxysulfate de titane ($TiSO_4$) ont ensuite été ajoutés à la solution. Ce réactif aide à former un complexe coloré avec H_2O_2 comme mentionné précédemment, permettant sa détermination quantitative.

2.4 Nanoparticules métalliques

La synthèse des nanoparticules d'argent commence par la préparation de la solution de précurseur métallique. L'$AgNO_3$ (réactif ACS à 99+%, Sigma-Aldrich) a été dissous dans de l'eau déminéralisée filtrée. Le citrate trisodique dihydraté (Sigma-Aldrich) est ensuite ajouté à la solution comme agent stabilisant. L'inclusion du citrate dans le processus de synthèse est d'une importance capitale car il sert à la fois d'agent réducteur et de stabilisant. Pour examiner l'impact des concentrations de précurseurs et de stabilisants sur les nanoparticules résultantes, une variation systématique de leurs concentrations respectives a été utilisée. Ensuite, 10 ml de chaque solution préparée ont subi un traitement par jet de plasma à pression atmosphérique et température ambiante, pendant une durée définie et des paramètres de fonctionnement fixes, comprenant un courant d'alimentation de 8 A, une fréquence de 25 kHz.

La synthèse des nanoparticules d'or suit une méthodologie similaire, en commençant par la préparation de la solution de précurseur métallique. Le chlorure d'or (III) hydraté ($HAuCl_4 \cdot xH_2O$, 99,995 %, MW : 339,79 $g.mol^{-1}$, Sigma-Aldrich) a été dissous dans de l'eau ultrapure (Direct-Q UV, Millipore). La polyvinylpyrrolidone (PVP, MW : 40 000 $g.mol^{-1}$) a également été achetée chez Sigma-Aldrich et utilisée comme agent stabilisant des nanoparticules. Ces deux produits ont été utilisés tels qu'achetés, sans autre purification. En faisant varier les concentrations du précurseur d'or et du PVP, l'influence de ces paramètres sur les nanoparticules résultantes a été étudiée. Par la suite, de la même manière que pour la synthèse de nanoparticules d'argent, 10 ml de chaque solution préparée ont subi un traitement utilisant le jet de plasma à pression atmosphérique.

De nombreuses techniques de caractérisation des nanoparticules ont été développées pour analyser les propriétés des nanoparticules, fournissant ainsi des informations précieuses sur

leurs caractéristiques physiques et chimiques. Dans cette section, nous nous concentrerons sur les techniques utilisées pour l'analyse des nanoparticules métalliques. Nous pouvons classer ces techniques dans les divisions suivantes en fonction de leur nature :

Techniques spectroscopiques :

- Spectroscopie ultraviolet-visible (UV-vis) : utilisée pour déterminer les propriétés optiques des nanoparticules et identifier leurs bandes de résonance plasmonique.
- Diffusion dynamique de la lumière (DLS) : mesure la distribution de taille des nanoparticules en solution en analysant la lumière diffusée.

Techniques de microscopie électronique :

- Microscopie électronique à balayage (MEB) : fournit des images haute résolution de nanoparticules, révélant leur taille, leur forme et leur morphologie.
- Microscopie électronique à transmission (TEM) : offre des images détaillées des nanoparticules à un grossissement plus élevé, permettant une analyse précise de la taille et de la forme.

Techniques d'analyse de surfaces :

- Microscopie à force atomique (AFM) : capture des images tridimensionnelles de nanoparticules sur des surfaces, fournissant des informations topographiques.

Techniques d'analyse structurelle :

- Diffraction des rayons X (DRX) : identifie la structure cristalline des nanoparticules en analysant le diagramme de diffraction des rayons X.
- Spectroscopie de rayons X à dispersion électronique (EDX) : Détermine la composition élémentaire des nanoparticules en analysant les émissions de rayons X.

3 Synthèse de nanoparticules métalliques par jet de plasma à pression atmosphérique

3.1 Caractérisation du plasma

Dans cette section, nous présentons une analyse complète du spectre d'émission optique allant de 200 à 750 nm, illustrant les espèces excitées générées par la configuration plasma sous différents paramètres de processus plasma.

Nous avons utilisé un spectromètre d'émission optique placé perpendiculairement à la source pour identifier les espèces présentes dans le jet. L'émission lumineuse du jet de plasma est caractéristique de ces espèces. Cela a permis d'étudier la distribution de l'émission lumineuse en fonction de la longueur d'onde, sur l'ensemble du jet, offrant ainsi un aperçu de la chimie induite dans la phase liquide suite au traitement par le plasma. Au sein de la source, le plasma est principalement composé d'espèces d'hélium provenant du gaz. Les émissions de OH, N_2 et N_2^+ sont induites principalement par les impuretés de l'air diffusées dans le flux d'hélium gazeux depuis l'air ambiant.

La distribution spatiale des espèces réactives (OH, N_2, N_2^+ et He) le long du jet de plasma a été étudiée. Les mesures ont été effectuées le long du jet de plasma (axe Y) d'une longueur de 6 mm avec trois cibles différentes : a) jet libre, b) en contact avec une solution et c) en contact avec une surface plane.

Les résultats ont montré que la distribution spatiale des émissions d'espèces n'est pas uniforme le long du jet de plasma. Deux tendances se dégagent de ces courbes. Le premier vers OH (308 nm) et He (706 nm), où les deux espèces présentent de fortes intensités d'émission à la sortie du tube, qui diminuent ensuite progressivement le long du jet de plasma. Cela suggère que la décharge perd de l'énergie à mesure qu'elle s'éloigne de la sortie du tube, expliquant la diminution des émissions. La deuxième tendance est observée pour les profils N_2 (337 nm) et N_2^+ (391 nm) où leurs intensités augmentent dès la sortie du tube, atteignent leur maximum à Y= 3 mm de distance de la sortie, puis diminuent progressivement le long du jet. Ce phénomène peut être attribué au mélange du gaz plasmagène et de l'air atmosphérique ambiant. À la sortie du tube à décharge, la présence d'air est minime, conduisant à une réduction des émissions de ces bandes spectrales. Néanmoins, à mesure que l'on s'éloigne de la sortie, l'afflux d'air dans le plasma s'intensifie, entraînant des émissions élevées. Après cela, la quantité d'air dans le mélange atteint un niveau où elle devient suffisamment importante pour empêcher la poursuite de la propagation du plasma, ce qui se traduit par une diminution des émissions.

La proximité d'une solution située à 6 mm du tube et en contact avec le plasma a un impact subtil sur la répartition spatiale des émissions d'espèces. Deux tendances distinctes ont également émergé, les profils N2 (337 nm) et N_2^+ (391 nm) affichant également des intensités accrues à Y = 4 mm et Y = 5 mm, respectivement. Alors que OH (308 nm) et He (706 nm) présentaient des intensités d'émission maximales à la sortie du tube, ils ont ensuite connu une légère augmentation à Y = 4 mm et Y = 3 mm, respectivement, avant de diminuer. Ce phénomène est attribué à l'interaction entre le plasma et la solution.

De plus, un changement plus prononcé et notable dans la distribution spectrale des émissions d'espèces a été observé lorsqu'une surface plane servait de cible en contact avec le plasma à une distance de 6 mm du tube. Dans ce scénario, OH (308 nm) a affiché une tendance opposée, tandis que He (706 nm) a présenté une intensité minimale jusqu'à atteindre Y = 5 mm, où elle a augmenté pour atteindre son maximum. L'introduction de la surface plane a considérablement augmenté l'émission de He à proximité de la cible.

Par conséquent, la sélection et la présence d'une cible en contact avec le plasma possèdent le potentiel de remodeler à la fois la distribution et les intensités des espèces générées par le jet de plasma.

3.2 Carctérisation chimique du liquide

La concentration de H_2O_2 dans la solution liquide, déterminée par les expériences décrites dans la section précédente, a été examinée. Les résultats ont révélé une augmentation de la production de H_2O_2 avec une durée d'exposition plasma prolongée atteignant 1,8 mM après 10 minutes d'exposition plasma. Selon la littérature, pour atteindre une concentration de H_2O_2 de 1,8 mM dans l'eau, il fallait une exposition plasma de 30 minutes. Cependant, notre étude utilisant l'APPJ a montré un contraste remarquable, puisque cette concentration a été atteinte dans les 10 minutes suivant l'exposition au plasma en solution. Il est difficile de comparer la concentration mesurée de peroxyde d'hydrogène en raison des nombreux types de jets de plasma et de la large gamme de solutions d'intérêt biologique utilisées.

3.3 Synthèse de nanoparticules d'argent

La synthèse de nanoparticules d'argent a été réalisée à l'aide d'un jet de plasma d'hélium à pression atmosphérique en contact avec une solution liquide. Une solution aqueuse d'argent de 10 ml contenant du nitrate d'argent et du citrate a été préparée sans ajout d'aucun autre composé chimique. Par la suite, la solution a été exposée à la décharge plasma dans des conditions de fonctionnement spécifiques, notamment un courant de décharge de puissance d'entrée de 8 A, une fréquence de 25 kHz et un flux d'hélium gazeux réglé à 3 $L.min^{-1}$ à une

distance d'environ 6 mm de la sortie du jet de plasma. Au cours de l'exposition, un changement notable dans la couleur de la solution a été observé, la transformant du transparent au jaune brunâtre. Cette couleur distinctive de l'échantillon a servi d'indication spectroscopique distinctive de la formation de nanoparticules d'argent.

Une série d'expériences a été menée en utilisant cinq durées de décharge différentes, allant de 0 à 10 minutes (0 indiquant l'absence d'exposition au plasma). Pour ces expériences, nous avons maintenu les concentrations d'$AgNO_3$ et de citrate à 1 mM et 1,5 mM, respectivement. Les spectres d'absorption UV-visible ont été enregistrés pour vérifier la présence de bandes d'absorbance, avec une apparition observable d'une bande à 406 nm après une durée de 3 minutes, fournissant une validation supplémentaire de la synthèse réussie d'AgNP. Notamment, en l'absence de décharge plasma, aucune bande d'absorbance correspondante n'a été observée, confirmant l'absence de nanoparticules d'argent. Il était évident qu'une interaction plasma prolongée entraînait une augmentation de l'intensité de la bande d'absorption, résultat attendu en raison de la concentration plus élevée de nanoparticules d'argent formées. De plus, une légère diminution de la longueur d'onde de la bande d'absorption maximale, se déplaçant vers des longueurs d'onde plus courtes, était perceptible. Il est également important de noter qu'au-delà d'une durée de 7 minutes, la solution présente une réduction de volume, attribuée à l'évaporation partielle provoquée par une augmentation de température générée lors de l'exposition au plasma. Sur la base de ces informations, une durée d'exposition au plasma de 5 minutes a été considérée comme le choix optimal pour des investigations plus approfondies. Alors qu'une durée de 3 minutes présentait une faible efficacité de synthèse, comme l'indique une intensité de bande d'absorbance plus faible, l'intervalle de 5 minutes facilitait un taux efficace et uniforme de synthèse de nanoparticules d'argent.

Le nitrate d'argent ($AgNO_3$), un sel métallique solide, a été choisi comme précurseur pour la synthèse des nanoparticules d'argent. Conformément à la littérature existante, la concentration de précurseur sélectionnée est comprise entre 1 et 5 mM $AgNO_3$. Cinq échantillons présentant des concentrations variables de précurseur et une concentration constante de 3 mM de citrate ont été soumis à un traitement au plasma de 5 minutes. L'observation d'une coloration jaune dans les solutions lors de l'exposition au plasma a servi d'indicateur initial de la formation de nanoparticules d'argent. Ceci a été en outre corroboré par la présence d'une bande d'absorption dans le domaine visible, résultant de la résonance plasmonique de surface (SPR). L'absorbance UV-visible normalisée a été examinée. Plus précisément, les bandes d'absorbance maximales ont été observées à 405, 410, 415, 420 et 425 nm pour des concentrations de nitrate d'argent de 1, 2, 3, 4 et 5 mM, respectivement. À mesure que la concentration du précurseur augmente, les bandes s'élargissent. On observe l'apparition progressive d'un épaulement aux longueurs

d'onde plus élevées, conduisant éventuellement à l'émergence d'une seconde bande large, indiquant soit une augmentation de la taille des nanoparticules formées, soit la présence de deux tailles distinctes de nanoparticules d'argent dans la solution traitée. La déconvolution des spectres révèle de multiples bandes de plasmons, suggérant la présence de nanoparticules de tailles et de formes variables. Cette observation suggère qu'une concentration plus élevée de nitrate d'argent pourrait favoriser la croissance des particules.

L'agent stabilisant utilisé dans cette étude est le citrate trisodique déshydraté. Une série de solutions contenant 1 mM de nitrate d'argent et des concentrations variables de citrate allant de 0,05 à 6 mM ont été préparées, traitées et analysées par spectroscopie UV-visible. Des concentrations plus élevées de citrate trisodique dihydraté conduisent à des couleurs de solution plus foncées et à une intensité UV-visible accrue en raison de la formation d'un plus grand nombre de nanoparticules. Comme prévu, la longueur d'onde de la bande d'absorption est restée inchangée à 405 nm avec des concentrations de citrate variables, tandis que l'intensité de la bande a augmenté proportionnellement avec des concentrations de citrate plus élevées. Pour confirmer nos observations et obtenir un aperçu visuel des nanoparticules, une analyse microscopie a ensuite été réalisée. L'échantillon avec la plus faible concentration de citrate (0,1 mM) présente des nanoparticules sphériques bien dispersées, caractérisé par un diamètre moyen de 13 ± 2 nm, déterminé en mesurant 200 nanoparticules sélectionnées au hasard. En revanche, une augmentation de la concentration en citrate entraîne un changement visible dans l'apparence de l'échantillon, les nanoparticules ayant tendance à s'agréger et à former des amas plus grands. Ce phénomène peut être attribué au taux de production de nanoparticules plus élevé dans les solutions présentant des concentrations accrues de citrate.

Il a finalement été conclu que l'obtention de nanoparticules d'argent uniformément sphériques, caractérisées par un diamètre moyen de 13 ± 2 nm, dépendait de l'établissement d'un rapport optimal entre les concentrations de nitrate d'argent et de citrate. Ce rapport optimal s'est avéré être de 1 mM pour le nitrate d'argent et de 0,1 mM pour le citrate. Une durée de traitement au plasma de 5 minutes a été identifiée comme la durée optimale pour générer un rendement substantiel de nanoparticules.

3.4 Synthèse de nanoparticules d'or

La synthèse de nanoparticules d'or a été réalisée à l'aide d'un jet plasma d'hélium à pression atmosphérique en contact avec une solution liquide. Une solution aqueuse d'or de 10 ml contenant $HAuCl_4$ et PVP a été préparée sans ajout d'autres composés chimiques. Par la suite, la solution a été exposée à la décharge plasma dans des conditions de fonctionnement spécifiques, notamment un courant de décharge de puissance d'entrée de 8 A, une fréquence

de 25 KHz et un flux d'hélium gazeux réglé à 3 $L.min^{-1}$ à une distance d'environ 6 mm de la sortie du jet de plasma. Au cours de l'exposition, un changement notable dans la couleur de la solution a été observé, la transformant du jaune clair au violet. Cette couleur distinctive de l'échantillon a servi d'indication spectroscopique distinctive de la formation de nanoparticules d'or.

Une série d'expériences ont été menées en utilisant six durées de décharge différentes, allant de 0 à 15 minutes (0 indiquant l'absence d'exposition au plasma). Pour ces expériences, nous avons maintenu une concentration fixe de 1 mM de $HAuCl_4$ et de 0,05 mM de PVP. L'absorption UV-visible des solutions a été mesurée où l'apparition d'une bande d'absorbance détectable à 533 nm après 3 minutes a confirmé en outre la synthèse réussie des AuNP. Nous avons observé que l'intensité de la bande d'absorption augmentait avec une interaction plasma plus longue, suggérant une concentration plus élevée de nanoparticules d'or formées tandis que la bande maximale restait inchangée à 533 nm. Avec l'augmentation de la durée d'exposition au plasma, une épaule émerge progressivement à une longueur d'onde plus élevée, indiquant la présence de deux tailles de nanoparticules différentes et de certaines agglomérations. Cependant, à 3 et 5 minutes d'exposition, les bandes de plasmons présentaient un degré élevé de symétrie et d'étroitesse, avec une largeur totale à mi-hauteur (FWHM) de 54 et 56 nm, respectivement. Cela suggère que les nanoparticules avaient principalement la même forme et la même taille et que les échantillons ne contenaient pas de particules agglomérées. Alors que 3 minutes semblaient insuffisantes pour une synthèse efficace, comme en témoigne la faible intensité de la bande d'absorbance par rapport aux autres échantillons, 5 minutes permettaient un taux de synthèse efficace et uniforme des nanoparticules d'or. Sur la base de ces observations, nous avons choisi 5 minutes comme durée optimale d'exposition au plasma pour des études ultérieures.

Cette étude visait à étudier l'influence de diverses concentrations de $HAuCl_4$ sur la morphologie et la distribution de taille des nanoparticules d'Au tout en maintenant une concentration fixe de l'agent stabilisant, PVP, à 0,05 mM. Les spectres d'absorbance UV-vis et les spectres normalisés de cinq solutions différentes avec des concentrations de $HAuCl_4$ allant de 0,1 à 1,5 mM, après 5 minutes d'exposition par décharge plasma. Fait intéressant, à mesure que la concentration de $HAuCl_4$ augmentait, un décalage vers le rouge notable de la position de la bande de plasmon était observé, passant de 525 nm à 536 nm. Ce décalage vers le rouge est généralement associé à une augmentation de la taille des nanoparticules. La concentration du précurseur de 0,1 mM présentait la bande d'absorbance la plus symétrique et la plus étroite à 525 nm avec un FWHM de 50 nm. Les images TEM ont montré une nette différence dans la façon dont la taille et la forme moyennes des nanoparticules d'or sont fortement affectées par

les variations de la concentration du précurseur. Par exemple, à une concentration en $HAuCl_4$ de 0,1 mM, les nanoparticules présentaient une géométrie sphérique uniforme, marquée par la dispersion et l'homogénéité. À des concentrations plus élevées, les nanoparticules présentaient un diamètre moyen plus grand, avec un large éventail de formes, notamment des triangles, des bâtonnets, des pentagones, et présentaient également une certaine agrégation dans certains échantillons.

En utilisant des paramètres du plasma comme d'habitude et en maintenant 0,1 mM de $HAuCl_4$, des solutions distinctes ont été soumises à une exposition à un jet de plasma de 5 minutes, englobant des concentrations de PVP allant de 0 (en considérant 0 car aucune PVP n'a été ajoutée à la solution) à 0,1 mM. Le rôle crucial joué par le PVP est devenu évident, en particulier dans l'échantillon dépourvu de l'agent stabilisant, qui présentait une bande d'absorbance distincte et notable. Cette large bande est passée d'environ 525 nm à environ 550 nm. Cela signifie la présence de particules plus grosses et d'une agglomération importante au sein de la solution. Ce comportement optique a été corroboré par l'analyse TEM, présentant la nucléation et la croissance incontrôlées qui ont conduit à la présence de particules d'or importantes et agrégées. Au fur et à mesure que le PVP est introduit, l'agrégation diminue, conduisant à la formation de nanoparticules bien séparées, le processus se poursuivant jusqu'à ce qu'un certain seuil de concentration soit atteint. À 0,05 mM, la taille des particules résultante était constamment maintenue. L'imagerie TEM a révélé que ces nanoparticules présentaient uniformément un diamètre moyen de 13 ± 4 nm, la majorité présentant des caractéristiques sphériques, bien dispersées et séparées.

Il a finalement été conclu que l'obtention de nanoparticules d'or uniformément sphériques, caractérisées par un diamètre moyen de 13 ± 4 nm, dépendait de l'établissement d'un rapport optimal entre les concentrations d'acide chloroaurique et de PVP. Ce rapport optimal s'est avéré être de 0,1 mM pour l'acide chloroaurique et de 0,05 mM pour la PVP. Une durée de traitement au plasma de 5 minutes a été identifiée comme la durée optimale pour générer un rendement substantiel de nanoparticules.

4 Synthèse de nanoparticules métalliques par plasma à pression atmosphérique bi-fréquence

4.1 Caractérisation du plasma

Cette section présente une caractérisation du jet de plasma à pression atmosphérique à double fréquence (DF-APPJ) utilisé dans cette étude. La géométrie, ainsi les paramètres d'entrée APPJ (courant et fréquence) et les débits de gaz ont été maintenu constant. Il a été observé que l'ajout de puissance RF augmente l'intensité lumineuse du plasma. Ce comportement a été attribué à l'augmentation de l'apport d'énergie et à l'augmentation ultérieure de la densité électronique.

Les spectres d'émission optique correspondant à la condition de 30 W de puissance RF pour les deux espèces gazeuses sont analysés. Notamment, le plasma d'argon présente une intensité d'émission globale nettement supérieure à celle de l'hélium. Dans les deux cas, à côté des conduites de gaz de procédé, nous avons identifié des caractéristiques distinctes, notamment le deuxième système positif d'azote (N_2 SPS), la bande moléculaire OH, ainsi que des raies d'émission atomiques d'oxygène et d'hydrogène proéminentes. Avec la modification des niveaux de puissance RF, les caractéristiques et les caractéristiques globales d'émission des spectres sont restées cohérentes. Cependant, des changements ont été observés dans les intensités de certaines raies d'émission spécifiques. Les émissions aux longueurs d'onde 706 nm pour l'hélium et 738 nm pour l'argon ont été choisies comme représentatives des raies He I et Ar I, respectivement. L'intensité de l'émission dans l'argon démontre une augmentation constante avec l'augmentation de la puissance RF fournie à la décharge. A l'inverse, pour l'hélium, l'émission reste relativement constante. Une augmentation de la température de rotation est présente dans les deux décharges. La température de rotation dans le scénario de gaz de traitement à l'hélium reste systématiquement inférieure à 500 K, comme prévu, située 100 à 200 K inférieure à celle observée avec l'argon. La température plus basse est également mise en évidence par l'absence d'émissions de NH à 336 nm. L'augmentation de la formation de NH pour le plasma de gaz argon peut également être due à une évaporation plus élevée de la solution, comme en témoigne l'augmentation des émissions de bande OH, d'O I et de H_α. Le plasma produit par l'argon pourrait potentiellement présenter une plus grande densité, comme le suggère l'élargissement accru de Stark de la raie H_α par rapport aux conditions d'hélium. Notamment, au sein de la décharge d'hélium, une nette augmentation de la température vibratoire est évidente, cohérente avec son état d'équilibre externe. Néanmoins, la conséquence majeure de l'augmentation des niveaux de puissance RF est une intensité accrue des émissions de radicaux OH, à la fois dans les configurations à l'hélium et à l'argon.

La charge collectée sous la solution jusqu'au sol est également présentée pour les deux gaz de procédé à différents niveaux de puissance RF. Lorsque la RF n'était pas appliquée et que seule la microimpulsion était active, le jet de plasma atteignait la surface du liquide et la charge correspondante pouvait donc être collectée dans le condensateur situé sous la solution. Pendant la pré-impulsion aucune charge n'est collectée, indiquant l'absence d'ionisation résiduelle entre les répétitions d'impulsions. Lorsque l'électrode supérieure devient positive, les électrons migrent vers elle, laissant derrière eux une charge spatiale positive. Ces charges positives dérivent ensuite vers le liquide, donnant naissance à un front auto-propagatif à propagation rapide, qui se déploie en quelques dizaines de nanosecondes. Cette progression forme un canal ionisé reliant le liquide et l'électrode micropulsée. Par conséquent, les oscillations qui ont suivi ont conduit à un couplage capacitif, comme le signifient les formes étroitement alignées des oscillations de tension et de charge. De toute évidence, la charge collectée à l'aide de l'hélium est environ la moitié de celle de l'argon, ce qui correspond de manière cohérente aux différences de densité de plasma observées lors des mesures OES.

L'introduction de la puissance RF entraîne une augmentation notable de la charge maximale collectée par le liquide. Il est intéressant de noter que cette augmentation affiche une dépendance minimale aux niveaux de puissance RF, même en faisant varier les niveaux de puissance RF ajoutés, la charge maximale collectée reste cohérente. Cette augmentation de la charge maximale collectée est très probablement attribuée au déplacement d'une région de plasma plus dense de l'intérieur du tube d'alumine vers la sortie, où est positionnée l'électrode RF. Ce déplacement ressemble au rapprochement de l'électrode micropulsée de la surface du liquide. En conséquence, les champs électriques résultants sont intensifiés. De plus, le seuil supérieur de la charge collectée sur le condensateur, lorsque l'argon est utilisé, reflète directement sa densité de plasma plus élevée.

4.2 Influence de l'hélium en tant que gas de procédé sur la morphologie des nanoparticules

Nos résultats ont révélé que l'utilisation de concentrations de 0,1 mM de $HAuCl_4$ et de 0,05 mM de PVP produisait des nanoparticules présentant une bonne homogénéité, une distribution de taille étroite et une agglomération négligeable. Pour lancer cette enquête, nous avons préparé six échantillons distincts, chacun comprenant 10 ml d'une solution contenant le précurseur et l'agent stabilisant. Ces échantillons ont ensuite été soumis à un traitement plasma dans un environnement d'hélium, tout en faisant varier les conditions opérationnelles clés. Plus précisément, nous avons exploré différents niveaux de puissance RF (0, 15, 30 W) et durées d'exposition au plasma (10, 20 min). Les spectres d'absorbance des solutions de nanoparticules d'or traitées ont été traités pour différentes puissances RF et durées de

traitement. Comme prévu, un temps de traitement plus long conduit à une densité de particules plus élevée. Aucune variation significative de la densité des particules n'est observée en fonction de la puissance RF, conformément aux conclusions tirées par la caractérisation électrique du plasma. L'augmentation de la durée du traitement de 10 à 20 minutes n'a pas modifié de manière significative le profil de bande ni la position maximale de la longueur d'onde de la bande du plasmon, mais a entraîné une augmentation de l'intensité de la bande. La bande maximale s'est déplacée vers des longueurs d'onde inférieures lorsque la puissance RF a été introduite, passant de 535 nm sans puissance RF à 531 nm avec une puissance RF de 30 W. Bien que ce changement puisse potentiellement résulter d'une diminution de la taille des nanoparticules, il pourrait également résulter de l'ajout de puissance RF provoquant une transition de formes asymétriques. Pour confirmer davantage cette analyse, la microscopie électronique à balayage (MEB) a été utilisée pour visualiser les nanoparticules formées. Les résultats ont montré que les nanoparticules sont synthétisées sans ajout de puissance RF pendant 10 min et révèlent des formes exotiques autres que des sphères telles que des bâtonnets, des triangles et des pentagones d'un diamètre moyen de 28 ± 3 nm. À une puissance RF de 30 W, les particules sont sphériques et bien séparées, sans agglomérations visibles sur les images avec un diamètre moyen de 22 nm et un écart type de 3 nm. Reconnaissant que les données SEM pourraient ne pas fournir la précision nécessaire, nous avons effectué une analyse par microscopie à force atomique (AFM) comme étape supplémentaire pour valider les tailles obtenues et ils ont confirmé que l'ajout de RF entraînait une réduction de la taille des nanoparticules d'or.

4.3 Influence de l'argon en tant que gas de procédé sur la morphologie des nanoparticules d'or

Reflétant la méthodologie employée précédemment, nous préparerons six échantillons en utilisant une concentration constante de 0,1 mM de $HAuCl_4$ et 0,05 mM de concentrations de PVP. Par la suite, ces échantillons subiront un traitement plasma dans un environnement argon, chacun avec un niveau de puissance RF différent allant de 0 W à 30 W et avec différentes durées d'exposition au plasma (10, 20 min). Les résultats d'absorbance UV-visible ont révélé des distinctions dans le comportement des nanoparticules lorsque l'argon est utilisé comme gaz de procédé. Nous observons notamment que les caractéristiques spectrales présentent un changement minime entre les échantillons d'addition de puissance RF à 15 W et 30 W, ce qui suggère que le niveau de puissance RF n'a pas d'effet important sur la forme et la taille des nanoparticules d'or. Le contraste important, cependant, devient évident lorsque l'on compare les scénarios sans ajout de RF aux scénarios d'ajout de RF et à 20 minutes d'exposition au plasma. Cette différence est apparue sous la forme d'un décalage vers le bleu à partir de 538 nm sans ajout de puissance RF et seule la micropulse he-APPJ fonctionnant à

533 nm lorsqu'une puissance RF de 30 W a été ajoutée pour le traitement. Ce phénomène pourrait être attribué à la formation de nanoparticules plus petites au sein des échantillons, contribuant à ce changement prononcé. Des micrographies SEM ont été enregistrées sur les échantillons afin de visualiser la morphologie des nanoparticules et de valider les résultats UV-vis. Les micrographies obtenues représentent une nanoparticule d'or individuelle pour chaque échantillon, la nature sphérique des nanoparticules est apparente selon différentes puissances RF et durées de traitement. Une observation distincte émerge dans les échantillons traités avec une puissance RF de 30 W, par rapport à l'échantillon sans ajout de puissance RF, les nanoparticules présentent une réduction notable de leur taille. Ces résultats suggèrent que l'ajout d'un plasma RF joue un rôle crucial dans la détermination de la taille des nanoparticules synthétisées par le procédé DF-APPJ au plasma d'argon. L'analyse par microscopie à force atomique (AFM) a également été utilisée comme étape supplémentaire pour valider les tailles obtenues et a confirmé notre analyse.

4.4 Implications de la configuration plasma bi-fréquente sur la production de nanoparticules d'or

Lorsque l'on considère l'hélium comme gaz de traitement, une série d'effets entre en jeu, notamment des températures de traitement plus basses, une densité de plasma réduite et, par conséquent, une densité de courant réduite. Ces facteurs, même en l'absence de puissance RF supplémentaire et en s'appuyant uniquement sur la source de plasma micropulsée, conduisent à la génération de nanoparticules d'or caractérisées par des formes et des tailles diverses. Bien que les origines exactes de ces variations nécessitent une exploration plus approfondie, ce qui reste cohérent est l'impact du couplage RF. Pour l'hélium et l'argon en tant que gaz de traitement, l'introduction du couplage RF déclenche une réduction notable de l'intensité des épaulements de longueurs d'onde plus élevées. Cette réduction favorise la production de nanoparticules sphériques et induit également une diminution de la taille des nanoparticules. De façon intéressante, le taux de production de nanoparticules ne présente pas de relation linéaire avec les niveaux de puissance RF, ce qui concorde avec l'observation selon laquelle les processus catalysant la formation de nanoparticules proviennent principalement de l'interaction à l'interface plasma-liquide, plutôt qu'au sein du plasma lui-même. Afin de comprendre de tels phénomènes, nous devons considérer comment le couplage du générateur peut affecter le processus de production. Nous avons montré que le couplage de la RF fait principalement passer le plasma d'un régime auto-propagatif à une configuration à couplage capacitif. Lorsque le plasma est couplé aux RF, il peut influencer le mouvement des particules chargées (ions et électrons) au sein du plasma. Le flux total d'ions dans le liquide environnant reste relativement constant. Cependant, ce qui change, c'est la manière dont ces charges sont transmises au liquide. Dans le régime d'auto-propagation, la libération d'énergie peut être plus

soudaine et plus intense, conduisant potentiellement à des densités de courant plus élevées. Lorsque le couplage RF est introduit, ce processus devient plus progressif, entraînant une réduction de la densité de courant. Ce changement dans la manière dont les charges sont transférées au liquide peut avoir un impact significatif sur le processus de synthèse. Une libération plus progressive des charges, induite par le couplage RF, pourrait conduire à des conditions plus contrôlées et plus stables pour la création de nanoparticules. La libération soudaine de charges dans le régime d'auto-propagation pourrait conduire à des résultats plus imprévisibles, provoquant potentiellement une agglomération ou une croissance inégale des particules. En revanche, la libération plus contrôlée dans la configuration à couplage capacitif pourrait offrir une plus grande précision et un meilleur contrôle du processus de synthèse, ce qui donne des nanoparticules avec des tailles et des caractéristiques plus uniformes.

Ces résultats ont mis en évidence que la configuration à double fréquence, associée à l'incorporation de la puissance RF et au choix du gaz de traitement, présentait une voie polyvalente pour adapter les caractéristiques des nanoparticules en fonction de la modulation des paramètres clés du processus.

Conclusions

La convergence de la nanotechnologie et de la science des plasmas offre une voie passionnante pour la synthèse et la manipulation contrôlées de nanomatériaux aux propriétés adaptées.

Dans cette étude, nous avons exploré la synthèse de nanoparticules d'argent et d'or à l'aide d'un jet de plasma atmosphérique d'hélium. Nous avons trouvé que les conditions optimales pour la synthèse de nanoparticules d'argent étaient une durée d'exposition de 5 minutes, une concentration de nitrate d'argent de 1 mM et une concentration de citrate de 0,1 mM. Cela a donné des nanoparticules d'argent uniformément sphériques, caractérisées par un diamètre moyen de 13 ± 2 nm. Les conditions optimales pour la synthèse de nanoparticules d'or étaient une durée d'exposition de 5 minutes, une concentration d'acide chloraurique de 0,1 mM et une concentration de PVP de 0,05 mM. Cela a donné des nanoparticules d'or uniformément sphériques, caractérisées par un diamètre moyen de 13 ± 4 nm.

Les résultats de cette étude démontrent le potentiel de la synthèse assistée par plasma pour la production contrôlée de nanoparticules métalliques aux propriétés adaptables. Cette méthode offre plusieurs avantages par rapport aux méthodes traditionnelles, telles que :

- L'utilisation de conditions de réaction douces, qui minimisent les dommages aux nanoparticules et aux matériaux environnants.
- La capacité de produire des nanoparticules avec des distributions de taille étroites, ce qui est important pour de nombreuses applications.
- Le potentiel de fonctionnalisation in situ des nanoparticules, ce qui permet d'ajouter des groupes fonctionnels spécifiques à la surface des nanoparticules pour les rendre plus compatibles avec une application particulière.

L'étude a également examiné l'effet de différents paramètres plasma, tels que le choix de gaz utilisé, l'addition de deux alimentations, sur le processus de synthèse des nanoparticules. Les résultats ont montré que ces paramètres peuvent avoir un impact significatif sur la taille, la forme et la morphologie des nanoparticules. Par exemple, une augmentation de la puissance radiofréquence a été associée à une diminution de la taille des nanoparticules. Ces résultats suggèrent que la synthèse assistée par plasma peut être utilisée pour contrôler avec précision les propriétés des nanoparticules métalliques.

Perspectives

La capacité de contrôler les propriétés des nanoparticules métalliques par la synthèse assistée par plasma pourrait conduire à de nouvelles avancées dans divers domaines :

- L'activité antibactérienne des nanoparticules d'argent a été explorée en utilisant *Escherichia coli* et *Staphylococcus aureus* comme sujets d'essai. Les nanoparticules d'argent ont montré des effets antibactériens, avec des concentrations plus élevées entraînant une inhibition plus importante de la croissance bactérienne. Des investigations supplémentaires sont nécessaires pour comprendre les mécanismes et la toxicité potentielle.

- L'étude a également exploré l'amélioration de l'excitation anti-Stokes des ions néodyme trivalent en utilisant des nanoparticules métalliques. La décoration de particules sub-micrométriques avec des nanoparticules métalliques a conduit à des améliorations significatives de l'excitation anti-Stokes, montrant des perspectives pour diverses applications impliquant des matériaux luminescents.

- La synthèse de nanoparticules core-shell argent-or. La combinaison de ces métaux nobles dans des nanostructures cœur-coquille pourrait offrir des propriétés optiques et catalytiques uniques, mais des caractérisations et recherches supplémentaires sont nécessaires pour explorer cette direction pleinement.

Ces applications potentielles soulignent le potentiel de la synthèse assistée par plasma pour révolutionner la façon dont nous utilisons les nanomatériaux.

Resumo estendido

Resumo estendido

Introdução

Plasmas são geralmente gases ionizados neutros que compreendem partículas carregadas (íons e elétrons) e neutras (átomos, moléculas e radicais). Os avanços na engenharia de plasma fornecem novas aplicações para plasmas não térmicos em vários campos. Embora o tratamento e a modificação da superfície de materiais sensíveis ao calor tenham sido as primeiras aplicações dos plasmas frios, os avanços recentes ampliaram o seu escopo. Por exemplo, o plasma não térmico é agora utilizado na indústria alimentar para conceber superfícies revestidas com agentes antibacterianos para limitar a formação de biofilme. A sua utilização estendeu-se à área biomédica, nomeadamente na regeneração de tecidos, cicatrização de feridas, tratamento do câncer e descontaminação microbiológica de superfícies e líquidos. É importante ressaltar que os plasmas se tornaram uma ferramenta poderosa para a síntese de nanopartículas, com possível controle sobre o tamanho, a morfologia e outras características das nanopartículas.

A nanotecnologia tornou-se um campo amplo com aplicações abrangendo vários setores. A síntese de nanopartículas, especialmente na fase líquida, oferece vantagens significativas, notadamente a possibilidade de adaptar as propriedades superficiais das nanopartículas às aplicações específicas. Entre as nanopartículas metálicas mais estudadas estão as nanopartículas de prata e ouro devido às suas inúmeras aplicações em fotônica, eletrônica, biomedicina, sensores e cosméticos. Na química de soluções convencionais, os íons metálicos são normalmente expostos a uma fonte de energia, como calor ou luz UV, juntamente com um agente redutor, para converter os íons metálicos em nanopartículas metálicas. Esses métodos de síntese têm limitações em termos de processos e eficiências ecologicamente corretos. A síntese de nanopartículas por plasma aplicado a um líquido, por sua vez, gera elétrons altamente energéticos a partir de descargas de plasma. Essas espécies energéticas dissociam moléculas de água em radicais ($O^{\cdot}$, $H^{\cdot}$, $OH^{\cdot}$) e íons ($H2O^{+}$, O^{2-}), que participam da redução de íons metálicos em nanopartículas. Isso nos leva ao presente estudo, que apresenta um método de redução de plasma para a síntese de nanopartículas metálicas que atende aos seguintes critérios de processo:

Processo de uma etapa - Um processo simples, que requer o menor número possível de etapas de síntese

A abordagem é um processo simples, caracterizado pela sua simplicidade e eficiência, envolvendo apenas um número mínimo de etapas de síntese. O processo começa com a preparação da solução do reagente, operação simples. Esta preparação envolve a dissolução do

precursor e do agente estabilizante em água. Uma vez preparada esta solução, ela será exposta ao jato de plasma, iniciando uma sequência de reações responsáveis pela formação de nanopartículas.

Economia de tempo - Um processo de curto tempo de reação para a síntese de nanopartículas

Um aspecto particularmente notável deste método é a criação quase instantânea de nanopartículas, destacando a notável eficácia da nossa abordagem. A duração do tratamento desempenha um papel central nesta investigação, onde é examinada sua influência na morfologia e tamanho das nanopartículas.

Ecológico - Um processo que não utiliza reagentes nocivos e perigosos

Esta abordagem oferece vantagens distintas em relação às metodologias convencionais, que muitas vezes envolvem o uso de reagentes perigosos, resultando na geração de subprodutos nocivos e resíduos desnecessários. Notavelmente, a síntese conduzida por plasma reduz com sucesso os sais metálicos presentes na solução, isto é possível pelas espécies reativas criadas pelo plasma.

Esta tese está estruturada em duas partes principais, cada uma empregando uma configuração distinta de jato de plasma para a síntese de nanopartículas metálicas. A primeira parte gira em torno da utilização de um jato de plasma de hélio à pressão atmosférica, equipado com uma fonte assimétrica de vidro borossilicato conectada a uma fonte de alimentação pulsada. Esta seção discute a produção de nanopartículas de prata e ouro separadamente. É realizada uma investigação aprofundada, explorando o impacto da duração da exposição plasmática, concentração do precursor e concentração do agente estabilizador nas características das nanopartículas sintetizadas.

Na segunda parte desta tese é estudada uma configuração diferente do plasma. Aqui, é usado um jato de plasma de pressão atmosférica de dupla frequência, consistindo de um tubo de aluminio conectado à fonte de alimentação de pulso e a um gerador de energia de RF. Esta configuração é explorada para estudar a síntese de nanopartículas de ouro. A investigação nesta parte concentra-se na compreensão dos efeitos e implicações dos principais parâmetros físicos do processo, incluindo a escolha do gás de processo e a adição de níveis de potência de RF nas características das nanopartículas de ouro sintetizadas.

O objetivo principal deste estudo é estudar a síntese de nanopartículas de prata e ouro utilizando um jato de plasma à pressão atmosférica em contato com uma solução aquosa de sal metálico através de estudos paramétricos.

Esta tese é composta por quatro capítulos divididos em seções:

Capítulo 1 pretende-se fornecer uma revisão da literatura: os conceitos fundamentais da nanotecnologia, as características ópticas, químicas e elétricas, as aplicações das nanopartículas de prata e ouro, os métodos de síntese (abordagens top-down e bottom-up) e plasmas frios.

Capítulo 2 fornece detalhes sobre os equipamentos e métodos experimentais utilizados ao longo deste trabalho: configurações experimentais de dispositivos de plasma, ferramentas de diagnóstico (elétrico e óptico), quantificação da concentração de peróxido de hidrogênio em solução, preparação e caracterização de nanopartículas metálicas de prata e ouro (tamanho, morfologia, etc.).

Capítulo 3 apresenta os resultados da síntese de nanopartículas de prata e ouro por jato de plasma à pressão atmosférica utilizando fornecimento de pulso com hélio como gás de tratamento para a geração da descarga: espectroscopia de emissão óptica (OES), distribuição espacial de espécies reativas, caracterização química do solução líquida, efeitos da duração da interação do plasma, da concentração do precursor metálico e da concentração do agente estabilizador no processo de síntese, efeito na sua forma e tamanho.

Capítulo 4 apresenta os resultados da síntese de nanopartículas de ouro por jato de plasma de pressão atmosférica de dupla frequência utilizando uma fonte de alimentação de micropulsos e um gerador de energia de RF para a geração da descarga de plasma: espectroscopia de emissão óptica com hélio ou argônio, temperaturas, níveis de potência nas características das nanopartículas.

Por fim, este trabalho termina com uma conclusão geral apresentando os resultados da nossa investigação, bem como as perspectivas.

1 Revisão da literatura

1.1 Introdução à Nanotecnologia

A nanotecnologia tornou-se um campo revolucionário de pesquisa e avanço tecnológico, oferecendo novas oportunidades para projetar e manipular materiais em nanoescala. A nanotecnologia é definida como o projeto, síntese, manipulação e caracterização de materiais cujas dimensões variam de 1 a 100 nanômetros. Porém, nesta escala, o comportamento da matéria pode desviar-se consideravelmente daquele observado em materiais na escala macro, dando origem a novas aplicações. A capacidade de projetar materiais nos níveis atômico e molecular possui um enorme potencial para o desenvolvimento de materiais avançados com funcionalidade personalizada e desempenho aprimorado, inaugurando uma nova era de descoberta científica e inovação tecnológica. A próxima revolução industrial poderá vir da nanotecnologia. A história da nanotecnologia remonta a tempos antigos, quando os humanos interagiam inconscientemente com materiais em nanoescala. No entanto, o estudo formal e o desenvolvimento da nanotecnologia como um campo separado começaram no século XX.

1.2 Nanomateriais: classificações e propriedades

Em geral, os nanomateriais podem ser classificados com base na sua composição, estrutura, morfologia e dimensão. Ao categorizar os nanomateriais com base na sua composição, fornece informações sobre os tipos de materiais que existem em nanoescala e suas propriedades distintas. Além disso, compreender a dimensionalidade dos nanomateriais permite-nos explorar as suas características estruturais e implicações em diversas aplicações. Primeiro, com base na sua composição, os nanomateriais podem ser amplamente classificados em materiais orgânicos e inorgânicos. Em segundo lugar, os nanomateriais também podem ser classificados com base na sua dimensionalidade, que se refere ao número de dimensões confinadas à nanoescala.

Os nanomateriais possuem uma gama de propriedades únicas que os diferenciam de seus equivalentes em massa. Essas propriedades são devidas ao seu pequeno tamanho e alta relação superfície-volume, levando a uma melhor capacidade de resposta e um comportamento novo. Algumas propriedades principais dos nanomateriais metálicos incluem propriedades ópticas, químicas e elétricas que serão detalhadas abaixo.
Nanopartículas metálicas exibem propriedades ópticas únicas, como ressonância de plasmôn de superfície localizados (LSPR), que resulta da interação da luz com elétrons livres. A absorção e dispersão da luz pelas nanopartículas metálicas podem ser ajustadas ajustando seu tamanho, forma e composição. Esta propriedade específica é a propriedade mais notável das nanoestruturas metálicas. Tudo começou no início do século XX com Gustav Mie quando

publicou o seu trabalho em 1908 explicando as surpreendentes propriedades ópticas dos colóides metálicos.

Nanopartículas metálicas exibem parâmetros químicos distintos que contribuem para suas propriedades e aplicações únicas. Primeiro, a química superficial das nanopartículas metálicas pode ser controlada com precisão pela funcionalização ou modificação de suas superfícies com ligantes, moléculas ou polímeros. Esta modificação de superfície permite interações personalizadas com outras substâncias, possibilitando aplicações específicas, como distribuição e detecção direcionada de medicamentos. Em segundo lugar, a sua reatividade superficial é significativamente melhorada devido à elevada relação superfície-volume. Esta maior reatividade os torna excelentes catalisadores em diversas reações químicas, onde sua presença acelera a taxa de reação.

As nanopartículas metálicas possuem propriedades elétricas notáveis que contribuem para sua ampla gama de aplicações. Primeiro, a sua natureza metálica confere-lhes uma condutividade eléctrica excepcional, permitindo um fluxo electrônico eficiente. Isso os torna valiosos em diversos campos, incluindo eletrônica, armazenamento de energia e revestimentos condutores. Em segundo lugar, em nanoescala, as nanopartículas metálicas podem apresentar efeitos de confinamento quântico. Esses efeitos resultam do movimento restrito de elétrons dentro das nanopartículas, resultando em níveis de energia discretos.

1.3 Aplicações de nanopartículas de prata e ouro

As propriedades acima mencionadas das nanopartículas metálicas são a principal razão para suas diversas aplicações em diversos campos. Com base nas suas características distintivas, estas nanopartículas encontram utilidade prática numa variedade de campos:

- Aplicações antibacterianas

As nanopartículas de prata exibem um mecanismo de ação único contra bactérias, tornando-as altamente eficazes na inibição do crescimento bacteriano e na prevenção de infecções. O pequeno tamanho e a grande área superficial das nanopartículas de prata melhoram sua interação com as células bacterianas, permitindo a penetração e rompimento eficiente das membranas celulares.

- ### Aplicações biomédicas

Nanossistemas baseados em nanopartículas de prata (AgNPs) surgiram como candidatos promissores para o transporte de diversas substâncias terapêuticas, como aquelas com propriedades antiinflamatórias, antioxidantes e anticancerígenas. E devido à sua atividade antimicrobiana, são adequados para diversas aplicações na cicatrização de feridas, engenharia de tecidos e controle de infecções. Além disso, as nanopartículas de ouro, devido às suas propriedades ópticas únicas, abriram caminho para aplicações em biossensor, imagem e terapia direcionada.

- ### Aplicações de catálise

AgNPs exibem excelente atividade catalítica devido às suas propriedades de superfície únicas e alta relação superfície-volume. A grande área superficial das AgNPs fornece numerosos sítios ativos para interações com moléculas reativas, promovendo assim uma conversão catalítica eficiente. Nanopartículas de ouro também são utilizadas como catalisadores devido às suas propriedades físico-químicas. Eles exibem uma capacidade de resposta notável mesmo em condições amenas, incluindo temperatura ambiente ou inferior.

- ### Aplicações eletrônicas

Nanopartículas de prata, por exemplo, são utilizadas em tintas condutoras e produtos eletrônicos impressos, possibilitando a criação de circuitos eletrônicos flexíveis e leves. Da mesma forma, as nanopartículas de ouro são utilizadas em vários dispositivos eletrônicos, particularmente na forma de revestimentos condutores, devido à sua estabilidade química e condutividade excepcional. A sua integração em sistemas eletrónicos garante um desempenho elétrico fiável e eficiente.

- ### Aplicativos de detecção

Apesar das muitas vantagens da prata sobre o ouro, como seus maiores coeficientes de extinção, bandas de extinção mais nítidas e maior relação difusão-extinção, ela foi menos comumente usada no desenvolvimento de sensores, com exceção de sensores baseados em espectroscopias aprimoradas de superfície. Isto se deve principalmente à menor estabilidade química das nanopartículas de prata em comparação ao ouro.

1.4 Métodos de síntese

Vários métodos sintéticos já foram desenvolvidos, permitindo aos pesquisadores adaptar o tamanho, a forma e as propriedades das nanopartículas a aplicações específicas e desbloquear todo o seu potencial em diferentes campos. Os métodos de síntese de nanopartículas podem ser amplamente classificados em duas abordagens principais: a abordagem *top-down* e a abordagem *bottom-up*.

A abordagem *top-down* começa com um material em macroescala, que então sofre redução de tamanho por meio de processos físicos e químicos para produzir partículas minúsculas como nanopartículas. Alguns métodos de síntese de cima para baixo incluem litografia, fresagem mecânica e ablação a laser.
A abordagem bottom-up utiliza átomos individuais e os transforma em nanomateriais maiores. Esta abordagem é amplamente utilizada para a síntese de nanopartículas porque oferece controle preciso sobre o tamanho, forma, composição e propriedades de superfície das nanopartículas. As abordagens bottom-up comumente usadas são síntese química, deposição química de vapor (CVD), método sol-gel e redução de plasma.

1.5 Introdução aos plasmas

Plasma é muitas vezes chamado de "quarto estado da matéria" junto ao sólido, líquido e gasoso. É um estado físico distinto no qual o gás se torna ionizado e é caracterizado por um grande número de partículas carregadas livres. Da mesma forma que a aplicação de energia faz com que um líquido ferva e se transforme em gás, o fornecimento de energia ao gás pode levar à criação de um plasma. Este plasma pode ser descrito como uma mistura de partículas carregadas, compostas por íons carregados positivamente e elétrons carregados negativamente. Somos capazes de projetar plasmas com propriedades únicas que encontraram muitas aplicações práticas em vários campos.

1.6 Plasmas: classificações e propriedades

Em geral, os plasmas podem ser classificados com base em vários fatores. Primeiro, com base na sua origem, os plasmas podem ser classificados em descargas plasmáticas naturais e provocadas pelo homem. Em segundo lugar, as descargas de plasma podem ser amplamente classificadas de acordo com a sua temperatura e grau de ionização. Os plasmas também podem ser classificados com base na sua pressão, que desempenha um papel crucial no seu comportamento e características. De modo geral, os plasmas podem ser classificados em três grupos principais: plasmas de baixa pressão, plasmas de pressão atmosférica e plasmas de alta pressão.

Os plasmas frios de pressão atmosférica têm recebido considerável atenção nos últimos anos devido à sua capacidade de operar em condições ambientais, tornando-os muito acessíveis e práticos para muitas aplicações. Esses plasmas oferecem muitos benefícios, incluindo processos de processamento eficientes e econômicos, modificações aprimoradas na superfície dos materiais e geração de espécies reativas para síntese química. Normalmente, os plasmas frios à pressão atmosférica são alimentados e mantidos através da aplicação de energia elétrica de diferentes fontes. Uma das principais propriedades do plasma frio é a sua capacidade de gerar espécies reativas enquanto mantém uma temperatura mais baixa do gás. Espécies reativas, incluindo íons, elétrons, radicais e moléculas excitadas podem interagir com materiais ou sistemas biológicos, levando a reações químicas, funcionalização de superfície e ataque seletivo. Outra propriedade importante do plasma frio é o seu confinamento espacial e alta energia eletrônica. Esta alta energia eletrônica no plasma frio permite a transferência eficiente de energia e a ativação de reações químicas, tornando-o útil para processamento de materiais, deposição de filmes finos e síntese assistida por plasma. O plasma frio também exibe propriedades elétricas e eletromagnéticas únicas. Pode ser facilmente ativado e mantido usando diversas fontes de energia; levando às reações químicas, funcionalização de superfície e ataque seletivo. Outra propriedade importante do plasma frio é o seu confinamento espacial e alta energia eletrônica. Esta alta energia eletrônica no plasma frio permite a transferência eficiente de energia e a ativação de reações químicas, tornando-o útil para processamento de materiais, deposição de filmes finos e síntese assistida por plasma. O plasma frio também exibe propriedades elétricas e eletromagnéticas únicas.

1.7 Aplicações de descargas de plasma

Os plasmas frios, com suas propriedades únicas e suas diferentes configurações experimentais, encontraram inúmeras aplicações em diversos campos:

- **Síntese química**

Os plasmas frios proporcionam um ambiente único para a formação controlada de nanopartículas. Introduzindo gases precursores no plasma ou expondo o plasma a uma solução contendo o precursor. Graças às diversas reações químicas induzidas pelas espécies reativas criadas pelo fluxo de plasma, as nanopartículas podem ser sintetizadas com controle preciso de seu tamanho, composição e morfologia. Este método permite a produção de nanopartículas com propriedades adaptadas.

- Tratamento de água

Uma aplicação importante do plasma frio é o tratamento de água, onde espécies reativas geradas pelo plasma, como radicais hidroxila e ozônio, podem efetivamente decompor contaminantes orgânicos e destruir microorganismos nocivos, fornecendo um método econômico e ecologicamente correto para purificação de água sem a necessidade de fontes externas de compostos como peróxido de hidrogênio e ozônio.

- Medicamento

O plasma atmosférico frio pode ser usado para curar pele, dentes e feridas, pois é adequado para tratamento in situ de tecidos vivos. Além disso, tem sido investigado como potencial para tratamentos de câncer devido à sua capacidade de induzir seletivamente a apoptose em células cancerígenas, poupando células saudáveis. Isto se deve principalmente à presença de RONS (espécies reativas de oxigênio e nitrogênio) no plasma.

1.8 Interações plasma-líquido

Quando um plasma entra em contato com um líquido, ocorre toda uma série de processos físicos e químicos, dando origem a fenômenos únicos. Um aspecto importante das interações plasma-líquido é a geração de espécies reativas no líquido, tais como espécies reativas de oxigênio e espécies reativas de nitrogênio. Existem muitas geometrias de reatores com princípios de funcionamento distintos, a configuração dos eletrodos determina se as descargas de plasma estão em contato direto com a fase líquida ou estão posicionadas acima do líquido e não têm contato direto.

Nas descargas de plasma acima da fase líquida, as interações entre o jato de plasma e a superfície de um líquido são divididas em três fases:

- Fase gasosa

Na fase gasosa, o jato de plasma é composto por um fluxo onde se formam espécies reativas primárias. Estes incluem partículas carregadas (íons e elétrons), átomos ou moléculas excitadas. Espécies reativas como OH, O^{2-} e $^1O_2$, caracterizadas por tempos de vida de 2 ns, 1 µs e 4 µs, respectivamente, são produzidas diretamente na região de descarga devido à interação entre o fornecimento de elétrons e moléculas de gás, e são impulsionadas em direção à superfície do líquido.

- **Fase interfacial plasma-líquido**

Esta fase ocorre quando o jato de plasma entra em contato com a superfície do líquido. As reações químicas que ocorrem neste nível resultam de interações entre espécies reativas primárias e moléculas presentes no ambiente circundante. Essas espécies são convertidas em espécies secundárias de vida longa, como peróxido de hidrogênio (H_2O_2), nitrito (NO_2), nitrato (NO_3) e ozônio (O_3). Em contato com a superfície do líquido, difundem-se no líquido, que corresponde à terceira fase.

- **Fase líquida**

Na fase líquida, os efeitos iniciados na fase interfacial propagam-se ainda mais para a fase líquida. As espécies reativas geradas na interface líquido-gás podem difundir-se no líquido e participar de diversas reações químicas. Estas reações podem envolver degradação de compostos orgânicos, modificação de propriedades superficiais ou geração de novos compostos.

1.9 Síntese de nanopartículas metálicas por jato de plasma à pressão atmosférica

Plasmas de pressão atmosférica em contato com um líquido fornecem uma abordagem vantajosa para a síntese de nanopartículas metálicas em condições ambientes e oferecem diversas vantagens, como a geração de uma grande quantidade de RONS que podem induzir reações químicas dentro de soluções e reduzir íons metálicos no líquido meio para produzir nanopartículas metálicas sem a necessidade de agentes redutores adicionais que poderiam ser considerados tóxicos. As reações de redução podem ser iniciadas por transferência de elétrons ou por transferência de átomos de hidrogênio de espécies reativas geradas por plasma. Após a redução do precursor metálico, o próximo passo na síntese de nanopartículas metálicas envolve processos de nucleação e crescimento, conforme já discutido na abordagem bottom-up para a síntese de nanopartículas. A nucleação envolve a agregação de átomos metálicos para formar aglomerados ou núcleos. Esses núcleos servem de base para o crescimento posterior. Através de vários mecanismos, os átomos metálicos agregam-se e acumulam-se nos núcleos existentes, levando ao crescimento de nanopartículas. À medida que mais átomos metálicos são adicionados, as nanopartículas aumentam de tamanho e massa, atingindo gradativamente as dimensões desejadas. A nucleação envolve a agregação de átomos metálicos para formar aglomerados ou núcleos. Esses núcleos servem como base para o crescimento futuro. Através de vários mecanismos, os átomos metálicos agregam-se e acumulam-se nos núcleos existentes, levando ao crescimento de nanopartículas. À medida que mais átomos metálicos são

adicionados, as nanopartículas aumentam de tamanho e massa, atingindo gradativamente as dimensões desejadas.

O tamanho e a forma das nanopartículas formadas em sistemas de descarga de plasma à pressão atmosférica são influenciados por parâmetros químicos e físicos. Assim, o controle dos parâmetros químicos e físicos em sistemas de descarga de plasma à pressão atmosférica é essencial durante o processo de síntese para alcançar os resultados desejados.

Os parâmetros químicos incluem a concentração de precursores metálicos e estabilizantes. A concentração de precursores metálicos determina a disponibilidade de íons metálicos para o processo de redução, influenciando assim o tamanho das nanopartículas resultantes. Concentrações mais altas de precursores geralmente levam a nanopartículas maiores devido ao aumento das taxas de nucleação e crescimento. Por outro lado, a concentração de agentes estabilizantes, frequentemente utilizados para controlar o tamanho e a estabilidade das nanopartículas, também pode afetar o seu tamanho e forma final. Eles podem se ligar às superfícies das nanopartículas e inibir seu crescimento, levando a nanopartículas menores e mais uniformes.
Parâmetros físicos, como a corrente aplicada, a distância entre o jato de plasma e o líquido e a duração da descarga, também desempenham um papel crucial na síntese de nanopartículas. A corrente afeta a energia e a temperatura do plasma, que por sua vez influenciam as reações de redução e a dinâmica de crescimento de nanopartículas, afetando os processos de nucleação e crescimento. A distância entre o jato de plasma e a superfície do líquido determina o tempo de exposição do líquido ao plasma, influenciando na cinética da reação e na formação de nanopartículas. Além disso, a duração da descarga, ou a duração total da exposição ao plasma, afeta a extensão das reações de redução e o crescimento das nanopartículas.

1.10 Metas e objetivos desta tese

O principal objetivo deste estudo é investigar o caminho emergente da convergência da nanotecnologia e da ciência do plasma, com foco na síntese e manipulação precisas de nanopartículas metálicas, particularmente prata e nanopartículas de prata. Este trabalho de tese irá aprofundar o aspecto crítico da síntese de nanopartículas dentro das nanotecnologias, destacando a importância de compreender e controlar as suas propriedades. A primeira fase da pesquisa é dedicada à caracterização do sistema de jato de plasma de hélio à pressão atmosférica conectado a uma fonte de alimentação pulsada. Outro objetivo central é a síntese de nanopartículas de prata e ouro utilizando o mesmo jato de plasma, envolvendo a exposição de uma solução aquosa de sais metálicos à descarga de plasma, seguido de uma caracterização. Da mesma forma, a fase seguinte é dedicada à caracterização de um jato de plasma de pressão

atmosférica de dupla frequência conectado a uma fonte de alimentação pulsada e a um gerador de RF. O objetivo é compreender a dinâmica complexa da formação de nanopartículas, particularmente sob condições variadas do gás do processo (hélio ou argônio) e potência de radiofrequência (RF), usando um jato de plasma à pressão atmosférica de dupla frequência.

2 Materiais e métodos

2.1 Configurações Experimentais de Plasma

Neste estudo, utilizamos duas configurações distintas de plasma para investigar seus efeitos na síntese de nanopartículas.

O jato de plasma à pressão atmosférica usado para gerar o plasma consiste em uma fonte assimétrica, uma fonte de alimentação e um fluxo de gás. Esta fonte assimétrica é composta de vidro borossilicato e consiste em um tubo de 4 mm de diâmetro em torno do qual é enrolado o eletrodo de alta tensão, além de um reservatório maior, de aproximadamente 35 mm de diâmetro, conectado ao eletrodo terra. Os eletrodos estão localizados fora da fonte e são feitos de alumínio (fita 3M, 425, espessura 120 µm). A configuração da fonte permite gerar uma descarga de plasma na parte superior, que depois se propaga no tubo menor, formando um jato de plasma. Na saída de cada tubo, as espécies reativas produzidas durante a descarga interagem com os componentes do ar ambiente, depois com o líquido alvo. A fonte de alimentação de alta tensão da empresa OLISCIE é utilizada para gerar a descarga. Os dois eletrodos na configuração experimental têm 25 mm de comprimento e estão espaçados aproximadamente 15 mm. A distância entre a extremidade do tubo pequeno e o eletrodo mede 8 mm. O gás utilizado para criar o plasma é 99,80% de hélio fornecido pela empresa Linde.

O jato de plasma de pressão atmosférica de dupla frequência inclui dois conjuntos de eletrodos de anel posicionados a aproximadamente 5 mm de distância, com cada conjunto conectado a fontes de alimentação separadas. A primeira fonte de alimentação, adquirida da empresa OLISCIE, utiliza tecnologia patenteada que aplica pulsos rápidos de tensão a uma carga capacitiva. A segunda fonte de alimentação é conectada a um eletrodo em forma de anel acoplado a um gerador de RF operando a 27,12 MHz (Seren R301) através de uma rede correspondente. Um fluxo controlado de gás é introduzido através de um tubo na fonte de plasma e entra no ar ambiente. O ar flui para resfriar os eletrodos e controlar a atmosfera ao redor do jato de plasma.

Várias ferramentas de medição têm sido utilizadas para caracterizar o plasma do ponto de vista elétrico e óptico.
Medições elétricas são realizadas para obter informações sobre a geração e dinâmica da descarga. Estas medições permitem calcular a potência e a energia depositada pela descarga. Todos os sinais elétricos são visualizados e registrados simultaneamente usando um osciloscópio digital (Rohde & Schwarz) com largura de banda de 2 GHz e taxa de amostragem de 5 GSa/s. A sonda de corrente está conectada ao eletrodo de alta tensão. Este é um modelo Pearson

Electronics 6585 com faixa de frequência de 40 Hz a 250 MHz e sensibilidade de 1 V/A. É fundamental ressaltar que a corrente de entrada da fonte de alimentação é de 8A, enquanto a corrente medida entregue pela fonte de alimentação é de aproximadamente 1,2A.

A espectroscopia de emissão óptica (OES) é uma técnica poderosa usada para analisar o espectro de emissão óptica de um jato de plasma. O princípio deste método é que átomos e íons excitados no plasma emitem luz característica em comprimentos de onda específicos quando retornam ao seu estado fundamental. Durante a descarga de plasma, os elétrons são excitados para níveis de energia mais elevados e, quando desexcitam, emitem fótons. Ao espalhar a luz emitida através de um espectrômetro, os comprimentos de onda emitidos podem ser separados e medidos, revelando informações valiosas sobre a composição elementar e os estados de excitação do plasma.

A configuração experimental utilizada para diagnóstico óptico consiste em uma fibra óptica de 600 µm de diâmetro conectada a um monocromador de alta resolução (Princeton Instrument, HRS-750) com distância focal de 75 mm. O monocromador está equipado com três redes de difração: 300 linhas.mm-1, 2.400 linhas.mm-1 e 3.600 linhas.mm-1. O espectro foi registrado no ponto de saída do jato de plasma da fonte, bem como em intervalos de 1 mm na direção axial até 6 mm, onde a distância entre a saída do jato e as amostras foi fixada em 6mm.

2.2 Alvo tratado com plasma

Um alvo líquido, contido num cristalizador, é posicionado sob o jato de plasma. Este cristalizador pode conter água ultrapura (Sistema de purificação de água Millipore Direct-Q 3 UV, Thermo Fisher Scientific) e, exceto quando especificado, a distância entre a saída da fonte e a superfície do líquido é fixada em 6 mm. O volume de líquido tratado é fixado em 10 mL, exceto para medições por absorção a laser e espectroscopia de emissão óptica, onde o volume de líquido preenche completamente o cristalizador. Esta precaução é tomada para evitar que a luz de plasma ou o feixe de laser se propaguem através do cristalizador.

2.3 Caracterização química do líquido

O peróxido de hidrogênio (H2O2) é considerado uma das principais espécies de radicais de oxigênio gerados no plasma e pode ser medido devido ao seu longo tempo de vida. Sua concentração em água destilada tratada com plasma foi quantificada por técnica colorimétrica. Neste estudo, um volume de 10 ml de água ultrapura foi submetido à descarga de plasma e imediatamente após o tratamento, 100 µl da amostra foram misturados com 5 µl de azida sódica (NaN3). O objetivo desta adição foi extinguir efetivamente as espécies reativas de nitrogênio (nitrito, nitrato) que poderiam potencialmente interferir na medição da

concentração de H2O2. Depois disso, 50 µl de oxissulfato de titânio (TiSO4) foram adicionados à solução.

2.4 Nanopartículas metálicas

A síntese de nanopartículas de prata começa com a preparação da solução precursora metálica. AgNO3 (99% de reagente ACS, Sigma-Aldrich) foi dissolvido em água desionizada filtrada. Citrato trissódico di-hidratado (Sigma-Aldrich) é então adicionado à solução como agente estabilizante. A inclusão do citrato no processo de síntese é de suma importância, pois serve tanto como agente redutor quanto como estabilizador. Para examinar o impacto das concentrações de precursor e estabilizador nas nanopartículas resultantes, foi utilizada uma variação sistemática de suas respectivas concentrações. Em seguida, 10 ml de cada solução preparada foram tratados com jato de plasma à pressão atmosférica e temperatura ambiente, por tempo definido e parâmetros operacionais fixos,

A síntese das nanopartículas de ouro segue metodologia semelhante, começando pela preparação da solução precursora do metal. O hidrato de cloreto de ouro (III) ($HAuCl_4 \cdot xH_2O$, 99,995%, PM: 339,79 g.mol-1, Sigma-Aldrich) foi dissolvido em água ultrapura (Direct-Q UV, Millipore). A polivinilpirrolidona (PVP, PM: 40.000 g.mol-1) também foi adquirida da Sigma-Aldrich e usada como agente estabilizante de nanopartículas. Estes dois produtos foram utilizados tal como adquiridos, sem purificação adicional. Variando as concentrações do precursor de ouro e PVP, foi estudada a influência desses parâmetros nas nanopartículas resultantes.

Muitas técnicas de caracterização de nanopartículas foram desenvolvidas para analisar as propriedades das nanopartículas, fornecendo assim informações valiosas sobre suas características físicas e químicas. Nesta seção, focaremos nas técnicas utilizadas para a análise de nanopartículas metálicas. Podemos classificar essas técnicas nas seguintes divisões com base em sua natureza:

Técnicas espectroscópicas:

- Espectroscopia ultravioleta-visível (UV-vis): usada para determinar as propriedades ópticas de nanopartículas e identificar suas bandas de ressonância plasmônica.
- Dispersão Dinâmica de Luz (DLS): mede a distribuição de tamanho de nanopartículas em solução analisando o espalhamento de luz.

Técnicas de microscopia eletrônica:

- Microscopia eletrônica de varredura (MEV): fornece imagens de nanopartículas em alta resolução, revelando seu tamanho, forma e morfologia.
- Microscopia Eletrônica de Transmissão (MET): Fornece imagens detalhadas de nanopartículas em maior ampliação, permitindo análise precisa de tamanho e forma.

Técnicas de análise de superfície:

- Microscopia de força atômica (AFM): Captura imagens tridimensionais de nanopartículas em superfícies, fornecendo informações topográficas.

Técnicas de análise estrutural:

- Difração de raios X (DRX): identifica a estrutura cristalina das nanopartículas por meio da análise do padrão de difração de raios X.
- Espectroscopia de raios X dispersivos de elétrons (EDX): Determina a composição elementar de nanopartículas por meio da análise de emissões de raios X.

3 Síntese de nanopartículas metálicas por jato de plasma à pressão atmosférica

3.1 Caracterização plasmática

Nesta seção, apresentamos uma análise abrangente do espectro de emissão óptica variando de 200 a 750 nm, ilustrando as espécies excitadas geradas pela configuração do plasma sob diferentes parâmetros do processo de plasma.

Utilizamos um espectrômetro de emissão óptica colocado perpendicularmente à fonte para identificar as espécies presentes no jato. A emissão de luz do jato de plasma é característica dessas espécies. Isto permitiu estudar a distribuição da emissão de luz em função do comprimento de onda, ao longo de todo o jato, oferecendo assim uma visão da química induzida na fase líquida após o tratamento com plasma. Dentro da fonte, o plasma é composto principalmente por espécies de hélio do gás. As emissões de OH, N_2 e N_2^+ são induzidas principalmente por impurezas do ar difundidas no fluxo de gás hélio do ar ambiente.

A distribuição espacial das espécies reativas (OH, N_2, N_2^+ e He) ao longo do jato de plasma foi estudada. As medições foram realizadas ao longo do jato de plasma (eixo Y) com comprimento de 6 mm com três alvos diferentes: a) jato livre, b) em contato com uma solução e, c) em contato com uma superfície plana.

Os resultados mostraram que a distribuição espacial das emissões das espécies não é uniforme ao longo do jato de plasma. Duas tendências emergem dessas curvas. A primeira em direção ao OH (308 nm) e ao He (706 nm), onde ambas as espécies apresentam altas intensidades de emissão na saída do tubo, e depois diminuem gradativamente ao longo do jato de plasma. Isto sugere que a descarga perde energia à medida que se afasta da saída do tubo, explicando a diminuição das emissões. A segunda tendência é observada para os perfis N2 (337 nm) e N2+ (391 nm) onde suas intensidades aumentam a partir da saída do tubo, atingem seu máximo em Y = 3 mm de distância da saída e depois diminuem gradativamente ao longo do jato. Este fenômeno pode ser atribuído à mistura do gás plasma e do ar atmosférico ambiente. Na saída do tubo de descarga a presença de ar é mínima, levando à redução das emissões destas bandas espectrais. No entanto, à medida que nos afastamos da saída, o influxo de ar no plasma intensifica-se, levando a emissões elevadas. Depois disso, a quantidade de ar na mistura atinge um nível onde se torna grande o suficiente para impedir a propagação do plasma, resultando em emissões mais baixas.

A proximidade de uma solução localizada a 6 mm do tubo e em contato com o plasma tem um impacto sutil na distribuição espacial das emissões de espécies. Também surgiram duas tendências distintas, com os perfis N2 (337 nm) e N2+ (391 nm) também exibindo intensidades aumentadas em Y = 4 mm e Y = 5 mm, respectivamente. Embora OH (308 nm) e He (706 nm) exibissem intensidades de pico de emissão na saída do tubo, eles experimentaram um ligeiro aumento em Y = 4 mm e Y = 3 mm, respectivamente, antes de diminuir. Este fenômeno é atribuído à interação entre o plasma e a solução.

Além disso, uma mudança mais pronunciada e perceptível na distribuição espectral das emissões das espécies foi observada quando uma superfície plana serviu de alvo em contato com o plasma a uma distância de 6 mm do tubo. Neste cenário, OH (308 nm) apresentou tendência oposta, enquanto He (706 nm) apresentou intensidade mínima até atingir Y=5 mm, onde aumentou até atingir seu máximo. A introdução da superfície plana aumentou significativamente a emissão de He próximo ao alvo.

Portanto, a seleção e presença de um alvo em contato com o plasma tem o potencial de remodelar tanto a distribuição quanto as intensidades das espécies geradas pelo jato de plasma.

3.2 Caracterização química do líquido

A concentração de H2O2 na solução líquida, determinada pelos experimentos descritos na seção anterior, foi examinada. Os resultados revelaram um aumento na produção de H2O2 com duração prolongada da exposição plasmática atingindo 1,8 mM após 10 minutos de exposição plasmática. Segundo a literatura, para atingir concentração de H2O2 de 1,8 mM em água foi necessária uma exposição plasmática de 30 minutos. Porém, nosso estudo utilizando APPJ mostrou um contraste notável, uma vez que essa concentração foi atingida 10 minutos após a exposição ao plasma em solução. É difícil comparar a concentração medida de peróxido de hidrogênio devido aos diversos tipos de jatos de plasma e à ampla gama de soluções de interesse biológico utilizadas.

3.3 Síntese de nanopartículas de prata

A síntese das nanopartículas de prata foi realizada utilizando jato de plasma de hélio à pressão atmosférica em contato com uma solução líquida. Uma solução aquosa de prata de 10 mL contendo nitrato e citrato de prata foi preparada sem adição de quaisquer outros compostos químicos. Posteriormente, a solução foi exposta à descarga de plasma sob condições operacionais específicas, incluindo uma corrente de descarga de energia de entrada de 8 A, uma frequência de 25 kHz, e um fluxo de gás hélio ajustado em 3 L.min-1 a uma distância de aproximadamente 6 mm da saída do jato de plasma. Durante a exposição foi observada uma

notável mudança na cor da solução, transformando-a de transparente para amarelo acastanhado.

Uma série de experimentos foi realizada utilizando cinco durações de descarga diferentes, variando de 0 a 10 minutos (0 indicando ausência de exposição ao plasma). Para estes experimentos, mantivemos as concentrações de AgNO3 e citrato em 1 mM e 1,5 mM, respectivamente. Os espectros de absorção UV-visível foram registrados para verificar a presença de bandas de absorbância, com um aparecimento observável de uma banda em 406 nm após uma duração de 3 minutos, proporcionando validação adicional do sucesso da síntese de AgNP. Notavelmente, na ausência de descarga plasmática, não foi observada banda de absorbância correspondente, confirmando a ausência de nanopartículas de prata. Ficou evidente que a interação plasmática prolongada levou a um aumento na intensidade da banda de absorção, resultado esperado devido à maior concentração de nanopartículas de prata formadas. Além disso, foi perceptível uma ligeira diminuição no comprimento de onda da banda de absorção máxima, mudando para comprimentos de onda mais curtos. É importante notar também que além da duração de 7 minutos, a solução apresenta redução de volume, atribuída à evaporação parcial causada pelo aumento de temperatura gerado durante a exposição ao plasma. Com base nesta informação, uma duração de exposição plasmática de 5 minutos foi considerada a escolha ideal para investigações adicionais. Embora a duração de 3 min tenha exibido baixa eficiência de síntese, conforme indicado pela menor intensidade da banda de absorbância no espectro eletrônico.
O nitrato de prata (AgNO3), um sal metálico sólido, foi escolhido como precursor para a síntese de nanopartículas de prata. Consistente com a literatura existente, a concentração do precursor selecionado está entre 1 e 5 mM de AgNO3. Cinco amostras com concentrações variadas de precursor e uma concentração constante de citrato 3 mM foram submetidas a um tratamento com plasma durante 5 minutos. A observação da coloração amarela nas soluções após exposição ao plasma serviu como indicador inicial da formação de nanopartículas de prata. Isto foi ainda corroborado pela presença de uma banda de absorção na faixa visível, resultante da ressonância plasmônica de superfície (SPR). A absorvância UV-visível normalizada foi examinada. Mais precisamente, bandas máximas de absorbância foram observadas em 405, 410, 415, 420 e 425 nm para concentrações de nitrato de prata de 1, 2, 3, 4 e 5 mM, respectivamente. À medida que a concentração do precursor aumenta, as bandas alargam-se. Observamos o aparecimento progressivo de um ombro em comprimentos de onda mais elevados, possivelmente levando ao surgimento de uma segunda banda larga, indicando ou um aumento no tamanho das nanopartículas formadas, ou a presença de dois tamanhos distintos de nanopartículas de prata na solução tratada. A deconvolução dos espectros revela múltiplas bandas de plasmons, sugerindo a presença de nanopartículas de diversos tamanhos e formas. Esta observação sugere

que uma concentração mais elevada de nitrato de prata poderia promover o crescimento de partículas.

O agente estabilizador utilizado neste estudo é o citrato trissódico desidratado. Uma série de soluções contendo nitrato de prata 1 mM e concentrações variadas de citrato variando de 0,05 a 6 mM foram preparadas, processadas e analisadas por espectroscopia UV-visível. Concentrações mais altas de citrato trissódico di-hidratado levam a cores mais escuras da solução e aumentam a intensidade do UV-visível devido à formação de mais nanopartículas. Como esperado, o comprimento de onda da banda de absorção permaneceu inalterado em 405 nm com concentrações variadas de citrato, enquanto a intensidade da banda aumentou proporcionalmente com concentrações mais altas de citrato. Para confirmar nossas observações e obter uma visão geral das nanopartículas, uma análise microscópica foi então realizada. A amostra com menor concentração de citrato (0,1 mM) apresenta nanopartículas esféricas bem dispersas, caracterizadas por diâmetro médio de 13 ± 2 nm, determinado pela medição de 200 nanopartículas selecionadas aleatoriamente. Em contraste, um aumento na concentração de citrato resulta em uma mudança visível na aparência da amostra, com as nanopartículas tendendo a agregar-se e formar aglomerados maiores. Este fenômeno pode ser atribuído à maior taxa de produção de nanopartículas em soluções com concentrações maiores de citrato.

Concluiu-se finalmente que a obtenção de nanopartículas de prata uniformemente esféricas, caracterizadas por um diâmetro médio de 13 ± 2 nm, dependia do estabelecimento de uma relação ótima entre as concentrações de nitrato e citrato de prata. Esta proporção ideal foi de 1 mM para nitrato de prata e 0,1 mM para citrato. Uma duração de tratamento com plasma de 5 min foi identificada como a duração ideal para gerar um rendimento substancial de nanopartículas.

3.4 Síntese de nanopartículas de ouro

A síntese das nanopartículas de ouro foi realizada utilizando jato de plasma de hélio à pressão atmosférica em contato com uma solução líquida. Uma solução aquosa de ouro contendo 10 mL contendo HAuCl4 e PVP foi preparada sem adição de outros compostos químicos. Posteriormente, a solução foi exposta à descarga de plasma sob condições operacionais específicas, incluindo uma corrente de descarga de energia de entrada de 8 A, uma frequência de 25 KHz e um fluxo de gás hélio ajustado em 3 $L.min^{-1}$ a uma distância de aproximadamente 6 mm da saída do jato de plasma. Durante a exposição foi observada uma notável mudança na cor da solução, transitando de amarelo claro para roxo. Esta cor distinta da amostra serviu como uma indicação espectroscópica da formação de nanopartículas de ouro.

Uma série de experimentos foi realizada utilizando seis tempos de descarga diferentes, variando de 0 a 15 minutos (0 indicando ausência de exposição ao plasma). Para estes experimentos, mantivemos uma concentração fixa de 1 mM de HAuCl4 e 0,05 mM de PVP. A absorção UV-visível das soluções foi medida onde a detecção de uma banda de absorvância detectável em 533 nm após 3 min confirmou ainda mais o sucesso da síntese de AuNPs. Observamos que a intensidade da banda de absorção aumentou com maior interação plasmática, sugerindo uma maior concentração de nanopartículas de ouro formadas enquanto a banda de pico permaneceu inalterada em 533 nm. Com o aumento do tempo de exposição ao plasma, um ombro emerge gradualmente em um comprimento de onda mais alto, indicando a presença de dois tamanhos diferentes de nanopartículas e algumas aglomerações. Porém, aos 3 e 5 min de exposição, as bandas de plasmon exibiram um alto grau de simetria e estreiteza, com largura total na metade do máximo (FWHM) de 54 e 56 nm, respectivamente. Isto sugere que as nanopartículas tinham em sua maioria o mesmo formato, além de que as amostras não continham partículas aglomeradas. Embora 3 min sugerir ser insuficiente para uma síntese eficiente, como evidenciado pela baixa intensidade da banda de absorção em comparação com outras amostras, 5 min permitiram uma taxa de síntese eficiente e uniforme de nanopartículas de ouro.

Este estudo teve como objetivo investigar a influência de várias concentrações de HAuCl4 na morfologia e distribuição de tamanho de nanopartículas de Au, mantendo uma concentração fixa do agente estabilizador, PVP, em 0,05 mM. Foram obtidos espectros de absorbância UV-vis e espectros normalizados de cinco soluções diferentes, com concentrações de $HAuCl_4$ variando de 0,1 a 1,5 mM, e após 5 minutos de exposição à descarga plasmática. Curiosamente, à medida que foi aumentada a concentração de $HAuCl_4$ aumentou, foi observado um notável desvio para o vermelho na posição da banda plasmônica, de 525 nm para 536 nm. Este desvio para o vermelho está geralmente associado a um aumento no tamanho das nanopartículas. A concentração precursora de 0, 1 mM exibiu a banda de absorvância mais simétrica e estreita a 525 nm com um FWHM de 50 nm. As imagens de MET mostraram uma clara diferença em como o tamanho e a forma médios das nanopartículas de ouro são fortemente afetados por variações na concentração do precursor. Por exemplo, a uma concentração de HAuCl4 de 0,1 mM, as nanopartículas exibiram uma geometria esférica uniforme, marcada pela dispersão e homogeneidade. Em concentrações mais elevadas, as nanopartículas exibiram um diâmetro médio maior, com uma ampla gama de formas, incluindo triângulos, bastonetes, pentágonos, e também exibiram alguma agregação em algumas amostras.

Utilizando parâmetros plasmáticos já definidos e mantendo HAuCl4 0,1 mM, as soluções separadas foram expostas a um jato de plasma de 5 min, abrangendo concentrações de PVP variando de 0 (considerando 0 porque nenhum PVP foi adicionado à solução) a 0,1 mM. O

papel crucial desempenhado pelo PVP tornou-se evidente, especialmente na amostra sem estabilizante, que exibiu uma banda de absorvância distinta e perceptível. Esta banda larga passou de cerca de 525 nm para cerca de 550 nm. Isto significa a presença de partículas maiores e aglomeração significativa dentro da solução. Este comportamento óptico foi corroborado pela análise TEM, exibindo nucleação e crescimento descontrolados que levaram à presença de grandes partículas de ouro agregadas. À medida que o PVP é introduzido, a agregação diminui, levando à formação de nanopartículas bem separadas, continuando o processo até que um determinado limite de concentração seja atingido. A 0,05 mM, o tamanho de partícula resultante foi mantido constante. A imagem MET revelou que essas nanopartículas exibiam uniformemente um diâmetro médio de 13 ± 4 nm, com a maioria exibindo características esféricas, bem dispersas e separadas. O processo continua até que um certo limite de concentração seja atingido.

Concluiu-se finalmente que a obtenção de nanopartículas de ouro uniformemente esféricas, caracterizadas por diâmetro médio de 13 ± 4 nm, dependia do estabelecimento de uma relação ótima entre as concentrações de ácido cloroáurico e PVP. Esta proporção ideal foi de 0,1 mM para ácido cloroáurico e 0,05 mM para PVP. Uma duração de tratamento com plasma de 5 min foi identificada como a duração ideal para gerar um rendimento substancial de nanopartículas.

4 Síntese de nanopartículas metálicas por plasma de pressão atmosférica de dupla frequência

4.1 Caracterização plasmática

Esta seção apresenta uma caracterização do jato de plasma de pressão atmosférica de dupla frequência (DF-APPJ) utilizado neste estudo. A geometria, bem como os parâmetros de entrada do APPJ (corrente e frequência) e as vazões de gás foram mantidos constantes. Foi observado que aumentar a potência de RF aumenta a intensidade da luz do plasma. Esse comportamento foi atribuído ao aumento da entrada de energia e subsequente aumento na densidade eletrônica.

Foram analisados os espectros de emissão óptica correspondentes à condição de 30 W de potência de RF para as duas espécies de gases. Notavelmente, o plasma de argônio exibe uma intensidade geral de emissão significativamente maior que a do hélio. Em ambos os casos, ao lado das linhas de gás de processo, identificamos características distintas, incluindo o segundo sistema positivo de nitrogênio (N2 SPS), a banda molecular OH, bem como linhas de emissão atômica de oxigênio e hidrogênio. Com a mudança dos níveis de potência de RF, as características gerais de emissão e as características dos espectros permaneceram consistentes. No entanto, foram observadas alterações nas intensidades de algumas linhas de emissão específicas. Emissões em comprimentos de onda de 706 nm para hélio e 738 nm para argônio foram escolhidas como representativas das linhas He I e Ar I, respectivamente. A intensidade de emissão no argônio demonstra um aumento constante com o aumento da potência de RF fornecida à descarga. Por outro lado, para o hélio, a emissão permanece relativamente constante. Um aumento na temperatura rotacional está presente em ambas as descargas. A temperatura de rotação no cenário de gás tratado com hélio permanece majoritariamente abaixo de 500 K, como esperado, localizada 100 a 200 K abaixo daquela observada com argônio. A temperatura mais baixa também é evidenciada pela ausência de emissões de NH em 336 nm. O aumento da formação de NH para o plasma de gás argônio também pode ser devido à maior evaporação da solução, como evidenciado pelo aumento das emissões da banda OH, O I e Hα O plasma produzido por argônio poderia potencialmente exibir maior densidade, como sugerido pelo aumento do alargamento de Stark da linha Hαem comparação com as condições de hélio. Notavelmente, dentro da descarga de hélio, é evidente um claro aumento na temperatura vibracional, consistente com o seu estado de equilíbrio externo. No entanto, a principal consequência do aumento dos níveis de potência de RF é um aumento da intensidade das emissões de radicais OH, tanto nas configurações de hélio como de argônio, conforme evidenciado pelo aumento das emissões da banda OH, O I e Hα

A carga coletada sob a solução para o solo também é apresentada para os dois gases de processo em diferentes níveis de potência de RF. Quando a RF não foi aplicada e apenas o micropulso estava ativo, o jato de plasma atingiu a superfície do líquido e, portanto, a carga correspondente pôde ser coletada no capacitor localizado abaixo da solução. Durante o pré-pulso nenhuma carga é coletada, indicando que não há ionização residual entre as repetições do pulso. Quando o eletrodo superior se torna positivo, os elétrons migram em direção a ele, deixando para trás uma carga espacial positiva. Essas cargas positivas então derivam em direção ao líquido, dando origem a uma frente de autopropagação que se propaga rapidamente e desdobra em algumas dezenas de nanossegundos. Esta progressão forma um canal ionizado conectando o líquido e o eletrodo micropulsado. Portanto, as oscilações que se seguiram levaram ao acoplamento capacitivo, conforme indicado pelas formas estreitamente alinhadas das oscilações de tensão e carga. Claramente, a carga coletada com o hélio é cerca de metade da do argônio, consistente com as diferenças na densidade do plasma observadas nas medições OES.

A introdução da potência de RF resulta num aumento notável na carga máxima recolhida pelo líquido. Curiosamente, este aumento apresenta uma dependência mínima dos níveis de potência de RF, mesmo ao variar os níveis de potência de RF adicionados, a carga máxima coletada permanece constante. Este aumento na carga máxima coletada é provavelmente atribuído ao movimento de uma região de plasma mais densa do interior do tubo de alumina em direção à saída, onde o eletrodo de RF está posicionado. Este movimento assemelha-se à aproximação do eletrodo micropulsado à superfície do líquido. Como resultado, os campos elétricos resultantes são intensificados. Além disso, o limite superior da carga coletada no capacitor, quando o argônio é usado,

4.2 Influência do hélio como gás de processo na morfologia das nanopartículas

Nossos resultados revelaram que o uso de concentrações de HAuCl4 0,1 mM e PVP 0,05 mM produziu nanopartículas com boa homogeneidade, distribuição estreita de tamanho e aglomeração insignificante. Para iniciar esta investigação, preparamos seis amostras separadas, sendo todas uma solução de 10 mL contendo o precursor e o agente estabilizante. Essas amostras foram então submetidas ao processamento de plasma em ambiente de hélio, variando as principais condições operacionais. Especificamente, exploramos diferentes níveis de potência de RF (0, 15, 30 W) e durações de exposição ao plasma (10, 20 min). Os espectros de absorbância das soluções de nanopartículas de ouro tratadas foram processados para diferentes potências de RF e tempos de tratamento. Como esperado, um tempo de processamento mais longo leva a uma densidade de partículas mais alta. Nenhuma variação significativa na densidade das partículas é observada em função da potência de RF, condizente com as

conclusões tiradas da caracterização elétrica do plasma. O aumento da duração do tratamento de 10 para 20 minutos não alterou significativamente o perfil da banda ou a posição do pico do comprimento de onda da banda plasmônica, mas resultou em um aumento na intensidade da banda. A banda máxima mudou para comprimentos de onda mais baixos quando a potência de RF foi introduzida, de 535 nm sem potência de RF para 531 nm com potência de RF de 30 W. Embora esta mudança possa potencialmente resultar de uma redução no tamanho das nanopartículas, também poderia resultar da adição de potência de RF causando uma transição de formas assimétricas. Para confirmar ainda mais esta análise, foi utilizada microscopia eletrônica de varredura (MEV) para visualizar as nanopartículas formadas. Os resultados mostraram que as nanopartículas sintetizadas sem adição de potência de RF por 10 min revelam formas exóticas além de esferas, como bastões, triângulos e pentágonos com diâmetro médio de 28 $\pm$ 3 nm. Na potência de RF de 30 W, as partículas são esféricas e bem separadas, sem aglomerações visíveis nas imagens com diâmetro médio de 22 nm e desvio padrão de 3 nm.

4.3 Influência do argônio como gás de processo na morfologia de nanopartículas de ouro

Espelhando a metodologia empregada anteriormente, prepararemos seis amostras usando uma concentração constante de 0,1 mM de HAuCl4 e 0,05 mM de PVP. Posteriormente, essas amostras serão submetidas a tratamento de plasma em ambiente de argônio, cada uma com um nível de potência de RF diferente variando de 0 W a 30 W e com diferentes durações de exposição ao plasma (10, 20 min). Os resultados de absorbância UV-visível revelaram distinções no comportamento das nanopartículas quando o argônio é usado como gás de processo. Em particular, observamos que as características espectrais mostram uma alteração mínima entre as amostras de adição de potência de RF em 15 W e 30 W, o que sugere que o nível de potência de RF não tem um efeito significativo na forma e no tamanho das nanopartículas de ouro. O contraste significativo, no entanto, torna-se evidente quando se comparam os cenários de adição sem RF com os cenários de adição de RF e 20 minutos de exposição ao plasma. Essa diferença apareceu como um deslocamento para o azul de 538 nm sem adição de potência de RF e apenas o micropulso he-APPJ operando a 533 nm quando 30 W de potência de RF foram adicionados para processamento. Este fenômeno pode ser atribuído à formação de nanopartículas menores nas amostras, contribuindo para esta mudança pronunciada. Micrografias MEV foram registradas nas amostras para visualizar a morfologia das nanopartículas e validar os resultados UV-vis. As micrografias obtidas representam uma nanopartícula de ouro individual para cada amostra, a natureza esférica das nanopartículas é aparente sob diferentes potências de RF e tempos de tratamento. Uma observação distinta emerge nas amostras tratadas com potência de RF de 30 W, em comparação com a amostra sem potência de RF adicionada, as nanopartículas mostram uma redução notável no tamanho. Estes resultados sugerem que a

adição de um plasma RF desempenha um papel crucial na determinação do tamanho das nanopartículas sintetizadas pelo método DF-APPJ ao plasma de argônio. A análise de microscopia de força atômica (AFM) também foi utilizada como etapa adicional para validar os tamanhos obtidos e confirmou nossa análise.

4.4 Implicações da configuração do plasma de dupla frequência na produção de nanopartículas de ouro

Ao considerar o hélio como gás de processo, uma série de efeitos entram em jogo, incluindo temperaturas de processo mais baixas, densidade de plasma reduzida e, portanto, densidade de corrente reduzida. Esses fatores, mesmo na ausência de potência adicional de RF e contando apenas com a fonte de plasma micropulsado, levam à geração de nanopartículas de ouro caracterizadas por diversos formatos e tamanhos. Embora as origens exatas dessas variações exijam uma exploração mais aprofundada, o que permanece consistente é o impacto do acoplamento de RF. Para o hélio e o argônio como gases de processo, a introdução do acoplamento de RF desencadeia uma redução notável na intensidade dos ombros de comprimento de onda mais elevados. Esta redução promove a produção de nanopartículas esféricas e também induz uma diminuição no tamanho das nanopartículas. Curiosamente, a taxa de produção de nanopartículas não exibe uma relação linear com os níveis de potência de RF, consistente com a observação de que os processos que catalisam a formação de nanopartículas surgem principalmente da interação na interface plasma-líquido, e não dentro do próprio plasma. Para compreender tais fenômenos, devemos considerar como o acoplamento do gerador pode afetar o processo de produção. Mostramos que o acoplamento de RF muda principalmente o plasma de um regime de autopropagação para uma configuração acoplada capacitivamente. Quando o plasma é acoplado à RF, pode influenciar o movimento de partículas carregadas (íons e elétrons) dentro do plasma. O fluxo total de íons no líquido circundante permanece relativamente constante. Porém, o que muda é a forma como essas cargas são transmitidas ao líquido. No regime de autopropagação, a liberação de energia pode ser mais repentina e intensa, levando potencialmente a densidades de corrente mais altas. Quando o acoplamento RF é introduzido, este processo torna-se mais gradual, resultando numa redução na densidade de corrente. Esta mudança na forma como as cargas são transferidas para o líquido pode ter um impacto significativo no processo de síntese. Uma liberação mais gradual das cargas, induzida pelo acoplamento RF, poderia levar a condições mais controladas e estáveis para a criação de nanopartículas. A liberação repentina de cargas no regime de autopropagação poderia levar a resultados mais imprevisíveis, causando potencialmente aglomeração ou crescimento desigual de partículas. Em contrapartida, a liberação mais controlada na configuração acoplada capacitivamente poderia proporcionar maior precisão e

controle sobre o processo de síntese, resultando em nanopartículas com tamanhos e características mais uniformes.

Esses resultados destacaram que a configuração de frequência dupla, juntamente com a incorporação de potência de RF e a escolha do gás de processo, apresentou uma rota versátil para adaptar as características das nanopartículas com base na modulação dos principais parâmetros do processo.

Conclusões

A convergência da nanotecnologia e da ciência do plasma oferece um caminho interessante para a síntese e manipulação controlada de nanomateriais com propriedades personalizadas.

Neste estudo, exploramos a síntese de nanopartículas de prata e ouro usando um jato de plasma de hélio atmosférico. Descobrimos que as condições ideais para a síntese de nanopartículas de prata foram um tempo de exposição de 5 minutos, uma concentração de nitrato de prata de 1 mM e uma concentração de citrato de 0,1 mM. Estas condições produziram nanopartículas de prata uniformemente esféricas, caracterizadas por um diâmetro médio de 13 ± 2 nm. As condições ótimas para a síntese de nanopartículas de ouro foram tempo de exposição de 5 minutos, concentração de ácido cloroáurico de 0,1 mM e concentração de PVP de 0,05 mM, produzindo nanopartículas de ouro uniformemente esféricas, caracterizadas por um diâmetro médio de 13 ± 4 nm.

Os resultados deste estudo demonstram o potencial da síntese assistida por plasma para a produção controlada de nanopartículas metálicas com propriedades adaptáveis. Este método oferece diversas vantagens em relação aos métodos tradicionais, tais como:

- O uso de condições de reação suaves, que minimizam os danos às nanopartículas e aos materiais circundantes.
- A capacidade de produzir nanopartículas com distribuições de tamanho estreitas, o que é importante para muitas aplicações.
- O potencial para funcionalização *in situ* de nanopartículas, que permite que grupos funcionais específicos sejam adicionados à superfície das nanopartículas para torná-las mais compatíveis com uma aplicação específica.

O estudo também examinou o efeito de diferentes parâmetros do plasma, como a escolha do gás utilizado e a adição de duas fontes de alimentação no processo de síntese de nanopartículas. Os resultados mostraram que estes parâmetros podem ter um impacto significativo no tamanho, forma e morfologia das nanopartículas. Por exemplo, um aumento na potência da radiofrequência tem sido associado a uma diminuição no tamanho das nanopartículas. Estes resultados sugerem que a síntese assistida por plasma pode ser usada para controlar com precisão as propriedades das nanopartículas metálicas.

Perspectivas

A capacidade de controlar as propriedades das nanopartículas metálicas através da síntese assistida por plasma pode levar a novos avanços em vários campos:

- A atividade antibacteriana das nanopartículas de prata foi explorada usando *Escherichia coli*e e *Staphylococcus aureus* como cobaias. As nanopartículas de prata apresentaram efeitos antibacterianos, com concentrações mais elevadas resultando em maior inibição do crescimento bacteriano. Mais investigações são necessárias para compreender os mecanismos e a potencial toxicidade.

- O estudo também explorou o aumento da excitação anti-Stokes de íons trivalentes de neodímio usando nanopartículas metálicas. A decoração de partículas submicrométricas com nanopartículas metálicas levou a melhorias significativas na excitação anti-Stokes, mostrando perspectivas para diversas aplicações envolvendo materiais luminescentes.

- A síntese de nanopartículas núcleo-invólucro prata-ouro. A combinação desses metais nobres em nanoestruturas núcleo-invólucro poderia oferecer propriedades ópticas e catalíticas únicas, porém, são necessárias mais caracterizações e pesquisas para explorar completamente essa direção.

Estas aplicações potenciais destacam o potencial da síntese assistida por plasma para revolucionar a forma como usamos os nanomateriais.